



Plasmon-based spectral filtering with metallic nanostructures for CMOS image sensors

Romain Girard-Desprolet

► To cite this version:

Romain Girard-Desprolet. Plasmon-based spectral filtering with metallic nanostructures for CMOS image sensors. Optics / Photonics. Université Grenoble Alpes, 2015. English. NNT : 2015GREAT053 . tel-01219375

HAL Id: tel-01219375

<https://theses.hal.science/tel-01219375>

Submitted on 22 Oct 2015

HAL is a multi-disciplinary open access archive for the deposit and dissemination of scientific research documents, whether they are published or not. The documents may come from teaching and research institutions in France or abroad, or from public or private research centers.

L'archive ouverte pluridisciplinaire **HAL**, est destinée au dépôt et à la diffusion de documents scientifiques de niveau recherche, publiés ou non, émanant des établissements d'enseignement et de recherche français ou étrangers, des laboratoires publics ou privés.

THÈSE

Pour obtenir le grade de

DOCTEUR DE L'UNIVERSITÉ GRENOBLE ALPES

Spécialité : **Optique et Radiofréquences**

Arrêté ministériel : 7 août 2006

Présentée par

Romain GIRARD-DESPROLET

Thèse dirigée par **Guy VITRANT**

et codirigée par **Salim BOUTAMI** et **Sandrine LHOSTIS**

préparée au sein du **CEA Leti de Grenoble**, du laboratoire **IMEP-LAHC Grenoble INP** et de la société **STMicroelectronics Crolles**
dans l'École Doctorale d'**Électronique, Électrotechnique, Automatique et Traitement du Signal**

Filtrage spectral plasmonique à base de nanostructures métalliques adaptées aux capteurs d'image CMOS

Thèse soutenue publiquement le **15/07/2015**,
devant le jury composé de :

M. Michael CANVA

Directeur de Recherche au CNRS, Institut d'Optique Palaiseau, Président

Mme Nathalie DESTOUCHES

Professeur des Universités, UJM Saint-Etienne, Rapporteur

M. Evgeni POPOV

Professeur des Universités, Institut Fresnel, Univ. Aix-Marseille, Rapporteur

M. David R.S. CUMMING

Professeur des Universités, Université de Glasgow, Examineur

M. Guy VITRANT

Directeur de Recherche à l'IMEP-LHAC, Grenoble INP, Directeur de thèse

Mme Sandrine LHOSTIS

Docteur-Ingénieur, STMicroelectronics Crolles, Co-encadrante

M. Salim BOUTAMI

Ingénieur-Chercheur, CEA Leti Grenoble, Co-encadrant



**Filtrage spectral plasmonique à base de nanostructures
métalliques adaptées aux capteurs d'image CMOS**

**Plasmonic spectral filtering using metallic
nanostructures envisioned for CMOS image sensors**

À mes parents.

Remerciements

Acknowledgements

Cette thèse a été réalisée dans le cadre d'une convention CIFRE au sein du « Laboratoire Capteurs et NANophotonique » (LCNA) du CEA-LETI de Grenoble, de la plateforme Photonique de l'IMEP-LAHC, basé à Minatec à Grenoble, ainsi que de l'équipe « 3D Integration » du groupe « Technology R&D » (TRD) de la société STMicroelectronics à Crolles.

Tout d'abord, je tiens à remercier les membres du jury qui ont accepté d'évaluer mon travail de thèse, et je remercie en particulier Michael CANVA d'avoir présidé mon jury de soutenance. Je remercie également Nathalie DESTOUCHES et Evgeni POPOV d'avoir jugé ce travail en tant que rapporteurs, ainsi que David R.S. CUMMING pour l'avoir évalué en tant qu'examinateur. J'en retiendrai notamment les échanges et les retours particulièrement enrichissants qui ont suivi la soutenance.

Je tiens ensuite à remercier très sincèrement mon équipe d'encadrants directs, à savoir Guy VITRANT, mon directeur de thèse à l'IMEP-LAHC, ainsi que Sandrine LHOSTIS et Salim BOUTAMI, co-encadrants du côté de STMicroelectronics et du CEA respectivement. Tous les trois, je vous remercie pour le suivi exceptionnel dont vous avez fait preuve à l'égard de mon travail, qui a constitué un environnement extrêmement favorable au bon déroulement de cette thèse. Merci pour vos disponibilités, vos encouragements, vos contributions, vos conseils, vos retours et votre temps que vous m'avez toujours généreusement accordé tout au long de ces trois belles années. Avoir eu l'occasion de travailler avec vous a été un immense plaisir pour moi, en particulier avec votre bonne humeur constante et vos belles personnalités ! Puissé-je (ouh là, attention...) être aussi bons avec mes futurs éventuels thésards que vous l'avez été avec moi !

Bien que ne faisant pas partie de la liste « officielle » des encadrants, je tiens également à remercier Laurent FREY et Lilian MASAROTTO qui m'ont suivi de très près et qui m'ont beaucoup aidé, notamment au développement de la partie process de cette thèse. Je remercie de la même façon Alexis FARCY pour le temps qu'il m'a accordé et pour ses nombreux et judicieux conseils.

Ce travail a impliqué des collaborations avec de nombreuses équipes à différents niveaux de la thèse. Je remercie Clémence JAMIN-MORNET, Jérôme VAILLANT et Marilyn ARMAND pour leur aide sur le développement des outils d'évaluation et d'optimisation. Je remercie Vincent FARYS et Charlotte BEYLIER pour leur participation à mon étude en lithographie UV. Je remercie également les très nombreuses personnes qui m'ont aidé pour la réalisation expérimentale de mes structures, notamment Anne ROULE pour les dépôts de couches minces, Sébastien PAULIAC en e-beam, Anthony DE LUCA pour la structuration des filtres, et Aurélien GINET pour le remplissage des structures. Un grand merci également à Fabien LAULAGNET et à Olivier LARTIGUE pour leur aide sur la caractérisation optique des filtres !

Merci aux nombreuses personnes qui m'ont aidé, de près ou de loin, à faire progresser mon travail de thèse : Pierre BRIANCEAU, Maryline CHARLES, Marie-Laure CORDINI, Perceval COUDRAIN,

Loubna EL MELHAOUI, Jean-Marc FABRY, Olivier GIRARD, Katia HAXAIRE, Nicolas HOTELLIER, Michel MARTY, Jean-Pierre NIETO, Catherine PELLE, et tant d'autres !

Merci à Jean MICHAILOS pour son accueil au sein du groupe 3D Integration, ainsi qu'à l'ensemble de l'équipe ST, et merci à Jérôme HAZART, à Christophe KOPP et à tout le labo LCNA pour leur accueil côté CEA.

Comment ne pas mentionner également tous les doctorants et jeunes docteurs avec qui j'ai partagé tant de bons moments durant l'aventure ! Benjamin, Simon, Yann (Team Building FTW), Émilie, François, Kévin, Louis-Michel, Olga, Papa, Rafael, Thomas, ainsi qu'Ainur, Anthony, Boris, Boubacar, Cédric, Hélène, Ivan, Julien, Justin, Mandiaye, Matthieu, Ujwol, Vipin...

Enfin, je remercie tout particulièrement ma famille, qui m'a toujours soutenu et qui je sais, me soutiendra encore, dans mes choix, mes décisions et dans les épreuves difficiles !

Contents

Contents	xi
List of symbols	xv
Acronyms.....	xvii
Introduction	1
1 Introduction to CMOS imaging applications and spectral filtering	5
1. 1 CMOS image sensors	6
1. 1.1 Principle of image sensing	6
1. 1.2 Structure of a CMOS image sensor.....	7
1. 1.2.1 Microlenses	8
1. 1.2.2 Color filters	8
1. 1.2.3 Photodiodes: the photoelectric effect	9
1. 1.2.4 Case of back-side illumination	10
1. 1.3 Image reconstruction.....	11
1. 1.3.1 Color interpolation	11
1. 1.3.2 White balance	12
1. 1.3.3 Color correction.....	13
1. 1.4 Main figures of merit	13
1. 2 Ambient Light Sensors	14
1. 2.1 Background.....	14
1. 2.2 Market trends	15
1. 2.3 Principle.....	16
1. 2.4 Structure and integration.....	17
1. 3 Review on spectral filtering solutions	18
1. 3.1 Organic resists	18
1. 3.2 Interference filters	19
1. 3.3 Diffractive filters.....	21
1. 4 The plasmonic alternative.....	21
1. 4.1 Electromagnetic waves propagation	21
1. 4.2 Optical properties of metals	22
1. 4.3 Surface plasmon resonances	24
1. 4.3.1 Surface plasmon polaritons	24
1. 4.3.2 SPP excitation conditions	25
1. 4.3.3 Plasmons properties in the visible range	26
1. 4.3.4 Localized plasmon resonances	27
1. 5 Thesis objectives: the challenges of plasmonic filtering	28
2 CMOS integration of nanostructures for plasmonic filtering.....	29
2. 1 Method for optical simulations: RCWA.....	30
2. 1.1 Numerical methods for periodic structures	30
2. 1.2 The RCWA principle	31
2. 1.3 Information about the code used.....	32

2. 2	Performance evaluation tools	33
2. 2.1	Ambient Light Sensors	33
2. 2.1.1	The global ALS sensitivity.....	33
2. 2.1.2	The performance criteria	34
2. 2.2	RGB image sensors	37
2. 3	Plasmonic structures for spectral filtering	38
2. 3.1	Metal-Insulator-Metal structures	39
2. 3.1.1	Generalities on MIM arrays	39
2. 3.1.2	Material for the dielectric core	40
2. 3.1.3	Structures investigation.....	41
2. 3.1.4	Angular stability.....	43
2. 3.2	Metallic patch arrays	43
2. 3.2.1	Introduction to metallic patch arrays.....	43
2. 3.2.2	Square patches.....	44
2. 3.2.3	Cruciform patches	45
2. 3.3	Hole arrays in a metallic layer	47
2. 3.3.1	Extraordinary Optical Transmission in subwavelength hole arrays	47
2. 3.3.2	Impact of the material properties	48
2. 3.3.3	Square arrays of holes	49
2. 3.3.4	Hexagonal arrays of holes	51
2. 3.3.5	RGB filters	53
2. 3.4	Conclusion on plasmonic structures	54
2. 4	Optimal integration solution for plasmonic ALS	54
2. 4.1	Integration level of plasmonic filters	54
2. 4.2	Location of the metallic layer	55
2. 4.3	Distance of the filters to the passivation layers	57
2. 5	Conclusion on Chapter 2	58
3	Evaluation of plasmonic filters for Ambient Light Sensors	61
3. A.1	Review on the impact of geometrical parameters	62
3. A.1.1	Metal thickness h_m	62
3. A.1.2	Effect of the a/P ratio	64
3. A.1.3	Shape factor b/a	66
3. A.1.4	Intercrosses distance d	68
3. A.2	Illustration with color filters.....	72
3. A.2.1	RGB filters selection	72
3. A.2.2	Color errors and illumination conditions	73
3. A.3	Conclusion on optimal design rules	75
3. B.1	Positioning of plasmonic filters.....	76
3. B.1.1	Evaluation of plasmonic filters performance	76
3. B.1.2	Angular tolerance	78
3. B.1.3	Other potential ALS structures	79
3. B.2	Noble metals alternative.....	80
3. B.2.1	Silver-based filters	81
3. B.2.2	Gold-based filters	82
3. B.3	Conclusion on ALS performances	82
3. B.4	Conclusion on Chapter 3	83
4	Robustness of plasmonic filters to process variations and Front-End fabs limitations.....	85
4. 1	Identification of the process limitations	86
4. 1.1	Simplified process route	86
4. 1.2	Expected hard points	87
4. 2	Materials-related dispersions.....	88
4. 2.1	Thicknesses and refractive index dispersions	88
4. 2.2	Metal oxidation.....	91
4. 3	Lithography inaccuracies	94
4. 3.1	Rounding of the crosses.....	94
4. 3.2	Impact of rounded corners on angular stability	99
4. 3.3	Variations of the apertures dimensions.....	100
4. 4	Filter nanostructuration	101

4. 4.1	RCWA modeling of etching slopes	101
4. 4.2	Impact of sloped profiles	102
4. 5	Holes filling	105
4. 5.1	Importance of the dielectric surrounding	105
4. 5.2	Impact of air gaps during holes filling	106
4. 6	Conclusion on Chapter 4	108
5	Realization and characterization of ALS plasmonic filters	111
5. 1	Experimental conditions	112
5. 1.1	Integration constraints and limitations	112
5. 1.2	Process route description	112
5. 1.3	Designs selection and Electron-Beam Lithography bases	115
5. 2	Development of a wafer-level integration	117
5. 2.1	Materials and interfaces quality	117
5. 2.2	Electron-beam lithography and corrections	122
5. 2.3	Aluminum nanostructuration	127
5. 2.4	Holes filling	133
5. 2.5	Validation of the bonding on glass wafers	137
5. 3	Evaluation of the fabricated ALS filters	141
5. 3.1	Responses and performance at normal incidence	141
5. 3.2	Angular tolerance of the filters	145
5. 4	Conclusion on Chapter 5	148
	Conclusion and Outlook	151
	Bibliography	155
	Appendix	169
	Appendix A	171
	Appendix B	173
	Appendix C	177
	Appendix D	181
	Communications and patents	183
	French summary	185

List of symbols

a	Pattern (hole, patch, MIM) size. Diameter for circles, size for squares, arm length for crosses
b	Arm width of cruciform patterns
B	Magnetic induction
c	Celerity of light in vacuum
d	Smallest inter-distance between two cruciform patterns
e	Free electron charge
D	Electric displacement
E	Electric field
ff	Fill factor
H	Magnetic field
h	Plank constant
h_{MAT}	Thickness of the layer made of material MAT
h_m	Thickness of a metallic layer
I	Intensity
k	Wavevector norm (vector if bolded)
l	Arm length of cruciform air gaps in SiO_2
L_{SPP}	Propagation length of plasmons
m_e	Free electron effective mass
n	Refractive index ($n = n' + i.n''$)
P	Period
R	Radius of curvature
Q	Electromagnetic radiant energy
Q_v	Luminous energy
S	Sensitivity (of a sensor)
SNR_{10Y}	Scene illuminance (lx) required to have a signal-to-noise ratio (SNR) equal to 10
sf	Shape factor of cruciform patterns (b/a)
w	Arm width of cruciform air gaps in SiO_2
Z	Acoustic impedance

α	Slope of slanted etching profile
γ	Damping frequency
δ	Penetration depth of plasmons
ΔE_{2000}	CIE color error
$\varepsilon(\omega)$	Dielectric function
ε_0	Dielectric permittivity of vacuum
ε_r	Relative dielectric permittivity
θ	Polar angle of incidence
λ	Wavelength
μ_0	Magnetic permeability of vacuum
μ_r	Relative magnetic permeability
ν	Frequency
ρ	Material density
ρ_{free}	Free charges density
σ	Standard deviation
φ	Azimuth
Φ	Electromagnetic radiant flux
Φ_v	Luminous flux
ω	Angular frequency

Acronyms

AA	Anti-Aliasing
ALS	Ambient Light Sensor/Sensing. <i>May be used as adjective to qualify the device. Ex: ALS sensor, ALS filter.</i>
BARC	Bottom Anti-Reflective Coating
BEoL	Back-End of Line
BSI	Back-Side Illumination
CCD	Charge-Coupled Device
CFA	Color Filters Array
CIE	Commission Internationale de l'Eclairage <i>International Commission on Illumination.</i>
CIS	CMOS Image Sensor
CMOS	Complementary Metal-Oxide-Semiconductor
CMP	Chemical Mechanical Planarization/Polishing
CVD	Chemical Vapor Deposition
EB(L)	Electron Beam (Lithography)
FDTD	Finite Difference Time Domain
FIB	Focused Ion Beam
FSI	Front-Side Illumination
FWHM	Full Width at Half-Maximum
HDP(CVD)	High Density Plasma (Chemical Vapor Deposition)
IMD	Inter-Metallic Dielectric
IR	Infrared
LSP(R)	Localized Surface Plasmon (Resonance)
NIR	Near Infrared
PEALD	Plasma-Enhanced Atomic Layer Deposition
PECVD	Plasma-Enhanced Chemical Vapor Deposition
PMD	Pre-Metallic Dielectric
PSG	Phosphorus Silicate Glass
PVD	Physical Vapor Deposition

RCWA	Rigorous Coupled Wave Analysis
RI	Refractive index
SACVD	Sub-Atmospheric Chemical Vapor Deposition
SEM	Scanning Electron Microscope/Microscopy
SNR	Signal-to-Noise Ratio
SOI	Silicon On Insulator
SPP	Surface Plasmon Polariton
QE	Quantum Efficiency
UV	Ultraviolet

Introduction

The microelectronics industry is one of the technological sectors experiencing the fastest market progressions. Combined with the considerable development of nanotechnologies, the continuation of the Moore's law [1], which describes the constant miniaturization rate of electronic components, has led to an explosion of the demand for embedded sensors with various functions. Those on which we will focus in this thesis constitute the family of light sensors in general. Among them, image sensors are the most widespread and have been omnipresent in our environment for a while, with for instance cameras, webcams or surveillance systems. More recently, the exponential growth of the wireless communication market has greatly renewed the demand for such sensors (Figure 1). In particular, the emergence of handheld device such as smartphones or tablets has generated a constantly rising interest for miniaturized image sensors with the embedding of camera functions. Ambient Light Sensor applications have been developed, which purpose is to smartly manage the screen backlight as a function of the surrounding brightness in order to improve the visual experience of the user and to reduce the energy consumption of the device. These sensors share a similar integration, characterized by the filtering of the photons useful to their respective functions, performed with organic resists in most cases. These resists however impose strict restrictions on the sensor integration due to their sensitivity to thermal treatments and require the use of an additional and thick IR-cut filter since they cannot filter the undesired infrared signal. The necessity of this external IR-cut glass increases the thickness of these sensors in a context where the market is motivated by the reduction of the costs and by the demonstration of technology showcase with always thinner devices. It has thus become important to find out innovative filtering solutions able to follow these market trends in order to propose competitive image or light sensors.

In recent years, there has been a growing interest in literature for an emerging field of photonics that allows for the manipulation of light at nanoscale with periodically structured metallic layers: Plasmonics. This domain owes its name from the engineering of confined electromagnetic waves located at a metal-dielectric interface known as plasmons. A surface plasmon is defined as a collective excitation of the free-electron gas at the surface of the metal that can be excited from a coupling with incident photons in proper conditions. In the case of periodic metallic array, an essential property of plasmons is that they are excited and resonate for specific wavelengths related to characteristic dimensions of the structures. This phenomenon makes plasmonics particularly suited for filtering applications, for which the operating wavelengths can be simply tuned by varying the size of the structures. In particular, since metals such as aluminum, silver or gold sustain plasmons in the visible and NIR ranges, many works have demonstrated the realization of color filters that would present the huge advantage of requiring a single lithography step only. Thanks to the electromagnetic properties of metals, these filters are furthermore able to cut the undesired infrared signal by themselves. However, most studies use materials that are avoided in industrial clean rooms and fabricate filters with processes that are not compatible with the high-throughput constraint of commercial productions. Very little information is thereby available in terms of integration and performance to envision a technological transfer of plasmonic filters from laboratories to industrial products.

Consequently, this thesis aims to assess the potential of plasmonic filters to provide an efficient and viable alternative to current filtering solutions in view of a future transfer towards industrial applications. In this PhD work, the targeted applications consist of image sensors and ambient light sensors. This objective is split into two major axes. The first one is the study and the selection among different plasmonic structures of those providing the best theoretical performance for light sensor applications, while fitting in the same time their associated technological challenges and the industrial constraints. The second axis is to assess the viability of the fabrication of such structures with respect to the integration issues inherent to plasmonic filters and to the process dispersions that have to be expected for a wafer-scale production. To achieve this, the thesis is articulated according to the outline presented below.

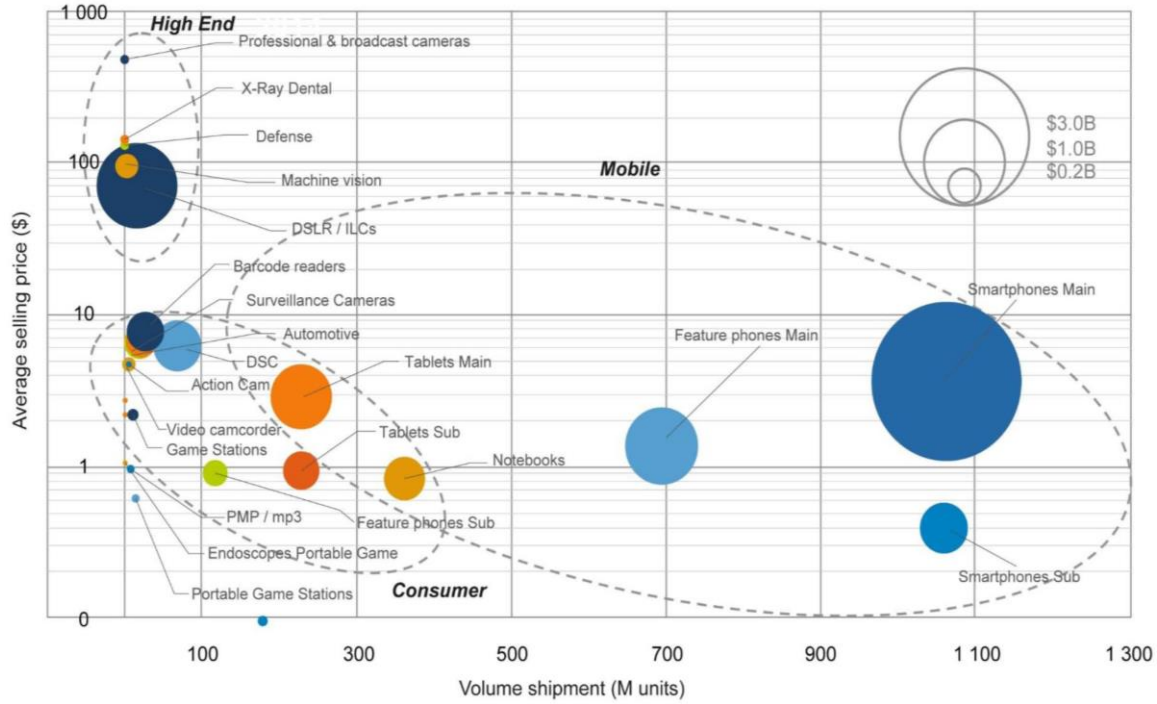


FIG. 1. 2014 CMOS image sensor market landscape [2].

First of all, we will describe in Chapter 1 the interest of plasmonic filtering for light sensors. First we will present the respective structures and principles of both CMOS image sensors and ambient light sensors, leading to the challenges of spectral filtering. A focus will be made on the filtering part of these devices with a review of the most widespread kinds of filters, with their advantages and their limits. The principle of plasmonic filtering will then be introduced. The potential of this solution for light sensor applications will be presented. The related challenges will be explained and the methodology chosen in this thesis work will be described.

Chapter 2 consists in the identification of plasmonic structures that would fulfill light sensor requirements. First, the simulation and evaluation software used in this work will be detailed. The specifications related to image sensors and ambient light sensors will be explained. From this, the selection of the most suited plasmonic structures will be performed through the evaluation of their ease of fabrication, optical properties and angular stability. A direct integration of filters respecting the CMOS compatibility required in industrial fabs will be proposed. This chapter will permit to identify the best CMOS-compatible structures and materials able to solve the targeted application-related issues.

In Chapter 3, the best plasmonic structures for ambient light sensor application will be evidenced. First, a comprehensive investigation of the angular properties of cross-shaped-hole array will be presented in order to limit the sensitivity of our plasmonic filters to the angles of incidence and to

polarization. From these results, the evaluation of plasmonic filters envisioned for ambient light sensors will be performed. We will be able at the end of this chapter to assess the theoretical potential of plasmonic filters and to propose optimal performances for this application.

In Chapter 4, the potential impact of process-related factors on plasmonic filters performance will be simulated. Since the plasmon resonances depend on the size and the shape of the structures, we will first evaluate the sensitivity of plasmonics filters to process inaccuracies. The main defects that can be expected at each step of the fabrication will be modeled. The variations on the main parameters will be studied according to typical dispersions of a 300-mm-wafer production for the deposition and the lithography step, together with the possible rounding of the cruciform holes. The respective impact of sloped profiles in the metal after the etching and of air gaps during holes filling will be evaluated. The critical steps of the fabrication will thus be identified and evaluated.

Chapter 5 is dedicated to the process and measurement of plasmonic structures. First, the process development of the plasmonic filters selected from Chapter 3 will be presented in the light of the previous studies with wafer-scale equipment. The main issues and dispersions of each fabrication step will be observed and compared with the simulation work of Chapter 4. The obtained filters will be optically characterized to evaluate their performance and to compare them to those calculated from the theoretical development of previous chapters. The viability of the plasmonic solution in terms of performance and integration will thus be assessed.

Finally, a conclusion will be made on the ability of plasmonic filters to propose efficient optical performance and to be transferred to industrial fabrication lines envisioned for commercial applications. A few thoughts on the prospective of this thesis will also be discussed.

Chapter 1

Introduction to CMOS imaging applications and spectral filtering

Digital image sensors have experienced a significant development since their first emergence in the late 60's and currently constitute a US\$10B market [2]. They have now reached a very attractive cost/performance ratio that makes them usable in various applications, from high-tech mobile device to spatial or medical equipment. Image sensors have thus quickly become a major technological issue in the microelectronics industry, with a forecast growth rate of 10.6 % from 2014 to 2020 and a US\$16.2B market to be reached in 2020. From the beginning of digital imagery, two distinct types of sensors have been coexisting: the CCD sensors (for Charge-Coupled Device) and the CMOS sensors. They mainly differ by the mechanism of the charges reading after the photo-conversion. In our case, we only focus on CMOS sensors, which give nowadays performance similar to CCD ones and are generally preferred for mobile electronic consumer goods owing to their low production costs and energy consumption [3]. In these sensors, the use of organic resists to perform filtering functions has progressively reached its limits due to two major issues. First, the thermal sensitivity of the resists blocks their position at the very last level of the sensors, letting very few options to consider more advanced integrations. Secondly, their inability to filter the infrared signal imposes the use of an external IR-cut glass. This glass has a thickness of about one millimeter, in a context where the thinnest flagship smartphones on the market fall below 5 mm. Moreover, recent trend in light sensors is the manufacturing of *combined* sensors, which feature two or more functions on the same chip, such as visible and infrared detections for instance (Figure 1.1). In such sensors, the IR-cut glass has to be patterned so that it covers only the corresponding areas of the sensors, and this patterning is expensive. These limitations nowadays represent an obstacle to the development of innovative integrations that would ensure the competitiveness of these sensors.

The first part of this chapter constitutes an introduction to the principle of color sensing and to the general structure of CMOS image sensors, where mainly the light travel is described from the incidence on the optical system to the photons conversion in the photodiodes. In a second part, we will describe this work's main concern which is another application of optical sensors in the visible range that has recently experienced a huge gain of interest in mobile device featuring a screen, since it allows for the automatic adjustment of the display's backlight: the Ambient Light Sensors (ALS). We will then specifically introduce the issue of the thesis regarding the spectral filtering step by first presenting the main existing filtering solutions that are used in images sensors. The plasmonic theory will finally be introduced to explain how it can provide an alternative filtering solution to organic resists.

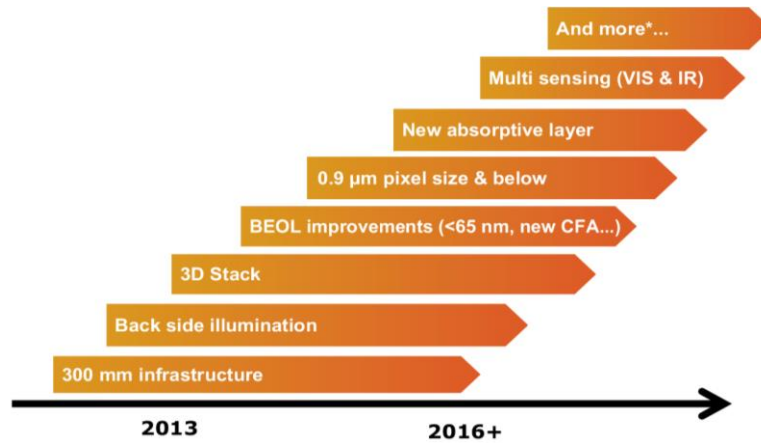


FIG. 1.1. CMOS image sensors' technological evolution, including the combined sensors (multi-sensing) [2].

1.1 CMOS image sensors

1.1.1 Principle of image sensing

A general schematic of the main steps of image sensing and image processing allowing for the capture and the conversion of the photons of a given scene into a digital image is presented in Figure 1.2. The operating principle of an image sensor can be explained by making the distinction between two different parts. The first one is the macro-scale complete device which features the packaging element of the sensor, the focusing lens, an infrared-cut glass filter and then the CMOS chip, which constitutes the second part. This micro-scale system on chip can itself be subdivided into two functions that are the analogic guidance and photo-conversion of the photons, and the digital treatment of the converted signal. We propose in the following section a brief description of the light path from the scene capture to the digitally processed image.

At first, the photons coming from the light source (i.e. the sun or an artificial lightning) are reflected by the elements of the scene. Depending on the properties of the materials composing these elements, only a portion of the impinging photons are re-emitted, whose wavelengths define the color that we see from these objects. These reflected photons are captured by the global sensor and pass through an optical system, namely the main lens that focuses them on the chip located at the end of the sensor. Before reaching this chip, the light also encounters an IR-cut filter and a low-pass antialiasing filter (denoted AA filter).

On top of the photosensitive area of the chip, an array of microlenses focuses the light towards each photo-site, which corresponds to the photosensitive area of one pixel. On each pixel, the photons are then filtered according to one given wavelength (or color), generally among the blue, green or red colors. They finally reach the silicon photodiodes where they are converted into electrical charges in the form of electron-hole pairs thanks to the photoelectric effect, themselves converted into an electrical tension. An analog-to-digital conversion of this electrical quantity is performed and several different processing are then realized to reconstruct the final image, including the color interpolation, the white balance and the color correction. More details on the role and the principle of each of these main steps are given in the following sub-sections.

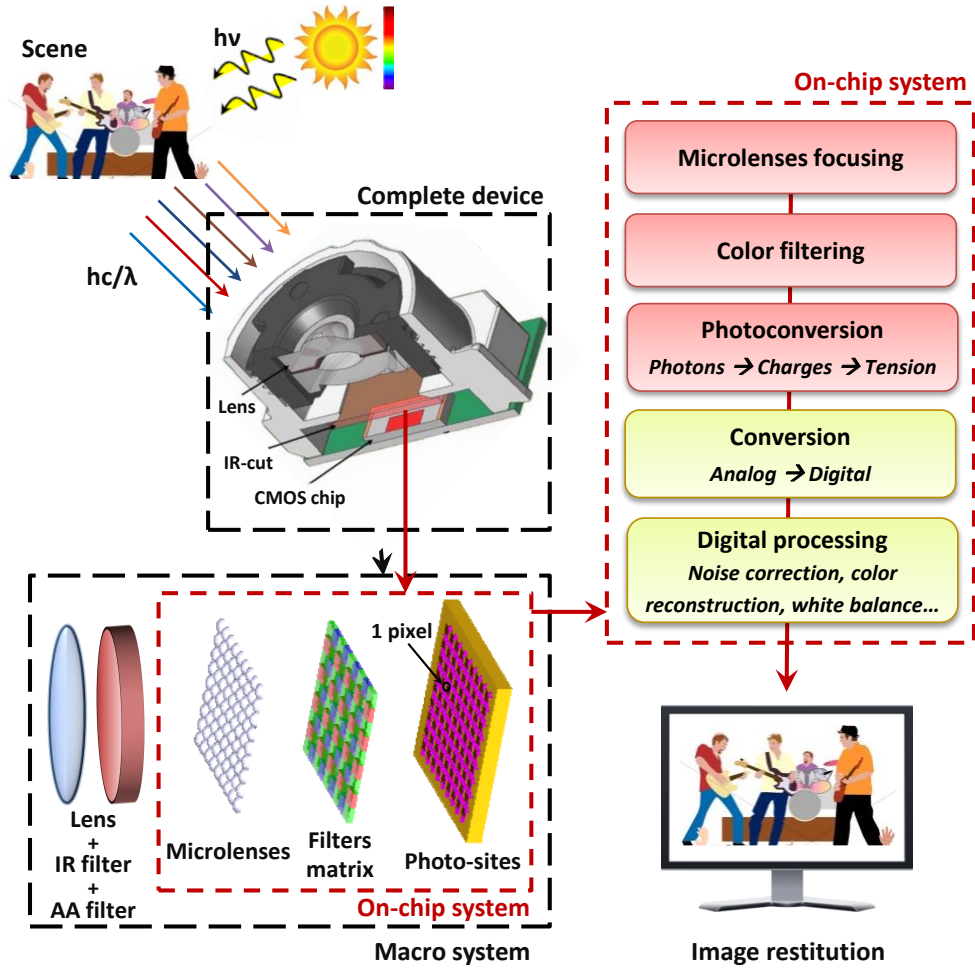


FIG. 1.2. General principle of image sensing. The main parts of an image sensor are summarized, from the capture of the scene photons to the reconstitution of the digital final image [4], [5].

1.1.2 Structure of a CMOS image sensor

The useful signal for an image sensor is exclusively within the visible range, which is defined between 380 nm and 780 nm. As we will see later, the silicon that constitutes the photodiodes absorb photons with wavelengths up to 1.1 μm , meaning that photons with wavelengths in-between 780 nm and 1.1 μm do not contain any color information and thus disturb the desired signal. That is why once the light has impinged the sensor and has been focused by the main lens, it first goes through an IR-cut filter to remove the near-infrared (NIR) signal that will not be filtered by the color filters. An additional filter is also required, known as a low-pass anti-aliasing filter whose purpose is to remove the high spatial frequencies components to avoid the spectral folding phenomenon, characterized by the appearance of moiré patterns.

Photons then hit the photosensitive area of the silicon-based CMOS chip, which contains the pixels array. Each pixel is itself composed of a microlens, a filter and a photosensitive site, the photodiode, surrounded by many transistors used to collect, to convert and to read the photo-generated electrons. The ratio of the photodiode area to the total area of a pixel is called its fill factor, typically in-between 30 % and 50%. The structure stack of one pixel is provided in Figure 1.3 and detailed in the following.

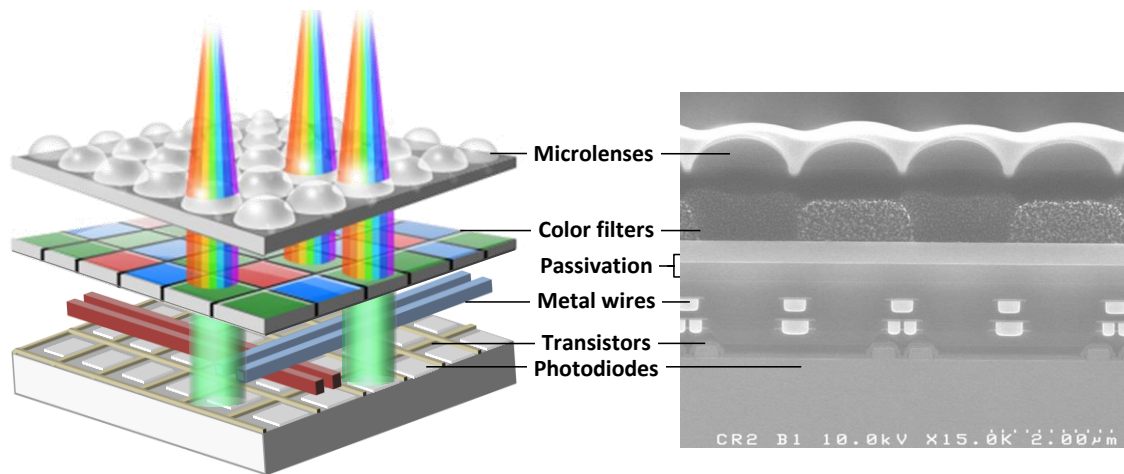


FIG. 1.3. Schematic and actual SEM cross section of a CMOS image sensor chip structure. The right picture represents a STMicroelectronics 2.2 μm pixel, fabricated with a 0.13 μm process technology.

1. 1.2.1 Microlenses

As we have seen in the introduction of *section 1.1.2*, the fill factor of the sensitive part of the pixels is inferior to half their total area, which means that a significant portion of the incoming light would not reach the photodiodes and would thus be lost. To increase the photons collection, an array of microlenses is fabricated on top of the structure to focus the incident light on the photodiodes. The presence of micro-lenses increases the photons absorption and can then raise the photodiode effective fill factor to 80 %, as explained in Figure 1.4. The fabrication of microlenses is performed with a photosensitive resist periodically patterned by photolithography and annealed to give them their drop-like shape.

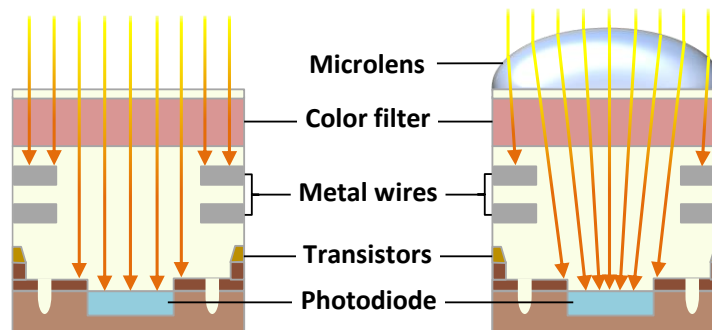


FIG. 1.4. Role of the microlenses array for the photons collection: photons collection without (left) and with microlens (right).

1. 1.2.2 Color filters

In 1802, Thomas Young hypothesized that the human vision was permitted by the existence of three elementary receptors, each sensitive to one particular color (these receptors are nowadays known as the blue, green and red cones). Pursuing Young's work, Helmholtz, and especially Maxwell demonstrated in 1855 that any visual light can be decomposed according to three particular colors (or wavelengths): the primaries. This Young-Helmholtz theory, also called the trichromatic invariance constitutes, with the proof that any color can be reproduced with the combination of three primary colors, the origin of our modern colorimetry.

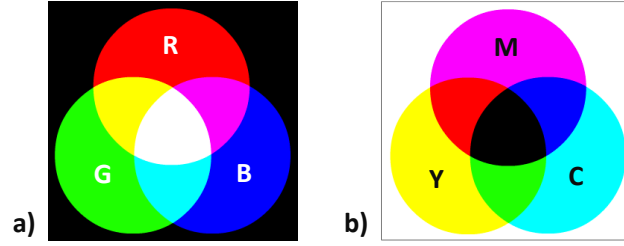


FIG. 1.5. a) Additive synthesis with R (red), G (green) and B (blue) components. b) Subtractive synthesis with M (magenta), Y (yellow) and C (cyan) components.

From this principle, two kinds of color synthesis are derived: the additive and the subtractive syntheses (Figure 1.5). The subtractive synthesis is used in painting or in printing since it relies on the selective absorption of the light by the materials (pigment, ink...). Conversely, the additive synthesis is used with the addition of light sources, where the absence of any primary colors results in the black color, whereas their addition in equal quantities results in the white color. This method is particularly used in display applications or in image sensing. In image sensors, we thus aim to collect only the primary color components of the scene by using a Color Filters Array (CFA) beneath the microlenses matrix. The global signal is thereby spatially sampled, with each pixel only filtering a single wavelength band, generally around the blue (about 460 nm), green (about 540 nm) and red colors (about 610 nm). Although several different arrangements exist, the most common pixel array in image sensors is the Bayer's matrix [6], from the name of the inventor who patented it (Figure 1.6). One can notice there are twice as many green pixels as the blue or the red ones. This specificity provides a high resolution on the green information, to which the human eye is particularly sensitive. The filters are generally realized with organic color resists. The filtering step of image sensors being the central part of this thesis, we will go into more details about it throughout this chapter.

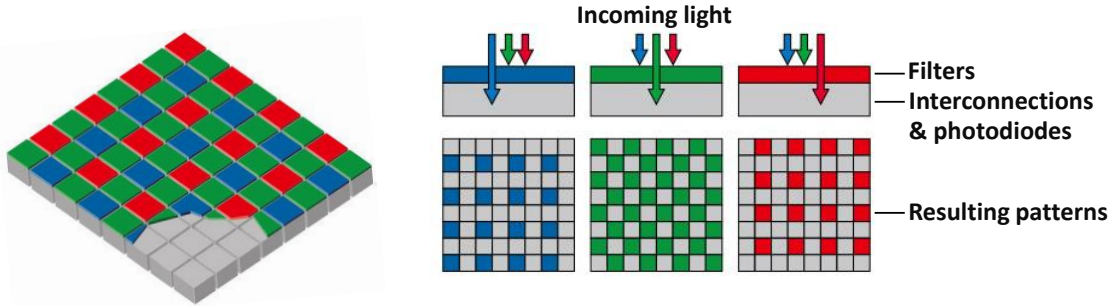


FIG. 1.6. Schematic of the Bayer's color filters pattern [7]. A distinction is made between the green pixels G_R in a red line and G_B in a blue line.

1.1.2.3 Photodiodes: the photoelectric effect

Beneath the metal interconnections wiring the transistors with each other, the silicon photodiodes collect the information related to luminance, i.e. the quantity of light (photons) that hit the pixels. The photodiodes are conceived around the PN junction principle, where a silicon area doped with electrons (N-doped) is put in contact with a silicon area doped with holes (P-doped). The absorption mechanism of light by matter in semi-conductors is due to the capture of photons by the electrons of the atoms composing the material, which elevates the electrons from their ground state in the valence band to excited states with higher energy in the conduction band (Figure 1.7). This excitation is only possible if the energy of the incoming photon $h\nu$ is superior to the forbidden band gap E_g , corresponding to the energy difference between the lowest energy level of the conduction band E_c and the highest energy level of the valence band E_v (see Eq. 1.1, where h stands for the Planck constant in $m^2.kg.s^{-1}$ and ν is the

frequency of the photon in Hz). In this situation, the photon absorption thus creates an electron-hole pair: this phenomenon constitutes the photoelectric effect [8]. The induced electric field E_i in the depletion region of the PN junction separates the holes from the electrons, which leads to the production of an electric current. The electrons being all identical, the potential exceeding energy ($h\nu - E_g$) is dissipated into the materials in the form of heat.

$$h\nu > E_g, \quad \text{with } E_g = E_c - E_v \quad (\text{Eq. 1.1})$$

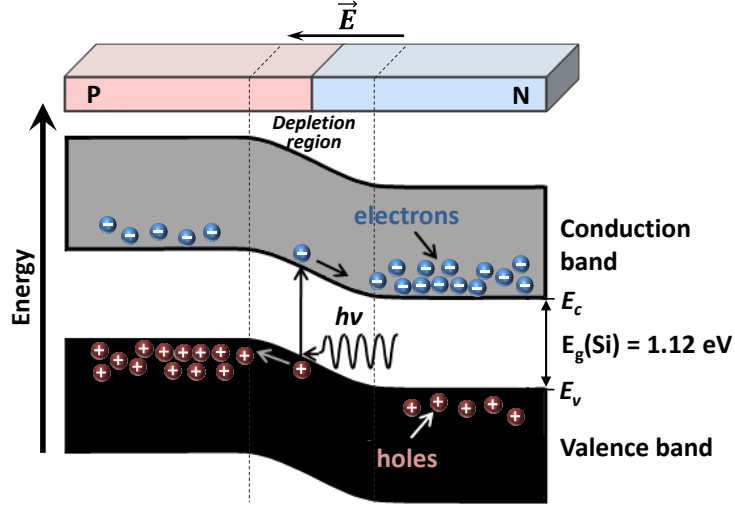


FIG. 1.7. Principle of the photoelectric effect: energy bands around the PN junction [4], [9].

From Eq. 1.1, the maximum wavelength λ_{max} at which the photoelectric effect occurs in a semiconductor can be deduced from the band gap energy (Eq. 1.2, with c the celerity of light in $m.s^{-1}$). Silicon has a band gap of 1.12 eV, and thereby absorbs photons with wavelengths up to 1.1 μm , which explains why a filter cutting the infrared signal is required above the sensor. The absorption of light in silicon occurs at different depths according to the photons wavelength. The light penetration is governed by a Beer-Lambert absorption law (Eq. 1.3), where I_0 stands for the intensity of the incident light, $I(z)$ for the intensity of the radiation at depth z and $k_{Si}(\lambda)$ for the absorption coefficient of silicon. There are different ways of managing the storage and the transfer of the created charges (CMOS, CCD), but they won't be discussed in this thesis.

$$\lambda_{max} = \frac{hc}{E_g} \quad (\text{Eq. 1.2})$$

$$I(z) = I_0 \cdot \exp\left(-\frac{4\pi k_{Si}(\lambda)}{\lambda} z\right) \quad (\text{Eq. 1.3})$$

1. 1.2.4 Case of back-side illumination

The image sensors market has been more and more demanding for the fabrication of higher resolution sensors at competitive price, which implies a high fabrication throughput. Yet, with the constant shrink of pixel size, less light is being captured in each pixel, which deteriorates the performance of the sensors, especially in low-light conditions. The most widespread structure presented in Figure 1.3 is known as the front-side illumination (FSI). We have seen that in this case, the fill factor of the active area is small (inferior to 50 %) due to the presence of the metal wiring and the transistors between the filters and the photodiodes, that take up a lot of space and hinder light propagation.

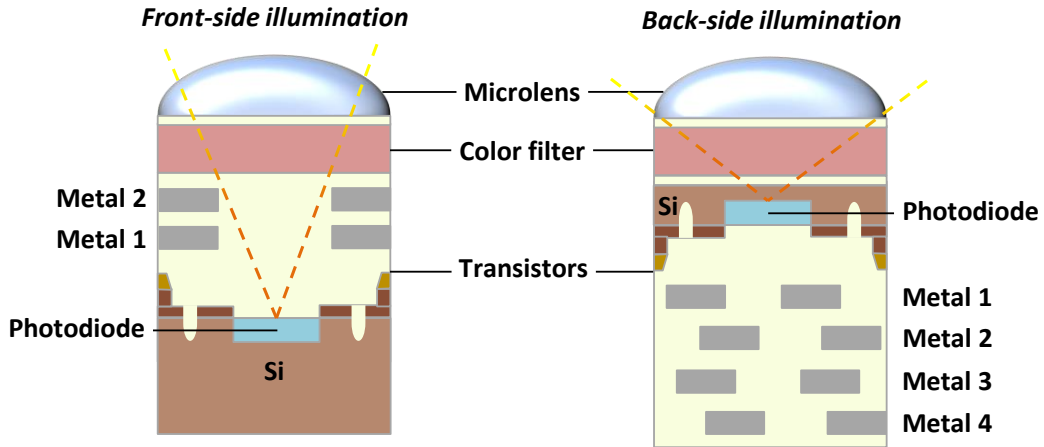


FIG. 1.8. Comparison of a FSI sensor (left schematic) with a BSI sensor (right schematic).

An innovative alternative was thus introduced by Sony in 2006 [10], called the back-side illumination (BSI). The principle of this structure is to place the photodiodes directly under the filters and to wire the transistors beneath the photodiodes, where they do not hinder light propagation. A description of the BSI principle is given in Figure 1.8. In practice, BSI and FSI sensors own the same elements, but the FSI ones are sequentially fabricated on the front on the silicon wafer, hence their name. Conversely in the BSI case, after the photodiodes then the metal interconnections are realized, the wafer is flipped and thinned so that the filters and the microlenses can be fabricated directly above the photodiodes, on the back-side of the wafer. This Sony development was made on SOI and demonstrated an increase on the quantum efficiency of the sensor (e.g. a 38 % increase at 540 nm) and a significant improvement of the angular response compared with the conventional FSI solution since the interconnections are not in the optical path [11]. STMicroelectronics and the CEA Leti-MINATEC also demonstrated in 2007 a BSI solution on SOI with a high level of miniaturization (1.45 μm pixel size) with a very low noise level [12]. In our case, BSI structures could provide interesting performance improvements, but they are a bit more expensive to fabricate.

1. 1.3 Image reconstruction

After the electrical charges have been collected and transferred, the corresponding tension at each pixel's output (CMOS) or pixels column's output (CCD) is digitally sampled. This analog-to-digital conversion allows for an easier processing of the captured image and can be directly done on the chip with its logic elements. The first processing from the raw image is the offset correction, which consists in removing the spatial noise by subtracting a black image obtained with hidden pixels to each color plane. Afterwards, there are three main treatment steps to go from the collected signal to the final image. The three steps consist of: the color interpolation, the white balance and the color correction. Other additional steps can be added for the image correction and for the image display on a screen.

1. 1.3.1 Color interpolation

Since each pixel only detects one color, the sensor signal does not contain any color information and the raw image is thus monochrome (blue, green and red pixels each return a single value related to their respective number of collected photons, which leads to a greyscale information: white for a high signal level and black for a theoretically null signal). As we have seen it with the trichromatic invariance, a color is defined with its combination of the three primary colors. In order to display a colored image on a

screen, each pixel has thus to contain not one, but three values corresponding to its red, green and blue components. For example, a red pixel only contains its red components, but lacks the blue and green information to reproduce the actual color of the scene.

The determination of the lacking information is performed with the color interpolation. This algorithm consists in interpolating the color information of the closest neighboring pixels, as shown in Figure 1.9. The most common method for a Bayer matrix is the bi-linear interpolation which calculates the lacking components simply as the mean of the components of the surrounding pixels. Each color is generally encoded in 8 bits, which corresponds to 256 shades (the human eye can distinguish about 250 shades). Each pixel is thus encoded in 24 bits after the color interpolation step (8 bits for each primary color), which leads to the possible restitution of more than 16 million colors.

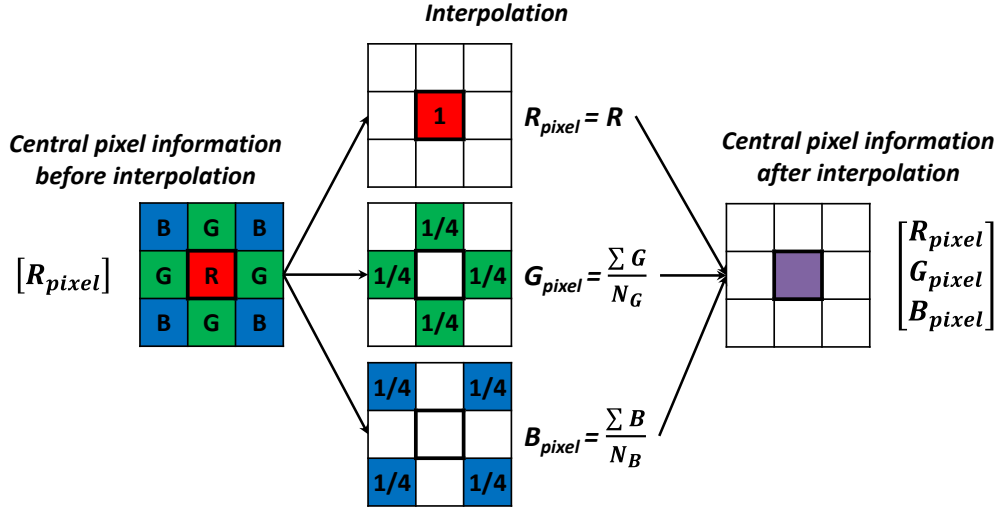


FIG. 1.9. Example of a bi-linear interpolation made on a red pixel of a Bayer matrix. Original schematic from [4].

1. 1.3.2 White balance

The term “light source” does not provide any quantifiable information regarding the spectral power distribution enlightening the scene (i.e. the amount of energy received at each wavelength). For colorimetric considerations, we rather talk about illuminant, which refer to a mathematical spectral power distribution instead of solely the nature of the source (sun, lamp, etc.) (Figure 1.10). An illuminant may represent an existing light source or only a theoretical spectral power distribution. The 'Commission Internationale de l'Eclairage' (CIE, from the French acronym) defined a set of reference illuminants that will be used later in this thesis. Since no illuminant has a constant spectral distribution, the spectrum of the illuminant enlightening the scene thereby has a substantial impact on the way the colors are sensed by the pixels. Furthermore, the sensor does not have the same sensibility for each color. In order to correct these effects, we use a correction called the white balance whose purpose is to make sure that a white object in the scene will indeed be white after the color correction. The correction is performed with a diagonal matrix given in Eq. 1.4.

$$\begin{bmatrix} R \\ G \\ B \end{bmatrix}_{WB} = \begin{bmatrix} R_{WB} & 0 & 0 \\ 0 & G_{WB} & 0 \\ 0 & 0 & B_{WB} \end{bmatrix} \cdot \begin{bmatrix} R \\ G \\ B \end{bmatrix}_{Interp} \quad (\text{Eq. 1.4})$$

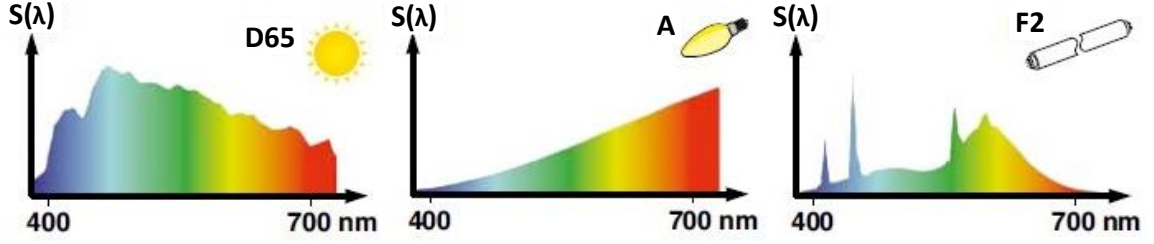


FIG. 1.10. Examples of relative spectral power distributions for 3 different illuminants as defined by the CIE (D65 sunlight, A incandescent lamp and F2 fluorescent lightning) [13].

1. 1.3.3 Color correction

The filters are not perfect and a portion of photons with undesired wavelengths can still reach the photodiode of a given pixel (spectral cross-talk) during the exposure. Photons can also reach the neighboring photodiodes due to the reflections and diffractions that may occur on the optical path (optical cross-talk). Similarly after the photo-conversion, some electrons can diffuse towards the neighboring photodiodes (electrical cross-talk). These phenomena induce additional color errors for the image restitution. For example, red pixels would still capture photons even if there is no red color in the scene. To compensate for these effects, a color correction is applied to the three color planes with a color correction matrix (CCM) given in Eq. 1.5.

$$\begin{bmatrix} R \\ G \\ B \end{bmatrix}_{Correc} = \begin{bmatrix} c_{RR} & c_{GR} & c_{BR} \\ c_{RG} & c_{GG} & c_{BG} \\ c_{RB} & c_{GB} & c_{BB} \end{bmatrix} \cdot \begin{bmatrix} R \\ G \\ B \end{bmatrix}_{WB} \quad (\text{Eq. 1.5})$$

1. 1.4 Main figures of merit

We provide below the definition of the main electrical and optical parameters of an image sensor that will be used or referred to throughout this thesis to quantify the performance of the filtering structures that will be presented later. The reader can refer to the thesis of Arnaud Tournier [4] for further information regarding the various noise sources in image sensors, and to the thesis of Clemence Jamin [9] for an extensive reading on optical performance and photometry.

Dark current: This value is defined as the current generated by the sensor in the absence of incident light. It is produced by the charge generation in different areas of a photodiode or a MOS capacity. The thermal energy is absorbed by the material and can create hole-electron pairs that can be collected and added to the signal. The dark current is very sensitive to the morphological defects of silicon and to the temperature. It is generally given in e^-/s .

Quantum efficiency (QE): The quantum efficiency of a sensor is defined as the ratio of the number of collected electrons to the total number of incident photons. The components that lead to a QE decrease in a pixel are: the fill factor, the reflection or the absorption of light in the optical path or the recombination of the photo-generated electrons.

Sensitivity: The sensitivity S of an image sensor is defined as the signal quantity at the pixel output under a given illumination and per unit exposure time. It is given in $V/(lx.s)$ or in $e^-/(lx.s)$. In the case of a Bayer matrix, the sensitivity for one color $i = R, G_R, G_B, B$ can be calculated according to Eq. 1.6, where A_{pix} stands for the increment distance of the pixel (m), h for the Planck constant ($J.s$), c for the celerity of

light in vacuum (m/s), Ill for the illuminant spectrum, QE for the quantum efficiency, for the wavelength (m) and V the luminous efficacy of the human eye.

$$S_i = \frac{A_{pix}^2}{hc} \cdot \frac{\int_{\lambda} Ill(\lambda) \cdot QE(\lambda) \cdot \lambda \cdot d\lambda}{\int_{\lambda} V(\lambda) \cdot Ill(\lambda) \cdot d\lambda} \quad (\text{Eq. 1.6})$$

Signal-to-noise ratio (SNR): The signal-to-noise ratio is defined as the ratio of the number of electrons of the useful signal to the number of electrons coming from the various noise sources of an image sensor, not described in this thesis. It is often given in dB according to Eq. 1.7.

$$SNR_{dB} = 20 \cdot \log \left(\frac{Signal}{Noise} \right) \quad (\text{Eq. 1.7})$$

1.2 Ambient Light Sensors

1.2.1 Background

An ambient light sensor (ALS) consists of a device used to sense and to measure the brightness of the incident light coming from the surrounding environment under a given illuminant. Although this kind of sensor has existed for some time in industrial tools requiring photometric measurements, the brightness information they provide has nowadays found applications in many current consumer goods with the emergence of handheld and mobile device such as smartphones, netbooks, tablets or PDAs (personal digital assistants) (Figure 1.11). In particular, the measured brightness level is used to improve the digital post-treatments of pictures taken with the device and to make the screen reading more comfortable with a smart adjustment of the backlight. In parallel, this latter functionality features the remarkable advantage of reducing the power consumption of the device. Indeed, the battery life currently constitutes one of the main limiting factors of these mobile devices since it is critical for a long-time use away from any power outlet, which is precisely what they are intended for. Power consumption has become a major technological concern in the conception of mobile device, especially with the introduction of energy-consuming color displays with larger sizes and higher resolutions. Several improvements are thus in progress throughout various levels of the microelectronic components manufacturing to reach a better power management. Among all the system functions, the display and especially the backlight were shown to be the most power-consuming elements [14], [15], with an exponential increase of the consumption when the brightness level of the screen is increased.

These results highlight the importance of controlling the backlight as a function of the outside brightness and thus explain the key role of ambient light sensors, which enable an automatic and immediate adjustment of the backlight level without requiring any user input. In broad sunlight conditions, the ALS sensor detects the high level of brightness and thus increases the backlight for a better readability of the screen. Conversely in low-light conditions at night or with moderate indoor lightning, it reduces the backlight to a sufficient level adapted to the low ambient brightness, thus limiting the user's eye strain and substantially saving the battery life of the device. We thereby understand that although ALS sensors constitute a significant asset to limit the power consumption of the backlight, they are also designed to offer considerable improvement to the visual experience of the user.



FIG. 1.11. Examples of ALS sensors in the Samsung Galaxy S6 Edge and in the Apple iPhone 6.

1.2.2 Market trends

The market of ambient light sensors has experienced a significant growth since 2007, especially thanks to their first integration in smartphones with the first iPhone. One can see that the global ALS revenue is about to reach 1 000 M\$ within the next two years (Figure 1.12(a)). In the chart, a distinction is made between conventional ALS and what we will call here RGB-ALS. ALS are the sensors we will focus on for the whole study. We will see in the following sub-sections that it only consists of a single “green” photodiode, whereas RGB-ALS consist of a combination of red, green, blue and potentially infrared photodiodes. The RGB-ALS purpose is the same than conventional ALS, but they also allow for the white balance of the displays. The use of three color photodiodes indeed brings more information regarding the color spectrum of the illuminant and the sensor’s output can thus be used to adjust the display’s backlighting to the color temperature of the ambient light. We can notice from Figure 1.12(a) that RGB-ALS tend to grow at the expense of ALS. Actually, it is likely that the market shares between the two types of sensors are quickly going to reach a steady state since RGB-ALS tend to be used in mid to high-end device, whereas ALS remain a cheaper and sufficient solutions for low to mid-end handsets. The chart takes into account both single ALS and combined ALS solutions, i.e. ALS combined with one or two additional functions (proximity sensor, etc.) on the same chip (see *multi-sensing* in Figure 1.1).

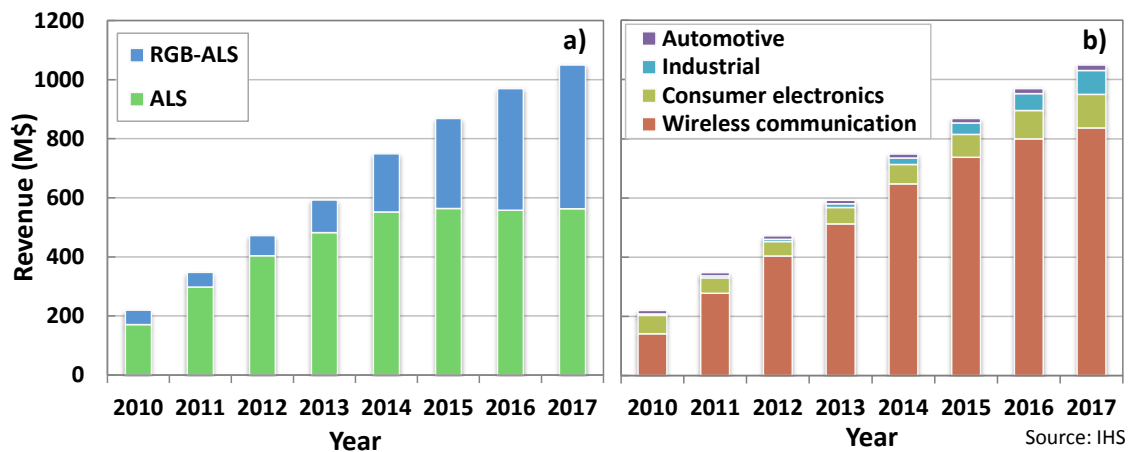


FIG. 1.12. (a) Global revenue of ALS and RGB-ALS. (b) Global revenue by application categories, regardless of the ALS type (Source: IHS).

As previously mentioned, the use of ALS in general has skyrocketed thanks to their integration in smartphones: nowadays, wireless communication constitutes 85 % of the global revenue of ALS (Figure 1.12(b)). Consumer electronics have also shown interest for ALS in laptops, tablets, PDAs, TVs, monitors, cameras and even in high-end white goods such as washing-machines or fridges.

Although their respective market shares are much lower, there is an increasing number of potential applications in the industrial and medical sectors (professional or diagnostic display-based equipment, etc.), the automotive field (electrochromic mirrors, brightness of central head units, etc.) and the street and office lightning management. For the following, ALS will only refer to conventional green ALS.

1.2.3 Principle

In order to properly adapt the backlight of the screen for the user, ambient light sensors must sense exactly what the human eye senses. The ALS operating function is thus to mimic the daytime human eye sensitivity. This sensitivity is called the photopic response, which is opposed to the scotopic vision that occurs in low-light conditions. The photopic response constitutes the luminous efficacy function of the eye, defined within the range from 380 nm to 750 nm and characterized by a maximum sensitivity in the green spectral range at 555 nm (Figure 1.13). Anatomically, the existence of these two different visual regimes is due to the presence of two different kinds of photoreceptors inhomogeneously located on the retina: the cones and the rods. The cones are mainly located at the center of the optical axe and are sensitive to the color information since three types of cones exist, each one for blue, green or red wavelengths. They are however not very sensitive, but are well-adapted for a daylight vision and are thus at the origin of the photopic vision. With a higher sensitivity than the cones, the rods are more suited for night-time conditions and are thus responsible for the scotopic vision. The rods are located in the peripheral area and are monochrome, which explains why our night vision is a peripheral vision and why we cannot discern colors in the dark.

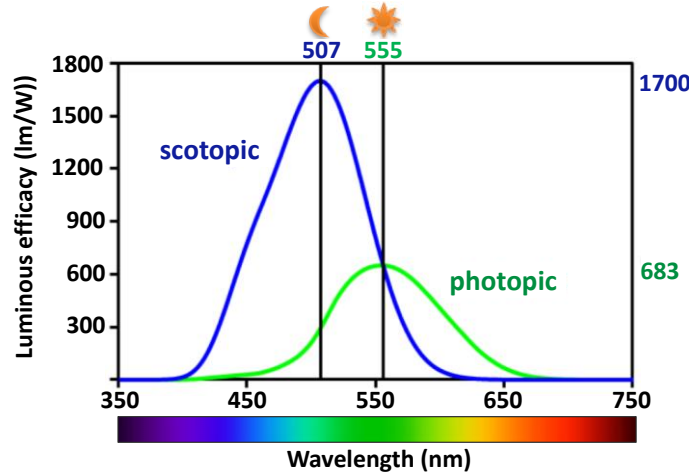


FIG. 1.13. Luminous efficacies of the human eye in the scotopic $V'(\lambda)$ and photopic $V(\lambda)$ regimes according to CIE standards. ALS have to reproduce the photopic vision. Original figure from [16].

As complementary information, we provide in Table 1.1 the correspondence between the main radiometric and photometric units. The energy of an electromagnetic radiation is called the radiant energy Q and is measured in J . Its power in W is defined as the radiant flux Φ . The electromagnetic power by unit area (W/m^2) is called the irradiance. These quantities are called radiometric units. Now, the principle of photometry is to weight these quantities with the eye luminous efficacy (the photopic response in lm/W of Figure 1.13) so that the human sensitivity is taken into account in the measurements.

By reminding that a lumen unit corresponds to a luminous intensity (cd) through a unit solid angle (sr), one obtains the equivalent photometric units given in Table 1.1. In particular, an ALS quantifies the surrounding illuminance, which is homogeneous to a luminous power incident on a surface and is thus measured in lm/m^2 or lx . It is important to keep in mind that we deal with luminous *efficacy* in photometric units, which corresponds to the portion of the total emitted electromagnetic radiation

actually usable for human vision (ratio of the luminous flux Φ_v to the radiant flux Φ). It should not be confused with the luminous *efficiency*, which stands for the efficiency of the conversion of input power into luminous flux.

	RADIOMETRY		PHOTOMETRY	
	Denomination	Unit	Denomination	Unit
Energy	Radiant energy Q	J	Luminous energy Q_v	$lm.s$
Power	Radiant flux Φ	W	Luminous flux Φ_v	lm
Power/area	Irradiance E	W/m^2	Illuminance E_v	lx

TABLE 1.1. Correspondence between the main radiometric and photometric units.

1.2.4 Structure and integration

The ALS solution of this PhD work is a green ALS combined with an IR proximity sensor. The integration of the ALS is made so that the sensor's aperture allows for the entrance of a light cone of $\pm 30^\circ$ of incidence. Above the packaging of the chip, a black window is deposited upon customer request so that the sensor is not visible to the user. In the current device, the filtering system used to reproduce the photopic response is performed with the association of an on-chip green organic resist and of an external IR-cut filter to remove the NIR signal that is not filtered by the resist (Figure 1.14). In practice, the chip structure is very similar to the structure previously described of an image sensor with two major differences. The first one is the lack of the main lens and of the microlenses above the color filter since we don't need to focus the light beam as in the case of an image reconstitution. The second one is the absence of pixels, since we don't want to sense an image: the photodetector is made of a large single photodiode which aim is to collect the photons corresponding to the photopic response, thus quantifying the level of brightness. The dimensions of the photodiode are in the order of $3 \times 3 \mu m^2$. A complete description of the sensor elements is provided in Figure 1.15. The materials stack above the photodiode is similar to the case of image sensors, with the intermetallic dielectric (IMD), the metallic interconnections and the passivation layers.

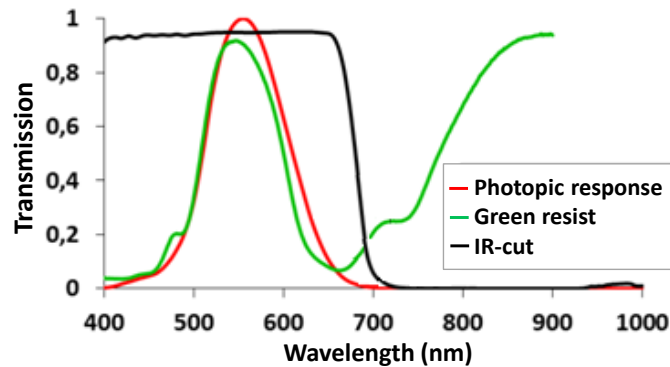


FIG. 1.14. Current filtering solution to reproduce the photopic response (red curve): a green organic resist (green curve) and an additional IR-cut filter (black curve).

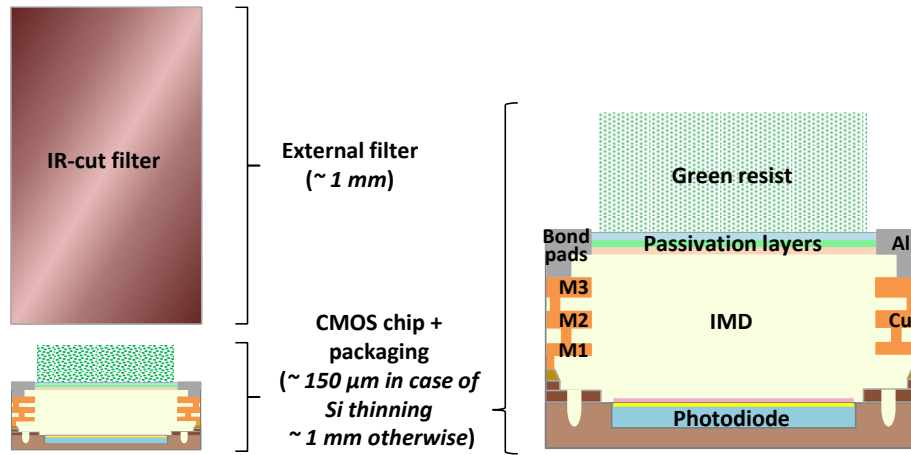


FIG. 1.15. Structure of the ALS chip and optical elements of the sensor's packaging.

The filtering system currently in use presents two drawbacks, both related to the necessary use of an additional IR-cut filter. First, this external filter is as thick (about 1 mm [17], [18]) as the chip composing the sensor (about 1 mm), since the IR-cut filter is fabricated on a glass substrate. It can then constitute 50 % of the total thickness of the sensor, or 80 % in the case where the silicon substrate of the CMOS chip is thinned. It means that the integration of ALS with this filtering solution becomes problematic and hindering when the trend is to make handheld devices always thinner: the thickness of common smartphones nowadays can be below 7 mm, and even below 5 mm for the thinnest ones. Finally, this IR-cut filter can generate an additional cost to the sensor fabrication if it has to be patterned, with a manufacturer dependence on the filter supplier, which is in contradiction with the trend for this kind of sensors to be implemented in low to mid-end device. In order to remain competitive on this sector, it is thus necessary to find another entirely on-chip filtering solution allowing for the removal of the NIR signal without the help of an additional IR-cut filter. After having presented the image sensor and ALS applications, we will now focus on the filtering part of these devices.

1.3 Review on spectral filtering solutions

In this section, we will present a succinct overview of the main existing optical filtering techniques than have been considered for the realization of color filters. The three major principles described below are the filtering by absorption, by interference and by diffraction.

1.3.1 Organic resists

The main marketed types of filters in the image or light sensors sector are the color organic resists. They are generally made of pigments or dispersive dyes and thus work by light absorption. For example, a green resist is composed of pigments or solvents that absorb the blue and red components of the incoming light, but that are transparent to green wavelengths. In most cases, the blue and green filters have a band-pass function centered at 450 nm and 540 nm respectively, whereas the red filter consists of a high-pass function with a steep slope and a transmission maximum reached around 610 nm. The red band-pass function is then obtained with the addition of an IR-cut filter (Figure 1.16). Organic filters present a few advantages when it comes to optical performance. They feature high transmission maxima (above 80 % or even 90 %), a low-sensitivity to the angle of incidence up to 35° and also low full widths at half maximum (FWHM) of around 100 nm with a filter overlap occurring at 50 %, which is beneficial to limit the amount of color correction required in post-processing.

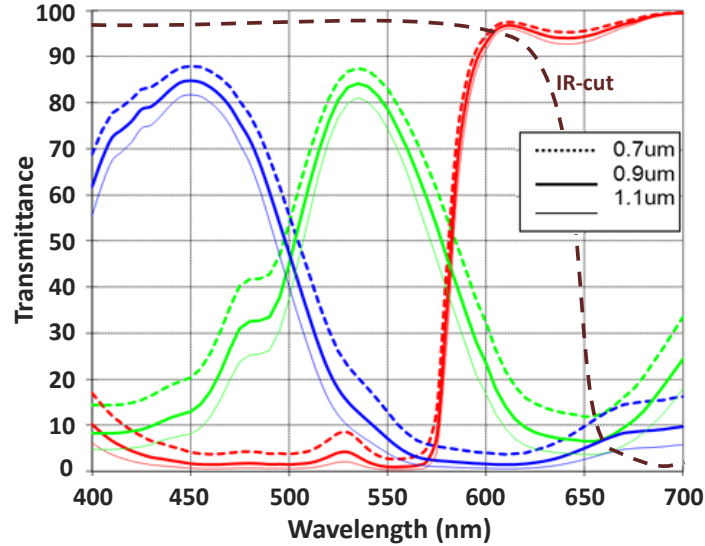


FIG. 1.16. Typical spectral responses of RGB organic resists for different thicknesses [19]. IR-cut's typical response added.

Color resists however have difficulties to filter the infrared signal as it can be seen in Figure 1.16. This parasitical signal is highly detrimental to a correct color reproduction and thereby imposes the use of an additional filter removing the IR wavelengths between 700 nm to 1.1 μm at which silicon is still absorbing. The IR-cut filter thus has a double objective: realizing the red filtering function and removing the undesired IR signal. Although the IR-cut filter requirement is our main concern here because of the significant thickness and the possible additional cost it can imply, organic filters also feature a few weak points. First, their thickness is between 700 nm and 1.1 μm , corresponding to half the total thickness of the dielectric stack above the photodiodes. It can hardly be reduced because the consequent decrease of pigments or solvent quantities on the optical path would deteriorate the resists' properties. Another serious limitation is their sensitivity to thermal treatment owing to their organic nature [20]. Studies showed that these resists flow and blacken when they undergo a treatment above 200°C, whereas the dielectric materials of the sensors including the passivation layers are deposited at around 400°C. This property is a major drawback since the process is locked once the resists are deposited, which removes any freedom of integration whereas the filtering element should ideally be as close as possible to the photodiodes to limit the spectral and the optical cross-talks [21]. Finally, a last disadvantage is their bad ageing. Color resists degrade when they are exposed to strong illuminations or to high temperatures, which modify their spectral profiles and thus misrepresent the colors of the reproduced images.

1.3.2 Interference filters

The filtering function can be performed by interference filters, for instance based on the Fabry-Perot (FP) interferometer principle. A FB interferometer consists of a cavity delimited by two mirrors, which principle is drawn in Figure 1.17. At each index discontinuity, the light is partially reflected or transmitted [22]. This back-and-forth propagation of light inside the spacer generates destructive or constructive interferences depending on the wavelength of the incoming light, on the angle of incidence and on the thicknesses and refractive indices of the layers (Figure 1.17(a)). With a proper tuning of these parameters, one can thus allow for the propagation of a specific wavelength and attenuate the undesired signal (Figure 1.17(b)), which can be applied to optical wavelengths in image sensors. The semi-reflective surfaces can be made with metallic layers or with a stack of alternating thin dielectric layers with high and low refractive indices. Two kinds of interference filters are thus obtained: the all-dielectric filters and the metal-dielectric ones.

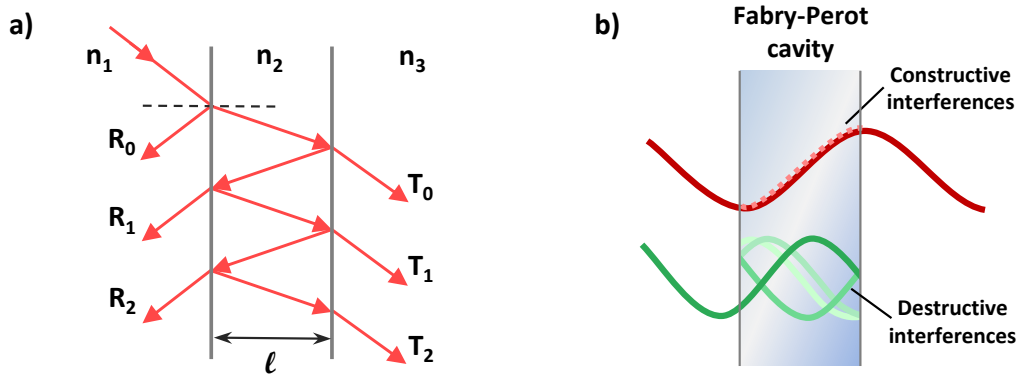


FIG. 1.17. (a) Schematic of light propagation and interferences generation in an example of Fabry-Perot filter with two spacers. (b) Visual representation of the wavelength selection mechanism.

These two solutions applied to image sensors can be found in literature. For all-dielectric filters, the semi-reflective media delimiting the spacer (or defect layer or cavity) are each realized with a stack of quarter-waves layer with alternating indices (Bragg mirror). The thickness of the defect layer determines the wavelength of the filter. Inaba *et al.* [20] and Koyama *et al.* [23] both demonstrated the optical performance of such RGB filters with a total thickness inferior to $1.5\ \mu\text{m}$ and with better lifetime than organic resists by using TiO_2 - SiO_2 stacks. On another hand, metal-dielectric multilayered filters have also been proposed to perform filters in the visible range, where the thickness of the inter-metal cavity is used to tune the operating wavelength in the same way, and where the metal plays the role of mirror instead of alternating Bragg layers. A first demonstration of RGB filtering with a single Ag-SiO_2 - Ag cavity was published by Yoon and Lee [24]. In 2011, Frey *et al.* proposed a similar approach with a refined Ag-SiN-AlN structure using two defect layers to improve the quality factor and the transmission of the filters [25], for half the thickness of organic resists. Although metal-dielectric filters suffer from lower transmission efficiencies than all-dielectric ones due to metal absorption, the resulting color errors applied to $1.75\ \mu\text{m}$ pitch CMOS sensor of the Fabry-Perot fabricated by Frey *et al.* show performance comparable to color resists.

Interference filters have been shown to be able to provide very interesting optical performance without IR-cut filter and with a lifetime higher than organic resists, but they are not flawless. The Fabry-Perot interferences are by nature quite sensitive to the angle of incidence, while typical image sensors can receive light with angles of incidence up to 30° . Fabry-Perot filters use a stack of several layers which optical indices and thicknesses are decisive for wavelength selection and the quality of the filters. A major issue with this solution is thus the necessity to have a severe control of all the layer deposition steps to correctly reproduce their optical thickness, which is critical with the small thicknesses of thin-film filters. At wafer level, it would require a very low dispersion that is difficult to reach on 300-mm wafers with current industrial deposition tools. Moreover, the metal-dielectric filters found in literature use silver, which is not CMOS-compatible and which deposition process at small thickness is challenging. Eventually, a final drawback in the case of image sensors is the need to pattern in a staircase shape the pixels in order to have three different cavity lengths for the three colors [26]. The use of several lithography steps is a constraint that complicates the fabrication and increases its costs.

Recent works proposed to solve the issue of the staircase structure and the multiple lithography steps by using a 2D nanostructuration of the optical cavity by horizontally alternating the low and high index dielectrics [27]. In this case, the optical thickness of the spacer is only tune by the modulation of the effective index in the cavity with the adjustment of the volume ratio between the two dielectrics [28]. This technique applied to image sensors would make the three RGB pixels have the same spacer thickness and would thus facilitate the integration of such filters [29]. A progressive nanostructuration

pitch from the center to the edges of the pixels has also been proposed with promising results to limit in the same time the angular sensitivity of interference filters [30], although the thickness control still remains a serious concern with this solution.

1.3.3 Diffractive filters

Diffractive filtering is widespread in longer wavelength ranges where it is mainly used for telecommunications applications. Nowadays, the technological progress of CMOS fabrication processes has allowed for the shift of this filtering solution towards visible wavelengths with the use of semi-conducting or dielectric materials. Although the following is not applied to the actual image sensors technology, it demonstrates the possibility to perform frequency selective structures adapted to red, green and blue colors. As an illustration, we can for example mention the work of Kanamori [31] and Yoon [32] for 1D silicon-based transmission filters, and the work of Fehrembach [33] or Magnusson [34] for reflective filters. These filters remain however rather uncommon in color sensors sector and present the huge disadvantage of being extremely sensitive to the angle of incidence, which is crippling for this kind of application.

1.4 The plasmonic alternative

A recently developed nanophotonic domain called *Plasmonics* may provide an interesting solution in our research for a new filtering concept that matches the requirement of CMOS image sensors. The first observation of plasmons is attributed to Wood, who noticed in 1902 fast intensity variations in the spectra of continuous light sources diffracted by optical gratings that have been for a long time known as the Wood's anomalies [35]. If many works were led to understand the nature of these anomalies and to eventually relate them to the concept of surface plasmons [36]–[39], it is only since the nineties that this emerging field nowadays widely known as *Plasmonics* has experienced a significant interest in various application sectors. The reader can refer to [40], [41] for extensive descriptions of the history of Plasmonics. We shall progressively present in this section the concept and the key properties for our applications of surface plasmons, starting with a brief overview of the electromagnetic and optical properties of metals. The articulation of this section is partly based on Maier's book [42].

1.4.1 Electromagnetic waves propagation

The propagation of electromagnetic waves in a given medium is fundamentally described with the four Maxwell's equations by linking the spatial and the temporal variations of the electric field \mathbf{E} , the magnetic field \mathbf{H} , the electric displacement \mathbf{D} and the magnetic induction \mathbf{B} (Eq. 1.8–1.11). The electric displacement and the magnetic induction can themselves be derived from the electric field and the magnetic field respectively with the following relations: $\mathbf{D} = \epsilon \mathbf{E} = \epsilon_0 \epsilon_r \mathbf{E}$ and $\mathbf{B} = \mu \mathbf{H} = \mu_0 \mu_r \mathbf{H}$. In these equations, ϵ_0 and μ_0 stand for the permittivity and the permeability of free space respectively, ϵ_r and μ_r for the relative permittivity and the relative permeability of the medium respectively, and since we consider metallic media, the free currents density \mathbf{J}_{free} and the free charges density ρ_{free} are also taken into account. In the context of our study, the system can be simplified by assuming a neutral non-magnetic metal ($\rho_{free} = 0$ and $\mu_r = 1$) and by using Ohm's law relating the free current density to the electric field with the electric conductivity σ in the form $\mathbf{J}_{free} = \sigma \mathbf{E}$.

$$\nabla \cdot \mathbf{D} = \rho_{free} \quad (\text{Eq. 1.8})$$

$$\nabla \cdot \mathbf{B} = 0 \quad (\text{Eq. 1.9})$$

$$\nabla \times \mathbf{E} = - \frac{\partial \mathbf{B}}{\partial t} \quad (\text{Eq. 1.10})$$

$$\nabla \times \mathbf{H} = \mathbf{J}_{free} + \frac{\partial \mathbf{D}}{\partial t} \quad (\text{Eq. 1.11})$$

The electric and magnetic fields of a plane wave can be described in the complex form as given in Eq. 1.12–1.13 with \mathbf{k} its wave vector in the reciprocal space associated to its wavelength λ ($k = 2\pi/\lambda$) and ω the angular frequency of the wave. By combining these equations of propagation with Maxwell's equations, one obtains the general dispersion relation inside the considered medium (Eq. 1.14), with $\varepsilon(\omega)$ the complex dielectric function which may depend on the frequency. Note that this relation can be simplified in $\omega^2 = c^2 k^2$ in free-space with $c^2 = 1/\mu_0 \varepsilon_0$, which defines the *light line* in dispersion diagrams (see 1.4.3 Surface plasmon resonances).

$$\mathbf{E} = \mathbf{E}_0 \exp i(\mathbf{k} \cdot \mathbf{r} - \omega t) \quad (\text{Eq. 1.12})$$

$$\mathbf{B} = \mathbf{B}_0 \exp i(\mathbf{k} \cdot \mathbf{r} - \omega t) \quad (\text{Eq. 1.13})$$

$$k^2 = \varepsilon(\omega) \mu_0 \omega^2 \quad (\text{Eq. 1.14})$$

The dielectric function being complex, it can be written as follows: $\varepsilon(\omega) = \varepsilon'(\omega) + i\varepsilon''(\omega)$. Consequently, the wave vector modulus in the general case is also complex and can be written with a similar decomposition $k = k' + ik''$. Considering a propagation of the wave along the z direction, the electric field of the plane wave in the metal of Eq. 1.12 can be decomposed as in Eq. 1.15 (the same calculation can be made with the magnetic field). In this new equation, the first exponential term corresponds to phase propagation along the z direction, whereas the second exponential term stands for the damping of wave amplitude due to the absorption of the material.

Two remarkable cases appear from Eq. 1.15. If $\varepsilon(\omega)$ is real and positive (ideal dielectric case), then the modulus of the wave vector k is also real ($k = k'$) and the plane wave thus preserves its free-space properties without attenuation (but dispersion can occur). On another hand, if $\varepsilon(\omega)$ is real and negative (ideal metallic case), then k is purely imaginary ($k = ik''$). In this case, the amplitude of the electric field decreases exponentially in the direction of propagation until the wave disappears. We will see thereafter that a metal-dielectric interface can support the propagation a special surface wave called *plasmon* which is *evanescent* (transverse exponential attenuation) in both metallic and dielectric surrounding materials. In the direction of propagation, surface plasmons propagate without attenuation in ideal metals but are attenuated in real ones. In the next sub-sections, we will explain the metal properties and the characteristics of plasmon waves and plasmon resonances.

$$\mathbf{E} = \mathbf{E}_0 \exp(i(k'z - \omega t)) \cdot \exp(-k''z) \quad (\text{Eq. 1.15})$$

1.4.2 Optical properties of metals

A simple treatment of the plasmonic phenomenon can be achieved with a classical approach. Paul Drude proposed a microscopic description of the optical and electrical properties of metals by considering the electronic plasma as an ideal gas and by adapting the kinetics theory of gas to electrons. In this model, the electron plasma is represented as a sea of classic point particles freely moving inside the atom matrix, defined by the heavier and motionless ions. The Drude-Sommerfeld description for a free electron gas is modeled according to the equation of motion of a damped oscillator given in Eq. 1.16, with m_e the effective free electron mass, e the free electron charge, γ a phenomenological damping term,

E_0 and ω the amplitude and the angular frequency of the applied electric field. The first order partial derivative stands for the damping effect corresponding to the collision of electrons with each other, with phonons or any other defect ($\gamma = 1/\tau$, with τ the mean time between two successive collisions).

$$m_e \frac{\partial^2 \mathbf{r}}{\partial t^2} + m_e \gamma \frac{\partial \mathbf{r}}{\partial t} = e \mathbf{E}_0 e^{-i\omega t} \quad (\text{Eq. 1.16})$$

Resolving this equation with a complex harmonic solution leads to the expression of the Drude dielectric function of a metal (Eq. 1.17), which also introduces the quantity ω_p known as the *bulk plasma frequency* (Eq. 1.18) with n_e the plasma density. This angular frequency corresponds to the eigenfrequency of the collective oscillation of the electron gas in a bulk infinite metal, also called the *volume* or *bulk plasmon*. Typical energies for bulk plasmon quanta $\hbar\omega_p$ of noble metals such as gold and silver are 9.03 eV and 9.01 eV respectively, and 10.8 eV and 14.8 eV for copper and aluminum respectively [43], [44]. Bearing in mind that our work focuses on visible and NIR ranges ($\hbar\omega$ between 1 eV and 3.5 eV), one can notice that these energies are much higher than the damping $\hbar\gamma$ of these metals (0.08 eV for aluminum for example). If we neglect the damping term in Eq. 1.17, the dielectric function of a metal in the visible range can thereby be approximated by Eq. 1.19.

$$\varepsilon(\omega) = 1 - \frac{\omega_p^2}{\omega^2 + i\gamma\omega} \quad (\text{Eq. 1.17})$$

$$\omega_p = \sqrt{\frac{n_e e^2}{m_e \varepsilon_0}} \quad (\text{Eq. 1.18})$$

$$\varepsilon(\omega) = 1 - \frac{\omega_p^2}{\omega^2} \quad (\text{Eq. 1.19})$$

Two frequency regimes are thus noticeable from Eq. 1.19 and make the link between the light frequency and the wave propagation in metals (*1.4.1 Electromagnetic waves propagation*). If ω is above ω_p , the refractive index of the metal $n = \sqrt{\varepsilon}$ is a real number. However if ω is smaller than ω_p , then the dielectric function is negative, and n becomes imaginary, which means the electromagnetic wave cannot propagate through the metal. This relation directly explains the optical behavior of metals. We have seen that noble metals typically have their respective bulk plasmon frequencies in the ultraviolet (UV) range, that is why metals look shiny in the visible range: visible and IR radiations are reflected due to the screen effect created by the free electron gas ($\omega < \omega_p$). Conversely beyond the UV range ($\omega > \omega_p$), the metal is transparent to electromagnetic waves because the electrons of the metal cannot react fast enough to the electromagnetic excitation.

This model is sufficiently accurate to describe the optical properties of metals with the intraband transitions mechanisms, especially for alkali metals or for noble metals up to the NIR range. In the visible range and beyond however, discrepancies have been observed from optical measurements, especially regarding the imaginary part of the dielectric function. This difference is due to interband transitions that may occur for some metals below 1 μm . This is the case for instance for gold (330 nm and 470 nm), for silver (320 nm) or for aluminum (850 nm) [45], [46]. The Drude-Lorentz model takes these effects into account, but its description is far beyond the scope of this thesis. In practice we preferred to use measured and tabulated values of the dielectric constant of the metals we considered [47].

1.4.3 Surface plasmon resonances

We have seen how the optical properties of bulk metals are related to their dielectric function and to their volume plasma frequency. We shall now look at the case where the metal is spatially confined and how this configuration gives rise to new optical properties thanks to interfacial phenomena: the surface plasmon resonances (SPR).

1.4.3.1 Surface plasmon polaritons

Let's consider the case where the metal is only semi-infinite. The existence of a metal-dielectric interface allows for a new possible excitation of the surface metal electrons. The physical properties of these excitations can be directly calculated from Maxwell's equations and from their continuity conditions at the interface. In particular, the k_x component of the incident wave vector is conserved at the interface for a plane wave. We consider an electric field under the form given in Eq. 1.20 for $z \geq 0$ (in the dielectric) and in Eq. 1.21 for $z \leq 0$ (in the metal). The development of the electromagnetic solution for surface modes is not described here, but the reader can refer to [40], [42], [48] for comprehensive theoretical studies of the phenomenon.

$$\mathbf{E} = \mathbf{E}_0^d \exp[i(k_x x + k_{z,d} z - \omega t)], \text{ for } z \geq 0 \quad (\text{Eq. 1.20})$$

$$\mathbf{E} = \mathbf{E}_0^m \exp[i(k_x x - k_{z,m} z - \omega t)], \text{ for } z \leq 0 \quad (\text{Eq. 1.21})$$

By denoting ε_d and ε_m the respective dielectric functions of the dielectric medium and the metal, one can then demonstrate that such a surface excitation is ruled by the fundamental dispersion relation given in Eq. 1.22 which is valid for both real and imaginary ε_m (i.e. without or with attenuation) [42], [48]. A set of equations is obtained for the components perpendicular to the interface of the wave vectors in the metal $k_{z,m}$ and in the dielectric $k_{z,d}$ (Eq. 1.23). The electromagnetic excitation corresponding to this dispersion is known as a *surface plasmon*. More accurately, since the excitation results from a strong coupling with a luminous wave, it is also called a *surface plasmon polariton* (SPP). A surface plasmon polariton consists of a collective oscillation of the surface free electron gas under the form of a longitudinal wave propagating along the metal-dielectric interface with a wave vector k_{spp} defined along the x -axis (Figure 1.18).

$$k_{spp} = \frac{\omega}{c} \sqrt{\frac{\varepsilon_d(\omega) \cdot \varepsilon_m(\omega)}{\varepsilon_d(\omega) + \varepsilon_m(\omega)}} \quad (\text{Eq. 1.22})$$

$$k_{z,i} = \frac{\omega}{c} \sqrt{\frac{\varepsilon_j(\omega)^2}{\varepsilon_d(\omega) + \varepsilon_m(\omega)}} \quad , \quad \text{with} \quad \frac{k_{z,d}}{k_{z,m}} = -\frac{\varepsilon_d}{\varepsilon_m} \text{ and } j = m, d \quad (\text{Eq. 1.23})$$

A few properties of SPPs can be derived from Eq. 1.22 and Eq. 1.23. We consider the case of ideal metals for the sake of simplicity ($\text{Im}(\varepsilon_m) = 0$). From the latter one, it can be seen that if $\varepsilon_d > 0$, then ε_m has to be negative with the sign convention of Eq. 1.20-1.21, which is true for metals in our considered wavelength range ($\omega < \omega_p$) and confirms that SPP can only occur at metal-dielectric interfaces. Furthermore, since we deal with a propagating mode along the metal surface, k_{spp} has to be a real number. The condition $\varepsilon_d \cdot \varepsilon_m < 0$ thereby implies that $\varepsilon_d + \varepsilon_m < 0$. The components $k_{z,m}$ and $k_{z,d}$ are thus purely imaginary, which means that SPPs are *evanescent* in the direction perpendicular to the interface in the metal and in the dielectric medium and are thus bound to the interface. Finally, the dispersion relation implies that SPPs lie at the right of the light line $\omega = ck$ on the dispersion diagram,

meaning that they cannot be directly excited by incident photons since the momentum of light is too small to cross the SPP dispersion curve (Figure 1.19). The excitation of SPP requires a coupling system that will be presented in the next sub-section. For large wave vectors k_x , the frequency of the SPP approaches an asymptotical value called the surface plasmon angular frequency $\omega_{sp} = \omega_p / \sqrt{1 + \epsilon_d}$. In the case of a real metal (ϵ_m complex), this frequency is reached for a finite wave vector that gives the lower possible wavelength of a surface plasmon $\lambda_{SP} = 2\pi/\text{Re}(k_{SPP})$ for a given metal-dielectric interface [42].

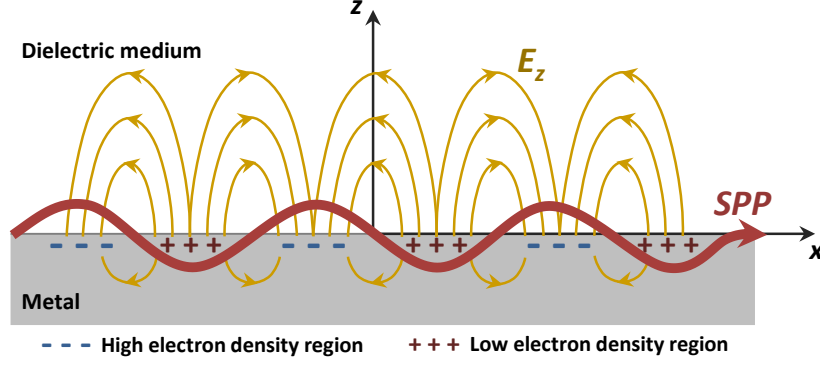


FIG. 1.18. Visual representation of a surface plasmon polariton propagating along a metal-dielectric interface. The excitation corresponds to a longitudinal oscillation of the surface charge density in the metal. The associated electromagnetic field exponentially decreases in the direction perpendicular to the interface. Schematic inspired from [49].

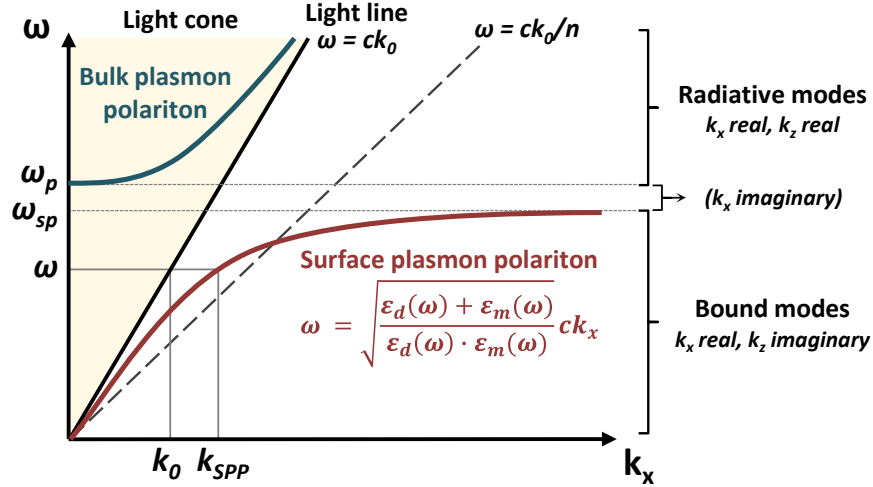


FIG. 1.19. Dispersion diagram of plasmons for an ideal metal with the frequency as a function of the parallel component k_x of the incident wave vector k_{inc} . Above the plasma frequency, light can excite bulk plasmons. When $\omega < \omega_p$, we are in the regime of surface excitations. Since the SPP dispersion curve is always at the right of the light line, an incident plane wave on a metal surface cannot directly excite SPP.

1.4.3.2 SPP excitation conditions

The excitation of surface plasmons with a plane wave is permitted if the conditions of energy conservation (ω) and wave vector conservation (k) are fulfilled. We have seen that whatever the wavelength, the SPP dispersion curve is always beneath the light line and never intersects it. In other words, we always have $k_{SPP} > k_0$, with $k_0 = \omega/c$ being the magnitude of the wave vector k_{inc} of incident free-space photons. In order to achieve the phase matching condition, an additional momentum must be

brought to the incident k_x , i.e. the component parallel to the interface of \mathbf{k}_{inc} , so that incoming light can couple to a SPP.

There are in particular two known methods to overcome this wave vector mismatch. The first one consists in the use of frustrated total reflection of light inside a prism. We won't use this method and its principle is thereby not presented here, but the reader can find the two reference prism uses in [50] for the Otto configuration and in [51] for the Kretschmann-Raether configuration. The second method that will be used throughout this thesis is the coupling via diffraction effects with a periodical structuration of the metal surface (Figure 1.20(a)) [40], [42], [48]. In this case, the incident wave vector is perturbed by the grating structure and the diffracted orders whose parallel component of their wave vectors $k_{x,m}$ matches k_{SPP} will couple to SPPs (Figure 1.20(b)). In the case of a 1D grating, the wave vector matching is given by Eq. 1.24, where $k_0 \sin \theta = k_x$ is the parallel component of the incident wave vector \mathbf{k}_{inc} , P_x the period of the grating, θ the angle of incidence of the impinging light and m an integer corresponding to the diffraction order.

$$k_{spp} = k_0 \sin \theta + m \frac{2\pi}{P_x}, \quad m \in \mathbb{Z} \quad (\text{Eq. 1.24})$$

This plasmonic property of structured metallic layers make them especially interesting for frequency selective applications since the operating wavelength can simply be tuned by changing the period of the grating. In particular, it demonstrates how plasmons can be used for filtering applications. We will see in Chapter 2 how SPPs can couple back to free-space photons in the case of subwavelength holes arrays.

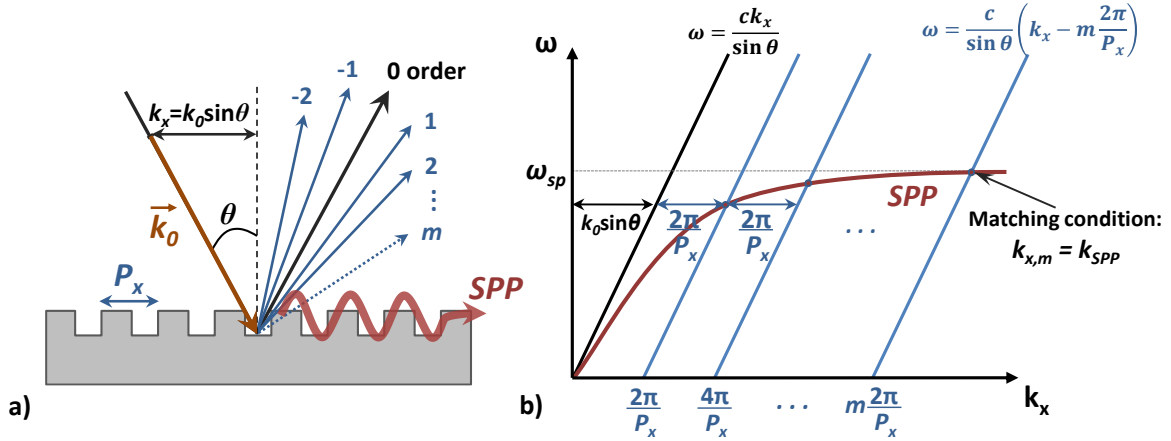


FIG. 1.20. (a) Schematic of the excitation of SPP with the diffracted orders generated by a grating. (b) Dispersion diagram with a representation of the phase-matching conditions between k_{SPP} and the parallel component of the wave vectors $k_{x,m}$ of the diffracted orders.

1.4.3.3 Plasmons properties in the visible range

We have seen that the k_z component of an SPP is imaginary in both the metal and the dielectric medium. From the exponential decrease of the electric field in the z direction, the spatial confinement of the SPP at the interface can be calculated and is known as the penetration depth. The SPP penetration depth δ_j in a medium j is defined as the distance z at which the exponential factor $\exp(-ik_{z,j}z)$ corresponding to the evanescent nature of the wave in the z direction equals $1/e$ (with e the Euler's number), that is: $\delta_j = 1/\text{Im}(k_{z,j})$ (Eq. 1.25) [40]. Typical values of δ are given in Figure 1.21 for silver, aluminum, gold and copper in the visible range in contact with SiO_2 , which will be widely used in the next chapters. The penetration depth in the metal is much lower than in the dielectric medium. This spatial confinement makes SPP very sensitive to interface conditions. One can also notice how the interband transitions are highlighted for each metal.

$$\delta_j = \text{Im} \left(\frac{\lambda}{2\pi} \sqrt{\frac{\epsilon_m + \epsilon_d}{\epsilon_j^2}} \right), \quad \text{with } j = m, d \quad (\text{Eq. 1.25})$$

When losses are taken into account (non-zero $\text{Im}(\epsilon_m)$), k_{SPP} is complex and SPPs are also characterized by their propagation length L_{SPP} along the metal-dielectric interface. This propagation length is defined as the distance at which the intensity of the electromagnetic field is reduced by a factor $1/e$. The distance is thus given by $L_{SPP} = 1/(2\text{Im}(k_{SPP}))$ [48]. Typical values of L_{SPP} for metals in the visible range are between 10 μm and 100 μm [42].

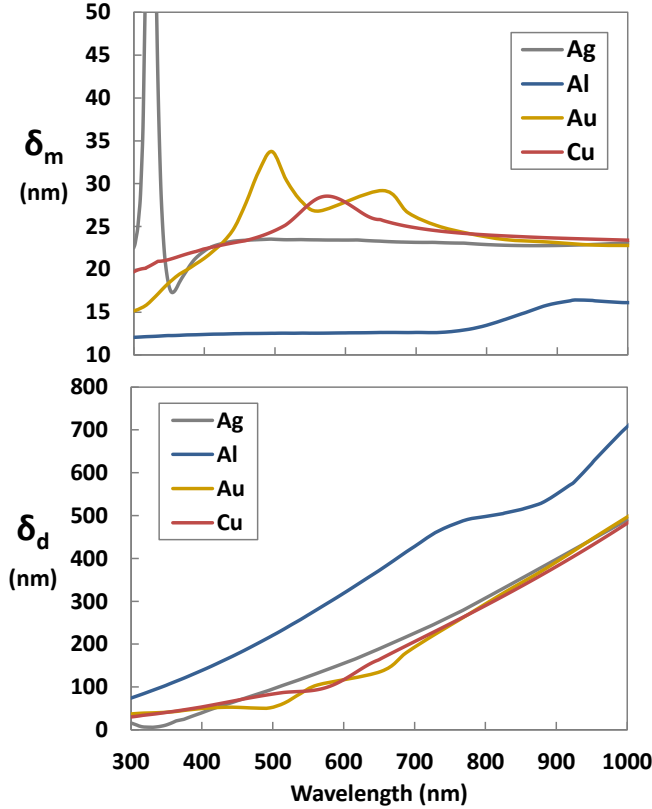


FIG. 1.21. Penetration depths in SiO_2 (δ_d) ($n = 1.46$) and in four metals (δ_m) (Ag, Al, Au and Cu) in the visible and NIR ranges. Refractive indices of the metals extracted from Palik [47].

1. 4.3.4 Localized plasmon resonances

In addition to surface plasmon polaritons which propagate along the metal surface, another kind of plasmon resonance can occur at a metal-dielectric interface: the localized surface plasmons (LSP). These resonances are confined inside nanostructures like a nanoparticle or a nanohole with a substantial increase of electromagnetic field in their vicinity compared with the excitatory field. We will talk more about localized plasmons in *Chapter 3* where we will see how these are especially sensitive to the nano-aperture shape and dimensions.

1.5 Thesis objectives: the challenges of plasmonic filtering

After having presented the general structure and operating principle of the two main light sensor types on which we will focus during this thesis (image sensors and ALS), we have seen how the filtering system have become critical for a further but cheaper integration of such sensors in thinner devices. The organic resists present the major drawback of requiring an external IR-cut filter that drastically enlarges its thickness. Maintaining the competitiveness on the market of light sensors in low to mid-end handset device imposes the development of an entirely on-chip filtering solution that does not need any additional filter to remove the infrared signal. One of the most serious known alternatives is the use of Fabry-Perot filters. We have however seen that their fabrication may necessitate several deposition and lithography steps, and especially requires a tough control of the thickness and of the optical properties of the deposited layers which may ask for dedicated and expensive tools.

As exposed in the previous section, plasmonics offers a few advantages regarding the technological challenges that we want to meet. The mechanism of plasmon resonances allows for a filtering function in the optical range with the simple use of a patterned metallic layer, the operating wavelength being tuned by the dimensions of the nanostructures. In practice, it means that the active element of a plasmonic filter (i.e. the metallic layer) is feasible with a single metal deposition and a single lithography step, even in sensors with pixels. Furthermore, the optical properties of metals naturally permit the suppression of the unwanted IR signal and thus remove the need for an IR-cut filter. Plasmonic filters, because of their structure and principle, however bring their own intrinsic technological challenges to meet the application requirements compared with the currently most widespread filtering solution, the organic resists. Indeed, their in-plane structuration inherently makes them sensitive to the angle of incidence (polar and azimuth), but also to the polarization, which were not issues with pigment-based resist. Similarly, the spectral response is directly dependent on the characteristic dimensions of the structures, namely, the period of the array, the size and the shape of the patterns. All these parameters induce reproducibility concerns with respect to the process dispersions related to the accuracy of the fabrication tools at each critical step of the filters realization, especially considering the fact that filtering visible wavelengths makes the structures dimensions fall to nanoscale. Furthermore, we are interested here in CMOS process, materials and equipment compatible with an industrial 300 mm wafer-scale production with high throughput requirements.

The aim of this work is thus to evaluate the potential of plasmonic filters to respond to the technological challenges specific to the considered applications, but also to the performance and fabrication concerns related to their working principle. This manuscript is thus articulated around the following issues:

- Determining the best plasmonic structures for our targeted applications in terms of angular stability and identifying the most direct integration into a conventional sensor fabrication route. The integration has to take into account the industrial and CMOS compatibilities (*Chapter 2*).
- Understanding the optical properties of the selected structures and evaluating their application-related performance to propose optimal filter designs (*Chapter 3*)
- Modeling process dispersions on the critical geometrical parameters to evaluate their impact on plasmon resonances and to approve the viability of plasmonic filters fabrication with respect to their sensitivity to the inaccuracies of industrial process tools (*Chapter 4*)
- Developing a process route to realize experimentally the optimized filters and to validate the plasmonic solution for industrial visible filtering applications (*Chapter 5*)

Chapter 2

CMOS integration of nanostructures for plasmonic filtering

We exposed in the first chapter how the principle of plasmonic filters makes them a theoretically attractive solution to perform wavelength-selective functions such as color filtering [52]–[55] or color sorting [56], [57] in various types of sensors. Their appealing advantages result from two main characteristics. The first one is the manipulation of the operating bandwidth with the nanostructures dimensions instead of using exclusively the optical properties of materials. The second one is their simple structure that allows for a fabrication of a filtering system with very few technological steps, especially regarding the patterning process. In our case, we want to investigate the ability of the plasmonic solution to provide exclusively on-chip filters for device such as image sensors where external filters (e.g. an additional IR-cut glass above the chip as discussed in *1. 5 Thesis objectives: the challenges of plasmonic filtering*) are not required anymore. This removal of any external filter is beneficial in terms of height reduction and cost decrease. The objective of our work is however not limited to the single optical performance of the potential plasmonic structures that can be considered to realize such filters. By mainly focusing on visible applications, we aim to identify the ability of plasmonic structures to perform efficient filtering functions such as color filters or ambient light sensors in the context of a mass production, and with a view to leading to industrial products meeting customers' expectations.

On this basis, the context of the study is to evaluate the performance of plasmonic filters by taking into account various considerations, from the structures' performances to the viability of their wafer-scale fabrication, including the fabrication costs and the potential process issues. Regarding the performance specifications, we are looking for a plasmonic solution that provides transmission efficiencies and quality factors comparable or better than those of color resists for the considered applications, image sensors or ALS sensors. The angular stability is of primary importance, especially in the case of ALS since no lens is used to focus the light beam. Customers' specifications impose a tolerance to polar angles of incidence up to at least 30° , although a tolerance to incidences of 60° would be preferred. One of our major concerns is also to envision a production in an industrial environment, which implies several constraints. Industrial clean rooms generally have a severe monitoring of the contamination of the wafers and inside the equipments, which leads to a restriction in the allowed materials. Our materials choice thus concentrates only on CMOS-compatible metals and dielectric for the structures selection. If we consider a compliance with standard 300mm-CMOS fabs, we also have to ensure that the filters can be fabricated with industrial techniques able to sustain a high throughput. Moreover, the fabrication at wafer-scale imposes a homogeneity of the optical performance on the whole surface of the wafer, and from wafer to wafer too, which implies a high robustness of the filters to process dispersions. Finally, we are interested in a low-cost integration that minimizes the changes

brought to the front-end process route, so that the technology can be directly transferrable to industrial clean rooms.

In this chapter, we mainly focus on the search for plasmonic structures that provide the best optical properties according to our expectations and on the identification of the applications that could make the most of the plasmonic filters. The simulation method and the performance evaluation tools will be presented for the main applications of visible sensing. Different kinds of filters will be simulated and evaluated among the major families of plasmonic structures with emphasis on their angular stability, which constitutes a major issue for light sensors. Their agreement with the CMOS materials constraint and the ease of fabrication with respect to industrial processes will also be taken into account. Once the best applications are discussed, we will thus propose an optimal integration of the plasmonic filters taking into account the CMOS compatibility and the low-cost transfer to industrial fabs.

2.1 Method for optical simulations: RCWA

2.1.1 Numerical methods for periodic structures

The simulation of the interaction between light and sub-wavelength structures imposes specific constraints in the choice of the calculation method. The small dimensions of the structures compared to the wavelength make the scalar theory of light propagation inappropriate and require the rigorous solving of Maxwell's equations. However, their analytical solutions are difficult to obtain, and new numerical methods were thus developed to solve such electromagnetic problems at the wavelength scale where resonances are expected to occur [58]–[60]. These methods are called rigorous vector theories as they take into account the polarization of the light [61]. They can use different operating principles to numerically solve Maxwell's equations, but it is generally the geometry of the problem that makes some more appropriate than others. In our case, we are strictly interested in periodical structures, be they 1D or 2D. The algorithms fitting with our needs can be divided in two main categories: the finite difference methods and the modal methods.

The differential algorithms are mainly represented by the finite-difference time-domain method (widely known as FDTD), introduced by Yee in 1966 [62]. Its principle relies on the spatial and time discretizations of the partial derivatives of the electric and magnetic fields (\mathbf{E} , \mathbf{H}) obtained from Maxwell's equations. It comes from the observation that each time derivative of the electric (magnetic, respectively) field components are governed by the spatial derivatives of the magnetic (electric, respectively) field components. The time-domain and spatial-domain discretizations are then performed so that the components of the electromagnetic field (E_x , E_y , E_z , H_x , H_y , H_z) are approached according to their second-order limited development. The wave propagation is thus calculated in a leapfrog manner where the solving of the electric (magnetic, respectively) at a given instant time t leads to the solving of the magnetic (electric, respectively) field at the next instant $t + \Delta t/2$, where Δt is the time step of the simulations. The advantage of the FDTD method is that it doesn't have theoretical restrictions, meaning that it is able to calculate waves propagation in any medium (metals, dielectrics, plasmas...) and with very complex geometries. Its main drawbacks however are the long calculation times and the large memory size it requires to solve the problems.

With the modal algorithms, the computation of the electromagnetic field is performed in the frequency-domain using a slicing of the structure along the vertical axis z (slices perpendicular to the direction of propagation in normal incidence) so that the permittivity ϵ is constant in each slice along the z direction (see Figure 2.1 in next section). For each slice, this z -invariance of ϵ reduces the calculation of the waves propagation to a system of equations solved as an eigen-value problem (hence the name of these algorithms). The overall solution is then obtained from the calculation of the energy exchanges at the slices interfaces by matching the tangential fields with the boundary conditions. The most-known

modal algorithm is the Rigorous Coupled Wave Analysis (RCWA): we will exclusively use this method in our work and its principle will be detailed in the next sub-section. Note that other known variants of modal methods can be found such as the Exact Modal Method (EMM) [63]–[65] or the C method [66], [67], whose specificities are not discussed in the scope of this thesis.

2.1.2 The RCWA principle

The RCWA method was popularized in the early eighties by Moharam and Gaylord [68], [69] considering first dielectric or metallic planar gratings sinusoidally modulated, and quickly generalized to surface-relief gratings [70] and to the tridimensional case [71]. They based their algorithm on the previous work of three physicists regarding the Fourier decomposition of the dielectric permittivity: Burckhardt [72], Knop [73] and Kaspar [74]. In addition to this technique, they defined the electromagnetic field in the modulated (inhomogeneous) layer in the form of coupled waves propagating along the z -axis and corresponding to the diffracted orders outside the array. The RCWA is thus a modal method that specifically relies on the Fourier expansion of the modes, hence its other denomination: the Modal Method by Fourier Expansion (MMFE). Note that although this property should inherently limit this method to periodical problems, new variations were also developed to deal with a-periodic situations [75]–[77], that will not be used in this work.

The solving principle of the RCWA can be decomposed in four main steps whose principles are explained below.

- The first one is to slice the structures along the z -axis so that in each layer the permittivity is periodically modulated along the x - y plane and constant along z . (Figure 2.1). In practice, it means that the shape of the periodic pattern is approximated with successive rectangles in order to delimit the refractive index change in each slice. If we consider the case of biperiodic arrays (as it will be the case in our work) with P_x and P_y the periods along the x -axis and y -axis, this slicing in piecewise z -invariant layers thus leads to the following properties of the permittivity in one given modulated layer j (Eq. 2.1):

$$\begin{cases} \varepsilon_j(x, y, z) = \varepsilon_j(x, y) & \text{for } z \in [z_j, z_{j+1}] \\ \varepsilon_j(x + mP_x, y + nP_y, z) = \varepsilon_j(x, y, z) & \text{with } (m, n) \in \mathbb{Z}^2 \end{cases} \quad (\text{Eq. 2.1})$$

- Thanks to this construction, the dielectric permittivity will depend on x and y in each horizontal slice in the situation of biperiodic arrays. Therefore, it can be expanded in Fourier series with a $2\pi/P_x$ and a $2\pi/P_y$ factors in the exponential functions to take into account the periodicity (Eq. 2.2). The eigen-values in the frequency-domain are then calculated in each modulated layer j from Maxwell's equations.

$$\varepsilon_j(x, y) = \sum_{m, n=-\infty}^{+\infty} \varepsilon_{j(m, n)} e^{i\left(m\frac{2\pi}{P_x}x + n\frac{2\pi}{P_y}y\right)} \quad (\text{Eq. 2.2})$$

- The coupling between the different layers is then computed with the boundary conditions, where the tangential fields are matched at every interface.
- The last step consists in calculating the resulting diffraction efficiencies and the total electromagnetic field.

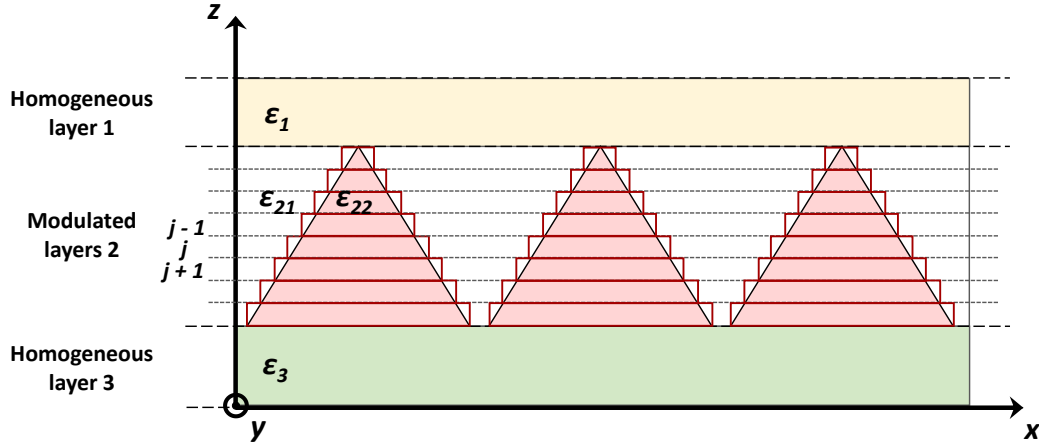


FIG. 2.1. Scheme of the principle of horizontal slicing of a periodical structure used with the RCWA algorithm. The dielectric permittivity is invariant in each slice along the z direction.

In practice, it is necessary for numerical computations to truncate the infinite Fourier expansion. The number at which we decide to truncate the expansion corresponds to the numbers of harmonics of the calculation. The choice of the truncation is made according to the problem that has to be solved, because the convergence and the accuracy of the calculations depend on this number. Continuous improvements brought to the numerical solving part from the mid-nineties [78]–[80] have contributed to make the RCWA one of the most-used algorithms for diffraction problems, applicable to a wide range of multilayered array structures.

One of the main advantages of this method is that it is considered as rigorous since no approximation is made in its mathematical development and since the calculations tend towards the exact solution when the number of terms in the Fourier expansion increases. It can be applied to model any motif and does not require advanced numerical methods. For our work, the RCWA constitutes also an interesting choice because it is able to easily handle oblique angles, which is crucial for our specifications regarding the angular stability of plasmonic filters.

2.1.3 Information about the code used

The execution of the RCWA method for our plasmonic structures is performed with a CEA in-house code built and developed by Jérôme Hazart, researcher at the CEA Leti Grenoble, France. This code was written in Matlab, by which the simulations are computed. It is available for infinite 1D or 2D arrays. The main running file contains the definition of the materials stack, the geometry of the periodic structures, the definition of the refractive indices and all information regarding the light source, such as the polarization state, the angles of incidence and the wavelength range. The number of harmonics taken into account in the field expansion is also chosen in this file. This code returns the absorption, the reflection and the transmission efficiencies of the structures. A similar version is also used to calculate field maps around and inside the structures.

The properties of the RCWA described in this part explain why it is particularly advantageous for our work since it is specifically dedicated to periodic structures and able to handle large angles of incidence. The fast computation of this algorithm constitutes also a significant asset for the simulation of several structures types and dimensions. We will now present the criteria used for the evaluation of the structures with respect to the targeted applications.

2.2 Performance evaluation tools

2.2.1 Ambient Light Sensors

We present in this section the methodology dedicated to the evaluation of filters aimed for the ALS application. The objective is to build software tools that take all the elements of the sensor involved in the optical path and return specific criteria that will allow for a quantitative evaluation of the impact of the different plasmonic filtering structures on the ALS sensor performance.

2.2.1.1 The global ALS sensitivity

The sole optical data contained in the spectral responses that are obtained from the RCWA simulations of the filters do not provide enough relevant information allowing for the proper evaluation of the performance of the global ALS device. The ALS performance calculation has to take into account the whole path of the light in the sensors, from the light incidence outside the sensor to the photons absorption in the Si photodiode, which is described in Figure 2.2.

We must first consider the different types of illuminant that can irradiate the sensors. For our calculations, we use a set of 18 illuminants supposed to represent the typical illuminations that are encountered in various situations. For example in indoor conditions, we use typical lightning such as fluorescent light sources, LEDs or the 3200 K blackbody, which emission is close to those of quartz-halogen light bulbs. To simulate outdoor conditions, we use the D65 illuminant which represents the emission of the sun [81]. The other illuminants are determined according to general specifications of STMicroelectronics's customers: the following calculations are still relevant for any number n of illuminants.

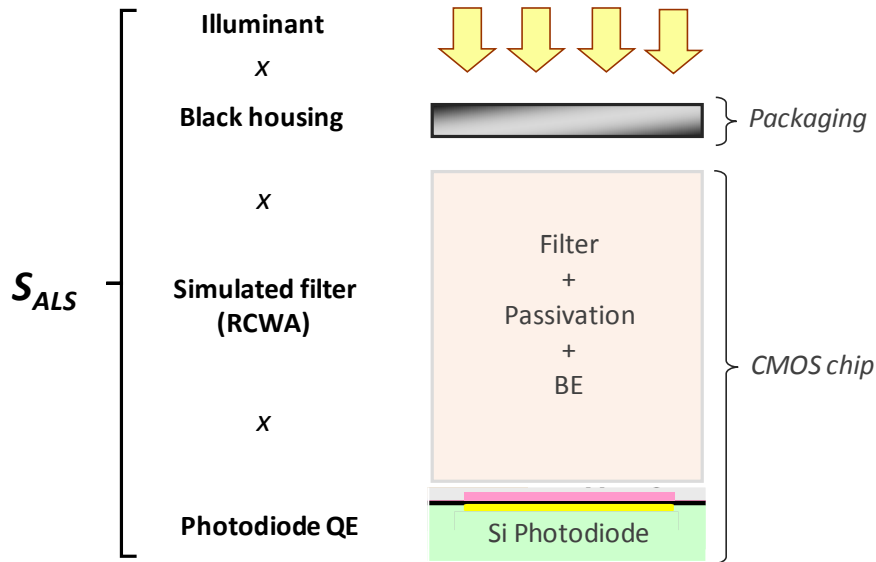


FIG. 2.2. Scheme of all the elements taken into account in the performance evaluation of ambient light sensors. The sensitivity of the device S_{ALS} (Eq. 2.1) is defined from: the type of illuminant, the black housing included in the packaging of the sensor, the filtering system (includes all the dielectric layers constituting the passivation layers and the back-end (BE) stack) and the quantum efficiency (QE) of the Si photodiode.

Thereafter, the methodology consists in taking into account all the sensor's elements located in the optical path. The first element encountered by the impinging light is a black housing included in the packaging of the sensors. This black housing is added owing to specific customers' request whose purpose is to make the sensors invisible to the users, especially in the case of smartphones. In practice, this black housing can be realized from a black window or a black resist which hinders the visible signal but has high transmissions in the NIR range. A typical spectral response of this black housing is given in Figure 2.3. This packaging thus does not facilitate the realization of ALS filters since the useful signal is centered at 550 nm. Secondly, the light impinges the filtering system. In our case, we consider the filtering element to be exclusively on-chip and is thereby composed of the plasmonic structures and of all the dielectric layers located above the photodiode, including the passivation layers (see 1. 2.4 *Structure and integration*). The spectral responses of the filters are extracted from the RCWA simulations. Finally, the last element taken into account is the absorption of the light in the photodiode, which is derived from the silicon quantum efficiency whose typical spectral response is shown in Figure 2.3.

Considering all these elements, we define the sensitivity of the sensors for a given illuminant i with the global ALS sensitivity S_{ALS} in $e^-/(lx.s)$, which is proportional to the spectrally integrated product of the relative spectral power distribution of the illuminant (defined as Ill), the black housing transmission (defined as $Black$), the filter spectral response (defined as $Filter$) and the photodiode quantum efficiency (defined as QE), relatively to the theoretical photopic response (Eq. 2.3). In this calculation, a denotes the size of the photodiode (m), hc/λ the photon energy (J), $F_{photopic}$ the photopic function and K_m its maximum sensitivity at 555 nm ($K_m = 683 \text{ lm/W}$).

$$S_{ALS}(i) = \frac{a^2}{hc} \cdot \frac{\int_{\lambda} Ill(i, \lambda) \cdot Black(\lambda) \cdot Filter(\lambda) \cdot QE(\lambda) \cdot \lambda \cdot d\lambda}{K_m \cdot \int_{\lambda} F_{photopic}(\lambda) \cdot Ill(i, \lambda) \cdot d\lambda} \quad (\text{Eq. 2.3})$$

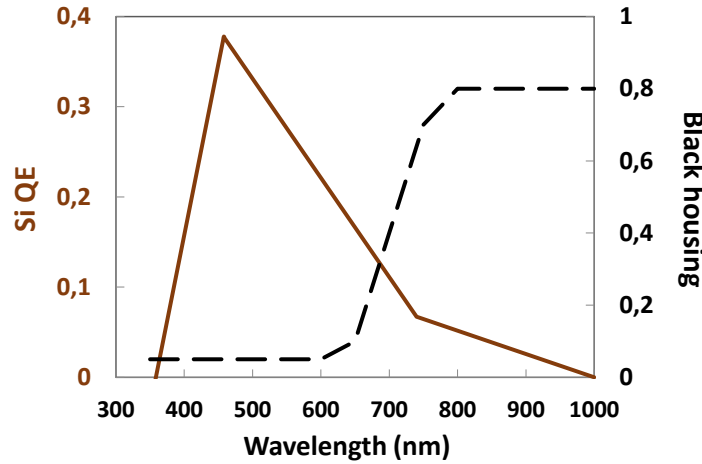


FIG. 2.3. Rough description of the silicon photodiode QE (brown curve) and of the black housing spectral response (black dashed curve). Only the trends are shown because the exact data are confidential. All the calculations in this thesis use the accurate data though.

2. 2.1.2 The performance criteria

From the ALS sensitivity that we defined in the previous sub-section, we derive two criteria in order to quantitatively position the different studied structures relatively to each other and to optimize the best designs according to the specifications of the global device. In practice, the integrated signal measured over the integration time on the ambient light sensor (in e^-) is multiplied by a calibration factor F_C . This

calibration factor aims to work with a photons flow instead of an electrons flow: it is then dimensionally equivalent to the inverse of a sensitivity (in $lx.s/e^-$). The calibration factor is calculated from two reference light sources $i = (REF_1; REF_2)$, chosen with an incandescent and a LED sources. More precisely, it corresponds to the geometric mean of the inverse of the two sensitivities $S_{ALS}(i)$ calculated under each reference illuminant (Eq. 2.4).

$$F_C = \sqrt{\left(\frac{1}{S_{ALS}(REF_1)}\right) \cdot \left(\frac{1}{S_{ALS}(REF_2)}\right)} \quad (\text{Eq. 2.4})$$

The first criterion is the ALS error. The purpose of this criterion is to quantify the stability of the sensitivity S_{ALS} of the ALS sensors with respect to the 18 different illuminants considered. It is defined as the relative variation of the dimensionless product of the sensitivity S_{ALS} and of the calibration factor F_C within the set of 18 illuminants, with respect to the two reference illuminants (Eq. 2.5). It is measured in decibel units. The relevant value of interest in our specifications is the *maximum* ALS error, which has to be inferior to 2.2 dB over the whole set of illuminants. The maximum ALS error is the main criterion that has to be respected. This 2.2 dB value corresponds to the maximum ALS error that was obtained on STMicroelectronics ALS sensors with a green resist associated with an external IR-cut filter at the beginning of this PhD work in 2012. This maximum 2.2 dB value constituted the objective of the thesis. In 2015, the maximum value obtained on STMicroelectronics sensors reached 1 dB with the use of a new IR-cut filter. In next chapters, these two reference values will be displayed in the evaluation charts, but the performance will only be compared to the 2.2 dB value. We show in Figure 2.4 an example of ALS error evaluation for a random filter structure. In this case, the filter does not fulfill our criterion since the ALS error exceeds 2.2 dB for 9 illuminants.

$$\text{ALS Error}_{\text{dB}}(i) = 10 \cdot \log_{10}(F_C \cdot S_{ALS}(i)) \quad (\text{Eq. 2.5})$$

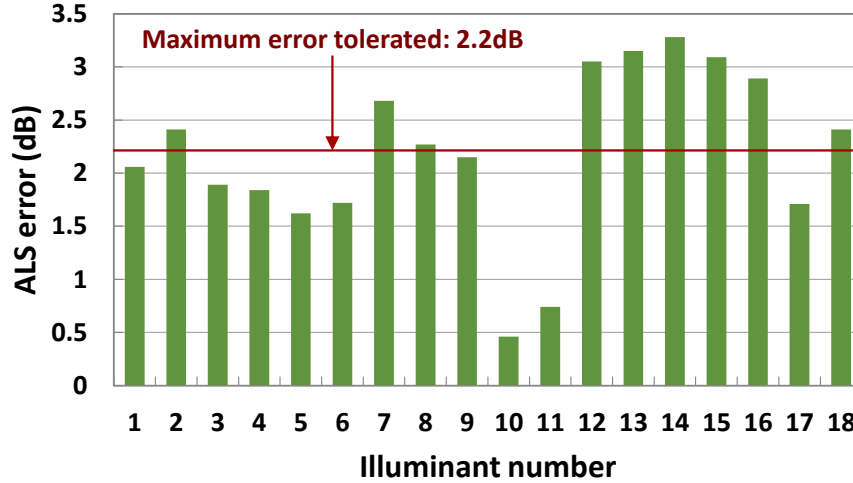


FIG. 2.4. Example of the ALS error evaluation over the set of 18 illuminants for a random filter. The relevant value for our study is the maximum ALS error obtained over the whole set.

The second criterion is the ALS dark. The aim of this criterion is to quantify the sensor sensitivity in low light conditions. It is defined as the signal given by the sensor in the dark at a given temperature T . This signal is calculated from the dark current of the photodiode C_{Dark} (in e^-/s) converted in lux with the calibration factor F_C of the sensor (Eq. 2.6). The constraint on this criterion is less severe than for the ALS error since no absolute value has to be respected in the specifications. For the filters optimization, the ALS dark simply has to be minimized. In order to fix a reasonable limit for the calculations, we

choose an arbitrary value of 100 lx as the maximum tolerable ALS dark (6 times the value of the current solution with the green resist and a new IR-cut filter (16.4 lx)). Metallic filters present the advantage of relieving the constraint on this ALS dark criterion compared with organic resists. Indeed, metallic filters are not degraded by thermal treatments and STMicroelectronics' studies demonstrated that a final annealing of the sensor could improve the photodiode quantum efficiency thanks to the thermal activation of the silicon dopants. Although the magnitude of this improvement is not accurately determined, it is expected to decrease the ALS dark value with a factor between 2 and 5.

We give in Figure 2.5 an example of the complete ALS evaluation of a random filter structure in a 2D scatter plot featuring the ALS dark and the ALS error. Bear in mind that although we draw the mean, the RMS and the maximum ALS errors for this example, the only relevant value for our evaluation that will be drawn in the following studies is the maximum error. The green area stands for the ranges in which the ALS performances meet the previously defined specifications (maximum ALS error < 2.2 dB and ALS dark < 100 lx). In other words, a dot in the green area means that the corresponding filter matches the ALS requirements.

$$\text{ALS Dark}_{\text{lx}}(T) = F_C \cdot C_{\text{Dark}}(T) \quad (\text{Eq. 2.6})$$

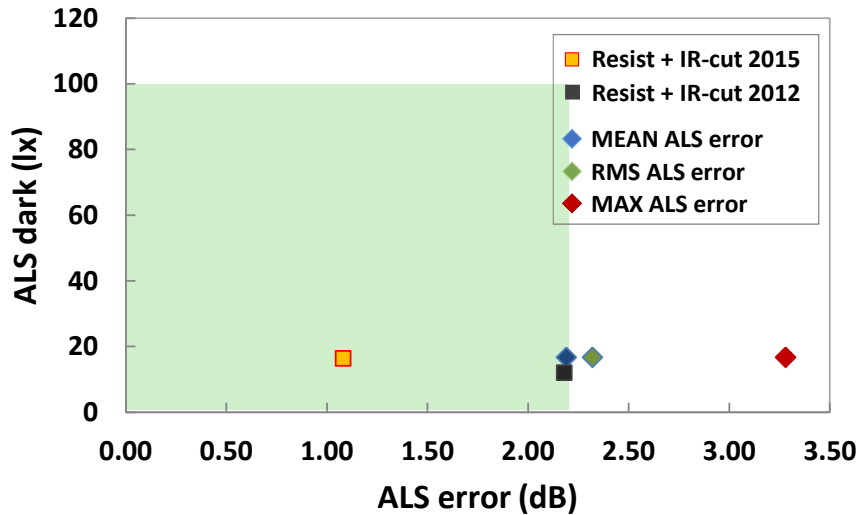


FIG. 2.5. Example of a complete ALS evaluation with the ALS dark and the ALS error on a random filter (blue, green and red dots). The green area delimits the ranges within which the specifications are respected (based on the maximum ALS error of the 2012 sensors at 2.2 dB (black dot)). The orange dot represents the performance (maximum ALS error) of the 2015 solution using a green resist combined with a new IR-cut filter. In the following work, only the maximum error will be used.

In order to estimate the sensitivity of these two ALS criteria with respect to the filter, we reproduce different theoretical spectral responses by using Gaussian bells (Figure 2.6). The green curve corresponds to the theoretical photopic response. Each other curve represents a single particular deviation from the photopic response: the blue curve and the red curve simulate a blueshift and a redshift of the peak respectively; the brown curve simulates a half transmission loss from the photopic response and the yellow and purple curves stand for a signal loss with a thinner FWHM or a signal gain with a wider FWHM respectively. It can be clearly seen from this chart that the ALS dark is directly related to the transmission efficiency of the filter. Any signal loss (half transmission for the brown curve or thinner peak for the yellow curve) induces an increase of the ALS dark. Conversely, any signal gain leads to a decrease of the ALS dark (wider peak for purple curve). Finally, the calculations also reveal that the ALS error is very sensitive to the wavelength range of the filtered signal. The performances corresponding to the blue and to the red curves indeed show a substantial increase of the ALS error once

the filtered signal deviates from the photopic response. In particular, we see that ALS filters require a strong rejection in the NIR range to prevent this ALS error increase.

This first analysis shows that the criterion of strong rejection in the NIR range constitutes a high constraint on the plasmonic filters' design since silicon absorbs photons with a wavelength up to 1.1 μm .

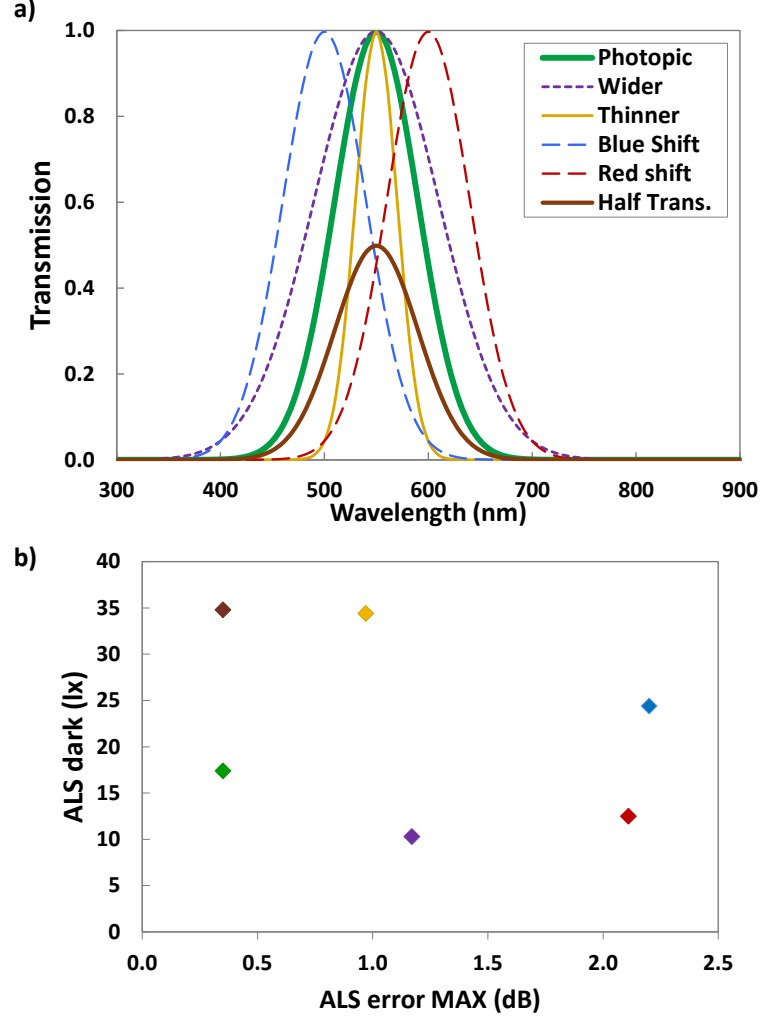


FIG. 2.6. (a) Theoretical Gaussian spectra corresponding to the photopic response (green curve) and to specific deviations. (b) Corresponding ALS performance evaluation.

2.2.2 RGB image sensors

The major part of this work is devoted to ALS sensors. However as the state of the art is essentially based on RGB sensors, some plasmonic structures were also evaluated for RGB sensors applications for reference. The evaluation of the RGB performances of plasmonic filters is performed with a dedicated tool developed internally in STMicroelectronics. This algorithm returns the RGB quality parameters from simulated images, and takes into account the whole imaging system, including the type of illuminant, the imaging optics and image sensor characteristics. An extensive description of the operating principle of the tool can be found in [9], [82]. Namely, the first factor that we consider is the color error ΔE_{2000} as defined in the CIELAB colorimetric space [83], which is calculated from the 24 color patches of the Gretag-MacBeth colorchecker [84]. A noise indicator is also evaluated through the SNR_{10Y} , which corresponds to the value of scene illuminance in lux required to have a signal-to-noise ratio (SNR) equal to 10, considered as the lowest acceptable value with camera-phones in low light

conditions. The SNR_{IOY} and the color error ΔE_{2000} must be as low as possible. We also compute the noise gain N_G , which gives the noise level brought only by the color correction matrix, whereas the SNR also takes into account the noises induces by the pixels and the signal level [9]. Its definition is given in Eq. 2.7, where β_i are the conversion factors of the luminance channel and c_{ij} the coefficients of the color correction matrix defined in *Chapter 1*, with $i, j = [R, G, B]$. The noise gain indicates the filtering quality, and especially the amount of correction required to compensate the color cross-talk. The ideal value of noise gain is $N_G = 1$, which means that the color correction matrix would be the unity matrix (no color correction needed).

$$N_G = \frac{\sqrt{\sum_{i=R}^B \beta_i^2 \cdot (\sum_{j=R}^B c_{ij}^2)}}{\sqrt{\sum_{i=R}^B \beta_i^2}} \quad (\text{Eq. 2.7})$$

For our calculations, we consider a 3 Mpixels sensor with 1.4 μm pixel size under a 3200K incandescent light source, a scene reflectance of 18 %, a transmission of the optical system of 80 %, an aperture $f\# = 2.8$, the monochrome response of a 3 μm -thick silicon layer, a frame rate of 15 fps, a noise floor of 3 e^- and a photo-response non-uniformity of 1 % [9], [25], [82].

The evaluation tools have now been presented for the two targeted applications. They have allowed us to establish accurate criteria defining the specifications that have to be met by the filters. We can now proceed to the evaluation of various plasmonic structures to identify those which best fit with the technological challenges of this work.

2.3 Plasmonic structures for spectral filtering

Now that the optical and integration requirements are fully established and that the numerical evaluation methods are described, we can focus on the core of the thesis issue: which plasmonic structures better address the specifications we are looking for? We explained in *Chapter 1* that the condition of EOT phenomenon with plasmonic resonances can be obtained with periodic arrays of metallic nanostructures. There are different kinds of structural color filters that can be found in literature. Depending on their structures, they each feature different optical properties and spectral responses that make some more appropriate for specific applications than others, such as color sorters [56], [57], color filters [52]–[54], [85], absorbers [86]–[89], waveguides [90]–[92] or displays [93]. In our case, we are only interested in a filtering solution involving transmissive filters since they can be equivalently used as a direct replacement of resist-like or Fabry-Perot-like filters in their principle of integration. Three major structures categories are investigated for such an application. The holes arrays constitute the most widespread solution [52], [53], [55], [85], [94], [95], but a few works on metallic patch arrays [96], [97] and metal-insulator-metal (MIM) structures [57], [98] also demonstrated transmissive filtering properties. Although a few recent papers seem to focus on CMOS-compatible materials [85], [94], [99]–[102], most do not take into account these considerations and propose studies using fabrication techniques and materials such as silver, gold or optical materials that are not found in industrial CMOS front-end fabs.

In this section, we present our results regarding the achievable performance of these main structures types when they are simulated by taking into account the CMOS-compliance constraint on the materials choice and the industrial integration constraint. In each of the following sub-sections, the only materials that we use are aluminum or copper for the metallic layers, and SiO_2 or Si_3N_4 for the dielectric medium, although TiO_2 is sometimes used as a comparison with a high refractive index dielectric. The

arrays are infinite in the x and y directions. The specifications of the targeted applications in the visible range, i.e. the angular stability and the performance of image sensors and ambient light sensors, are also considered to estimate which designs feature the most required properties.

2.3.1 Metal-Insulator-Metal structures

2.3.1.1 Generalities on MIM arrays

MIM stacks are widespread structures in the field of nanophotonics. Two noticeable applications in particular can be cited: plasmonic waveguides and photon absorbers, which are generally able to provide high absorption efficiency all over the IR spectrum, depending on the dimensions of the structures and on the dielectric cavity thickness [88], [99], [103]. These devices are generally fabricated with an array of metal-insulator patches lying onto a continuous metallic layer [89], [104]. In 2010, Xu *et al.* demonstrated the color filtering effect of MIM gratings composed of aluminum and ZnSe for the dielectric core [98], [105]. MIM planar structures are known to sustain two plasmonic eigenmodes, called the antisymmetric mode and the symmetric mode according to the symmetry of the longitudinal electric field E_x (Figure 2.7) [106]. Xu *et al.* reported that the antisymmetric mode has a near-linear dispersion across the visible range, making the design of transmissive filters easy for any color. The simulation and the fabrication of such RGB filters showed transmission efficiencies up to 60 % and a FWHM of about 100 nm.

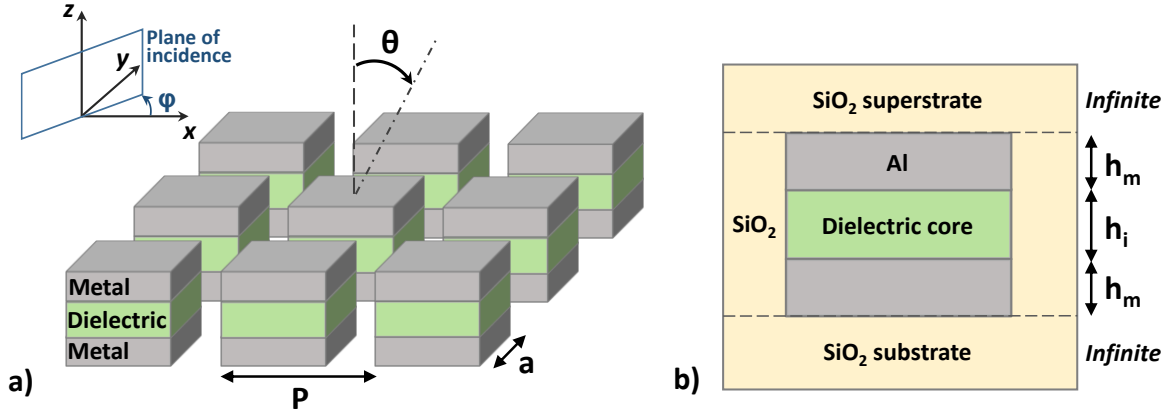


FIG. 2.7. (a) Scheme of a typical MIM filter with a square array (period P) of square patches (size a). (b) Slice view of the elementary cell with a MIM stack composed of two metallic layers of thickness h_m , separated with a dielectric core of thickness h_i . The surrounding of the patches, the superstrate and the substrate are made of SiO_2 .

Although this work demonstrated promising results, its limits are quickly reached when it comes to its use in an industrial context of the applications we are aiming for. The structures consist of 1D gratings that are inherently polarization-dependent, which make them interesting for the fabrication of polarizers, but not for high-yield sensors since almost half of the signal of unpolarized lights is lost [100], [103], [107], [108]. Furthermore, the optical performances are obtained with a high-RI dielectric (ZnSe) which use would not be possible in industrial CMOS front-end clean rooms. In this section, we investigate the main optical properties of MIM structures by simulating 2D arrays of MIM patches to overcome the polarization-dependency and by using CMOS-compatible materials only. The structure of the filters is given in Figure 2.7. Here, we only consider a square array of period P of square patches of size a . We define the fill factor of the structure as the ratio $ff = a/P$. The metal thickness h_m is considered the same on the top and at the bottom of the dielectric core, whose thickness is denoted h_i . The substrate,

the superstrate and the inter-patch dielectric are all made of SiO_2 (with a constant refractive index $n = 1.46$). The superstrate and the substrate are considered infinite. The dielectrics are considered as lossless materials ($n'' = 0$). In order to evaluate the angular stability of MIM structures, the filters responses are calculated at different polar and azimuthal incidence angles θ and φ . The azimuth φ is defined as the angle between the x-axis and the incidence plane. The filters are also simulated with both TM and TE polarizations to evaluate their dependence on polarization. TE polarization is defined with the electric field \mathbf{E} along the y-axis and \mathbf{H} in the (xz) plane when $\varphi = 0$. Consequently, TM polarization is defined with \mathbf{E} in the (xz) plane and \mathbf{H} along the y-axis for $\varphi = 0$. Due to the symmetry of the array, the response of the filters at normal incidence is the same under TM and TE polarizations.

2.3.1.2 Material for the dielectric core

Given the high number of parameters that can be studied for such structures, the materials used for the metallic layer and for the dielectric surrounding the MIM patches are fixed. Aluminum is chosen for its optical properties in the visible range [45], [46], [109], and SiO_2 is chosen for the dielectric surrounding owing to its general use in optical structures and in the CMOS industry. The selection of the remaining dielectric core included between the two metallic layers is of prime importance for the optical response the filter [98], [105]. Typically, the resonance occurs in the visible region when h_i is in the range of a few hundreds of nanometers. The effective index theory n_{eff} has to be used to account for the coupling of the plasmons of each metallic layer. It is related at first order to the skin depth of the metal and to the cavity thickness h_i (Eq. 2.8) [91].

$$n_{eff} = n_{cavity} \cdot \left(1 + \frac{\delta}{h_i}\right) \quad (\text{Eq. 2.8})$$

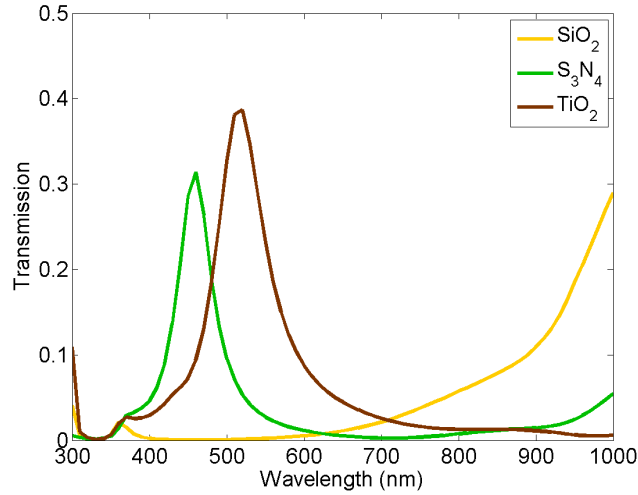


FIG. 2.8. Impact of the refractive index of the dielectric core of the MIM stacks on the spectral response. The filter's dimensions are: $h_m = 50$ nm, $h_i = 50$ nm, $P = 200$ nm and $a = 150$ nm.

The impact of the refractive index of the dielectric core is thus studied by simulating three different dielectrics. SiO_2 and Si_3N_4 are used respectively as low and medium RI dielectrics ($n_{\text{SiO}_2} = 1.46$ and $n_{\text{Si}_3\text{N}_4} = 2$). Although its integration in CMOS clean rooms is not common, TiO_2 is also used to model a higher RI dielectric ($n_{\text{TiO}_2} = 2.5$). The results are drawn in Figure 2.8. First, we can verify here that this kind of structures is able to provide optical filtering properties with a strong rejection outside of the resonance peak. In addition to the spectral redshift of the resonance, it is noticeable that a high refractive index of the dielectric core significantly increases the transmission efficiency. We note however that this

improvement only raises the transmission to 40 % for the simulated filter. This observation suggests that the performance of CMOS-compatible MIM structures will be limited in terms of transmission level. For the following studies, Si_3N_4 will be used for the dielectric core in order to maximize the transmission while respecting the CMOS compliance constraint.

2.3.1.3 Structures investigation

These MIM structures are characterized by different parameters that can be used to tune the optical response of the filters. Although the results in the state-of-the-art have confirmed their filtering properties, they also revealed a weak performance in transmission. In this sub-section, we want to study how MIM filters behave with respect to each geometrical parameter in order to see if the transmission can be improved. First, the effect of the array periodicity on the resonance is plotted in Figure 2.9(a). The linear redshift of the resonance as P increases is well noticed. It can however be seen that the transmission efficiency hardly exceeds 35 %, which is far too weak for an image sensor application. On Figure 2.9(b), we show that an increase of the fill factor leads to higher transmissions, but at the cost of a significant degradation of the rejection, especially in the NIR range for low fill factors. This bad IR rejection would require the use of an external IR-cut filter as it is the case for organic resists. This would thus reduce the interest of plasmonic filters regarding the removal of any additional filters above the sensors.

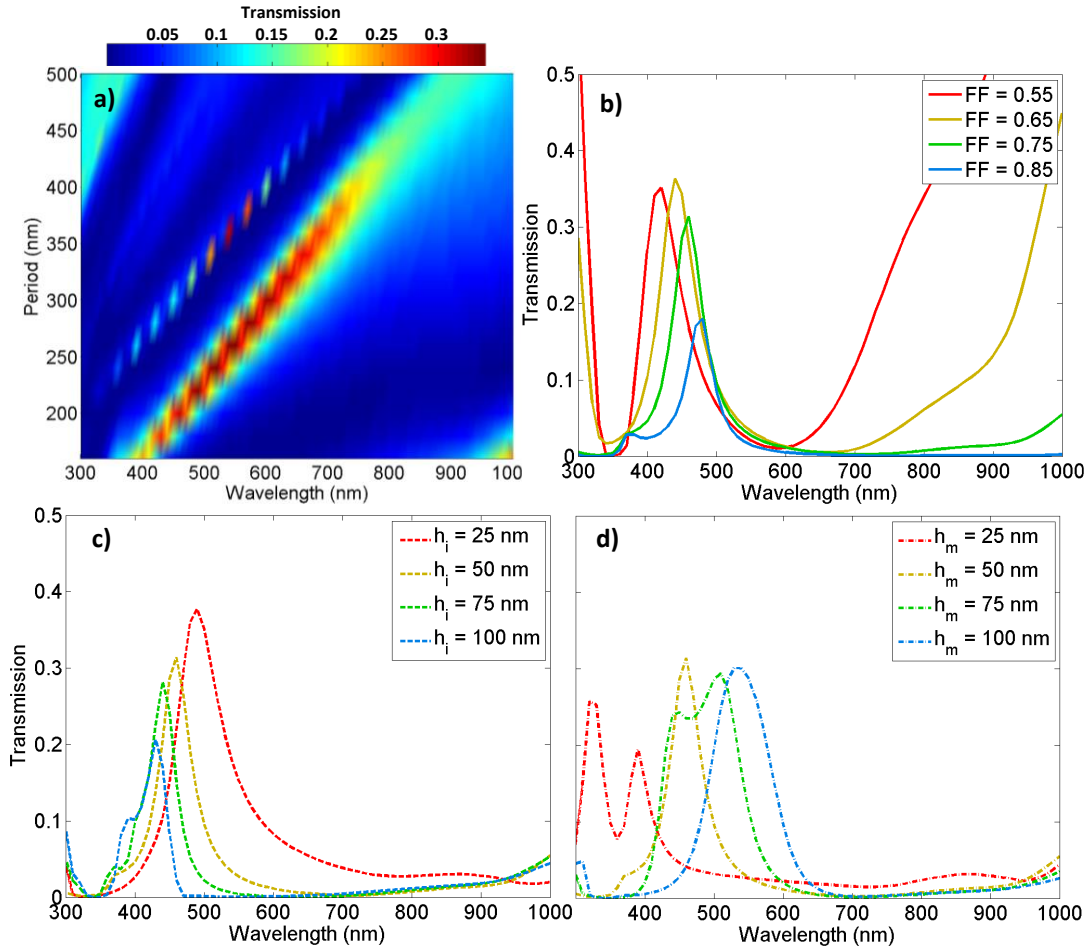


FIG. 2.9. (a) Evolution of the resonance with the period of the array P . (b) Evolution of the filter's response with the fill factor ff ; (c) with the insulator thickness h_i . (d) with the metallic thickness h_m . The filter's dimensions are: $h_m = 50$ nm, $h_i = 50$ nm, $P = 200$ nm and $a = 150$ nm.

The effect of the thicknesses of the different layers composing the MIM stacks is described in Figure 2.9(c)-9(d). The insulator thickness has a weak impact on the transmission efficiency and on the FWHM, but we can observe a slight redshift of the resonance when h_i decreases (Figure 2.9(c)). This redshift is due to the higher coupling between the plasmons of the two metallic layers, leading to an increase of the effective index n_{eff} as shown in Eq. 2.8. Conversely, the filter response is substantially impacted by the thickness of the two metallic layers (Figure 2.9(d)). The results suggest that there is an optimal value of h_m for which the transmission and the quality factor of the filter are maximized (50 nm in our case). When h_m is increased, the decrease in transmission can be attributed to higher metallic losses. Although it has to be investigated in details, the theoretically predicted lowering of the transmission when h_m is decreased may be attributed to a stronger coupling between the plasmons of the $\text{SiO}_2 - \text{Al}$ and the $\text{Si}_3\text{N}_4 - \text{Al}$ interfaces through tunnel effect across the thinner metallic layers.

In the hypothetical case where TiO_2 could be used in industrial clean rooms to maximize MIM performances, one can obtain, with a finer tune of the geometrical parameters, RGB spectra corresponding to the wavelength of each color pixel (B: 460 nm, G: 540 nm and R: 610 nm approximately) as shown in Figure 2.10. Note that the presented spectra could not be considered as an optimal parameters study to perform RGB filters. As mentioned earlier, MIM filters suffer from low transmissions with a maximum of 42 % for the blue pixel, when current organic resists provide transmissions nearing 90 %. Moreover, the blue filter shows a drastic increase of the transmission above 800 nm in the NIR region that would impose the use of an additional IR filter, which we would precisely like to avoid. The analysis of the color accuracy with such filters can be performed with the RGB evaluation tool, described in the previous section 2. 2.2. The results are given in Table 2.1 and compared to a model of RGB color resists [9], [19]. We can see that the color error is 74 % higher and the noise gain 18 % higher for the MIM arrays. Moreover, the SNR10Y is severely degraded with a 250 % increase compared with the resists. MIM structures thus do not present any interesting RGB performance compared with the color resists currently in-use.

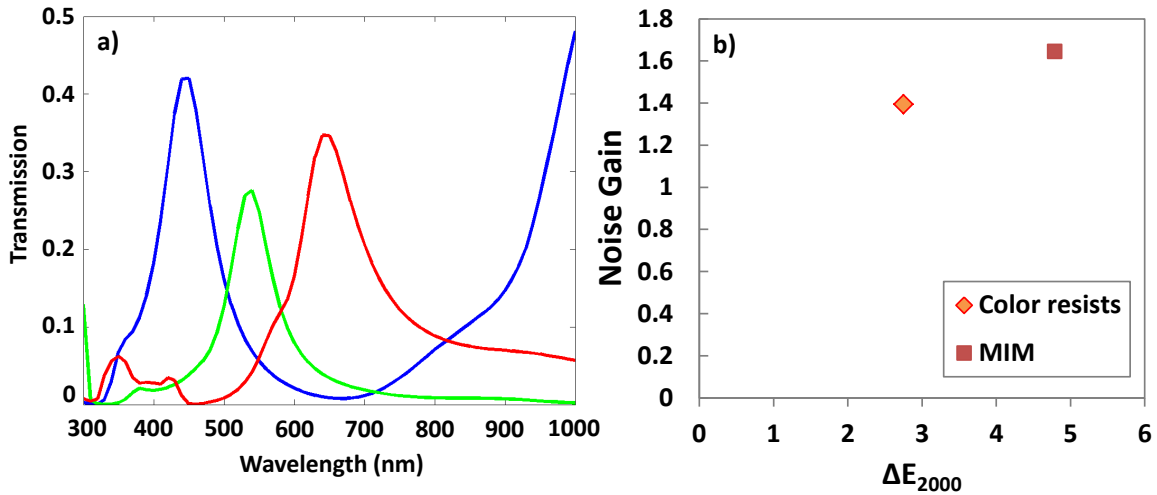


FIG. 2.10. (a) Example of a RGB filters set using MIM with TiO_2 as the dielectric core. The filter's dimensions are: $h_m = 50$ nm, $h_i = 50$ nm and $P = 170$ nm and $a = 110$ nm for the blue filter; $P = 210$ nm and $a = 170$ nm for the green filter; $P = 280$ nm and $a = 210$ nm for the red filter. (b) Comparison of the RGB performances obtained with the set of RGB MIM arrays and with color resists.

	ΔE_{2000} RMS	ΔE_{2000} Max	Noise Gain	SNR10Y
Color resists	2.75	6.25	1.39	89.6
MIM arrays	4.79	8.71	1.65	314.4

TABLE 2.1. Corresponding performances calculated with the RGB evaluation tool.

2.3.1.4 Angular stability

In addition to the global response of the filters, one of the main specifications for filters on chip without lens system is the robustness of the structures to severe off-normal incidence conditions. Specifically, the structures are simulated at different polar angles of incidence θ , but also at different azimuths φ . The nature of the filters with the 2D structuration of the metallic layer indeed makes them inherently sensitive to the azimuthal angle, which is seldom taken into consideration in the investigation of plasmonic filters to our knowledge. Typically, the structures have to provide a stable response until $\theta = 60^\circ$ in our specifications for RGB filters, and until $\theta = 30^\circ$ for the ALS sensor as detailed in *Chapter 1*. Both filter types have to be insensitive to the azimuth φ , which is only simulated in the $[0^\circ; 45^\circ]$ range, owing to the symmetries of square arrays.

We present the angular responses with varying θ of the red filter defined in the previous subsection for both TE and TM polarizations, at azimuth $\varphi = 0^\circ$ (Figure 2.11(a)) and $\varphi = 45^\circ$ (Figure 2.11(b)). Note that the values of polar angles θ are given in air as if there was a very thick SiO_2 superstrate between the metallic patches and the air above the sensor. At $\varphi = 0^\circ$, a stronger sensitivity is noticed with respect to the TM polarization with significant variations of the transmission and a noticeable redshift of the resonance, when the TE polarization remains stable and only experiences a decrease in transmission for $\theta = 60^\circ$. At $\varphi = 45^\circ$, the two polarizations behave similarly with progressive transmission loss and redshift when θ is increased.

The last results have demonstrated the difficulty of MIM structures to provide transmission exceeding 40 %, together with poor polarization robustness and angular stability, which rapidly degrades the filters' response even for low angles of incidence. Other structures have thus to be investigated to answer our technological challenges.

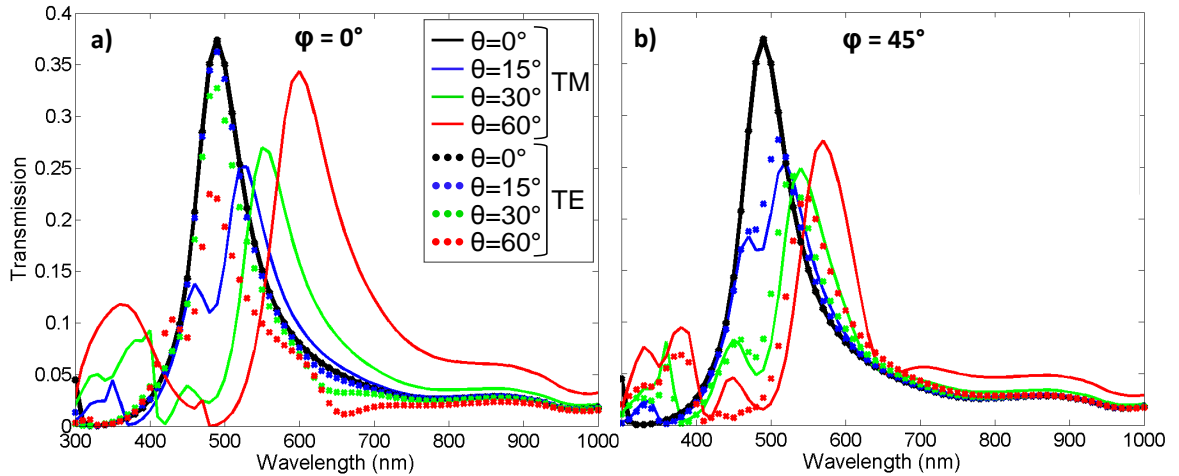


FIG. 2.11. (a) Evolution of a MIM filter response with increasing θ for both TE and TM polarizations at $\varphi = 0^\circ$. (b) Same evolution at $\varphi = 45^\circ$. The filter's dimensions are: $h_m = 50$ nm, $h_i = 25$ nm, $P = 200$ nm and $a = 150$ nm.

2.3.2 Metallic patch arrays

2.3.2.1 Introduction to metallic patch arrays

As discussed previously, the MIM arrays have shown their limits in terms of optical performance and ease of fabrication for the application requirements we are targeting. In literature, simpler structures made of a single metallic layer can be used to excite plasmon resonances and to realize optical filtering. These structures consist of periodical arrays of metallic patches in a dielectric medium and are thus

easier to fabricate, since a single lithography step is sufficient to perform the nanostructuration of the metallic filters. Unlike MIM structures, the optical phenomenon behind metallic patch arrays is related to the physics of metallic nanoparticles. Although the use of metallic particles to realize colorful textures has been known for centuries (a famous example of this technique is the Roman Lycurgus cup [110]), the underlying theory has only been explained recently thanks to the development of Plasmonics. In this case, the color filtering effect is due to the excitation of localized surface plasmon (LSP) resonances at the metal-dielectric interface that leads to strong absorption and scattering of the incoming light by the particles. The theoretical background of metallic nanoparticles is not in the scope of this thesis, but the reader can find more information about this plasmonic effect with the Mie scattering [111]. Such structures have been widely investigated for light absorption, especially in the NIR range [112], [113]. Since 2012, a few studies have also investigated in more detail the potential use of metallic patch arrays to perform filtering applications in the visible range, even with 1D arrays [114]. With 2D arrays, different patch shapes have been studied, from squares [97] to asymmetric crosses [96]. Those works demonstrate a potential filtering application with complementary colors (CMY instead of RGB color filters), but little information is found on the angular dependence of these structures or on their ability to realize a green filter as in the case of the ALS application.

In this sub-section, we aim to properly evaluate the performance of metallic patch arrays relatively to the specifications of our targeted applications, especially regarding the angular stability of such structures. In our simulations, we use 2D square arrays of aluminum patches of thickness h_m in an infinite lossless SiO_2 surrounding ($n = 1.46$). Two shapes are studied for the metallic patches: squares with size a (Figure 2.12(a)) and crosses with arm length a and arm width b (Figure 2.12(b)). The angular stability of the metallic patch arrays is calculated under different polar and azimuthal incidence angles θ and φ . The azimuth φ is defined as the angle between the x-axis and the incidence plane. They are also simulated with both TM and TE polarizations to evaluate their dependence on polarization. As in the case of MIM structures, TE polarization is defined with the electric field \mathbf{E} along the y-axis and \mathbf{H} in the (xz) plane when $\varphi = 0$. Consequently, TM polarization is defined with \mathbf{E} in the (xz) plane and \mathbf{H} along the y-axis for $\varphi = 0$. Due to the symmetry of the array, the response of the filters at normal incidence is the same under TM and TE polarizations.

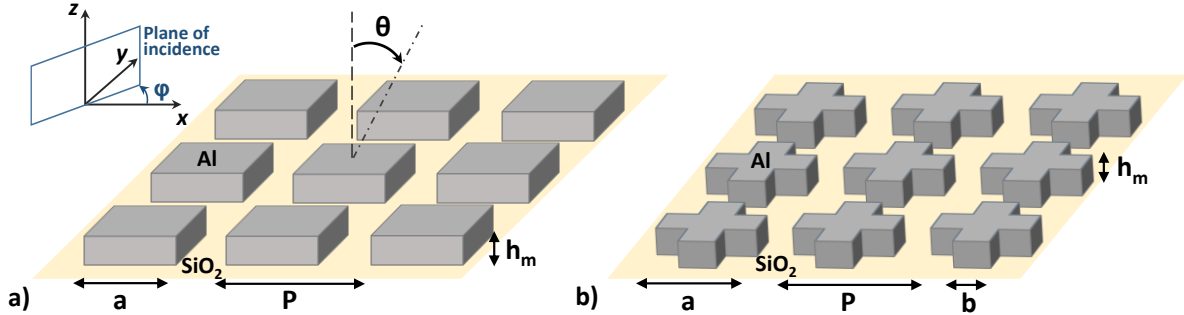


FIG. 2.12. (a) Scheme of a typical metallic-patches filter with a square array (period P) of square patches (size a) with thickness h_m . (b) Scheme of a metallic-patches filter with a square array (period P) of cruciform patches (arm length a and arm width b) with thickness h_m .

2.3.2.2 Square patches

The results found in literature suggest a difficulty to realize transmissive RGB filters with arrays of square patches [97]. The spectral responses of such structures indeed have the characteristics of complementary color filters with a transmission dip rather than a transmission peak. It can be seen in Figure 2.13(a) that the transmission of the simulated filter ($h_m = 200$ nm, $P = 200$ nm and $a = 100$ nm) has a dip in the blue wavelengths and experiences a quick increase in the green and the red wavelengths, which would approximately correspond to a yellow filter in a CMY pixels matrix. Conversely, a distinct

reflection peak can be observed around 500 nm, which implies that metallic patch arrays can be used as RGB reflective filters.

The angular and polarization dependencies of the same filter are then studied similarly to the MIM structures. The filter is simulated for both polarizations TM and TE with different polar angles of incidence θ up to 60° , at azimuth $\varphi = 0^\circ$ (Figure 2.13(b)) and $\varphi = 45^\circ$ (Figure 2.13(c)). The values of polar angles θ are given in air as if there was a very thick SiO_2 superstrate between the metallic patches and the air. There is not obvious distinction between the case $\varphi = 0^\circ$ and $\varphi = 45^\circ$. In both situations, there is a progressive signal loss between 400 nm and 500 nm and a decrease of about 10% in transmission over the whole spectrum when θ is increased up to 60° , for both polarizations. It is difficult to estimate the angular stability of these structures from such spectra, but the sole transmission line shape at normal incidence makes them inadequate for our applications anyway.

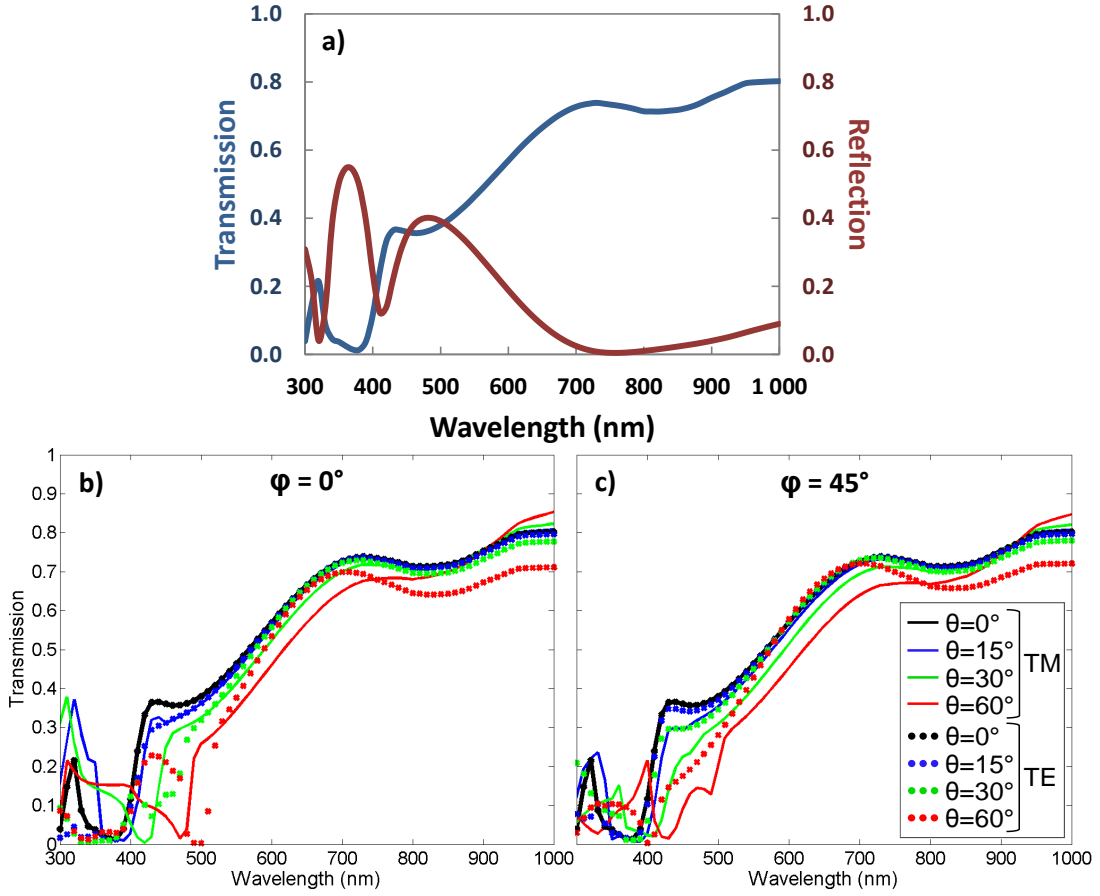


FIG. 2.13. (a) Transmission and reflection spectra of a square metallic patches filter. (b) Evolution of the filter response with increasing θ for both TE and TM polarizations at $\varphi = 0^\circ$. (c) Same evolution at $\varphi = 45^\circ$. The filter's dimensions are: $h_m = 200$ nm, $P = 200$ nm and $a = 100$ nm.

2.3.2.3 Cruciform patches

A different shape of metallic patches was investigated in literature with asymmetric crosses, which showed interesting polarizing effects [96]. This property is however an undesired effect that we precisely want to avoid for our applications. We thus propose a study of a more basic shape with symmetric cruciform metallic patches as described in Figure 2.12 so that the polarization dependency of the filters is suppressed at normal incidence. Unlike square patches, our simulations show that it is possible with a proper tuning of the geometrical parameters to obtain a transmission peak allowing for a RGB filtering (Figure 2.14(a)). Although the rejection could be improved with a higher metal thickness, the spectral

response of the presented filter ($h_m = 50\text{ nm}$, $P = 300\text{ nm}$, $a = 240\text{ nm}$ and $b = 96\text{ nm}$) exhibits a well-defined peak at 520 nm reaching a transmission of 65% and a FWHM of about 150 nm . In this case, the reflection curve does not feature remarkable properties.

As in the case of square patches, we simulate the angular and polarization sensitivities of this filter for the two azimuths $\varphi = 0^\circ$ (Figure 2.14(b)) and $\varphi = 45^\circ$ (Figure 2.14(c)). The results show that this kind of structure is also drastically sensitive to off-normal incidence conditions even for low polar angles of incidence ($\theta = 15^\circ$). Unlike MIM structures, it can be seen that the behavior of the two polarizations is inverted at $\varphi = 0^\circ$ and $\varphi = 45^\circ$. At $\varphi = 0^\circ$, the spectral response of the TE polarization severely deteriorates with θ , whereas the TM polarization is less impacted, and conversely for $\varphi = 45^\circ$. Even if the cruciform patches are able to provide refined transmission peaks, their strong angular and polarization sensitivities make them unusable relatively to our specifications. Further work is thus required to find out better structures fitting our needs.

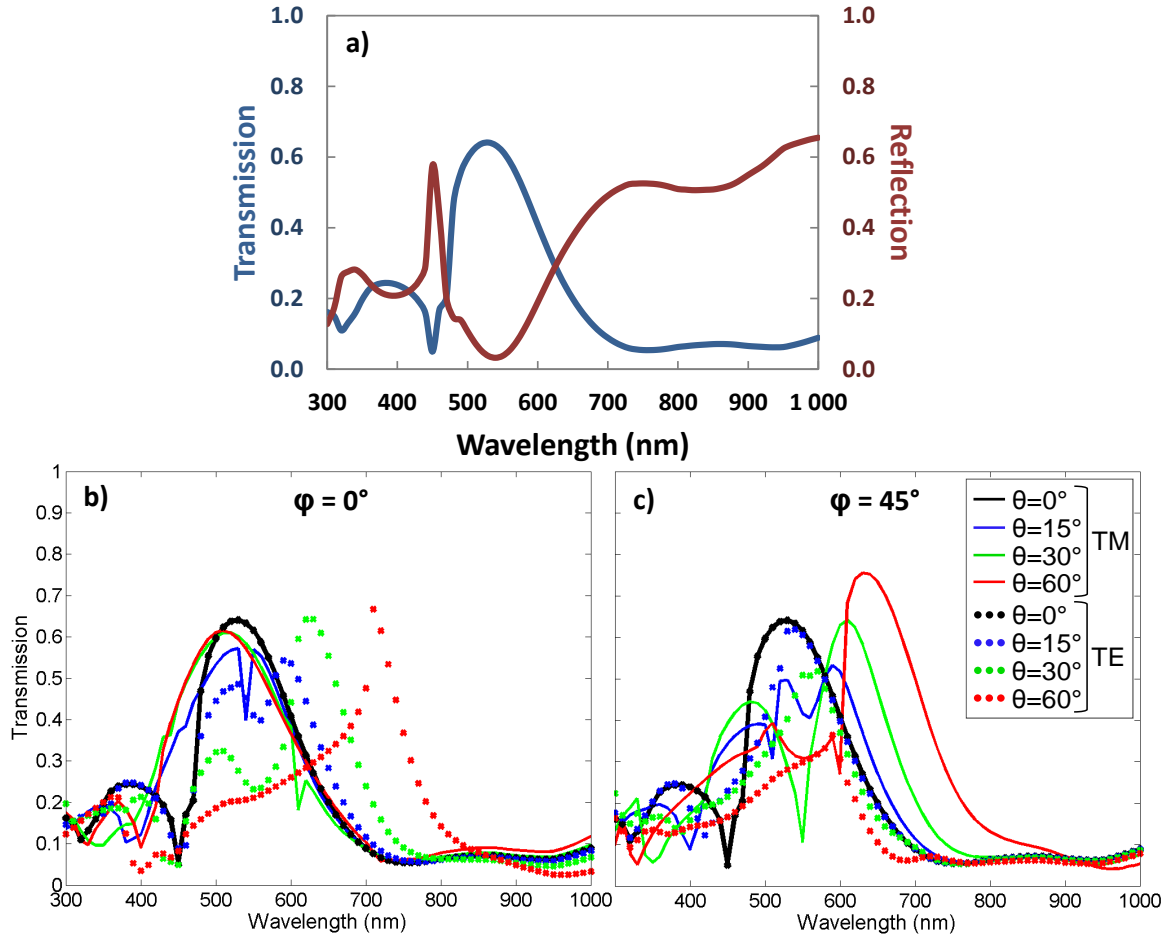


FIG. 2.14. (a) Transmission and reflection spectra of a cruciform metallic patches filter. (b) Evolution of the filter response with increasing θ for both TE and TM polarizations at $\varphi = 0^\circ$. (c) Same evolution at $\varphi = 45^\circ$. The filter's dimensions are: $h_m = 50\text{ nm}$, $P = 300\text{ nm}$, $a = 240\text{ nm}$ and $b = 96\text{ nm}$.

2. 3.3 Hole arrays in a metallic layer

2. 3.3.1 Extraordinary Optical Transmission in subwavelength hole arrays

The most widespread structures for plasmonic filtering are definitely the dielectric hole arrays in a metallic layer. In 1998, T.W. Ebbesen *et al.* published the first experimental evidence of the role of surface plasmons in the transmission of light through sub-wavelength apertures [115]. With transmission measurements through arrays of circular holes in a 200-nm-thick Ag layer, they observed transmission peaks occurring at wavelengths larger than the holes diameter, and with intensities much higher than the theoretical signal normalized to the total aperture area. These results quickly appeared as groundbreaking in the field of nanophotonics since it contradicted the previously established diffraction theory of light through small apertures [53], [116]. This theory stated that in the case of a hole in an infinitely thin and perfect metal sheet, the transmission efficiency would be extremely weak, decreasing with the wavelength to the fourth power below the cutoff wavelength of the aperture. The work of Ebbesen *et al.* thus demonstrated the high potential of plasmonics to manipulate light propagation at nanoscale, which they called the Extraordinary Optical Transmission (EOT).

This optical phenomenon exists thanks to the resonance of plasmons inside the structures. When the incoming light impinges the periodically structured metallic layer, a coupling between the electromagnetic field and the free electron gas of the metal is created by the diffraction of the light on the array. These diffraction effects add an additional momentum to the parallel component k_{\parallel} of the light wavevector k_0 which allows for the momentum matching with the surface plasmon wavevector k_{spp} (see 1. 4 *The plasmonic alternative*). This coupling thus generates a collective oscillation of the electron plasma propagating at the metal-dielectric interface, known as a surface plasmon polariton (SPP). In the case of 2D hole arrays, the plasmon wavevector k_{spp} can be written as presented in Eq. 2.9, with θ the polar angle of incidence, φ the azimuthal angle defined as the angle between the parallel wavevector k_{\parallel} and the x -axis, P_x and P_y the periods of the array along the x - and y -axes respectively, and i, j two integers corresponding to the scattering orders of the array [53], [117]–[119]. This equation directly highlights the dependency of the surface plasmon polaritons on the angle of incidence and on the azimuth.

$$k_{spp} = \sqrt{\left(k_0 \sin \theta \cos \varphi + i \frac{2\pi}{P_x}\right)^2 + \left(k_0 \sin \theta \sin \varphi + j \frac{2\pi}{P_y}\right)^2} \quad (\text{Eq. 2.9})$$

In such structures, the surface plasmons generated at the top metallic surface resonate at a specific wavelength directly related to the dimensions of the array, and can couple back to radiative modes on the opposite surface. The EOT discovery has since raised a growing interest in the study of hole arrays in a metallic layer for applications such as color sorters or color filters. Many works have investigated theoretically and experimentally the properties of gratings at first [100], [120]–[122], then those of 2D arrays with different hole shapes or types of array in order to understand the mechanisms of the plasmon resonances in these structures. Around the apertures, the localized plasmon resonances are also strongly dependent on the hole shape and dimensions, and the optical behavior of single apertures has also been studied [123]–[126]. In particular, the most studied shapes are basic geometries such as squares [127]–[129], rectangles [129]–[133], circles [101], [131]–[133], triangles [101] or crosses [134]–[137], each arranged either with a square or a triangular arrangement [101], [118]. Although hole arrays are generally able to reach higher transmission efficiencies than MIM structures and to give spectral responses well-suited to transmissive filters compared to patch arrays, their angular and polarization sensitivities are seldom considered in literature. Only a couple of papers deal with these considerations, but the studied structures are not exactly hole arrays [138]–[140]. Yet, the future integration of plasmonic filters in typical industrial products such as image sensors or light sensors will only be

possible if they meet the technological specifications of each application. Namely, sensors must provide a signal stable with respect to the incidence and to the polarization state of the light. In the following sub-sections, we summarize our work on these different potential structures with a strong accentuation on the sensitivity to the light incidence, by taking into account, in the same time, the stability with respect to the angle of incidence θ , the azimuth φ and the polarization state.

2.3.3.2 Impact of the material properties

Most authors generally work with materials as gold or silver, but some of them also take into account the concern of CMOS-compatibility by using aluminum or copper for the metallic layer. The choice of the used metal is crucial to the plasmonic effect since the resonance wavelength is related to its dielectric permittivity, thus determining the energy range in which it can be used as an effective transmissive filter (Eq. 2.10). Actually, this equation does not provide the position of the transmission maxima, unlike what was originally supposed [42], [117]. This is due to the fact that it does not account for the whole transmission phenomenon, which is not solely due to the surface plasmon polaritons. Experiments have indeed evidenced a redshift of the resonant peak position compared with the predictions obtained with this equation [53], [141], [142]. Both theoretical and experimental work have shown that this equation is in fact more related to the location of the transmission minima of the Fano-like resonance, resulting from destructive interferences between the SPP and the incident or emerging light in the holes [109], [143], [144]. The respective role of the SPP and the LSP will be discussed more in *Chapter 3*.

$$\lambda_{SPP} = \frac{2\pi}{k_{SPP}} \cdot \sqrt{\frac{\epsilon_m \epsilon_d}{\epsilon_m + \epsilon_d}} \quad (\text{Eq. 2.10})$$

Our simulations show that among the potential CMOS-compatible metals, aluminum gives the best results in the visible range with the highest transmissions reached around blue wavelengths, whereas copper is better for the NIR range and is only able to provide distinct transmission peaks from 600 nm (Figure 2.15(a)). These results are in agreement with the different studies on the metals properties for plasmonic applications which relate their optical properties to the real and imaginary parts of their dielectric constants or to additional effects such as interband transitions and loss mechanisms [45], [46], [109], [145]. With respect to our targeted applications and their respective operating wavelengths located in the visible range, aluminum will then be our favored material for this whole study. Despite an interband transition located at 825 nm which implies a substantial increase of the absorption for wavelengths longer than 550 nm, aluminum is indeed the best metal fitting with our optical and fabrication specifications.

Similarly, the dielectric material around the aluminum layer and inside the holes is changed with a progressive refractive index increase to study the best materials configuration (Figure 2.15(b)). The tested dielectric are air ($n = 1$), SiO₂ ($n = 1.46$), Si₃N₄ ($n = 2$) and TiO₂ ($n = 2.5$). They all are considered lossless. It can immediately be noticed that at constant metal thickness and aperture dimensions, a lower index dielectric induces a higher transmission and a sharper resonance. Since we want to favor the transmission efficiency and the quality factor of the filters, we will mainly use SiO₂ as dielectric medium around the metal layer and inside the holes. Moreover, this material is widely used in microelectronics; its properties and its fabrication processes are thus well known and will be profitable in the realization of our filters. The use of air would require thinking about an integration of the filters in a free-standing configuration which is not the scope of this work, and will not be considered.

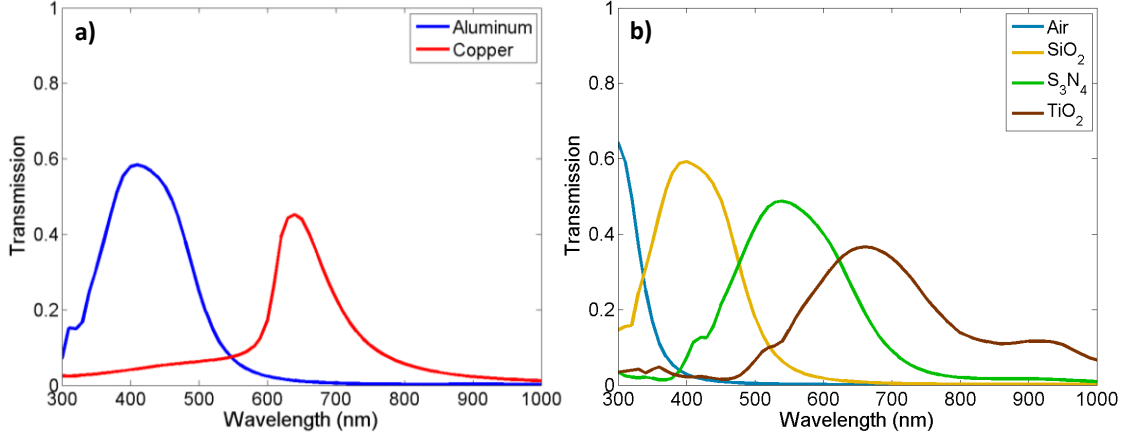


FIG. 2.15. (a) Transmission spectra for the same hole array filter obtained with aluminum (blue curve) and copper (red curve). (b) Transmission spectra for the same filter with aluminum for different refractive indices of the dielectric material around the metal and inside the holes. The filter consists of a square array of square holes with the following dimensions: $h_m = 175$ nm, $P = 200$ nm, $a = 130$ nm.

2.3.3.3 Square arrays of holes

The simpler structures studied in literature are square arrays. We simulated such structures with different hole shapes such as squares, circles and crosses, according to the schemes presented in Figure 2.16. The metal thickness is denoted h_m , the metallic layer being embedded in an infinite SiO_2 medium. The period is the same in the x and y directions and is denoted P . For square and circular holes, a corresponds to the size or the diameter of the holes respectively. For cruciform holes, a is the arm length of the crosses and b their arm width. The TE polarization is defined with the electric field \mathbf{E} along the y -axis and \mathbf{H} in the (xz) plane when $\varphi = 0$. Consequently, the TM polarization is defined with \mathbf{E} in the (xz) plane and \mathbf{H} along the y -axis for $\varphi = 0$. The response of the filters is the same under TM and TE polarizations at normal incidence, owing to the symmetry of square arrays.

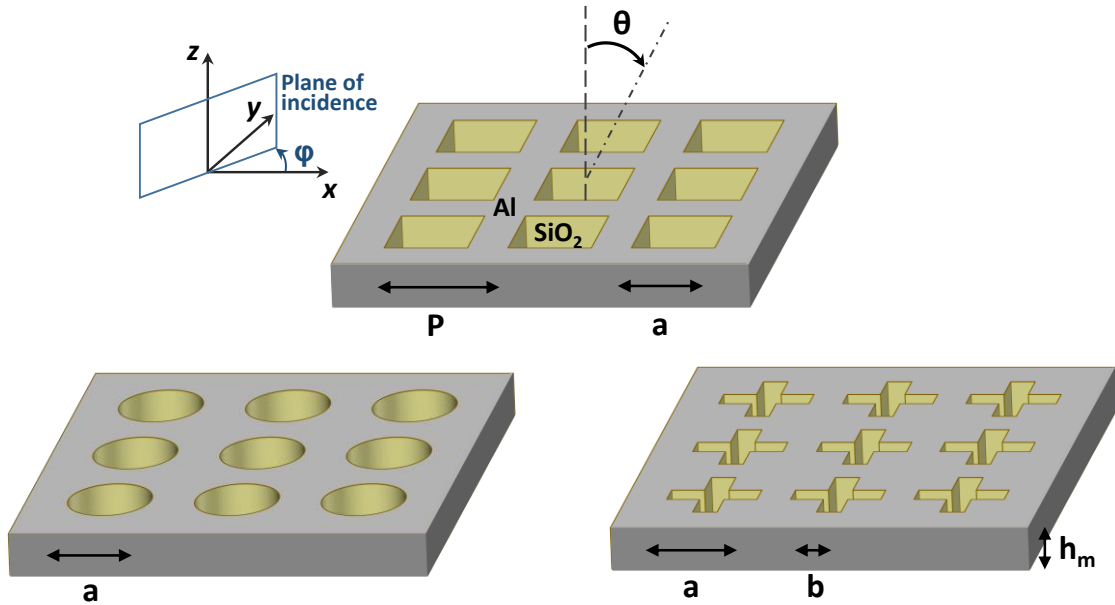


FIG. 2.16. Schemes of typical hole array filters with a square array (period P) of square holes (size a), circular holes (diameter a) and cruciform holes (arm length a and arm width b), with thickness h_m . The SiO_2 superstrate and substrate are considered infinite.

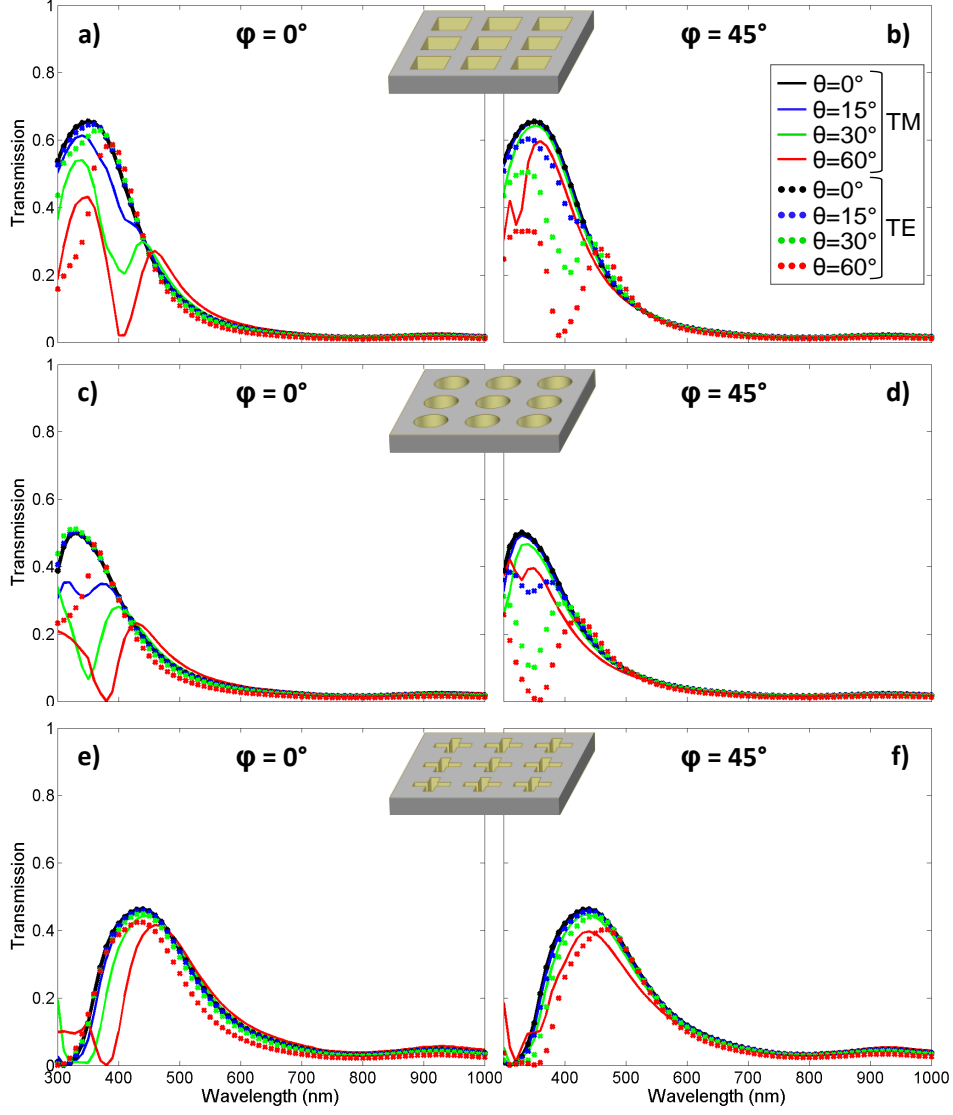


FIG. 2.17. Spectral responses of a filter with square holes under two different polarizations and with different incidence angles for (a) $\varphi = 0^\circ$ and (b) $\varphi = 45^\circ$. Same evolution for a filter with circular holes with (c) $\varphi = 0^\circ$ and (d) $\varphi = 45^\circ$. Same evolution for a filter with cruciform holes with (e) $\varphi = 0^\circ$ and (f) $\varphi = 45^\circ$. The filters' dimensions are: $h_m = 100$ nm, $P = 150$ nm, $a = 105$ nm (squares), $a = 120$ nm (circles), $a = 125$ nm and $b = 60$ nm (crosses).

We gather in Figure 2.17 our results regarding the polarization sensitivity and the angular stability with respect to the polar angle of incidence θ and to the azimuth φ for the three different hole shapes. The evolution of the spectral responses with increasing θ for the TM and the TE polarizations is given each time for $\varphi = 0^\circ$ and $\varphi = 45^\circ$, which correspond to the extreme azimuth values, given the symmetries of the arrays. Remember that θ is given in air as if there was a finite but very thick SiO_2 layer between the aluminum layer and the air. For each shape, one can notice that the behavior of the TE and the TM polarization at $\varphi = 0^\circ$ and $\varphi = 45^\circ$ is inverted compared with the metallic patch arrays. Here the stable polarization at $\varphi = 0^\circ$ is the TE one and not the TM one. For circular and square shapes (Figure 2.17(a)-17(d)), the spectral responses at $\varphi = 0^\circ$ under TE polarization are stable up to $\theta = 30^\circ$ and only experience slight redshift and transmission loss (about 5 %) for $\theta = 60^\circ$. Under the TM polarization, the transmission quickly decreases even for low angles of incidence. The above observations on the polarizations are inverted when $\varphi = 45^\circ$. The cruciform shapes however reveal a different behavior (Figure 2.17(e)-17(f)). In this case, no obvious difference between the TE and TM polarizations is

observed, and the spectral responses remain exactly similar to the normal incidence situation for the two azimuths and for a polar angle of incidence up to 30° . For a larger angle ($\theta = 60^\circ$), a low transmission loss (5 %) is noticed, together with a slight shift towards larger wavelength (40 nm) for the TM (TE) polarization at $\varphi = 0^\circ$ ($\varphi = 45^\circ$). Square arrays of crosses thus demonstrate a very high potential for filtering applications requiring a significant robustness to large incidence angles and to the polarization state, namely, both the ALS and the RGB sensors could benefit from this property. We note however in our simulations that the transmissions (50 % – 60 %) are still lower than those of color resists ($> 80\%$). Higher transmissions are possible with hole-array filters, but this signal gain generally implies at the same time a wider FWHM and a worse rejection.

2.3.3.4 Hexagonal arrays of holes

A common alternative in the study of plasmonic filters is the hexagonal (or triangular) array of holes [101], [118]. In this case, the arrangement is made so that each hole is equidistant from its six closest neighbors, which correspond to the angles of a regular hexagonal pattern (see Figure 2.18). Although this structure might limit the dependence of the filter to the azimuth, it also features a mismatch between the periodicities along the x - and the y -axes which induces a more noticeable difference in behavior with respect to the TM and TE polarizations, even at normal incidence (Figure 2.18(a)). In order to keep the symmetry of the filter for TE and TM polarizations at normal incidence, we propose to slightly distort the arrangement so that the structure has the same periodicity along the x and the y directions (Figure 2.18(b)). Basically, this new structure is equivalent to a square array with a 45° rotation of the hole patterns, and allows for the same behavior of the filter with respect to TE and TM polarizations at normal incidence. The materials and the polarizations are defined in the same conditions than with the square arrays. In the following, we thus focus on this particular arrangement. Despite the slight deviation from the regular hexagonal arrays found in literature, we will call this particular arrangement “hexagonal” in this thesis, whereas the regular one will be referred as “triangular”.

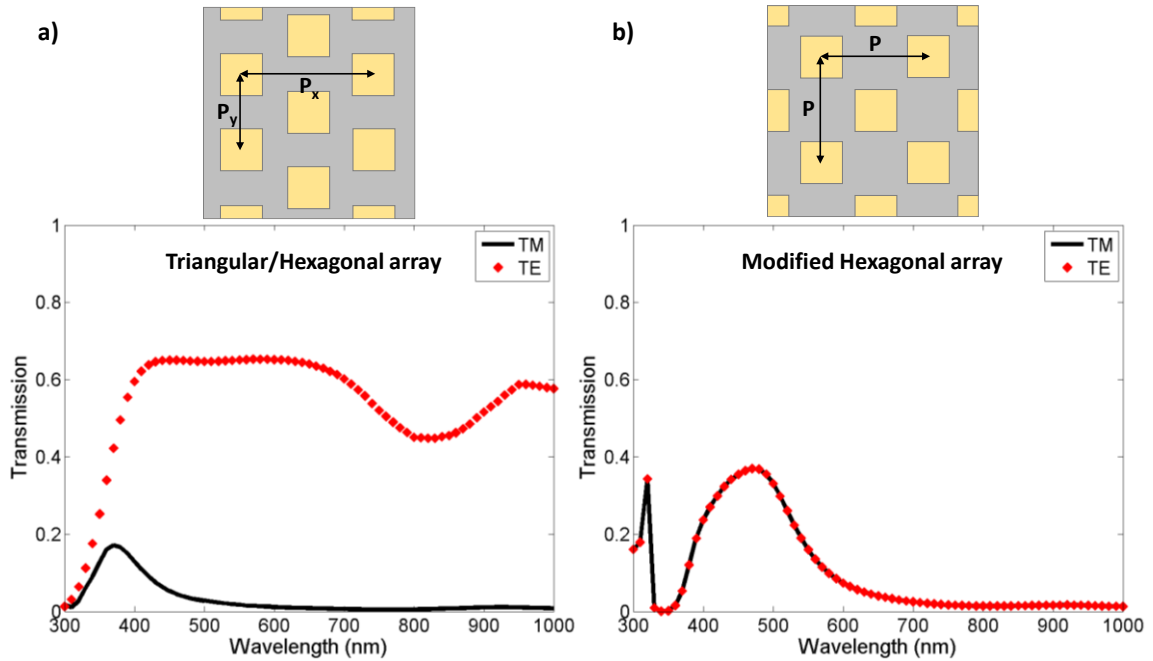


FIG. 2.18. (a) Top view of a triangular-array filter ($h_m = 100$ nm, $P_x = 300$ nm, $P_y = P_x/\sqrt{3}$, $a = 120$ nm) and corresponding spectral responses under two different polarizations at normal incidence. (b) Top view of the modified hexagonal-array filter ($h_m = 100$ nm, $P_x = P_y = 300$ nm, $a = 120$ nm) and corresponding spectral responses under two different polarizations at normal incidence. Scale of the arrays not respected.

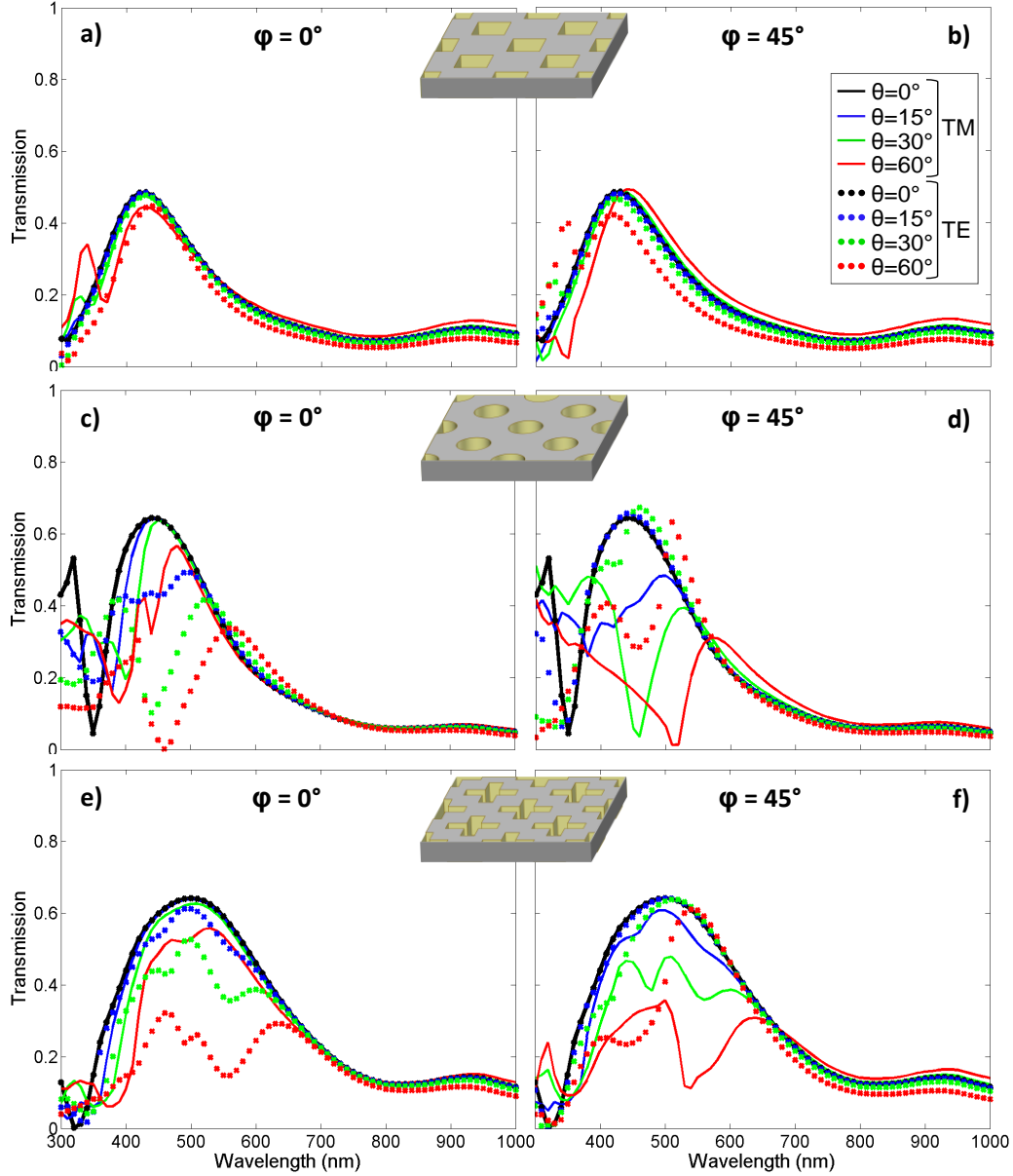


FIG. 2.19. Spectral responses of a filter made of a hexagonal array of square holes under two different polarizations and with different incidence angles for (a) $\varphi = 0^\circ$ and (b) $\varphi = 45^\circ$. Same evolution for a filter with circular holes with (c) $\varphi = 0^\circ$ and (d) $\varphi = 45^\circ$. Same evolution for a filter with cruciform holes with (e) $\varphi = 0^\circ$ and (f) $\varphi = 45^\circ$. The filters' dimensions are: $h_m = 100$ nm, $P = 300$ nm, $a = 180$ nm (circles), $a = 185$ nm and $b = 90$ nm (crosses) and $h_m = 50$ nm, $P = 200$ nm and $a = 90$ nm (squares).

As in the case of square arrays, we summarize here our results regarding the polarization dependency and the angular stability of hexagonal arrays according to the hole shapes such as squares, circles and crosses (Figure 2.19). At first, one can notice that the TE and TM polarizations still have this symmetric behavior between the $\varphi = 0^\circ$ and $\varphi = 45^\circ$ configurations. However, hexagonal arrays have a stable response at $\varphi = 0^\circ$ ($\varphi = 45^\circ$) for the TM (TE respectively) polarization, which is the opposite behavior from square arrays. This is attributable to the fact that in our modified hexagonal configuration, the holes arrangement is equivalent to a square array with the hole shapes rotated by an angle of 45° as explained before, which thus explains this behavior difference of the polarizations between our square and hexagonal arrays. Regarding the impact of the shapes, circular holes are still highly sensitive to polarization and to off-normal incidence conditions. In this case of hexagonal array, it appears that crosses lose the stability properties that we have seen in square arrays. Finally, squares designed in a

hexagonal array seem to feature an angular stability comparable to the one observed for square arrays of crosses. This structure could then also be of major interest for ambient light sensor applications. We however notice in our simulations more difficulty to find such stable designs over the whole visible range compared with the square arrays of holes, which are more easily tunable thanks to the arm width that provides further design possibilities.

2.3.3.5 RGB filters

An example of RGB set obtained with cross-shaped-hole arrays is simulated (Figure 2.20) and evaluated in Table 2.2. Note again that these filters cannot be considered as an optimized RGB set. When compared with the organic resists, the color error increases by 40 % and the noise again is doubled; that can be explained by the high level of color cross-talk that can be observed in Figure 2.20. As for MIM structures, the SNR_{10Y} (see 2.2.2 RGB image sensors) is very high compared to the resists, with a 293 % increase. Although they feature interesting angular properties, cross-shaped-hole arrays do not suggest any performance gain in the view of realizing RGB filters for CMOS sensors. However the recent tendency of light sensors is leaning towards RGB-ALS sensors that would allow the identification of the color temperature of the scene illumination (see 1.2.2 Market trends). Specifications for such an application are not yet well defined, but they noticeably differ from the requirements of image sensors. In the case of RGB-ALS sensors only, plasmonic filters could thus provide an interesting alternative to RGB color resists for this application since the three color filters could be patterned with a single lithography step.

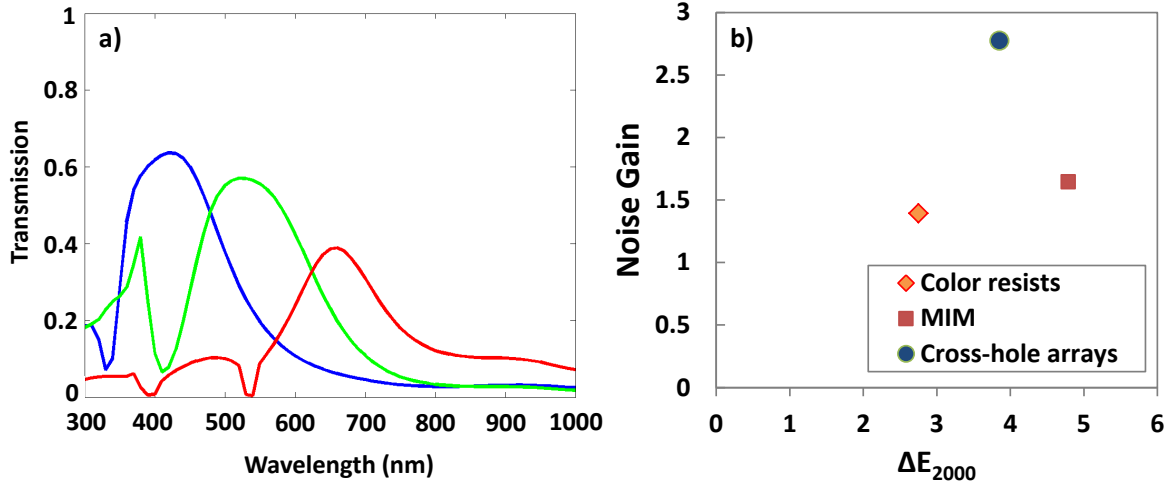


FIG. 2.20. (a) Example of a RGB filters set using cross-shaped-hole arrays with SiO_2 and aluminum. The filter's dimensions are: $h_m = 100$ nm, $P = 200$ nm, $a = 140$ nm and $b = 98$ nm for the blue filter; $h_m = 200$ nm, $P = 250$ nm and $a = 200$ nm and $b = 120$ nm for the green filter; $h_m = 70$ nm, $P = 350$ nm, $a = 175$ nm and $b = 158$ nm for the red filter. (b) Comparison of the RGB performances obtained with the set of RGB cross-hole arrays, with the set of RGB MIM arrays and with color resists.

	ΔE_{2000} RMS	ΔE_{2000} Max	Noise Gain	SNR_{10Y}
Color resists	2.75	6.25	1.39	89.6
MIM arrays	4.79	8.71	1.65	314.4
Cross-hole arrays	3.85	7.93	2.77	352.7

TABLE 2.2. Corresponding performances calculated with the RGB evaluation tool.

2.3.4 Conclusion on plasmonic structures

The three dominant plasmonic structures for optical filtering found in literature have been reviewed with an emphasis on the specifications that would be asked for their industrial integration in image or light sensors. The sensitivities to the polarization and to the incidence angles constitute the major concern we look after. For MIM structures, the transmission efficiencies are too low and the color errors too important to compete with current RGB filters. Furthermore, they do not show satisfying angular stability for their use in such sensors. Metallic patch arrays have demonstrated a very high sensitivity to light incidence that immediately disqualifies them for our applications.

Hole arrays feature the best compromise in terms of ease of fabrication and of optical performance. Plasmonic filters in general do not reach the transmission levels of organic resists, which prevents them from being serious candidate to replace the resists in high-quality CMOS image sensors. However, some structures such as the square arrays of crosses or the hexagonal arrays of square have a very high stability with respect to the incidence conditions, even for large angles of incidence. The crosses present the advantage of having more possibilities to tune their spectral response thanks to their shape that provides an additional geometrical parameter. These characteristics make these cruciform structures particularly interesting for the ALS application, which does not require as much transmission efficiency as RGB sensors, but needs a high angular stability. The following studies will thus focus on the integration of aluminum cross-hole-array in an ALS device and on the search for optimized performance.

2.4 Optimal integration solution for plasmonic ALS

2.4.1 Integration level of plasmonic filters

One of our objectives in this work is to find an integration solution that is not only compatible with the CMOS environment and with the proper functioning of the ALS device, but that is also easily transferrable in the standard process routes of sensors in general, be they color sensors or ALS in our case. In practice, it means that the implementation of the filters in the device structure has to minimize the number of changes brought in already existing front-end fabrication flows. In addition to facilitating the technological transfer of plasmonic filters to industrial clean rooms, this would also greatly reduce the development costs of the technology.

Before performing an in-depth study of the integration solutions of plasmonic filters, we have to identify at which level of the fabrication process of image sensors their implementation is the most convenient. We present below in Figure 2.21 a rough description of the main bricks constituting the fabrication route of an image sensor in the case of front-side illumination. Above the front-end level where the transistors and the photodiodes are located, three metallic levels of interconnections based on a standard image sensor technology of STMicroelectronics are fabricated with copper according to a dual-damascene method, that consists of an additive patterning of the metal (the trenches are filled with the metal, instead of etching the pattern in a full metallic layer) [146]–[149]. Copper is restrained between diffusion barriers (generally Ta/TaN barriers) and the interconnections lines are embedded in a silicon dioxide called IMD (intra-metallic dielectric). This brick requires a consequent number of deposition, etching, Chemical-Mechanical Planarization (CMP) and lithography steps, and the integration of plasmonic filters in such a flow would not be direct. The filters could however be fabricated before the realization of the aluminum bond pads. Once the pads have been added, the chips are recovered with the passivation layers (Phosphorous Silicon Glass (PSG) and Si_3N_4) and a SiON top coat to preserve the sensor from the external moisture. These are the last steps when the plasmonics filters can be integrated without heavy change in the process flow, right before the pad opening.

The easiest potential integrations of plasmonic filters seem thus to be either before the first etching step of the realization of the bond pads, or between the end of the pads fabrication and their opening, which corresponds to the brick where the passivation layers and the top coat are deposited.

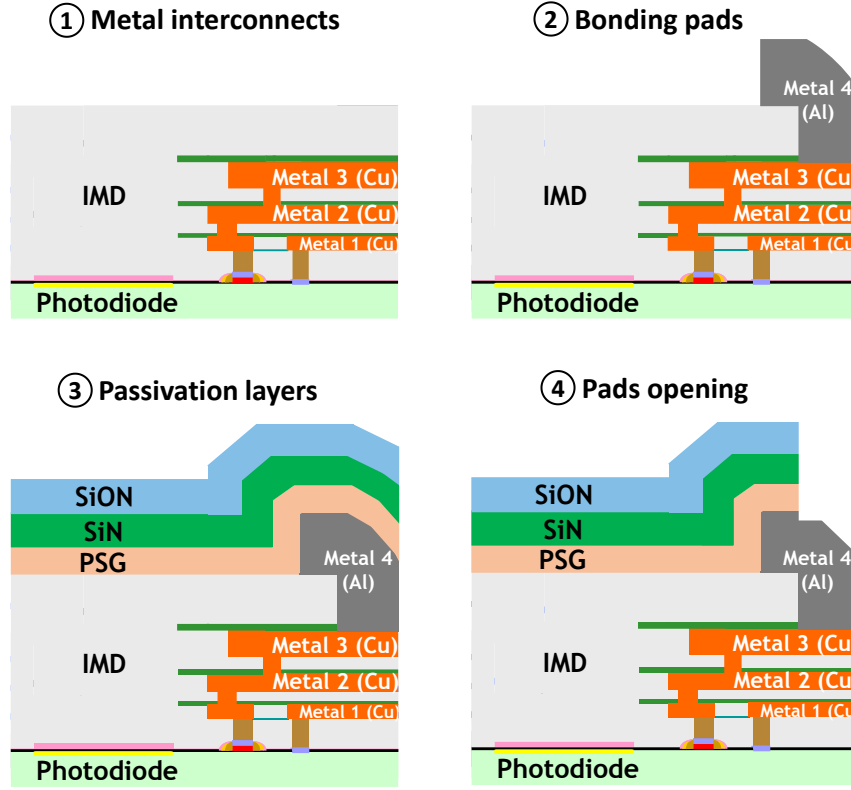


FIG. 2.21. Rough description of the main process bricks involved in the standard fabrication of the front-end part of an image sensors. The most direct integrations of plasmonic filters are directly after brick 1 or directly during brick 3.

2. 4.2 Location of the metallic layer

We have seen in the previous sub-section that plasmonic filters could easily be integrated in a CIS process flow right before the realization of the bond pads or during the deposition of the passivation layers. From this conclusion, we have thus a few different options regarding the deposition of the metallic layer. If we decide to realize the filters right before the bond pads, the metallic layer will be embedded in SiO_2 (the IMD is a silicon dioxide). On the other hand, if we decide to fabricate the filters at the same level than the passivation layers, we have thereby the choice to use the PSG layer, the Si_3N_4 layer or the SiON top coat as the dielectric medium around the metallic layer. The refractive indices of PSG is very close to those of standard SiO_2 [150] and we will consider them to be the same material. Among the four potential levels of integration, we are thus left with three dielectric materials: the metallic layer can be embedded in SiO_2 ($n = 1.46$), SiON or Si_3N_4 ($n = 2$). The top-coat is a low-index SiON whose refractive index was measured internally at STMicroelectronics ($n = 1.48$ at $\lambda = 550$ nm).

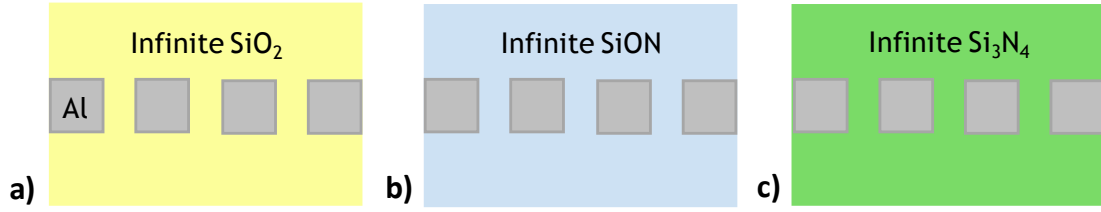


FIG. 2.22. Stacks considered for the evaluation of the impact of the dielectric refractive indices on the ALS performances. The plasmonic filters are simulated in an infinite dielectric medium such as SiO_2 , SiON or Si_3N_4 , which also fills the holes. The structure used is a cross-shape-hole array in aluminum.

Although we have shown in the previous part that a low dielectric index was preferable around the metal to maximize the transmission efficiency, we don't know the impact of the refractive index on the ALS performance. We decide to evaluate its impact by simulating an aluminum cross-shaped-hole array embedded in an infinite dielectric medium corresponding to each material we are considering: SiO_2 , SiON and Si_3N_4 (Figure 2.22). The corresponding spectral response are then inputted in the ALS evaluation tool which returns the values of ALS dark and ALS error related to each situation (Figure 2.23). The first data that were initially asked by the customers were the ALS dark and the mean ALS error. At this stage, the integration was thus thought relatively to the mean ALS error (Figure 2.23(a)), but we add here the evaluation for the maximum ALS error (Figure 2.23(b)). While the maximum values are logically higher than the mean ones, we can see that the conclusions are unchanged considering mean or maximum ALS errors: embedding the filters in an infinite SiON layer gives the lowest ALS error, which represents our major concern compared with the ALS dark. Given the very slight difference between the SiON layer and the SiO_2 layer (0.03 dB in maximum ALS error), one could consider both solutions for the integration of the filters. We choose to make use of this little performance improvement for our latter design optimization and then to use the SiON layer. Note however that a dielectric with a higher refractive index such as Si_3N_4 severely deteriorates the performance. We attribute this to the trend that we observed in 2. 3.3.2 *Impact of the materials properties*: a dielectric with a high RI widens the resonance, which make the filters catch undesired signal, especially in the NIR range.

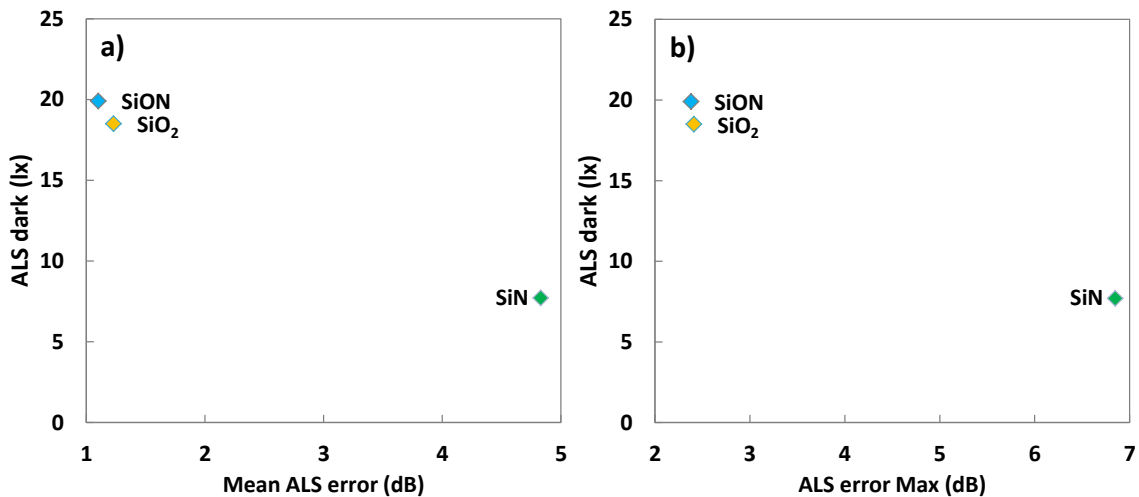


FIG. 2.23. (a) Evolution of ALS performance with the mean ALS error when the refractive indices of the dielectric surrounding are changed among those of SiO_2 , SiON and Si_3N_4 . (b) Same evaluation with the maximum ALS error. The plasmonic filter is a cross-shaped-hole array with the following dimensions: $h_m = 275$ nm, $P = 225$ nm, $a = 190$ nm and $b = 105$ nm.

2. 4.3 Distance of the filters to the passivation layers

We have shown that hole-array filters give slightly better ALS performances when the metallic layer is surrounded by SiON rather than SiO₂. We now know that it would be more efficient to place the plasmonic filters fabrication at the SiON top coat level in order to have at the same time a direct implementation in the CIS standard process route and an integration promoting the best possible performances. The calculations of the previous sub-section have been made in an infinite dielectric surrounding and do not take into account the whole materials stack the light has to travel through before it reaches the photodiode. Although the PSG, the IMD and the PMD (Pre-Metal Dielectric) can be assimilated to the same material, the Si₃N₄ layer has a distinct refractive index from SiO₂ and SiON. This difference may create undesired optical phenomena such as a lessening of the device performance or Fabry-Perot-like interferences. In this sub-section, we aim to determine whether we can find an optimal distance between the metallic layer and the Si₃N₄, so that the impact of the latter one on the ALS performances is minimized.

Since we want to take into account the whole path of the light inside the sensor before it impinges the photodiode, we consider the stack described in Figure 2.24. From above the photodiode, then all along the metallic interconnections until the passivation layers, we have different successive kinds of SiO₂ such as the PMD, the IMD and the PSG. Given their close refractive indices [150], they are all considered as optically identical and to behave like the standard SiO₂ used in previous simulations. The thickness of this silicon dioxide is simulated as an infinite substrate in our RCWA code. Above it, we place the 500 nm thick Si₃N₄ corresponding to the second passivation layer (the first one being the PSG layer). There is then a first SiON layer between the Si₃N₄ and the metallic layer constituting our plasmonic filter. We call it the "intermediate" layer and we aim to determine its optimal thickness. The following layer is the aluminum layer of the filter. The holes are filled with SiON. Finally, we place a last SiON layer above the aluminum layer which purpose is to protect our filter and the sensor from the external atmosphere. Its thickness is not critical in the sensor fabrication and we consider it as an infinite superstrate to avoid any unwanted optical effect due to the air – SiON interface that would be present in an experimental device.

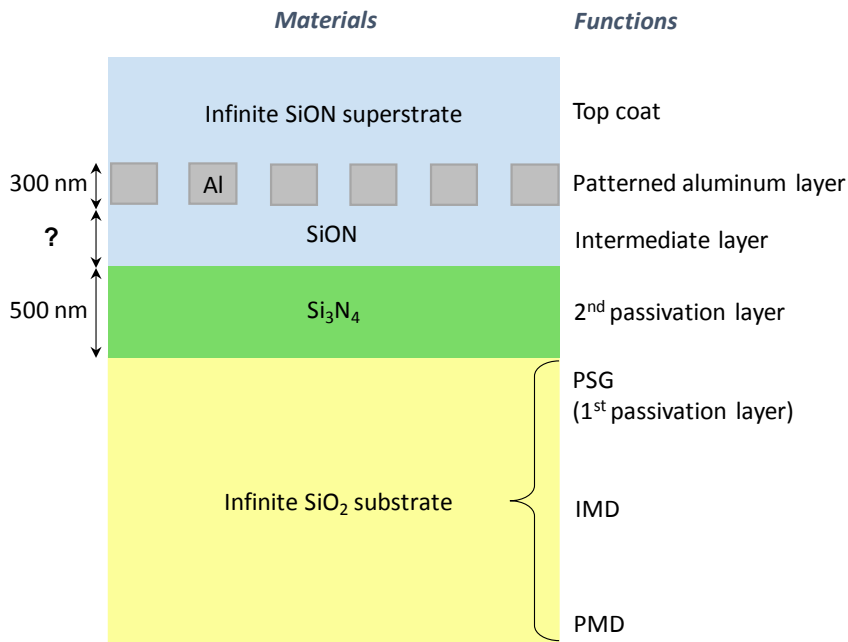


FIG. 2. 24. Stack considered for the simulation of the plasmonic filters where all the dielectric materials above the photodiode are taken into account in the case of an ALS sensor. The ALS performances are evaluated for different thicknesses of the intermediate SiON layer. The scale is not respected.

The results given in Figure 2.25 represent the evolution of the ALS performance of such a stack for different thicknesses of the intermediate SiON layer. Similarly to Figure 2.23, the integration was first thought according to the mean ALS error due to customer request. We also provide the evaluation with the maximum ALS error for comparison in Figure 2.25(b). In this situation, the results are slightly different but the trend is similar. Indeed, we see that although the types of ALS criteria do not substantially impact the device's performances, there exists an optimal value of intermediate layer thickness for which the ALS error, our primary criterion, is minimized. With the mean values, this optimum is reached at 325 nm, whereas it is reached at 350 nm with the maximum values. This difference is not aberrant given the thickness dispersion induced by the deposition tools during the fabrication, with a measured standard deviation of about 2 % at 3 σ . Compared with the theoretical case where the filter is embedded in an infinite SiON medium, we notice a 0.07 dB decrease in mean ALS error for only a 0.6 lx loss in ALS dark at 325 nm. We can thus deduce from these calculations that the optimal integration of plasmonic filters in an ALS device without modifying the front-end process consists in using the structure given in Figure 2.25 with a thickness of 325 nm for the intermediate SiON layer. This integration in which the plasmonic filters are embedded in the SiON top coat is directly transferable to a standard industrial fabrication of image sensors while ensuring the best reachable performance at lowest manufacturing cost.

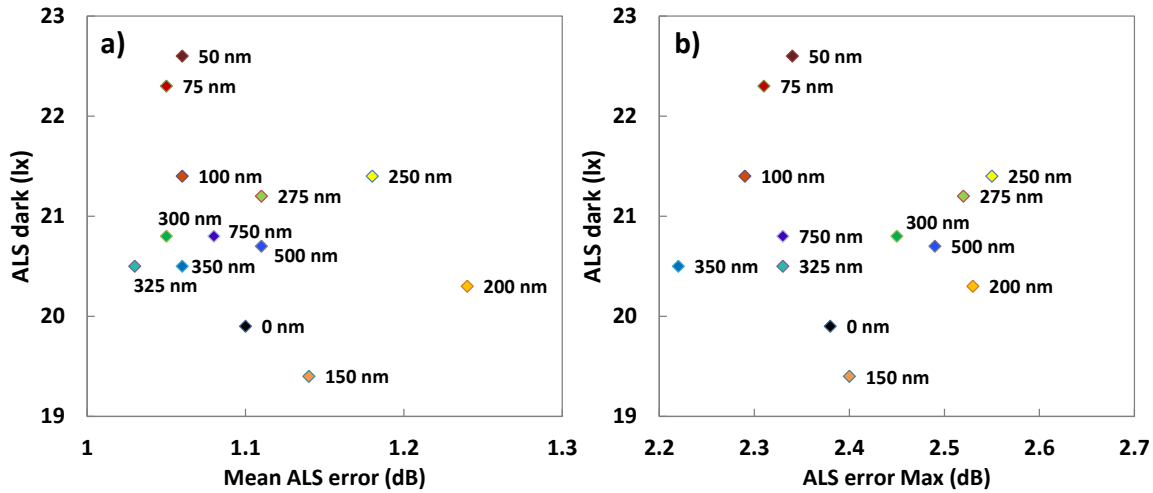


FIG. 2.25. (a) Evolution of the ALS performance with the mean ALS error for the considered stack when the thickness of the intermediate SiON layer is changed. (b) Same evolution with the maximum ALS error. The plasmonic filter is a cross-shaped-hole array with the following dimensions: $h_m = 275$ nm, $P = 225$ nm, $a = 190$ nm and $b = 105$ nm.

2.5 Conclusion on Chapter 2

Throughout this chapter, we have described the simulation and evaluation tools we use to answer the technological challenges intrinsic to plasmonics and we have defined the specifications that will allow for the comprehensive evaluation and optimization of filters. The RCWA is particularly suited to our situation since we will only consider periodical structures and since the calculations are fast enough to allow for the study of many structures and parameters. Regarding the applications, the ALS filters have to meet two performance criteria. The first and most important one is the maximum ALS error, which is directly related to the quality of the filtered signal and thus to the quality factor and to the rejection of the filter. It must not exceed 2.2 dB. On the other hand, the ALS dark is more related to the performance of the sensor in low-light conditions, which is linked to the transmission of the filter. Its upper limit is fixed at 100 lx.

We ran the simulations of the major structure types of plasmonic filters with strong emphasis on the sensitivity to polarization and on the angular stability in the same time, including the angle of incidence and the azimuth. These properties are fundamental to seriously consider a potential integration of plasmonic filters in industrial products as a replacement of organic resists combined with IR filters. In addition to the process difficulties of their fabrication, MIM structures have not shown any advantage in terms of transmission efficiency or of angular stability. Metal patch arrays, while easy to fabricate, feature a drastic sensitivity to the incidence of the light which is crippling for their use in the applications that are considered in this thesis. The best combination of the ease of fabrication and of the optical performance is obtained with hole-array filters. Although none of these three plasmonic structures can achieve the same transmission performance as organic resists, hole arrays distinguish themselves with the possibility to obtain a very high angular stability. Crosses give the best results when it comes to the robustness to the polarization and to the light incidence, besides providing more tuning possibility due to their additional geometrical parameter: the arm width. The low transmissions generally obtained with plasmonic filters (or higher transmissions with very poor quality factors) complicates their integration in high-end CMOS image sensors, but these angular properties however make hole arrays, and especially cross-hole-array filters, a very promising solution to perform ALS filters. The rest of the study will thus be focused on the optimization of the performance and on the fabrication concerns of cross-hole-array plasmonic filters. We will especially present in *Chapter 3* how their angular behavior can be improved. In the light of this work, we patented a solution to limit the sensitivity of plasmonic filters in general to azimuth on image sensor applications [151].

Finally, the integration of this kind of plasmonic filters has been studied with the aim to obtain the most direct integration in a standard imagers flow. The configuration that we defined is thus to fabricate the filters above the Si_3N_4 and SiO_2 passivation layers located above the metallic interconnections, just before the pads opening. The solution that gives optimal ALS performance consists in the embedment of the aluminum nanostructured sheet inside the SiON layer, which is used as the surrounding dielectric material for the plasmonic filter. To limit the optical impact of the underlying Si_3N_4 layer, the intermediate SiON layer in-between the nitride and the aluminum must have a thickness of 325 nm. This configuration thus defines the complete optical stack that has to be considered in the simulations to evaluate plasmonic filters in an actual ALS sensor.

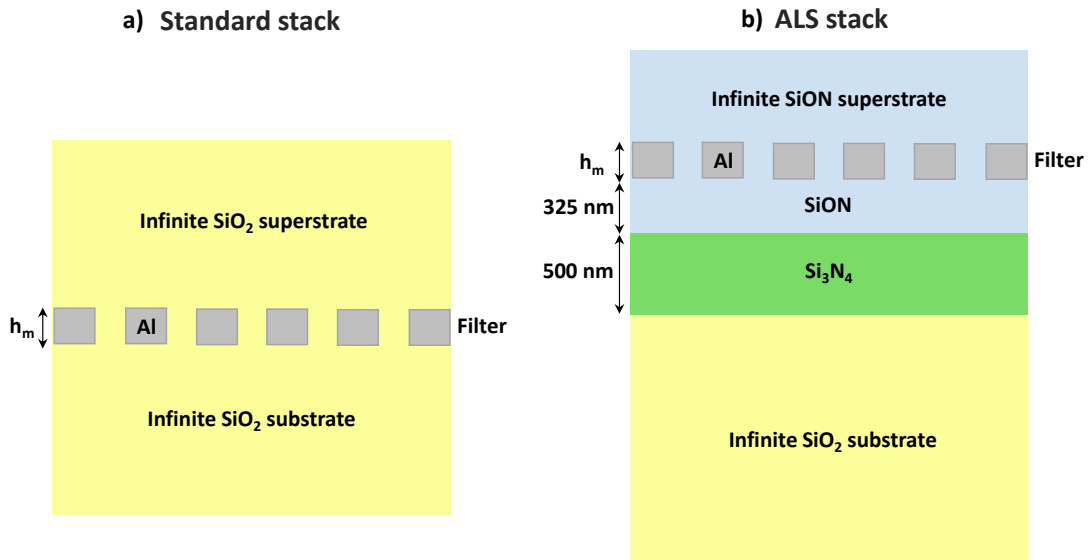


FIG. 2.26. (a) Description of the “standard stack”, where the filter is embedded in an infinite SiO_2 medium and where the holes are also filled with SiO_2 . (b) Description of the ALS stack, including all the dielectric layers (passivation, Back-End-of-Line (BEOL)) and the filter located above the photosensitive area of an ALS sensor.

As a consequence of the previous studies, we define in Figure 2.26(a) and in Figure 2.26(b) the two reference stacks that will be used in the following chapters. The “standard stack” corresponds to the nanostructured aluminum layer embedded in an infinite SiO_2 medium. It will be used for theoretical studies of the plasmon resonances in our structures. On the other hand, the “ALS stack” refers to the complete stack including every material located above the photodiode in an ALS sensors, which includes the SiON-embedded aluminum filter, the passivation layer and the BEOL dielectric. It will be used for the evaluation and the optimization of the plasmonic ALS device.

Chapter 3

Evaluation of plasmonic filters for Ambient Light Sensors

This chapter is split into two main parts. In the first section, the resonances of cross-shaped-hole arrays are comprehensively investigated in order to connect the geometrical characteristics of the structures to their optical properties in general. The results are used to determine the proper design rules required to obtain angularly stable and polarization insensitive filters. In the second part, the simulation tools described in *Chapter 2* are used to evaluate and optimize the performance of the selected plasmonic structures relatively to the Ambient Light Sensors (ALS) criteria. The conditions of angular stability defined in the former part are taken into account in the evaluation. At the end of this chapter, we will be able to propose plasmonic designs fitting with every optical requirement of ALS.

3. A – Resonance and angular properties of cross-shaped-hole arrays

It has been seen in *Chapter 2* that square arrays of cruciform holes have a better robustness to incidence angles (polar angle θ and azimuthal angle φ) and polarization states than more basic hole shapes like square and circle (2. 3.3 *Hole arrays in a metallic layer*). Yet, this property appears to be dependent on the design's dimensions [152]. Simulations show that some cross-shaped-hole arrays may not guarantee the angular and polarization stability we are looking for, as shown in Figure 3.1(b). In part A, we thus investigate in detail how the geometry of cross-shaped-hole arrays influences the plasmon resonances and subsequently, how the angular and polarization properties are affected. All the simulations included in part A are performed with infinite arrays and 8x8-harmonic RCWA method using the generic stack (infinite SiO₂ substrate and superstrate), all defined in *Chapter 2*. This study will provide us accurate geometrical criteria to design stable filters that will be used in the evaluation of plasmonic ALS. This work resulted in a publication [153] and a poster in conference [154].

In this part, the simulated structure corresponds to the standard stack defined in 2. 5. *Conclusion on Chapter 2* with an aluminum layer surrounded by infinite SiO₂ superstrate and substrate. A filter consisting of a square array of cruciform holes (Figure 3.1(a)) with period $P = 150$ nm, arm length $a = 120$ nm and arm width $b = 72$ nm, is used as a reference filter around which a given parameter is changed so that its influence on the angular stability can be clearly identified. The main parameters investigated throughout the following reading are the metal thickness h_m , the crosses size relatively to the period with the ratio a/P , the shape factor b/a , and eventually the distance d between crosses.

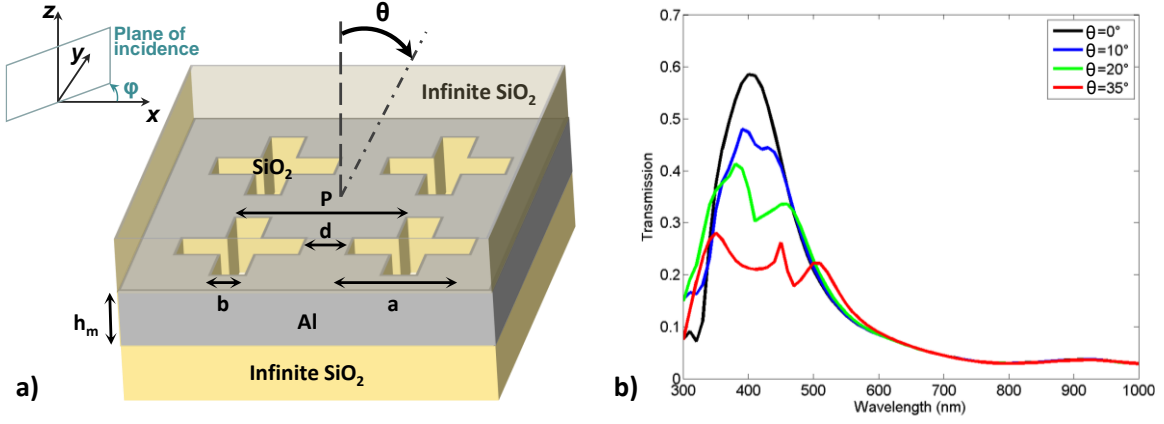


FIG. 3.1. (a) Scheme of the studied cross-hole array structure. (b) Example of a cross-shaped-hole array presenting a substantial sensitivity to the polar angle of incidence θ with constant ϕ . Filter dimensions: $h_m = 75$ nm, $P = 190$ nm, $a = 125$ nm and $b = 85$ nm.

3. A.1 Review on the impact of geometrical parameters

3. A.1.1 Metal thickness h_m

Since the discovery of the Extraordinary Optical Transmission phenomenon (see 2. 3.3.1 *EOT in subwavelength hole arrays*), many computational and experimental studies have been led to observe the effect of the geometrical parameters involved in the design of metallic nanostructures. The objectives of these works were to explore the properties and potential applications of such devices, but also to understand the underlying physics of plasmon resonances in the EOT, which describes the high level of transmission of light through holes smaller than the wavelength in an opaque film. In particular, the sensitivity of EOT to the thickness of the metallic layer was addressed in the early years of its discovery with the description of the resonance mechanism of plasmons inside the holes.

In 2001, Martín-Moreno *et al.* proposed an analytical model to study the transmission of light with 2D hole arrays in thick metallic films [127]. It shows that the transmission of photons in thick films lies on a two-regimes mechanism due to the competition between two quantities: the lifetime t_{rad} of a Surface Plasmon (SP) on an isolated surface to couple into a radiative mode, and the time t_{res} required for two SPs of opposite surface to couple. For thin metallic layers, $t_{res} \ll t_{rad}$ and photons can travel back and forth several times in the holes creating constructive interferences and thus leading to a highly enhanced transmission and a redshift of the resonance. Conversely for thick films, photons trapped in a SP on the incoming surface simply tunnel through the holes to the SP of the opposite surface and radiate (*sequential tunneling*), implying smaller transmission levels. Experimental results have confirmed the relevance of this model by revealing the two regimes and their characteristics [155]: thick layers exhibit an exponential decrease of the transmittance with h_m , whereas the peak broadens and levels-off going to small thicknesses.

In our case, we propose to deepen the analysis of the thickness impact by taking into account the sensitivity of cross-hole arrays to incidence angles and polarization in the analysis.

The filter of reference, now described with $P = 150$ nm, $a/P = 0.8$, $b/a = 0.6$ and $d = 30$ nm according to the parameters used in this study is simulated for various thicknesses ranging from 25 nm to 300 nm. In this way, the transition from the case of thin films to the case of thick films is covered. The spectra corresponding to a thin Al layer (50 nm) and a thick one (200 nm) are given in Figure 3.2 with different polar and azimuthal angles of incidence (θ and φ respectively) and for two polarization states TM and TE. The definitions of the angles of incidence and of the polarizations are the same as in 2.3 *Plasmonic structures for spectral filtering*. The angular stability shows no obvious reduction between the two thicknesses, although a faster decrease of the transmission is noticed in the 200 nm case when θ is increased. It can be seen however that there is a symmetric behavior of the TM and TE polarizations at $\varphi = 0^\circ$ and $\varphi = 45^\circ$ respectively. At $\varphi = 0^\circ$, the filter under TM polarization is shown to be sensitive to the polar angle of incidence θ , whereas it remains very stable under TE polarization. This result corroborates the work of Lin and Roberts on crosses [152]. In our case, we also show that for an azimuth $\varphi = 45^\circ$, the stabilities of the TM and TE polarizations are inverted compared to the case $\varphi = 0^\circ$.

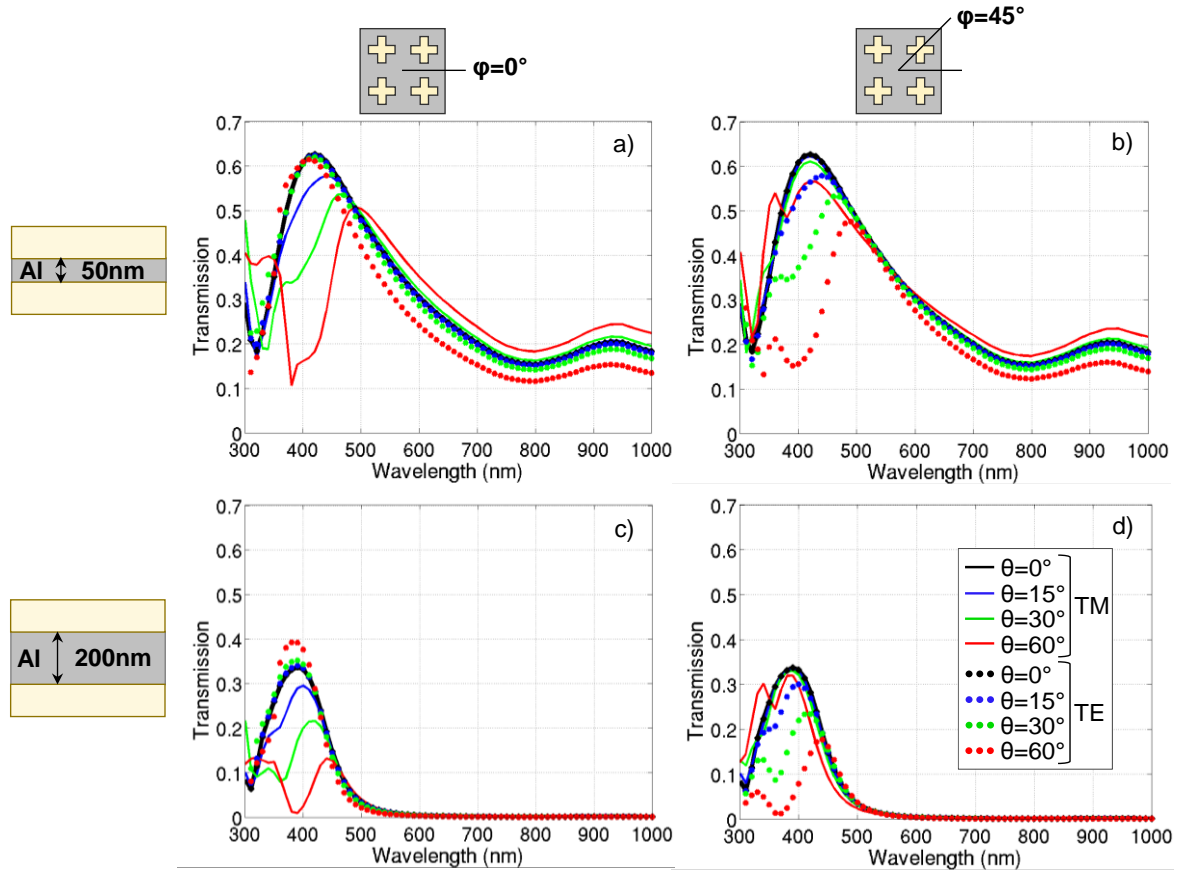


FIG. 3.2. Spectral responses of filters ($P = 150$ nm, $a/P = 0.8$, $b/a = 0.6$, and thus $d = 30$ nm) under two different polarizations and with different incidence angles for (a) $\varphi = 0^\circ$ and (b) $\varphi = 45^\circ$, with $h_m = 50$ nm. Spectral responses for (c) $\varphi = 0^\circ$ and (d) $\varphi = 45^\circ$ with $h_m = 200$ nm.

In order to go deeper into the analysis, the shifts of the resonance wavelength as a function of the polar angle θ and of the thickness are given in Figure 3.3, for two azimuth values $\varphi = 0^\circ$ and $\varphi = 45^\circ$. As we saw in Chapter 2, a shift of the resonance can lead to significant ALS error increases and has thus to be avoided. In this figure, the spectral responses are calculated from the average of the two polarizations states TE and TM. It can clearly be observed here that the resonance at normal incidence is redshifted going from thick films to thinner films around 25 nm or 50 nm. This is explained by the coupling of the SPs of each opposite surface that is allowed only for thicknesses inferior to three times the skin depth [155], the latter corresponding to 12 nm for aluminum in the visible range. Furthermore, the charts

demonstrate that for thin metallic films, the resonance is substantially shifted towards longer wavelengths when the polar angle θ is increased. This redshift is explained in literature by the fact that the LSP resonance gets closer to the $(-1,0)$ SPP mode when increasing the polar angle [152]. For thicknesses superior to 200 nm however, the resonance remains stable even for high values of θ .

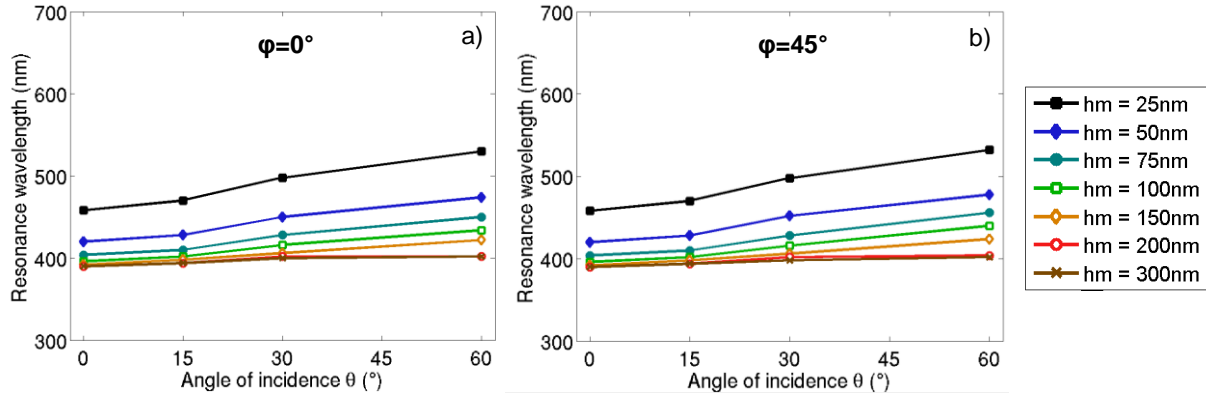


FIG. 3.3. Resonance peak position as a function of the incident angle for increasing metal thicknesses at (a) $\varphi = 0^\circ$ and (b) $\varphi = 45^\circ$ calculated for the average response between TE and TM polarizations responses. ($P = 150$ nm, $a/P = 0.8$, $b/a = 0.6$, and thus $d = 30$ nm).

We have seen that although the metal thickness has not a significant impact on the stability of cross-hole plasmonic filters, it is preferable to have a thick enough metallic layer (typically, superior to 150 nm) to avoid any coupling between the SP of the opposite surfaces and to reduce the sensitivity to the polar incident angle. Given this result, it is worth noting however the existence of a trade-off between the stability, the transmission level and the rejection quality of the filter. If a high metal thickness improves the stability of the filter and its rejection, it also implies a limited transmission, and the opposite is true for thin metallic films. The metal thickness has thus to be carefully chosen depending on the targeted applications. For the remaining part of this section A, the metal thickness of the reference filter is set to 75 nm in order to avoid any coupling effect and also to have acceptable transmission and rejection when studying the other parameters.

3. A.1.2 Effect of the a/P ratio

In this sub-section, we now focus on the influence of the size of the crosses relatively to the period P , described with the ratio a/P . This ratio is scanned by varying only the arm length a and by keeping the other parameters constant (the period $P = 150$ nm, the metal thickness $h_m = 75$ nm and the shape factor $b/a = 0.6$ are those of the reference filter). In Figure 3.4 are presented the spectral responses of a small cross ($a/P = 0.53$) and a wider one ($a/P = 0.8$) with different polar angles of incidence, for $\varphi = 0^\circ$ and $\varphi = 45^\circ$ and under the two polarization states TE and TM. No obvious change is observed in the evolution of the angular stability for the two cross sizes, whatever the azimuth. The only effect that can be noticed is that the a/P ratio can be tuned to monitor the transmission efficiency and the quality factor of the resonator, related to the Full-Width at Half Maximum (FWHM): a filter with small crosses (low a/P) will have a high selectivity but a poor transmission because of the decrease of the aperture area: 28 % for $a/P = 0.53$ and 64 % for $a/P = 0.8$.

The resonance shift is also presented in Figure 3.5 as a function of the polar angle of incidence for various a/P ratios. At normal incidence, it can be seen, with the average polarization, that the resonance is significantly redshifted when a/P is increased, since it also depends on the arm length of the crosses [135]. Out of normal incidence however, the evolution of the stability when comparing filters with low and high- a/P ratios is very weak.

There is thus no restriction on the choice of a/P to get stable filters, but a compromise is still required between the rejection of the filters and their transmission level. In the following sub-sections, a ratio $a/P = 0.8$ is kept to favor a sufficient transmission efficiency of the filters between 40 % and 60 %. The quality of the rejection is not our main concern for the study of the angular behavior of crosses.

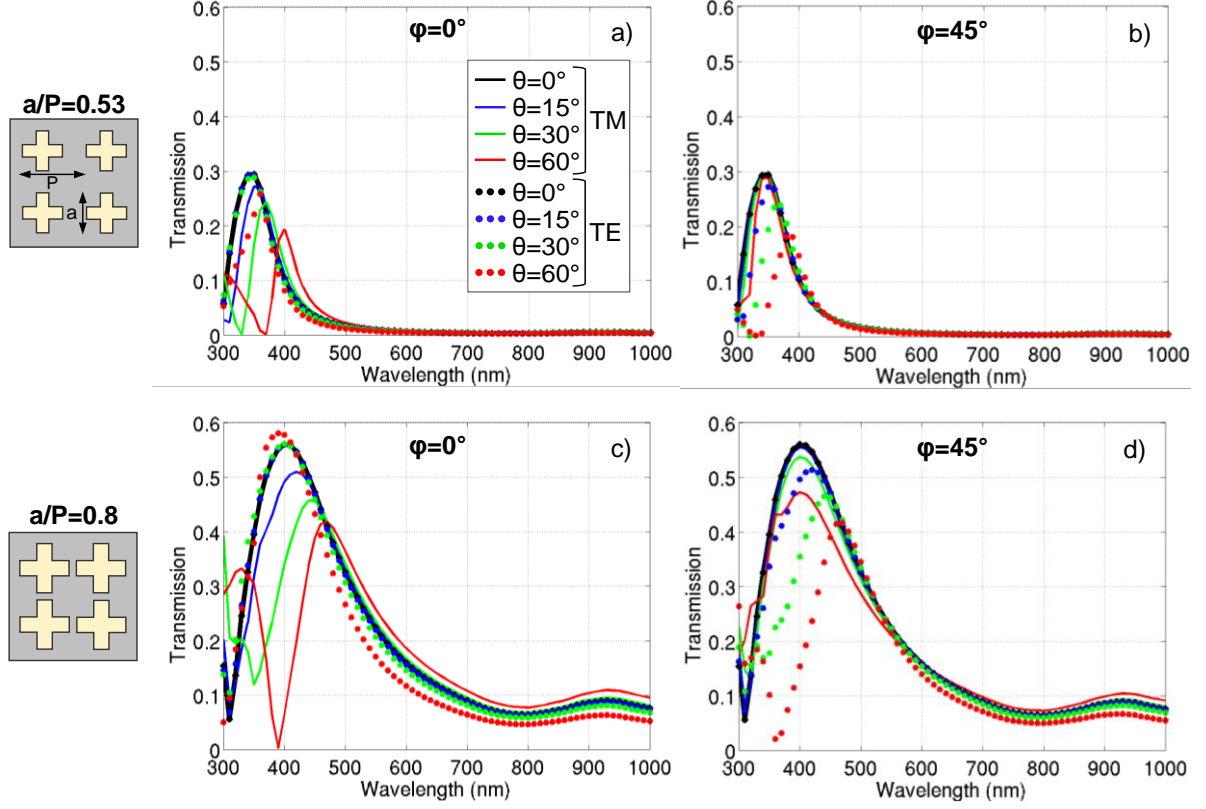


FIG. 3.4. Spectral responses of filters ($h_m = 75$ nm, $P = 150$ nm, $b/a = 0.6$) under two different polarizations and with different incidence angles for (a) $\varphi = 0^\circ$ and (b) for $\varphi = 45^\circ$ with $a/P = 0.53$. Spectral responses for (c) $\varphi = 0^\circ$ and (d) $\varphi = 45^\circ$ with $a/P = 0.8$.

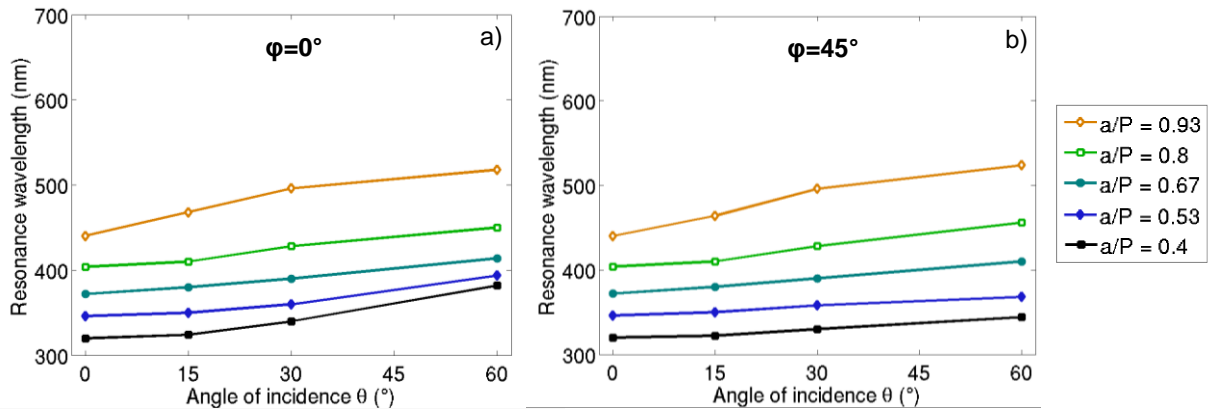


FIG. 3.5. Resonance peak position as a function of the incident polar angle for increasing a/P ratios at (a) $\varphi = 0^\circ$ and (b) $\varphi = 45^\circ$ calculated for average polarization.

3. A.1.3 Shape factor b/a

One interesting point about crosses compared to squares and circles is that they feature a second parameter in addition to the cross size: the cross width b . This additional dimension allows for the design of distinct cross shapes even for a given size, leading to different optical properties. It has been seen for example in our simulations and also in literature that decreasing the width of the crosses induces a substantial redshift of the resonance and a lowering of the maximum transmittance [135]. This can be directly related to the results obtained with rectangular holes, where a much higher field enhancement and an increase of the normalized transmission are observed when increasing their aspect ratio [125], [132], [133]. In order to identify the potential impact of the crosses width on their angular and polarization properties, we study the effect at different angles of incidence of the geometrical parameter b/a , previously defined as the shape factor (SF), to depict all the possible shapes of the crosses: from the theoretical case where the arms of the crosses are infinitely thin ($b/a = 0$) to the particular case where the crosses become squares ($b/a = 1$).

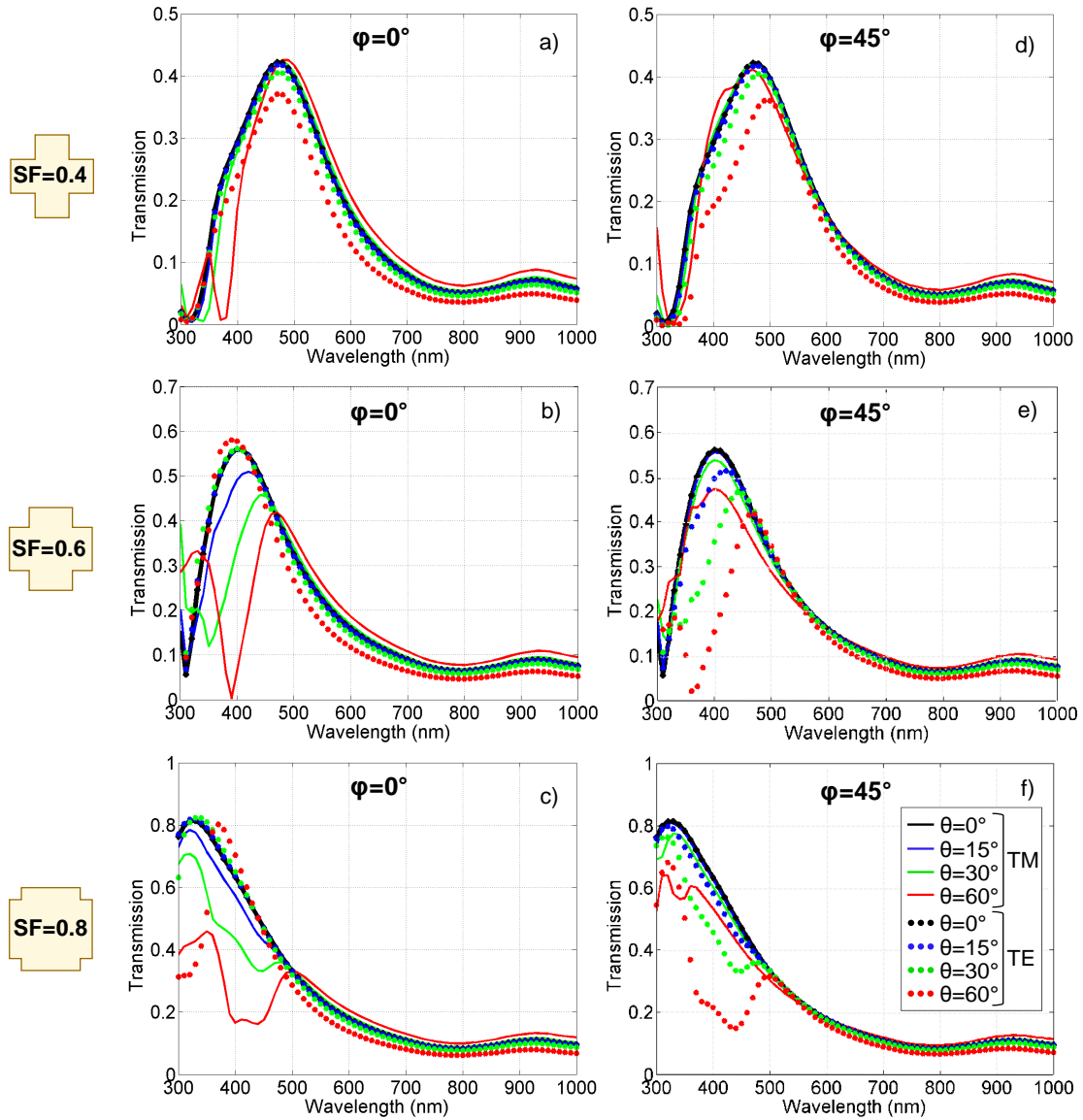


FIG. 3.6. Spectral responses of filters ($P = 150$ nm, $h_m = 75$ nm, $a/P = 0.8$ and thus $d = 30$ nm) under two different polarizations and with different polar incident angles for (a) $b/a = 0.4$ and $\phi = 0^\circ$. (b) $b/a = 0.6$ and $\phi = 0^\circ$. (c) $b/a = 0.8$ and $\phi = 0^\circ$. (d) $b/a = 0.4$ and $\phi = 45^\circ$. (e) $b/a = 0.6$ and $\phi = 45^\circ$. (f) $b/a = 0.8$ and $\phi = 45^\circ$.

In Figure 3.6, we show the spectral responses of three variations of the reference filter characterized by different shape factors $b/a = 0.4$, $b/a = 0.6$ and $b/a = 0.8$ for the azimuths $\varphi = 0^\circ$ (Figure 3.6(a)-(c) respectively) and $\varphi = 45^\circ$ (Figure 3.6(d)-(f) respectively). The two polarization states TE and TM are displayed in each chart. The symmetry previously observed in *sections 3. A.1.1* and *3. A.1.2* for the two polarizations at $\varphi = 0^\circ$ and $\varphi = 45^\circ$ is still noticed, but it can be seen this time that varying the shape factor greatly impacts this behavior. The spectral response under TM polarization at $\varphi = 0^\circ$ is severely affected when θ is increased for $b/a = 0.8$, but it tends to experience less deterioration under the same illumination conditions when the shape factor gets smaller. In the case where $b/a = 0.4$, the spectral responses of both polarizations at angles of incidence up to 60° are very close to the normal incidence situation. The same observations can be done for the TE polarization at $\varphi = 45^\circ$.

Those results under b/a variation clearly demonstrate the relevance of investigating the geometrical dimensions of the cross-shaped-hole arrays to properly tune their optical properties. This behavior shows that these structures can be made nearly insensitive to the polarization state of the light and to its incidence angles by changing the b/a ratio. From the computations, the condition of stability is reached for values of shape factor inferior or equal to 0.5. No obvious improvement of the stability was noticed when decreasing the shape factor to excessively low values (e.g., $b/a = 0.2$) compared to the case $b/a = 0.4$ presented in Figure 3.6. Furthermore, such a low ratio would lead to very weak transmission levels and considerable technological difficulties that make it of low interest for image sensor applications.

Normalized electric field maps on the top surface of the aluminum layer have been calculated with a RCWA code to comprehend this property of cruciform holes. They are shown in Figure 3.7 for four shape factors ($b/a = 0.2$, $b/a = 0.4$, $b/a = 0.6$ and $b/a = 0.8$) at their resonance wavelengths ($\lambda = 580$ nm, $\lambda = 475$ nm, $\lambda = 400$ nm and $\lambda = 330$ nm respectively). The calculations are done at normal incidence and for TE polarization. The results for the TM polarization can be deduced by a 90° rotation.

The electric field intensity and location significantly change when the shape factor sweeps from low to high values. In the stable case presented above where $b/a = 0.4$, the field is highly localized in the internal corners of the crosses. This particular field enhancement may explain the stability of crosses with small shape factors since it can directly be related to localized surface plasmons. Localized resonances are known to depend mostly on the geometrical shape of the holes and not on the illumination conditions [86], [152]. When the shape factor is increased, the field intensity is reduced and the location of the resonances becomes more scattered. For large shape factors (e.g., $b/a = 0.8$), the field distribution gets closer to a cavity resonance where the field intensity is decreased and mainly located on two opposite long edges of the crosses perpendicular to the incident electric field for TE polarization. The loss of stability for large crosses may thus be attributed to the delocalization of the resonance, related to the delocalized propagating surface plasmons. Eventually, one can notice that the field distribution of large- b/a crosses becomes similar to that of square or rectangular holes [125], [156], where the little internal corners have no specific impact on the resonance. This study thereby brings additional contributions to the understanding of the transmission process and of the electromagnetic properties of hole arrays, and also confirms the importance of localized plasmon resonances in the extraordinary optical transmission phenomenon [136], [144], [157].

As for this work, we have shown that a shape factor below 0.5 is required for the realization of stable cross-shaped-hole filters owing to the high enhancement of the localized plasmon resonances in the internal angles of the crosses.

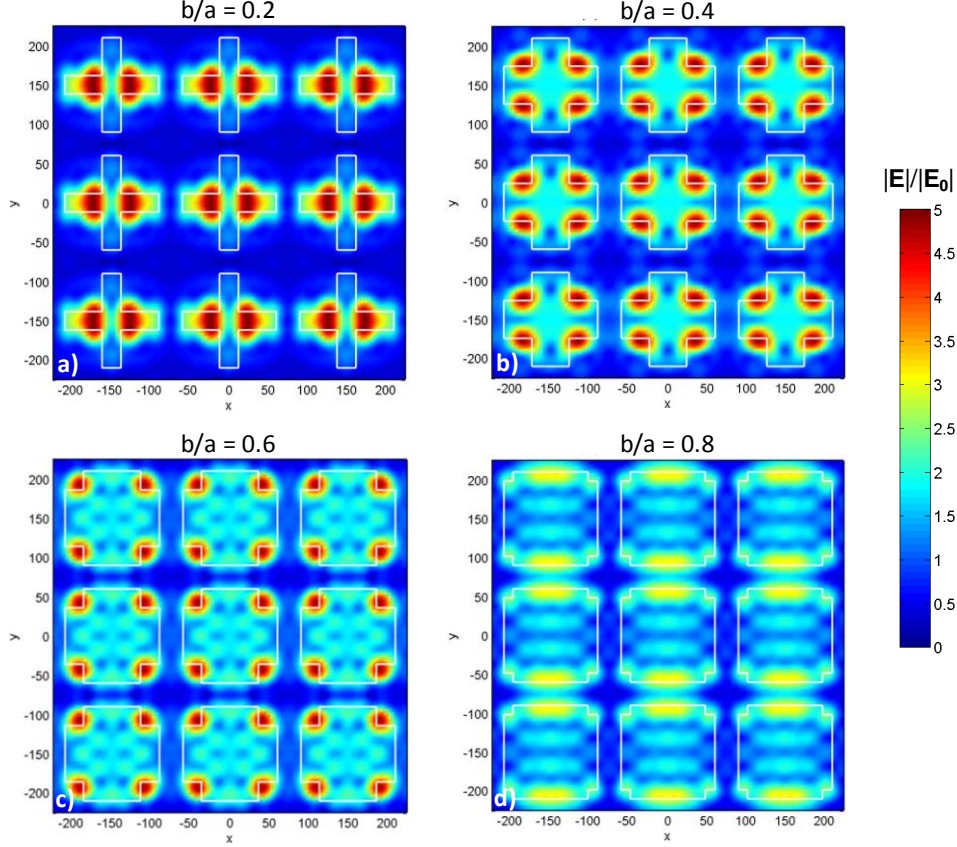


FIG. 3.7. Electric field norm $|E|$ normalized to the incident one $|E_0|$ on top surface of the metallic filter ($P = 150$ nm, $h_m = 75$ nm, $a/P = 0.8$ and thus $d = 30$ nm), for normal incidence and TE polarization and for (a) $b/a = 0.2$ and $\lambda = 580$ nm. (b) $b/a = 0.4$ and $\lambda = 475$ nm. (c) $b/a = 0.6$ and $\lambda = 400$ nm. (d) $b/a = 0.8$ and $\lambda = 330$ nm. The x and y axes are given in nm.

3. A.1.4 Intercrosses distance d

In the previous sub-section, we have seen that the width of the crosses has a significant impact on the plasmon resonances, and thus that the stability properties of these structures can be widely and simply controlled by changing one characteristic dimension. In the case of 2D arrays, it is also relevant to consider how the holes interact with each other and how this may affect the sensitivity of these filters to the light incidence. We focus now on the effect of the spacing between crosses that we defined earlier as $d = P - a$. Since a is kept constant, this can be assimilated to a variation of the period P , although the main effects can be attributed to the change of d .

In Figure 3.8, the impact of the intercroses distance is illustrated with the dimensions of the reference filter ($P = 150$ nm, $a = 120$ nm and $b = 72$ nm) with three spacing values. The spectral responses for TE and TM polarizations are given for angles of incidence up to 60° and only for an azimuth $\varphi = 0^\circ$. The charts put in evidence that the arrays with the closest distances between crosses tend to get a more stable response under off-normal incidences as the case $d = 20$ nm presents the lowest resonance shift and transmission losses when θ is increased. The deterioration of the spectral response is more severe when d is progressively increased to 50 nm and 100 nm. This observation implies that arrays with crosses close to each other are preferred to obtain filters with angular and polarization stabilities.

To complete these results, the evolution of the behavior of near-crosses arrays with the azimuth is presented in Figure 3.9 with $d = 20\text{nm}$. The symmetry of the TE and TM polarizations is still observed for $\varphi = 0^\circ$ and $\varphi = 45^\circ$. We can also see that the response of the two polarizations are very similar in the case $\varphi = 22.5^\circ$, and that their deterioration when θ increases is lower than in the two extreme cases ($\varphi = 0^\circ$ and $\varphi = 45^\circ$).

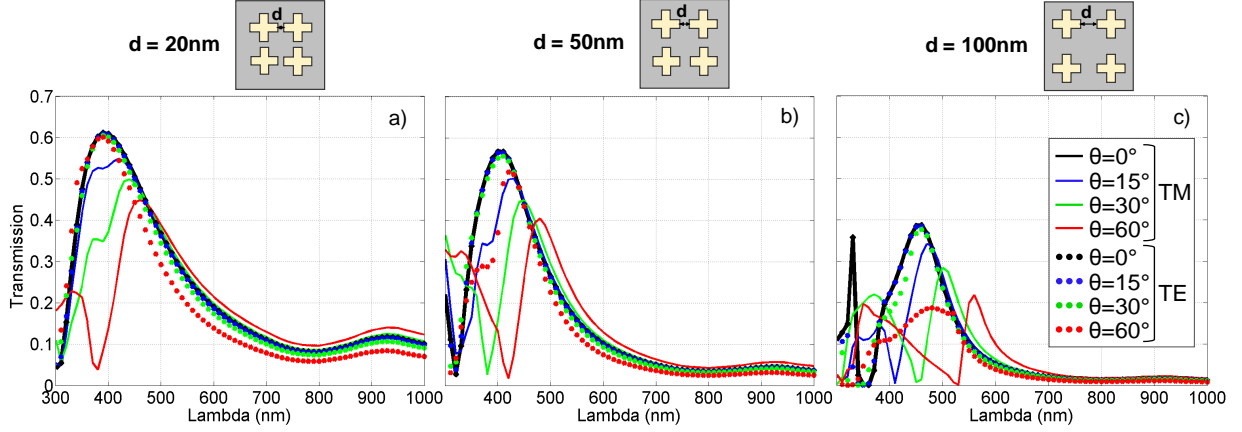


FIG. 3.8. Spectral responses of the reference filter ($h_m = 75\text{ nm}$, $a = 120\text{ nm}$, $b/a = 0.6$) for both TM and TE polarizations at different polar incident angles for $\varphi = 0^\circ$ and (a) $d = 20\text{ nm}$. (b) $d = 50\text{ nm}$. (c) $d = 100\text{ nm}$. The schematics actually correspond in the simulations to infinite arrays of crosses.

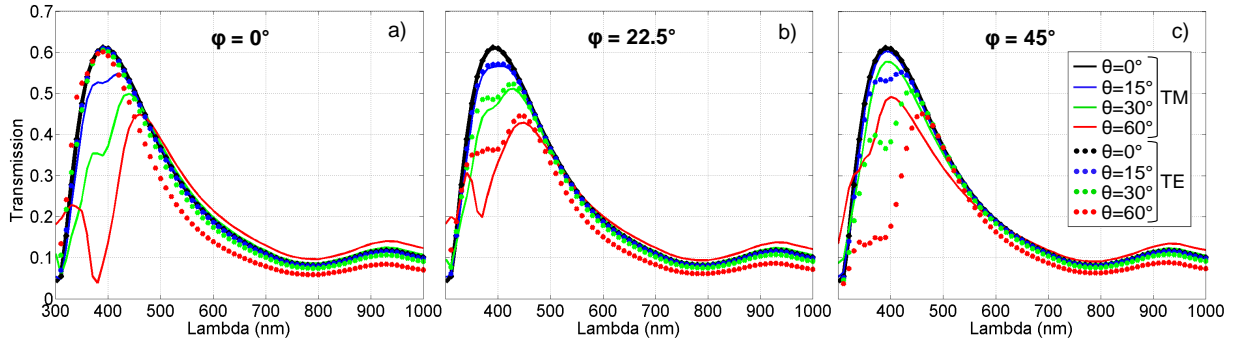


FIG. 3.9. Spectral responses of the reference filter ($h_m = 75\text{ nm}$, $a = 120\text{ nm}$, $b/a = 0.6$) with $d = 20\text{ nm}$ for both TM and TE polarizations at different polar incident angles and for (a) $\varphi = 0^\circ$. (b) $\varphi = 22.5^\circ$. (c) $\varphi = 45^\circ$.

In order to go further in the analysis, the evolution of the resonant wavelength of the main transmission peak is given in Figure 3.10 as a function of polar angle of incidence with different intercrosses spacing d and for three azimuths. The data that we present in Figure 3.10 are calculated with 8 harmonics, with a 2 nm wavelength step and averaged over the TE and the TM responses. Furthermore, this evolution is calculated in the cases of two arrays, one with a small shape factor ($b/a = 0.4$) and the other one with a larger shape factor ($b/a = 0.6$). The other dimensions of the filters presented in the charts are those of the reference filter.

At first glance, one can notice that the filters are more sensitive to the polar angle of incidence for large intercrosses distances, as their spectral responses experience more substantial shift towards long wavelengths when θ increases. The redshift is however considerably reduced for small values of intercrosses distances, which is especially visible in the case $b/a = 0.4$ where the resonance occurs at the

same wavelength whatever the angle of incidence for $d \leq 50$ nm. One can notice that the sensitivity to θ for large intercrosses distances is progressively reduced when the azimuth φ is swept from 0° to 22.5° and from 22.5° to 45° . For example, in the case $b/a = 0.4$ and $d = 150$ nm, the resonance shift between normal incidence and $\theta = 60^\circ$ is 122 nm for $\varphi = 0^\circ$, 98 nm for $\varphi = 22.5^\circ$ and 45 nm for $\varphi = 45^\circ$.

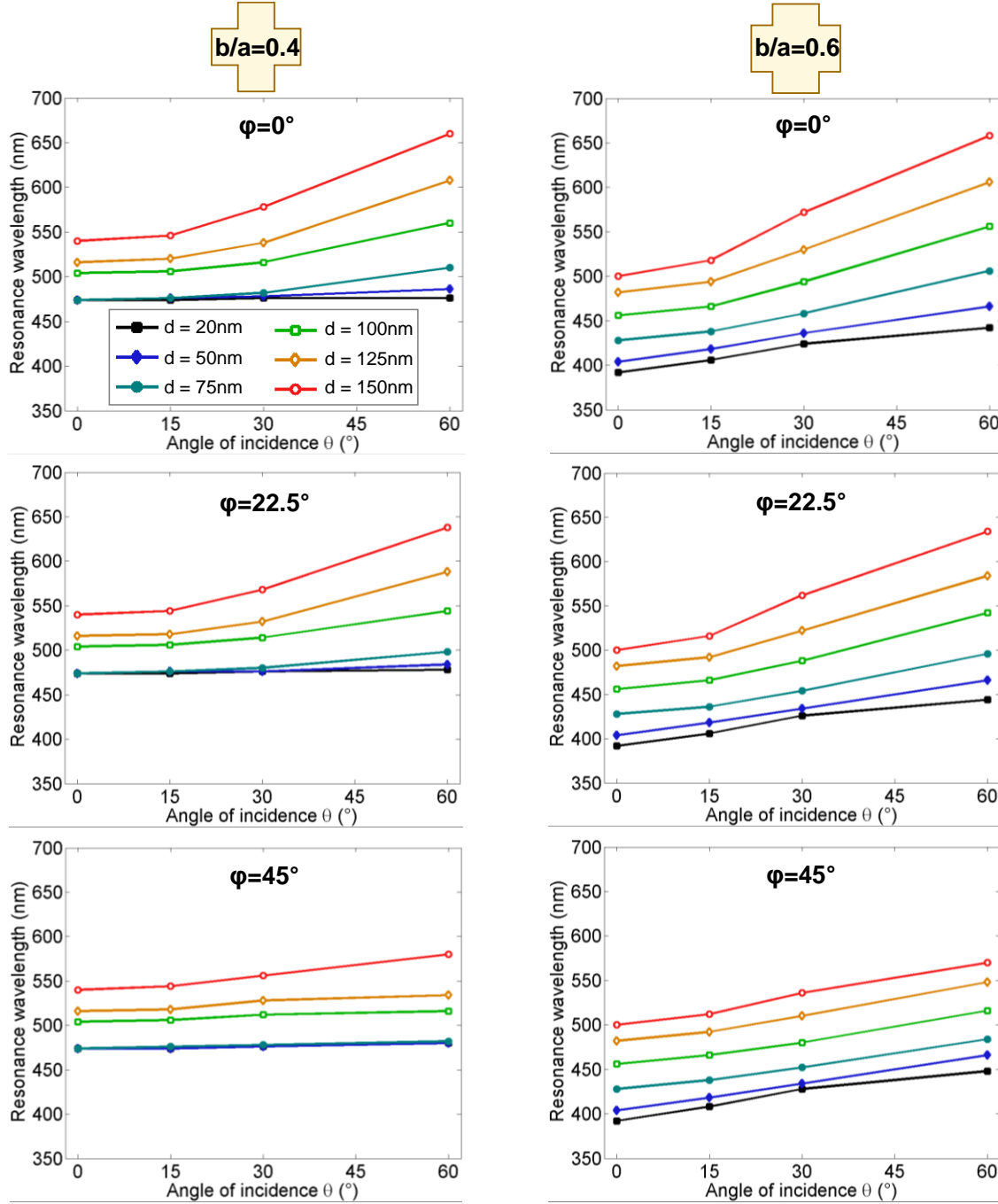


FIG. 3.10. Evolution of the resonance peak shift induced with the polar incident angle θ and calculated from the average of the TM and TE response, for different intercrosses distance d , and for different azimuths and two distinct shape factors $b/a = 0.4$ and $b/a = 0.6$. Filter dimensions are: $h_m = 75$ nm and $a = 120$ nm.

Here is a potential explication to this impact of the intercrosses distance. When crosses are close to each other, the metal layer becomes almost discontinuous and thus the surface plasmon polaritons can hardly propagate along the metal surface, leading to the predominance of localized resonances. Localized plasmon resonances are known to be nearly insensitive to the light incidence and are more related to the shape and to the geometry of the apertures [144]. That would explain the stability of low- d filters regardless of the light incidence and azimuth. On the other hand, when crosses get farther from each other, the "corridors" between crosses are widened and the propagation of surface plasmon polaritons (SPPs) is progressively facilitated. For high values of intercrosses spacing (e.g., $d \geq 100$ nm), the contribution of surface plasmon polaritons becomes predominant. This would explain the deterioration of the filters stability, owing to their sensitivity to light incidence. These results highlight the coexistence of these two types of resonance of LSPs and SPPs and their respective contribution to the optical properties at off-normal incidence of these structures as a function of the spacing between patterns. These findings also support the work done by Lin and Roberts on cross-shaped-hole arrays at normal incidence [136], [144]. In their work, the spectral behavior of closely packed crosses is shown to be mainly dictated by the localized resonance related to the apertures themselves, whereas for large spacings, the excitation wavelength of the surface plasmon polaritons gets closer to that of the localized plasmons, making the surface plasmon polaritons contribution predominant. The competition between propagating and localized plasmons and their relative importance according to the spacing between apertures have also been pointed out in a similar way for square holes [156], rectangular holes [130] and coaxial apertures [158], [159], but their respective influence on the angular and polarization sensitivity had not been clearly established yet.

We propose here an explanation on the angular and polarization sensitivities: we have noticed in Figure 3.10 that the degradation of the stability with θ for large intercrosses distances is more severe at $\varphi = 0^\circ$ and then decreases when φ increases. This could be explained by the fact that the propagation of surface plasmon polaritons is facilitated in the directions of the pathways between two adjacent crosses, which correspond in our case to the x and y axes for $\varphi = 0^\circ$, via the (0,1) and (1,0) diffraction orders. We attribute the gain in stability when the illumination deviates from $\varphi = 0^\circ$ to the increasing number of dielectric apertures encountered by the surface plasmon polariton on the way, which hinder its propagation, thus limiting its impact to the benefit of localized resonances. The stability of the filter thus progressively improves until reaching its maximum at $\varphi = 45^\circ$, because the corridor, available via the (1,1) diffraction order, is thinner than for $\varphi = 0^\circ$. A rough visual description of this phenomenon is proposed in Figure 3.11. Note that for a given configuration with an optical system, the stability should be studied with a sum of all the possible incidences over a solid angle. This study of the behavior of the spectral responses of the filters with the angles of incidence and the polarization is thus of prime importance for actual sensors, especially if no optical system is used as it is the case for ALS sensors.

We note that even for very small intercrosses distances, a worse stability is observed for the large shape factor ($b/a = 0.6$) than for the smaller one ($b/a = 0.4$), where the resonance wavelength is stable regardless of the polar angle of incidence. This demonstrates that the shape factor is the main criterion of stability for cross-shaped-hole array filters. As for this sub-section, it can thus be concluded from these simulations that realizing a structure with crosses close to each other is preferable to make filters nearly insensitive to the incident angles and to the polarization state of the impinging light. The best case can be summed up as an array of crosses with a thickness superior to 150 nm, a shape factor b/a below 0.5 and an intercrosses distance inferior to 50 nm.

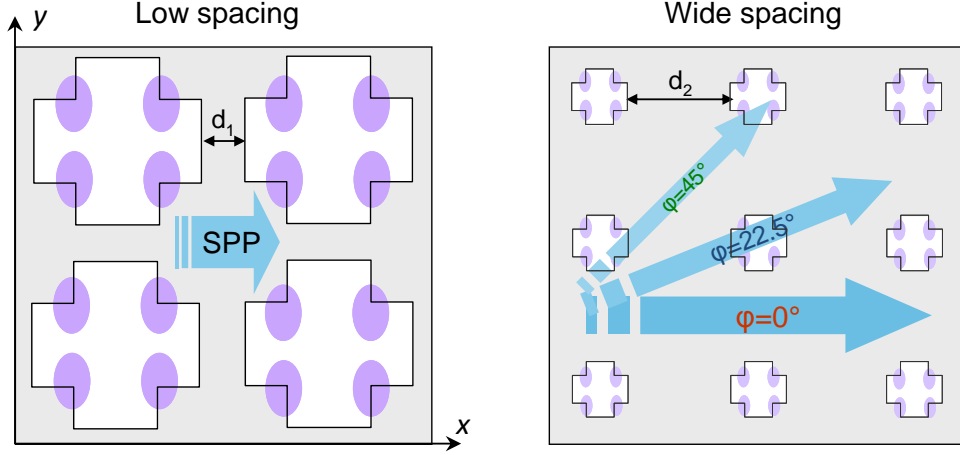


FIG. 3.11. Impact of localized resonances (purple areas) and SPPs (arrows) depending on the intercrosses distance d and azimuth φ . The crosses all have the same dimensions, only the scale and the intercrosses distances are changed between the two schemes.

3. A.2 Illustration with color filters

We have demonstrated in *section 3. A.1* that it is possible to considerably tune the optical properties of cross-shaped-hole arrays with proper geometrical designs. The main parameters that impact the angular and polarization sensitivities of these structures are the shape factor of the crosses b/a and the distance between crosses d . In the following section, we will illustrate how these results can be exploited to realize a stable filter in the case of a RGB sensor whose response does not depend on the illumination conditions and can support a wide range of incidence angles.

3. A.2.1 RGB filters selection

The realization of an image sensor requires a set of three color filters (red, green and blue filters at 460 nm, 540 nm and 610 nm respectively) in the case of the standard Bayer arrangement. In our example, we focus on the angular and polarization dependency of the filters rather than in their transmission and color accuracy. In addition to the stability criteria that we have found out in the previous *section 3. A.1*, we added other constraints to the set of RGB filters.

The material used for the three filters is aluminum. For an easy process, the metal thickness is fixed for the three filters. It is set to 50 nm to favor the level of transmission and to facilitate the fabrication of crosses with small shape factor, as the aspect-ratio is reduced for the etching step. We have chosen to design the blue and the green filters with the same period $P = 150$ nm, but a higher period $P = 250$ nm was necessary to obtain the red filter. The shape factors for the three color filters are inferior to 0.5 to fit the stability condition: $b/a = 0.4$ for the blue filter, $b/a = 0.25$ for the green one and $b/a = 0.3$ for the red one. All of these parameters ensure to the extent possible low intercrosses distance with $d = 60$ nm (blue filter), $d = 45$ nm (green filter) and $d = 100$ nm (red filter). The spectral responses of the three filters are presented in Figure 3.12 with resonances at 430 nm, 530 nm and 640 nm for the blue, green and red filters respectively. It can already be noticed with the spectra that producing pure colors with aluminum structures may be hard, especially when the wavelength of the filter gets closer to the near-infrared region. This will be explained in the next sub-section.

We have now defined our three RGB filters with geometries that meet the stability criteria established in *section 3. A.1*.

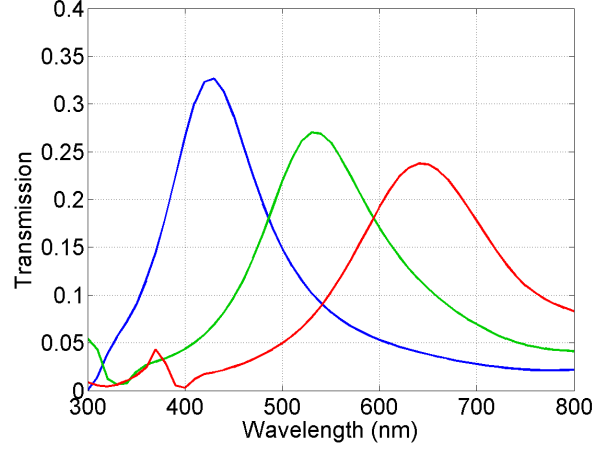


FIG. 3.12. Example of RGB filters at normal incidence using cruciform-holes arrays with small shape factors. Blue filter: $P = 150$ nm, $h_m = 50$ nm, $a/P = 0.6$, $b/a = 0.4$. Green filter: $P = 150$ nm, $h_m = 50$ nm, $a/P = 0.7$, $b/a = 0.25$. Red filter: $P = 250$ nm, $h_m = 50$ nm, $a/P = 0.6$, $b/a = 0.3$.

3. A.2.2 Color errors and illumination conditions

In order to illustrate the applicability of the stability results to an image sensor application, we want to evaluate how much the variations of the spectral response of the filters upon different illumination conditions impact their chromatic signal. The CIE diagrams [83], [84] provide a useful tool to represent visually the variation of the chromatic components of a filter.

For each color filter defined in *section 3. A.2.1*, the spectral response is simulated in every potential illumination conditions all combined, which means: for several values φ in the interval $[0^\circ; 45^\circ]$, for several polar angles of incidence θ in the interval $[0^\circ; 60^\circ]$ and for both TE and TM polarizations. For each combination, the chromatic components of the corresponding spectral response are extracted and reported on a chromaticity diagram by a dark dot. In Figure 3.13, we gather all these calculations for the three color filters. The white crosses give the chromatic components of the blue, green and red filters at normal incidence. The dark dots around the crosses give the chromatic components of all the possible off-normal incidence conditions, i.e. all the couple of values $(\theta; \varphi)$ for both TE and TM polarizations. The results are given on three chromaticity diagrams for better clarity, each one featuring a more or less severe range of polar angles of incidence θ : $[0^\circ; 15^\circ]$, $[0^\circ; 30^\circ]$ and $[0^\circ; 60^\circ]$. On Figure 3.13(a), the CIE diagram shows the color variations of the three color filters for the different possible illuminations resulting from the chosen range of azimuths and polarizations with polar angles of incidence θ up to 15° only. This presentation helps to see how the signal of the image sensor is progressively impacted going from angles close to normal incidence to larger ones.

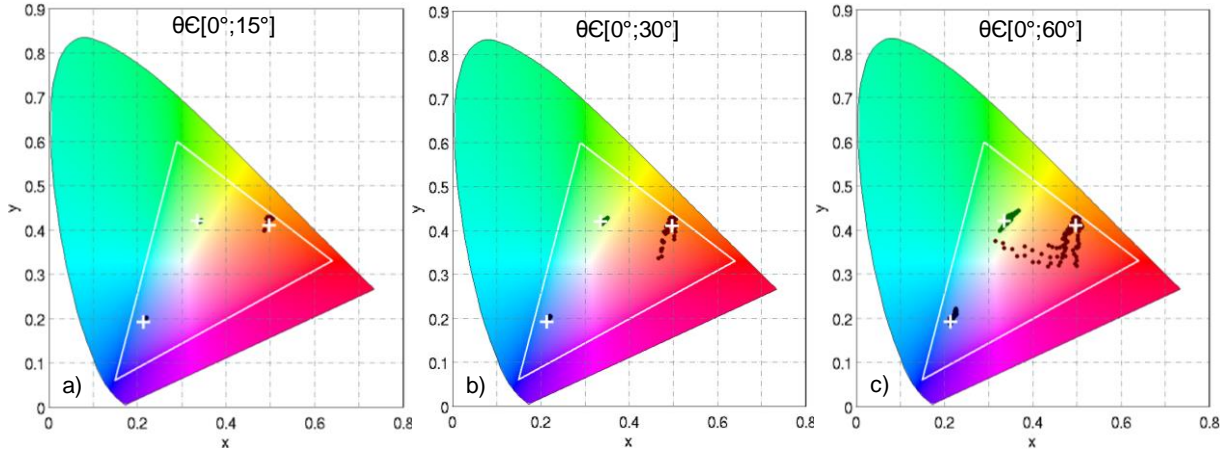


FIG. 3.13. (a) CIE diagram representing the color variations of each R,G and B filters when simulated with TM or TE polarizations, with all possible azimuth values and for $\theta \in [0^\circ, 15^\circ]$ range. (b) for $\theta \in [0^\circ, 30^\circ]$. (c) for $\theta \in [0^\circ, 60^\circ]$.

The CIE diagrams evidence that the blue and green filters remain very stable up to 30° with slight color variations when the incidence and the polarization of light are changed. The blue filter is the most stable with chromatic components stable even for large polar angles of incidence (up to 60° in the third diagram). The red filter, although respecting the design criteria, presents more variations even for low and medium angles of incidence. For $\theta = 60^\circ$, its chromatic components severely deviate from the original red color and even approaches the white color. We attribute the progressive deterioration of the stability when approaching the near-infrared wavelengths to the significant increase of the absorption of aluminum in this wavelength range as shown in Figure 3.14 [45]–[47]. The peak of absorption in the $\varepsilon''(\omega)$ structure is related to interband transitions occurring at energy close to 1.5 eV (825 nm) [113], [160], which negatively affects the transmission efficiency and plasmonic properties of localized resonances. The use of another compatible metal for the red filter such as copper, silver or gold, which all have better optical properties in this wavelength range, with the same geometrical criteria, may improve the stability of the spectral response and allow for low color errors even for large angles of incidence. Note however that the use of different metals on a pixel matrix would complicate the fabrication of the image sensors. We deposited two patents allowing for an easy integration of plasmonic filters in the standard process flow of an image sensors and that also facilitate the use of different metals for each pixel color [161], [162].

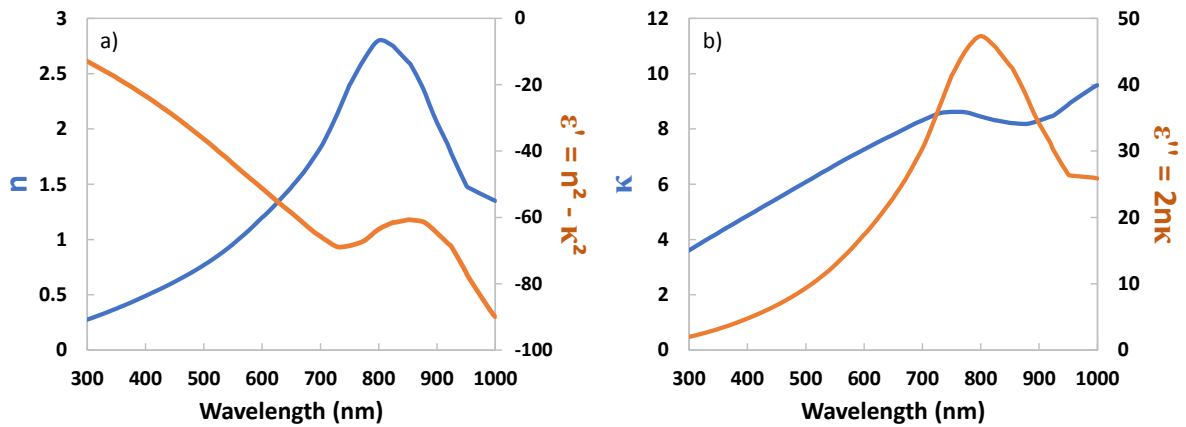


FIG. 3.14. (a) Real parts of the refractive index and of the dielectric permittivity of aluminum. (b) Imaginary parts of the refractive index and of the dielectric permittivity of aluminum. Data extracted from Palik Handbook [47].

3. A.3 Conclusion on optimal design rules

We have demonstrated in part A that the optical properties of cross-shaped-hole arrays such as their angular and polarization sensitivities can be accurately tuned by changing characteristics dimensions of these structures. The two major parameters governing their electromagnetic behavior are the shape factor, defined as the ratio of the arm width to the arm length of crosses b/a , and the spacing between crosses d . A low shape factor (inferior to 0.5) and a short intercrossoes distance below 75 nm enhances the localized plasmon resonances on the apertures to the detriment of the propagating plasmons, which ensures less dependence of the filters on the illumination conditions. The metal thickness has to be superior to 150 nm to provide an improved stability, but its influence is small compared to the shape factor and the intercrossoes distance. The impact of the azimuth for 2D arrays and the ways to limit it have been investigated, which is very seldom taken into account for hole arrays in literature to our knowledge. We believe that this study brings a further contribution to the understanding of the respective roles of localized plasmons and surface plasmon polaritons in the EOT process. Moreover, it demonstrates the ability of cross-hole arrays to make filters with a high angular stability and a polarization insensitivity, provided that the established design rules are respected and that the choices of materials are coherent with the targeted wavelength range.

3. B – ALS filters evaluation and optimization with the constraints of the study

We have seen in the previous part that cross-shaped-hole arrays are able to give a stable spectral response regardless of the polarization and of the incidence angle of the illuminating light, as long as their geometry respects specific criteria that have been identified and quantified. These properties of crosses can be used to fabricate stable filters targeted for a wide range of applications where the sensitivity to polarization and light incidence are critical for the device performance. In this second part, we aim to assess quantitatively if plasmonic filters can provide an efficient alternative to standard filtering solutions in the case of Ambient Light Sensors (ALS). Remember that we defined two ALS criteria in *section 2. 2.1*. Basically, the ALS error stands for the deviation of the filter's spectral response with respect to the theoretical photopic response, whereas the ALS dark indicates the sensitivity of the filter in low-light conditions. A filter with low transmission will have a high ALS dark value.

In addition to the evaluation tool that was described in *Chapter 2*, the filters evaluation will be done by taking into account the stability results of the former part in order to respond to all the requirements of Ambient Light Sensors. The performance of potential designs will be optimized to obtain the best sets of dimensions. Finally, plasmonic structures different from cross-shaped-hole arrays and advanced solutions with noble metals will also be presented. This part will allow us to propose ALS filters that meet all the specifications of the application in terms of performances and angular robustness. A portion of the following results was published and presented in conference [163].

In this part, all the simulations and optimizations are performed with the ALS stack defined in *section 2. 5 Conclusion on Chapter 2* where the aluminum layer is embedded in a SiON layer, which is itself above a 500 nm Si₃N₄ layer and an infinite SiO₂ substrate. The aluminum layer is patterned with an array of cruciform apertures filled with SiON and the filter simulations are made with a 5x5-harmonics RCWA method.

3. B.1 Positioning of plasmonic filters

3. B.1.1 Evaluation of plasmonic filters performance

This section will put in evidence whether the plasmonic structures with crosses can give satisfying ALS performances, i.e. an ALS Dark inferior to 100 lx and a maximum ALS error inferior to 2.2 dB (which corresponds to the green area in the (ALS error ; ALS dark) plot defined in *Chapter 2*). Several filter designs are thus simulated with RCWA to find the set of parameters P , a , b and h_m that best fits to the specifications of the ALS sensor. This wide scan is made on the metal thickness h_m , the period P and the arm length a within the following ranges: i) $125 \text{ nm} < h_m < 300 \text{ nm}$ (25 nm step), ii) $125 \text{ nm} < P < 300 \text{ nm}$ (25 nm step) and iii) $0.5 < a/P < 0.9$ (0.05 step). a/P is chosen superior to 0.5 to avoid small apertures and provide sufficient transmittance, thus lowering the ALS dark. All those parameters generate as much as 576 filters designs per simulation run.

In order to take into account the angular stability of the filters, the geometrical conditions defined in part A are also used as a constraint in the evaluation tool. The scans are thereby performed for five values of the shape factor b/a , with $0.4 < b/a < 0.6$ with a 0.05 step. Smaller values would result in a high ALS dark due to the narrowness of the crosses whereas higher values would imply a dramatic loss of the stability properties of cross-hole filters. The data for the shape factors 0.4, 0.5 and 0.6 are gathered in Figure 3.15 as scatter plots of 576 filters each. Note that the intercrosses distance $d = P - a$ is not implemented as a condition to avoid too much restriction on the performance evaluation and because the shape factor is predominant in the stability of these structures.

The spectral responses of all the filters are then extracted and inputted in the ALS evaluation code defined in section 2. *2.1 Ambient light sensors*. For every filter, the corresponding maximum ALS error and ALS dark are obtained. The evaluation results can then be gathered and plotted on 2D-graphs, with the ALS error Max on the x -axis and the ALS dark on the y -axis. Five scatter plots are thus obtained for the five b/a values, each one containing 576 filter designs which performances are compared to the 2.2 dB reference consisting of a green resist and an IR-cut, represented with a black square as shown in Figure 3.15. Only 3 plots are presented here, with $b/a = 0.4$, $b/a = 0.5$ and $b/a = 0.6$. Only the filters having an ALS dark below 100 lx are shown for easier reading and to focus on potentially interesting designs.

The first relevant information that we can learn from Figure 3.15 is that for a given set of filters with one b/a value, we can find a few designs close to the reference and inside the specifications range. The filters whose ALS error Max is above 2.2 dB should be abandoned since it is our most critical criterion (see *Chapter 2*). On the other hand, filters with a low ALS error Max but with a high ALS dark (above 30 lx) can nevertheless be considered. Indeed, we explained in *Chapter 2* that apart from this thesis, STMicroelectronics in-house calculations revealed that a final annealing of the ALS sensor could improve the Quantum Efficiency (QE) of the photodiode, which should lead to a decrease of ALS dark by a factor from 2 to 5. While this anneal step cannot be considered with organic resists, it could be possible for plasmonic filters. We will address this aspect in *Chapter 5*.

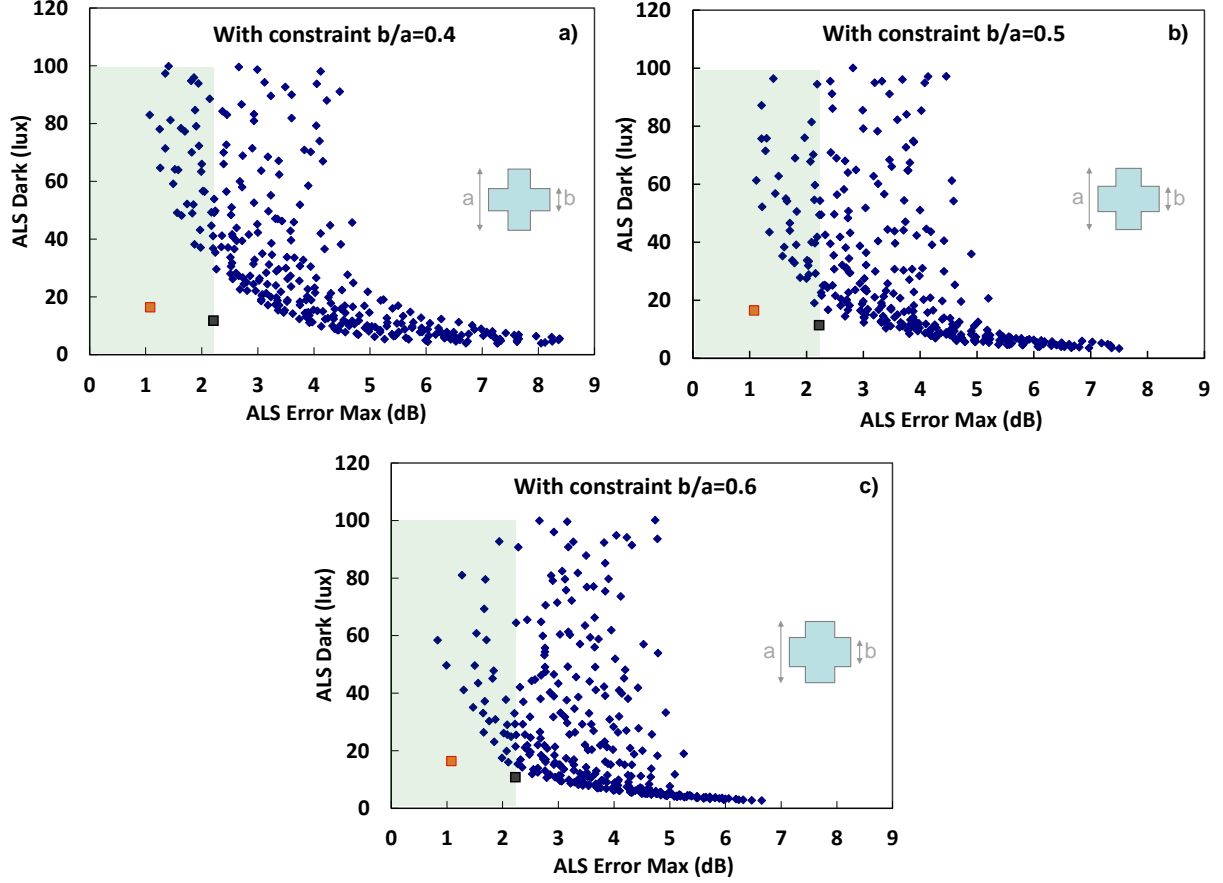


FIG. 3.15. (a) ALS performances for several designs with $b/a = 0.4$, each dot corresponding to one filter. (b) With $b/a = 0.5$. (c) With $b/a = 0.6$. Only filters with reasonable ALS dark (< 100 lx) are given. ALS filters must have an ALS error Max < 2.2 dB corresponding to the performance of the 2012 STMicroelectronics reference (green area). The 2012 and 2015 references are plotted with a black square and an orange square respectively.

This ALS plots representation gives us additional information. One can see a significant trend in the charts: the lower the b/a ratio (i.e. the higher the angular stability), the worse the ALS performances. Both the ALS dark and the ALS error are increased, i.e. deteriorated when the crosses are made with a thinner arm width, which may imply that small crosses are more sensitive to illuminants than large ones. The ALS dark increase is most probably due to the lower transmission efficiencies of small crosses. Similarly, the ALS error Max increase would be due to the difficulty to approach the photopic response with small aperture areas. These results thus show us that a trade-off has to be made between strong angular stability and high ALS performance. Although not highlighted on the charts, the results indicate that the best filters generally have a thickness superior to 225 nm, which means that the rejection of the filters is primordial to get a low ALS error, according to *section 2.1.2.2*. We can also note that the filters fitting the specifications have their dimensions confined in narrow ranges, with a period between 250 nm and 300 nm and a a/P ratio between 0.6 and 0.75. We saw in Chapter 2 that the ALS error criterion is highly sensitive to the rejection in the near-infrared range. For the following studies on the robustness of ALS filters, we choose an ALS filter of reference in the intermediate case $b/a = 0.5$ which combines both the angular stability and the ALS performance. A low ALS error Max is favoured rather than a low ALS dark. The dimensions of this ALS reference filter are $h_m = 300$ nm, $P = 275$ nm, and $a/P = 0.655$. Its ALS dark is 61 lx and its maximum ALS error is 1.12 dB.

3. B.1.2 Angular tolerance

Now that we have shown that plasmonic designs can be found in the specifications range of Ambient Light Sensors, it is worth evaluating how the performance are impacted in off-normal incidence. This challenge is important since we saw in *Chapter 1* that ALS sensors do not use any optical system. Even with the b/a constraint, we must ensure that the sensitivities to angles of incidence and to polarization do not lead to a critical dispersion in terms of ALS criteria.

In Figure 3.16, we provide a global representation of the angular stability for three b/a values, each one with a scan over 175 filters. The parameters scans have been reduced to: i) $200 \text{ nm} < h_m < 300 \text{ nm}$ (25 nm step), ii) $200 \text{ nm} < P < 300 \text{ nm}$ (25 nm step) and iii) $0.55 < a/P < 0.85$ (0.05 step). This allows for a better readability of the charts. The performance of every filter is calculated with a spectral response averaged over the TE and the TM polarization states and for three polar angles of incidence θ (15° , 30° and 60°). The scatter plots of each angle θ are drawn with a different color to highlight the performance dispersion due to the sensitivity to θ and to the polarization.

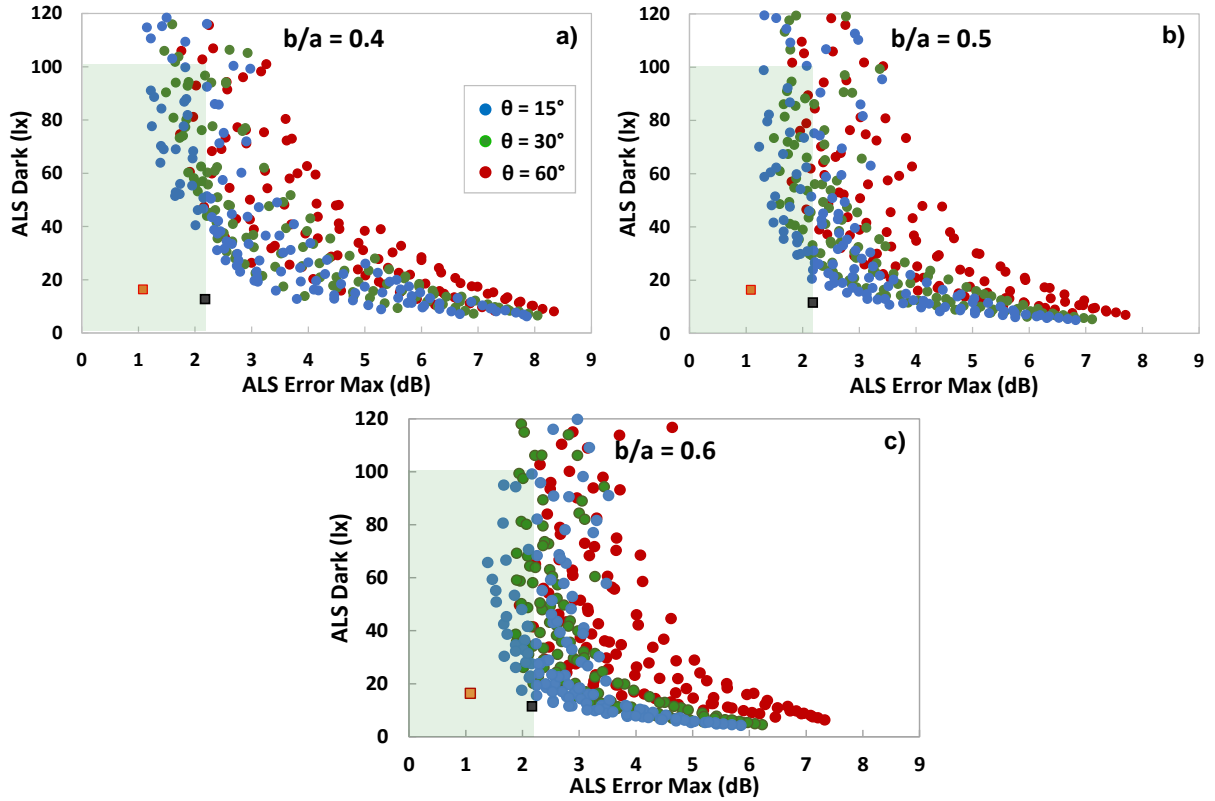


FIG. 3.16. (a) ALS performance dispersion for 175 designs with $b/a = 0.4$ but various geometrical parameters such as period, thickness and hole size, for different angles of incidence θ , each dot corresponding to one filter. The spectral response are averaged over the TE and the TM polarization. (b) With $b/a = 0.5$. (c) With $b/a = 0.6$. The 2012 and 2015 references are plotted with a black square and an orange square respectively. The green area represents the specifications range.

First, the charts show that the dispersion of the performance is more significant when b/a is increased. This result, while expected owing to the work realized in part A, confirms the sensitivity of the performance criteria to light incidence and thus the relevance of the b/a constraints in the evaluation of the ALS filters to ensure the respect of the specifications range of the application. Another information from these charts is that the performance dispersion is low until $\theta = 30^\circ$, which means that the filters' performances are quite stable except for large angles of incidence such as $\theta = 60^\circ$ in our case, which is a drastic incidence condition.

The azimuth is not taken into account in the previous scatter plots and the study of the impact of the light incidence on the ALS performance cannot be considered as complete yet. In order to gather the influence of the polar angle θ , the azimuth φ and the polarization state of the light on the same chart without overcrowding the data, we focus on the complete angular sensitivity of the ALS reference filter defined in the previous sub-section, since the general sensitivity to θ has been demonstrated with the parameters scans. The performance of this filter ($b/a = 0.5$) are extracted from its spectral response calculated for different polar angles θ , azimuths φ and averaged over the TE and the TM polarizations. The results are plotted in Figure 3.17 where each color corresponds to a polar angle value θ and the points of the same color to different azimuth values φ (0° , 9° , 18° , 27° , 36° and 45°). The chart puts in evidence that the ALS performances remain in the specifications range even when the azimuth and the polar angle up to 30° are combined. Large incidence angles ($\theta = 60^\circ$) are too severe to fit with the ALS criteria and show the limits of the angular stability of the ALS cross-shaped-hole arrays.

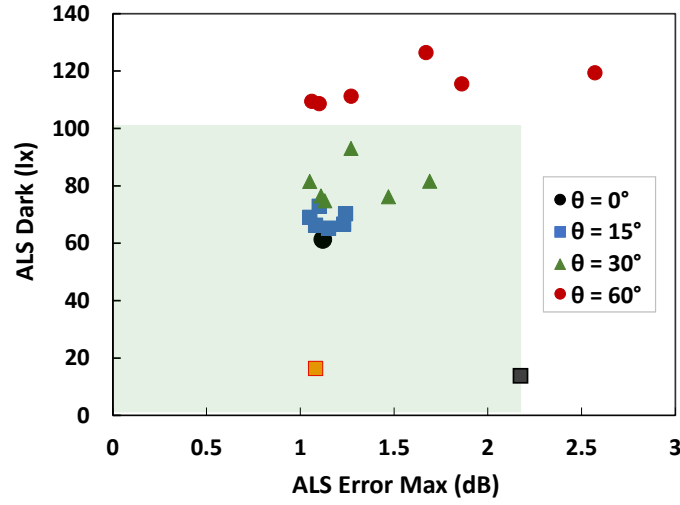


FIG. 3.17. ALS performances obtained at normal incidence $\theta = 0^\circ$, $\theta = 15^\circ$, $\theta = 30^\circ$ and $\theta = 60^\circ$ for the ALS reference filter ($h_m = 300$ nm, $P = 275$ nm, $a = 180$ nm and $b = 90$ nm). For the same polar angle of incidence θ , 6 azimuthal angles φ are taken into account (0° , 9° , 18° , 27° , 36° and 45°). The 2012 and 2015 references are plotted with a black square and an orange square respectively. The green area represents the specifications range.

3. B.1.3 Other potential ALS structures

We have seen that in spite of the benefits of the design rules used for cruciform holes, the angular and polarization stabilities can reach their limits for high angles of incidence such as $\theta = 60^\circ$. Given the relative difficulty to accurately fabricate crosses compared to square and circular apertures, we want to check the potential use of more basic shapes such as squares and circles as ALS filters targeting the case where the angular stability requirement is of lesser importance. Hexagonal arrays of crosses are constructed similarly to those presented in section 2. 3.3.4. As in section 3. B.1.1, we scan the characteristics dimensions of those structures and calculate their ALS performance to verify if they can meet the specifications of the application. The parameters ranges used are: i) $125 \text{ nm} < h_m < 300 \text{ nm}$ (25 nm step), ii) $125 \text{ nm} < P < 300 \text{ nm}$ (25 nm step) and iii) $0.4 < a/P < 0.9$ (0.05 step) (with a being either the square size or the diameter in the case of circular apertures), implying a total of 704 designs tested per shape. For the hexagonal arrays, the period is calculated from the smallest distance between crosses d which is scanned from 40 nm to 125 nm (see sections 2. 3.3.3 and 2. 3.3.4 for more details regarding the structures).

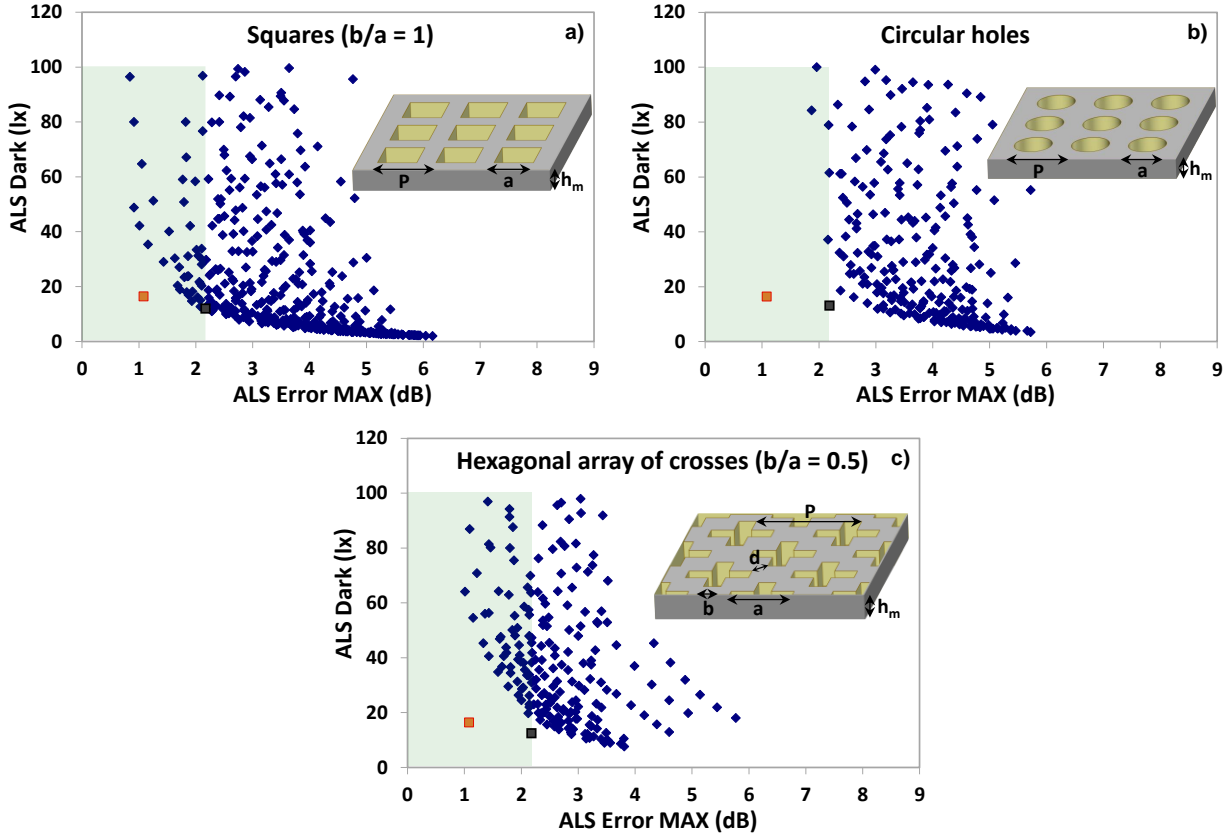


FIG. 3.18. (a) ALS performances for several designs with square arrays of square holes ($b/a = 1$), each dot corresponding to one filter. (b) With square arrays of circular holes. (c) With hexagonal arrays of crosses ($b/a = 0.5$).

The corresponding scatter plots are given in Figure 3.18. It appears that circular holes are not able to provide sufficient ALS performance as nearly no design falls into the specifications range. This may be due to the specific resonances of circular apertures which are not governed by localized plasmon resonances, and thus cannot provide a well-defined peak approaching the photopic response. On the contrary, squares come close to the performances of the green resist combined with an IR-cut. At equivalent maximum ALS error, some designs give a lower ALS dark than those with cruciform holes. However, the angular stability of square apertures cannot compete with crosses as shown in *Chapter 2*. No obvious improvement is noticed with hexagonal arrays of crosses with $b/a = 0.5$ compared with the equivalent square arrays. These results show that not all hole-array structures are capable of fitting the ALS performance, and that the shape of the apertures has a predominant role in this task. It can be assumed that this shape-dependent behavior is related to the resonances occurring in the structures, and especially to their properties to enhance localized plasmons at the holes (*section 2.3.3*).

3. B.2 Noble metals alternative

The previous study was limited to materials allowed in CMOS front-end fabs in view of a direct integration of the filters in standard image sensors. We present here the evaluation of other metals such as silver or gold in the case where the fabrication could be realized in an area compatible with contaminant materials.

3. B.2.1 Silver-based filters

Although its presence in CMOS front-end clean rooms is severely restricted for contamination purpose, silver can be studied as an upstream solution to make high-performance Ambient Light Sensors due to its ideal plasmonic properties in the visible region [45], [46]. If the performances of silver-based ALS filters are attractive, it may be assumed that its introduction in the very last steps of the fabrication could be envisioned. The same approach is used as in *section 3. B.1* to evaluate the silver ALS designs with similar scans over the different geometrical parameters of the structures. We focus here on the square arrays of cruciform (Figures 3.19(a)–(b)) or square apertures (Figure 3.19(c)).

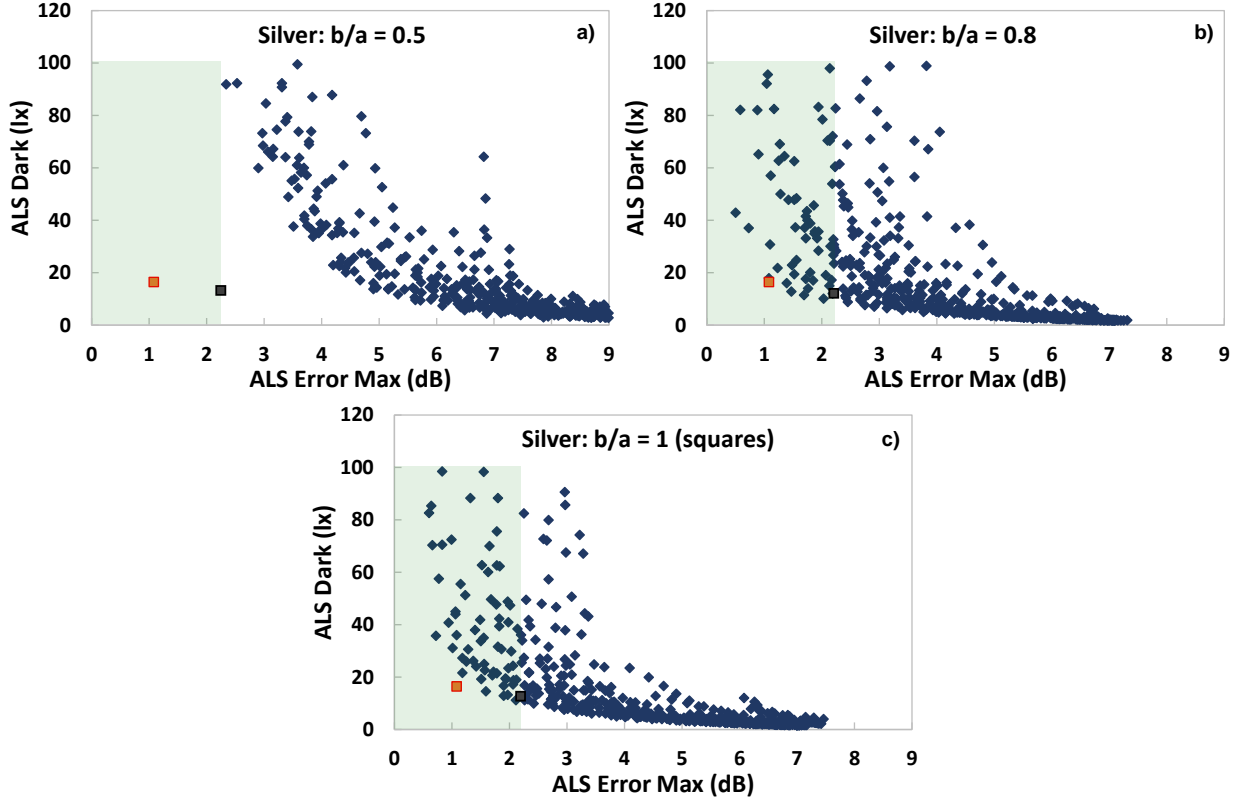


FIG. 3.19. (a) ALS performances for several designs with square arrays of cruciform holes fabricated with silver instead of aluminium ($b/a = 0.5$), each dot corresponding to one filter. (b) With square arrays of cruciform holes ($b/a = 0.8$). (c) With square arrays of square holes ($b/a = 1$).

Silver-based filters using cross-shaped-hole arrays are not able to match both the ALS performance and the stability requirement. With a constraint $b/a = 0.5$, no design can be found in the specifications range unlike the same structures with aluminum. However, increasing the shape factor drastically improves the filters performances, and results similar to the aluminum structures (for both crosses and squares) are obtained with $b/a = 0.7$. It can be seen that for $b/a = 0.8$, the performances of plasmonic filters reach those of the green resist and IR-cut used as reference. The angular stability conditions of silver-based cross-shaped-hole arrays have to be investigated to see if they behave similarly to the case of aluminum-based filters though. Square apertures provide very efficient ALS filters and would be easier to process than crosses with high shape factors. It may even be assumed that an optimization could potentially lead to a slightly better performance than the 2015 reference (orange dot). Regarding the dimensions of these filters, the closest design to the reference with square holes has a metal thickness of 300 nm, a period of 200 nm and a hole size of 130 nm. These results demonstrate the ability of silver to provide high-performance ALS filters at normal incidence. However, there is a

blocking point regarding the issue of the mass production of such structures since the etching of silver is hard to realize. Indeed, it is generally performed in literature with Focus Ion Beam (FIB) [114] or lift-off techniques [137], and for very thin films. Further improvements on the etching of thick silver films are required before considering an industrial production of silver-based ALS filters.

3. B.2.2 Gold-based filters

Gold is also a metal whose use in clean rooms is severely restricted for contamination issues. Like the silver study, the same computations on the geometrical parameters were made by replacing aluminum with gold in order to evaluate its potential to give efficient ALS filters. The results are shown in Figure 3.20. Similarly to silver, crosses with small shape factors return performances far from the specifications range (more than 4 dB in maximum ALS error). In the gold case however, increasing the shape factor until reaching square apertures does not give interesting ALS filters; the performances, while improved compared to small shape factors, do not meet the specifications of the application at all. This result is explained owing to the optical properties of gold which make it more appropriate for the infrared range than for the visible range [45], [46].

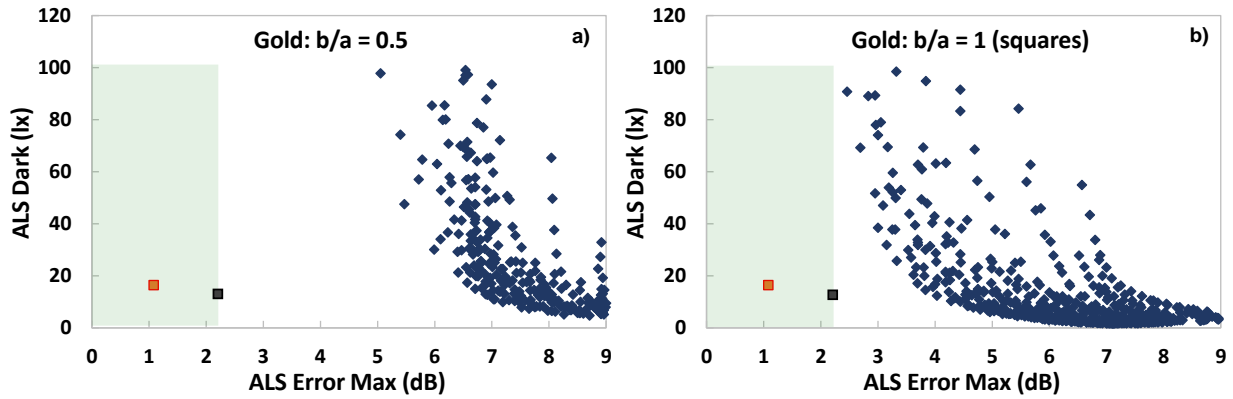


FIG. 3.20. (a) ALS performances for several designs with square arrays of cruciform holes fabricated with gold instead of aluminium ($b/a = 0.5$), each dot corresponding to one filter. (b) With square arrays of square holes ($b/a = 1$).

3. B.3 Conclusion on ALS performances

The work presented in part B shows that plasmonic filters are able to meet the specifications of the ALS specifications and to come close to the ALS error of the combination of a green resist and an IR-cut glass (2012). They can also approach the maximum ALS error value of the 2015 reference, but they present higher ALS dark values between 40 lx and 50 lx. This is expected to be lowered due to a final annealing of the device that plasmonic filters can support unlike organic resists, which will be experimentally verified in *Chapter 5*. Only specific holes shapes such as arrays of square or cruciform holes are able to reach competitive performance, which leads us to assume that localized plasmon resonances play a key role in obtaining a well-defined spectral response fitting with the photopic one. The application requires the filters to have a thick aluminum layer generally superior to 225 nm, which implies a very good rejection around the useful signal, and a period between 250 nm and 300 nm together with a a/P ratio between 0.6 and 0.75. The dispersion of the performance due to the sensitivity to the polar angle, the azimuth, and the polarization are proven to be limited and contained in the specification ranges with small shape factors. The limits of the stability of crosses are however reached

for $\theta = 60^\circ$ where the performance are more or less out of range depending on the filter design. More advanced solutions have been proposed with silver or gold instead of aluminum. Although gold is not appropriate for transmission filters in the visible range, silver is able to provide highly efficient ALS filters comparable to the 2015 reference for square holes or for crosses with a high shape factor ($b/a \geq 0.7$). This implies that silver is a promising alternative to aluminum for filtering although the conditions of stability of crosses may not be fulfilled. The nanostructuration of silver thin films with industrial equipment is also a significant issue for the introduction of this metal in clean rooms.

3. B.4. Conclusion on Chapter 3

The study of the relation between the geometrical parameters of cross-shaped-hole arrays and their optical properties has demonstrated that these structures can be made nearly insensitive to the polarization and incidence angle of light, including the azimuth which has never actually been investigated to our knowledge for hole arrays. The two major parameters that are the shape factor b/a and the intercrosses distance d have to be low to favor the localized plasmon resonance in the transmission process and thus to ensure the non-dependence of the filter response to the illumination conditions. This work provides accurate geometrical criteria to design filters whose stability properties may potentially be used in a wide range of applications, even beyond the visible range if the materials are adequately chosen. In the same time, it also tends to support the theory that localized resonances at the apertures have a predominant role in the transmission process, unlike propagating plasmons which rather negatively affect the optical properties of cross-shaped-hole arrays [144].

In our case, these results could be applied to the ALS applications by using the established geometrical criteria in the design and the evaluation of the filters. Although a trade-off has to be made between high ALS performances and a high angular stability, we have shown that plasmonic structures can fulfill the ALS specifications and that respecting the geometrical rules allows for lower variations of the performance when the incidence and the polarization are changed. Despite this angular robustness, it has appeared however that when the polar angle of incidence gets too large ($\theta = 60^\circ$) the dispersion is wide enough to obtain ALS errors out of the specifications range. Silver-based ALS filters have been proposed as an upstream solution and have shown very good performances to the detriment of the angular stability since only squares or high- b/a crosses are working. Moreover, further developments of the nanostructuration of thick silver films would be required for a robust industrial production of silver-based ALS filters.

Chapter 4

Robustness of plasmonic filters to process variations and Front-End fabs limitations

The work presented in *Chapter 3* has demonstrated that cross-shaped-hole arrays can provide ALS filters with competitive performances and that they can support different illumination conditions with different polarizations and angles of incidence. In addition to their appealing optical properties and performance, such plasmonic structures may also present a financial interest. Their simple structure only consists in a single patterned metallic layer even for multi-colors filtering. It implies a few number of fabrication steps, unlike Fabry-Perot filters which are made of several layers with varying thicknesses requiring different lithographic steps [25], [164]. Cross-shaped-hole arrays also do not require any external infrared filter thanks to their infrared rejection capability, unlike color resists. All these features make these plasmonic filters particularly attractive for industrial fabs. However, the integration of plasmonic structures in industrial products requires a reliable fabrication guaranteeing drastic dispersions specifications. In the visible range though, the holes dimensions are small and fabricating such structures while keeping an accurate shape definition may be challenging, especially working at wafer level, on 300-mm silicon wafers. In practice, the final processed shapes may substantially deviate from the targeted ones due to process limitations at each critical step of the fabrication route. A very recent trend in literature demonstrates a growing interest for the effect of process inaccuracies related to different stages of the fabrication of nanophotonic and plasmonic devices [57], [165]–[167].

In this chapter, we aim to identify the main critical weaknesses of each step of the fabrication of aluminum-based cross-shape-hole arrays and to estimate how they impact the performance of the plasmonic structures. Each section of this chapter corresponds to one fabrication step. We first present the influence of the film thickness and optical index standard deviations. The presence of a native oxide on the metal surface is also simulated. Then, we consider lithography inaccuracies using optical proximity calculations. In particular, the effect of rounded corners on the filter performances is studied. A strategy is presented to obtain the best performances after the lithography step. The influence of sloped profiles of the metal holes due to the etching step is investigated. Finally, we see how the holes filling can affect the responses of the filters by simulating the presence of voids.

For each fabrication step, the impact of the process dispersions is studied both on the spectral response of plasmonic filters in general, and on the variations of ALS performance more specifically. In the first case, the simulated stack corresponds to the standard stack defined in 2. 5 *Conclusion on Chapter 2*, where the aluminum layer is in-between two infinite SiO_2 media. This will lead to a further understanding of the plasmon resonances in such structures and will show how they can be impacted by process variations through the study of the spectral responses. In the ALS case, we use the optimal integration also described in 2. 5 *Conclusion on Chapter 2* where the aluminum filter is embedded in a SiON layer, which lays on a Si_3N_4 layer and an infinite SiO_2 substrate. The effect of the process

variations on the ALS performance of these plasmonic structures is thus directly estimated with the evaluation tool and the interest of the plasmonic solution for ALS can be discussed. In both cases, the process dispersions are simulated on two reference plasmonic filters with cruciform apertures with an intermediate shape factor $b/a = 0.5$. One is taken with a low ALS error max (1 dB) and the other one with a higher ALS error max (2 dB) in order to observe whether their behaviors are comparable. The dimensions of the 1dB reference filter are $h_m = 300$ nm, $P = 275$ nm, $a = 180$ nm and $b = 90$ nm (ALS error = 1.12 dB and ALS dark = 61 lx). The dimensions of the 2dB reference filter are $h_m = 300$ nm, $P = 250$ nm, $a = 200$ nm and $b = 100$ nm (ALS error = 2.14 dB and ALS dark = 19 lx).

This chapter will establish which steps are critical in the reliable fabrication of plasmonic filters and how the process dispersions can be limited to provide an efficient filtering solution, especially for ambient light sensors. The obtained results were published [168] and presented in conferences [163], [169].

4.1 Identification of the process limitations

4.1.1 Simplified process route

One of the advantages of hole-arrays plasmonic filters is their simple structure: a single periodically patterned metallic layer embedded in a dielectric medium. However, the dimensions of the structures can fall below 100 nm for applications in the visible range, which raises some technological issues regarding the nanostructuration of filters. These issues also depend on the materials chosen for the filters realization, especially regarding the metallic layer. One can find several ways to pattern the metal. Below is a non-exhaustive list of solutions.

The most common one would be to first deposit the metallic layer and to pattern it thereafter with a lithography step and an etching step. We will name it the *metal etching* technique. In this case, the main limitations for the development of such filters in a semiconductor fab are the accuracy of the lithography resist patterning, which depends on the CMOS technology node used, and on the ability of the etching technique to selectively and accurately etch the metal with small dimensions (which depends on the chemistry or on the type of plasma used). This technique implies the use of a metal that can be patterned with a dry etching, that is anisotropic and thus better to perform straight hole profiles. Dry etching can be done with aluminum, but not with copper. In the case where the nanostructures have to be filled with a dielectric material, we must also ensure that we can find a deposition technique able to properly fill the apertures.

A second method to obtain a patterned metal layer consists as first step in depositing a thin film dielectric material, then patterning it, filling the gaps with the metal and finally planarizing the metal layer using a Chemical-Mechanical Planarization (CMP) technique. This method is known as the *damascene* process [146]. This technique has two main limitations: the capability of the deposition tool to fill small gaps with the metal thin film and the requirement of a CMP step to remove the undesired metallic layer above the dielectric apertures.

Another method to get patterned metal layers is the nano-imprint process [134], [170], [171]. In this case, a stamp is pressed on the resist to print the patterns and the metallic layer is then etched above the dielectric apertures. This method is similar to the etching technique but requires the fabrication of the stamp beforehand, which is generally patterned with an electron beam. It is more convenient to pattern a lot of nanostructures with a high throughput, but this method is not common in semiconductor fabs.

In the case of the work described here, we are interested in a fabrication method directly transferable to an industrial semiconductor clean room and we thus only consider the first two methods (the etching technique and the damascene one). The metal required for the fabrication of the ALS filters

is aluminum owing to its properties for making filters in the visible range. The damascene process would probably allow for a better control of the holes dimensions since the etching of a dielectric material such as SiO_2 or SiON is very accurate even for small dimensions. However, the filling of the nanostructures with aluminum may be challenging using the deposition tools available either at CEA-LETI or at STMicroelectronics Crolles, which are essentially Physical Vapor Deposition (PVD) tools. According to our previous analysis (see *Chapter 3*), the spacing between two adjacent crosses should be smaller than 100 nm with high aspect-ratios up to 4 depending on the filter requirements. Besides the issue of aluminum holes filling, the CMP step may require an adhesive layer between aluminum and the dielectric material. This layer, that can be a 50-nm-thick Ti/TiN barrier for example [172], [173], would suppress the plasmonic resonances of the filters because these types of metals have poor plasmonic properties according to our simulations and to literature [45], [46].

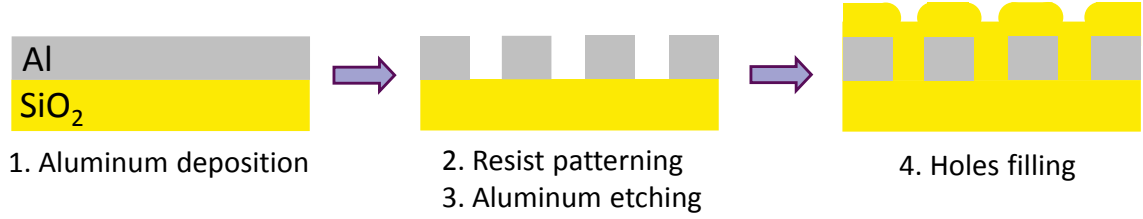


FIG. 4.1. Schematic view of the main steps of the fabrication of aluminum-based hole-array filters with aluminum etching.

Based on the previous considerations, we choose the etching method as the most appropriate way for the fabrication of aluminum-based plasmonic filters. A schematic description of this method is proposed in Figure 4.1. It is composed of the following main process bricks: i) the aluminum thin film deposition, ii) the lithography resist patterning, iii) the aluminum layer etching and iv) the nanostructures filling with dielectric material. By using this process route, the metal thickness is better controlled since there is no CMP step and the nanostructures filling with SiO_2 is achievable with standard deposition techniques such as Plasma-Enhanced Chemical Vapor Deposition (PECVD) or with deposition techniques more suited to high-aspect-ratio nanometric structures, such as Plasma-Enhanced Atomic Layer Deposition (PEALD) or High-Density Plasma Chemical Vapor Deposition (HDPCVD) (see *Chapter 5*).

4. 1.2 Expected hard points

In the previous sub-section, the process route for the fabrication of plasmonic filters with aluminum was selected to be via metallic etching. In order to evaluate the potential blocking points preventing the reliable fabrication of plasmonic filters at wafer scale, we first need to identify the main weaknesses of each process step and then study how they potentially impact the filters performance. The dispersion on the main relevant parameters related to each process step is thus thoroughly investigated. These process dispersions are gathered in Figure 4.2.

Metal and dielectric thin films deposition leads to non-uniformities of the metal thickness and of the dielectric material refractive indices across the substrate's surface, to which the plasmon's wave vector and the transmission of the filters are directly related. The variations of the refractive indices of aluminum are not considered here. Regarding the material stability, a native aluminum oxide is likely to form at the Al – air, Al – SiO_2 or Al – SiON interfaces. The presence of this oxide on the metallic surface will affect the plasmon excitation at the metal-dielectric interfaces. The second issue comes from the patterning of the photoresist and the metallic layer. With the inherent relation between the plasmonic effect and the structures' dimensions, the photolithography is of primary importance in the fabrication of the filters. Given the nanometric scale of the structures, variations of the holes' dimensions and shape

deformations (corners rounding especially for cruciform apertures) need to be taken into consideration and their respective impact have to be quantified. In addition to these potential issues, the etching of aluminum could be not perfectly straight and may thus create holes with sloped profiles which can be problematic given the narrowness of the apertures. This effect has never been studied in the case of image sensors to our knowledge. Finally, the last expected difficulty is the partial filling of the nanostructures with the dielectric material. While the metal-dielectric interface would fit the aperture design requirements, the presence of voids would change the effective refractive index inside the holes and this effect has never yet been studied to our knowledge.

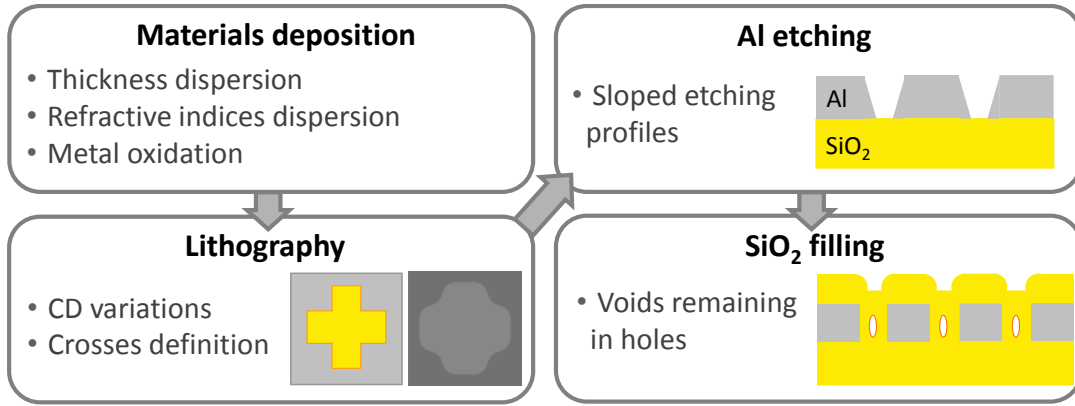


FIG. 4.2. Respective process dispersions expected in the main process bricks for the fabrication of plasmonic filters using the metallic etching method.

The following sections will now comprehensively investigate the impact of all the above-mentioned process dispersions in terms of plasmonic resonances in general and observe how the performance of ALS sensors is influenced. Each section corresponds to one process brick. All charts are drawn from 300 nm to 800 nm, but the ALS performance calculations take into account the signal from 300 nm to 1000 nm, except in the case of the native oxidation of aluminum (our experimental data at CEA Leti on the Al₂O₃ refractive index stop at 800 nm). In each chart, the 2012 and 2015 references are plotted with a black square and an orange square respectively. The green area stands for the ALS specifications range (see *section 2. 2.1*).

4. 2 Materials-related dispersions

4. 2.1 Thicknesses and refractive index dispersions

Thin films deposition steps can induce two kinds of process dispersions at wafer-scale: deviations from the targeted thicknesses and fluctuations of the materials refractive indices, which are of primary importance for the dielectrics surrounding the metallic layer. The wave vector of a surface plasmon is indeed directly related to the refractive index of the media surrounding the metal, as shown in *Eq. (1.4)*. These two effects are taken into account in our study. With the standard stack, we consider here typical process dispersions that can be found in 300-mm CMOS front-end foundries by using the data of the corresponding deposition tools of the clean room of STMicroelectronics Crolles: the standard deviation on the metal thickness σ_{hm} is chosen at 3 % and the standard deviation on the refractive index of silica σ_{RI} is taken at 1.6 % [174].

We observe here the effect of thickness dispersion on the spectral response. In Figure 4.3, the 2dB reference filter is simulated with maximum dispersions of $\pm 3\sigma$ as generally considered in statistical

process controls for the metallic thickness alone (blue curves), for the silica refractive index alone (green curves) and for the combination of the two dispersions (orange curves). These three configurations show the trend of the most extreme cases of the possible combinations of process dispersions on the filters. This representation does not take into account the statistical probability of such combinations of dispersion on a given wafer [174]. The results show that these process variations have a moderate impact on plasmonic filters. Typically, the variations of the metal thickness only induce a change in the transmission efficiency without shifting the resonance. As expected, the decrease (increase) of the dielectric refractive index leads to a blueshift (redshift respectively) of the resonance wavelength, but also to an increase (decrease respectively) of the transmission level (see section 2. 3.3.2 *Impact of the materials properties*). When the two parameters variations are combined, the corresponding spectral responses show that the individual effects of each parameters are simply added: the spectral shifts are the same than those induced by the variations of the refractive index, and the transmission level increase or decrease correspond to the sum of the transmission gain or loss induced by the refractive index dispersion and by the metal thickness dispersion. The same observations are obtained for the 1dB reference filter.

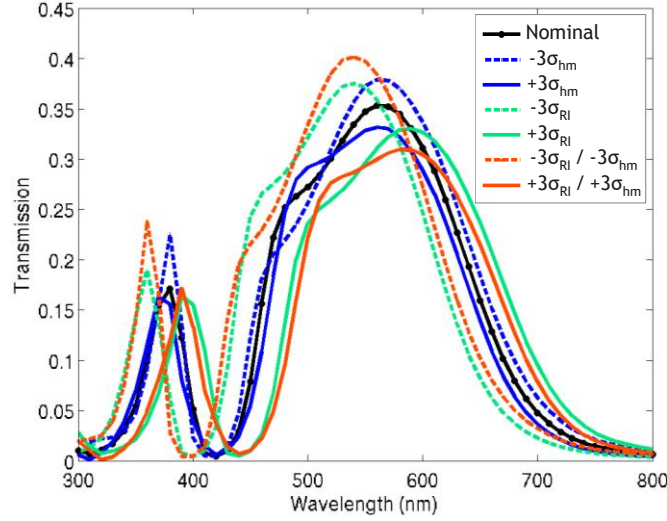


FIG. 4.3. Spectral response variations of the 2dB reference filter with the standard stack induced by process dispersions at $\pm 3\sigma$ for metal thickness with $\sigma_{hm} = 3\%$ (blue), silica refractive index with $\sigma_{RI} = 1.6\%$ (green) and both combined (orange). Filter dimensions are: $P = 250$ nm, $a = 200$ nm, $b = 100$ nm, $h_m = 300$ nm.

The effect of the process deviations on the spectral response of the 2dB reference plasmonic filter ($P = 250$ nm, $a = 200$ nm, $b = 100$ nm, $h_m = 300$ nm) does not provide a direct information regarding their impact on an ALS filter's performance, which are defined in section 2. 2.1. Remember that basically, the ALS error quantifies the deviation of the filter's spectral response relatively to the theoretical photopic response. The ALS dark criterion is related to the sensitivity of the sensor in low-light conditions, which implies that a filter with low transmission leads to a high ALS dark value. We now want to see whether the variations of the films thicknesses and refractive indices are critical in the case of a plasmonic ALS. Based on the ALS integration scheme proposed previously (section 2. 5 *Conclusion on Chapter 2*), we take into account the dispersion on the thickness σ_{diel} and on the refractive index σ_{RI} for the SiON around the filter, the Si_3N_4 and SiO_2 passivation layers, which we consider to be the same for the three materials (gathered as a common dielectric dispersion). The thickness variations σ_{Al} are taken into account for the aluminium layer only since this is the only layer directly related to the plasmonic effect. Based upon internal data and estimations, three levels of process dispersion are considered, with increasing severity in terms of process development:

- level 1: $\sigma_{Al} = 3 \%$, $\sigma_{diel} = 2.7 \%$, $\sigma_{RI} = 1.6 \%$
- level 2: $\sigma_{Al} = 2.25 \%$, $\sigma_{diel} = 2 \%$, $\sigma_{RI} = 0.16 \%$
- level 3: $\sigma_{Al} = 1.5 \%$, $\sigma_{diel} = 1.35 \%$, $\sigma_{RI} = 0.13 \%$

Level 1 corresponds to the process dispersions that are generally obtained in a fab on 300-mm wafers and are the same than those used with the standard stack, whereas level 2 is an estimation of the dispersions that can be reached with a severe optimization of the process conditions. Level 3 represents optimistic dispersions that are most probably unlikely to be achieved in a 300-mm semiconductor fab with standard deposition tools, but that can show what profit could be theoretically gained with ideally low dispersions.

The robustness of the filters is evaluated for the three levels, each one with all possible combinations of thicknesses and refractive index errors in a range of $\pm 3\sigma$ as generally considered in statistical process control. This allows for the simulations of more than 99 % of the potential combinations that can be created with the considered process dispersions. Figure 4.4 shows the ALS performance dispersions obtained with the three levels of dispersion for both the 1dB and the 2dB plasmonic reference filters so that we can compare their respective behavior. We define the maximum amplitude of performance dispersion relative to an ALS criterion as the gap between the most distant dots in a given scatter plot along the corresponding axis of ALS performance charts. Considering the 1dB reference filter, it can be noticed that the performance dispersion is low for the three process dispersion cases and remains within the specifications, especially regarding the ALS error. From process dispersion level 1 to level 3, the ALS dark maximum dispersion is decreased by 15.2 lx and the ALS error maximum dispersion by 0.17 dB.

Regarding the 2dB filter, the dispersion scatter plots have a different shape from the 1dB filter. Whereas the 1dB filter experiences more dispersion on the ALS dark than on the ALS error, the 2dB filter shows low variations for the ALS dark and stronger ones for the ALS error, which is comparable to what has been noticed with interferential filters [174]. From level 1 to level 3, the ALS dark maximum dispersion is decreased by 11.7 lx and the ALS error maximum dispersion is decreased by 1.16 dB.

We attribute this difference of ALS performance dispersion to the fact that nominal filters with a high ALS error have a higher transmission compared with filters with a high constraint on the ALS error (close to 1dB). The dispersion on the metal thickness for high ALS error filters is thus less critical and induces small variations of the ALS dark. On the contrary, their higher transmission efficiency tends to make any resonance shift have a more substantial impact since more useful signal is lost or more unwanted signal is gained depending on the spectral shift of the filter's response.

We thus show that a better control on the standard deviation on materials thickness and optical parameters would be profitable to avoid fluctuations of the transmission efficiency and the resonance wavelength, and therefore to limit the dispersions of the ALS performance. Although high ALS error filters are more sensitive, the impact of the process dispersions are however not critical for the ALS application targeted in this work. This result is mainly due to the low effect of the metal thickness on the transmission efficiency and to the slight resonance shift induced by the variations of the dielectric refractive indices, as show in Figure 4.3. This is an advantage compared to Fabry-Perot filters which are more sensitive to these process dispersions [174].

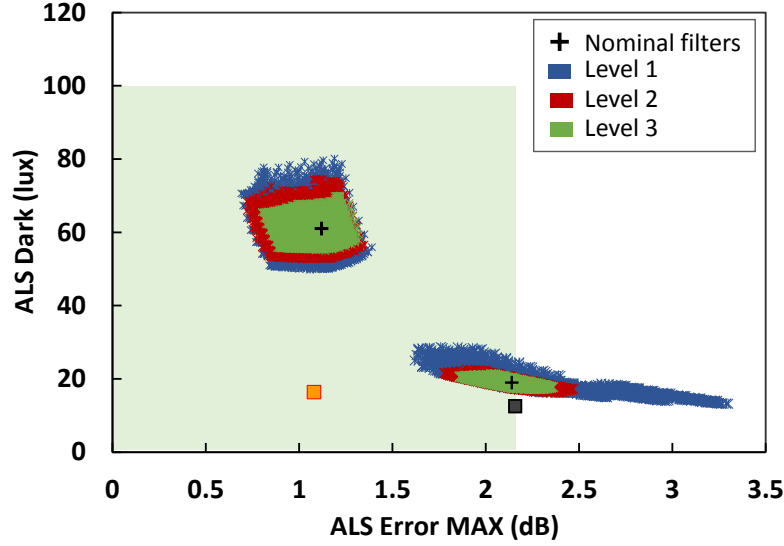


FIG. 4.4. Dispersion of the ALS performances taking into account the thicknesses and the refractive index dispersions shown the 1dB reference plasmonic filter ($h_m = 300$ nm, $P = 275$ nm, $a = 180$ nm and $b = 90$ nm) and for the 2dB reference plasmonic filter ($h_m = 300$ nm, $P = 250$ nm, $a = 200$ nm and $b = 100$ nm), for three gradual levels of dispersions. The 2012 and 2015 references are plotted with a black square and an orange square respectively. The green area stands for the ALS specification ranges.

4.2.2 Metal oxidation

Another effect regarding the material deviations is the potential oxidation of the metallic layer. Several studies regarding plasmonic filters use aluminum as metallic layer [85], [94], [101], [102], [118], but do not take into account a possible oxidation of the aluminum film on its surface. The effect of aluminum oxidation was investigated in Al nanodisks [175] or nanoparticles [176], and only recently in the case of Al hole arrays [177]. Indeed, either a formation of a native oxide passivating Al_2O_3 layer occurs at the Al surface when the metal layer is in contact with air, as for example during chamber changing between two process steps, or a formation of an aluminum oxide when it is in contact with another oxide such as SiO_2 . In both cases, a few-nanometers-thick interfacial layer is formed with a stoichiometry close to Al_2O_3 . The thickness of alumina generally grows up to a maximum of 10 nm under room temperature [177], [178]. In this work, different values of alumina thickness are simulated to observe the evolution of the spectral response first and then observe its influence on the ALS performance.

Theoretically, the stoichiometry of the aluminum oxide is not the same depending on the oxidizing material the metal is in contact with. For modeling simplification, we consider that the oxidation thickness is the same on all sides of aluminum, including the bottom and the top of the Al layer and at the holes sidewalls as well. We also approximate that a 1 nm growth of alumina leads to a 1 nm loss of aluminum, although their lattice parameters are not exactly the same [177]–[180]. The refractive index of Al_2O_3 is taken from CEA in-house measurements on stoichiometric Al_2O_3 ($n = 1.666 + 0.0032i$ at $\lambda = 633$ nm). We now study the impact of this native oxide on the 2dB reference filter with the standard stack. The study of the 1dB filter leads to identical conclusions. The simulation results presented in Figure 4.5 show that the oxidation of aluminum leads to an increase of the transmission efficiency, a substantial widening of the spectrum and also a red-shift of the resonance, the latter being due to the higher refractive index of alumina compared to SiO_2 . There is however a bias in these results: the transmittance increase and the peak broadening may be partly due to the fact that the simulations take into account that the oxidation process removes metallic atomic layers at the metal-dielectric interface, as shown in the filter cross section scheme in Figure 4.5(a). This consideration makes the obtained metallic filter different from the reference design in dimensions, with larger aperture area and thinner metal, thus leading to higher transmission efficiencies.

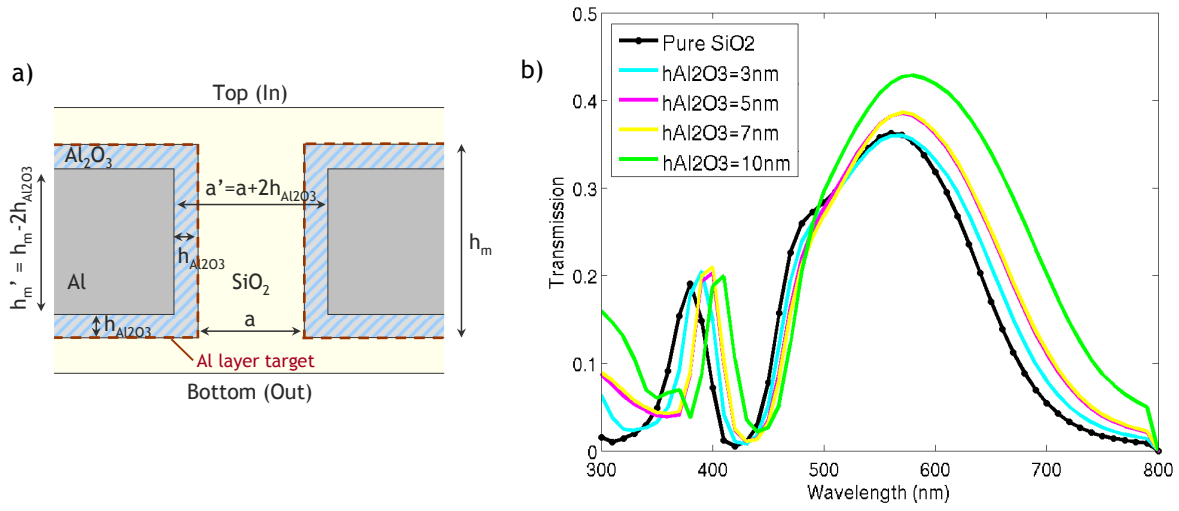


FIG. 4.5. (a) Case of oxidation leading to a reduction of aluminum dimensions. (b) Corresponding spectral response evolution of the 2dB SiO_2 -Al filter with different Al_2O_3 thicknesses around the aluminum layer. Filter dimensions are: $P = 250$ nm, $a = 200$ nm, $b = 100$ nm, $h_m = 300$ nm.

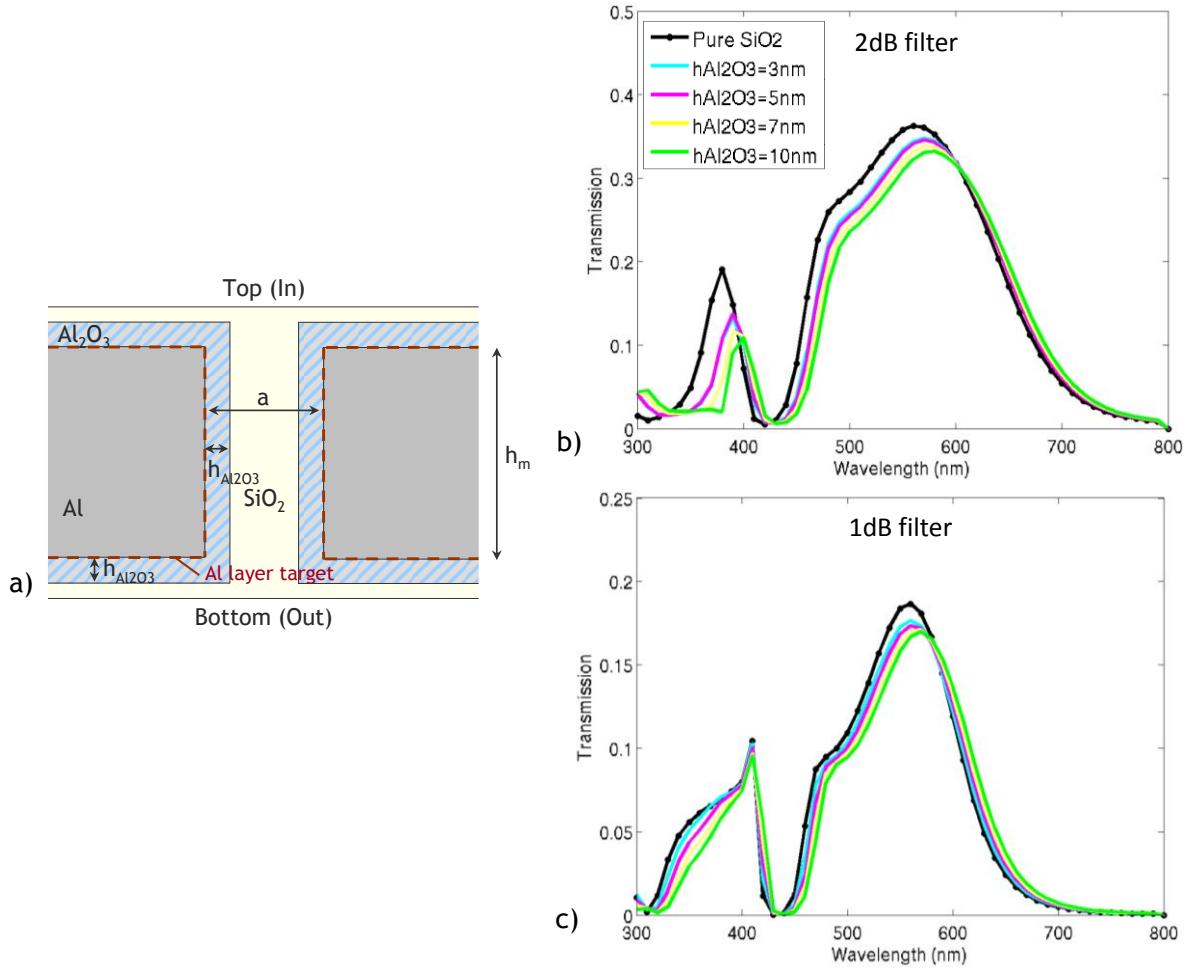


FIG. 4.6. (a) Case of oxidation with no modifications of aluminum dimensions (anticipation of metal dimensions through deposition and mask design). (b) Corresponding spectral response evolution of the 2dB SiO_2 -Al filter with different Al_2O_3 thicknesses around the aluminum layer. 2dB plasmonic filter dimensions are: $P = 250$ nm, $a = 200$ nm, $b = 100$ nm, $h_m = 300$ nm. (c) Corresponding spectral response evolution of the 1dB filter. 1dB plasmonic filter dimensions are: $P = 275$ nm, $a = 180$ nm, $b = 90$ nm, $h_m = 300$ nm.

In order to understand the actual effect of alumina at the aluminum-dielectric interfaces, it is necessary to dissociate from its effect the geometrical changes induced by the oxidation process. This can be easily done in practice by tailoring the aluminum thickness deposition specification and the masks design so that the aluminum shape initially targeted is obtained after oxidation, as shown in Figure 4.6(a). In practice, we would increase the metal thickness and tighten the holes dimensions so that the formation of the native oxide retrofits the filter to its desired dimensions. In these conditions, it can be observed in Figure 4.6(b) that the alumina layer itself does not have a significant impact on the filter spectrum when the holes size and the metal thickness are kept constant. Increasing the oxide thickness nearly does not change the transmission of the filter. A slight red-shift is observed though, since plasmons are interface phenomena related to the refractive index of the dielectric directly in contact with the metal, the alumina having a higher refractive index than silica. This red-shift is consistent with the observations of Schwind *et al.* on the corrosion of aluminum-based nanohole arrays [177].

We have identified the impact of the oxidation of the aluminum layer in terms of plasmonic resonances with the evolution of the spectral response. We have shown that the dimensions variations induced by the aluminum oxidation can be anticipated with deposition and mask tailoring to limit the alteration of the filter response.

As in the previous sub-section, we are now interested in the evaluation of the ALS performance variations induced by the presence of this native oxide. Both the 1dB and the 2dB reference filters are studied by using the ALS stack with the SiON and the passivation layers. We only consider the case where the aluminum oxidation adjusts the filter dimensions to the targeted ones (like in Figure 4.6 but with SiON and the passivation layers). The results are drawn in Figure 4.7.

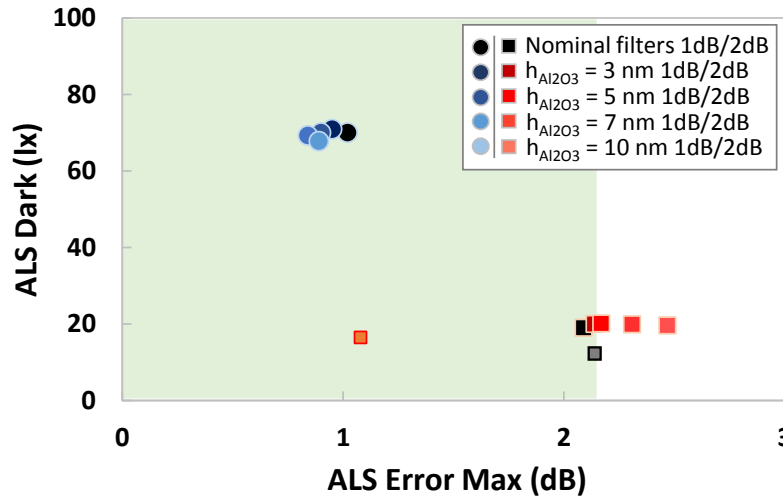


FIG. 4.7. Evolution of the ALS performances when different thicknesses of aluminum native oxide are taken into account for the 1dB reference filter (blue dots) ($h_m = 300$ nm, $P = 275$ nm, $a = 180$ nm and $b = 90$ nm) and for the 2dB reference filter (red dots) ($h_m = 300$ nm, $P = 250$ nm, $a = 200$ nm and $b = 100$ nm). The 2012 and 2015 references are plotted with a grey square and an orange square respectively.

It can immediately be noticed that the two filters are not equivalently impacted by the presence of the aluminum oxide. The 1dB filter undergoes a slight decrease of the ALS error when the alumina thickness is increased, whereas the opposite trend is observed with the 2dB filter, for which the error variations are wider than those of the 1dB filter. We note however that the ALS dark remains almost unchanged for the two filters. These differences may be explained as follows: for the 2dB filter, it can be seen in Figure 4.6 that the presence of alumina not only shifts but also reduces the resonance peak, which implies a loss of the useful signal compared with the photopic response that is used as a reference

in the calculations of the ALS criteria. Moreover, we have shown that a redshift of the resonance drastically impacts the ALS performance (see *Chapter 2*). These variations of the filter response in the NIR region are more significant in the case of the 2dB filter than for the 1dB filter as shown in Figure 4.6(c). We believe that the low transmission of the filters with low ALS error but high ALS dark makes the relative variations of the spectral response induced by the oxidation lower than in the case of filters with higher transmission, therefore explaining the difference in their behavior regarding the ALS performance.

4.3 Lithography inaccuracies

4.3.1 Rounding of the crosses

The step following the metal deposition is the lithography pattern to print the hole shape that will be etched in the metal layer. For a filtering application in the visible range, the dimensions of the holes are approximately between 50nm and 250nm. For such small dimensions with current lithography techniques as 193 nm deep-UV, the internal and external right angles of the crosses are expected to be rounded after the photoresist reveal, and subsequently on the final etched patterns. The rounding of sharp patterns constitutes an issue that progressively raises interest regarding the manufacturing of plasmonic structures [57], [166].

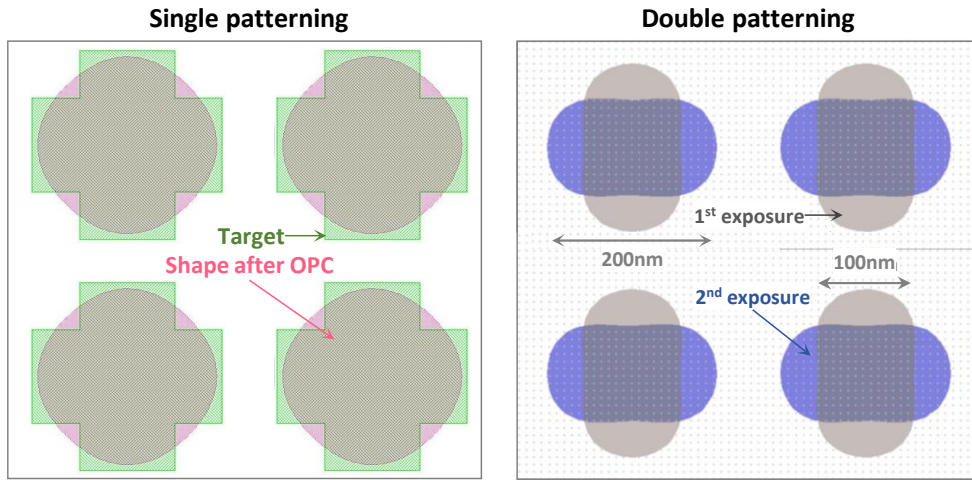


FIG. 4.8. Optical proximity effects calculations for the array of crosses of the 2dB filter. The left scheme shows the difference between the targeted shape (green) and the obtained shape with a single patterning (red). The right scheme show the shape obtained with a double patterning with 193 nm deep-UV lithography and 28nm CMOS technology node, from the same targeted shape. Filter dimensions are: $P = 250$ nm, $a = 200$ nm, $b = 100$ nm, $h_m = 300$ nm.

We have used optical proximity calculations tools to predict the actual shape of cruciform holes after lithography. A few options have been investigated to decrease the deviation from the targeted design based on different lithography strategies with various technological nodes available in industrial clean rooms. Because of the underlying aluminum layer, significant reflections of the electrons are generated, leading to detrimental optical effects for the realization of the patterns. Namely, thin film interferences effects are produced, resulting in standing waves or swing curves [181] that create sinusoidal variations of critical lithographic parameters with the resist thickness, such as the linewidth of the pattern. The use of a Bottom Anti-Reflective Coating (BARC) was thus necessary beneath the

photoresist to avoid these optical issues. In particular, a BARC limits reflections from the metal layer and thus limits or suppresses standing waves effects. Through different Optical Proximity Corrections (OPC) calculations, we found that the strategy using a BARC combined with a double patterning, where the two arms of the crosses are exposed sequentially, constitutes the best solution. For instance, the shape obtained for the 2dB reference filter with a double patterning in 28nm CMOS technology with a 193 nm deep-UV lithography is given in Figure 4.8 (right scheme) and is compared with the single patterning result (Figure 4.8, left scheme).

These results help us to anticipate the main defaults of the actual shape that can be obtained after UV exposure and etching. The effect of rounded corners on cross-holes plasmon resonances had not been investigated yet to our knowledge. We have performed here a dedicated simulation study with crosses rounded with different radii R , in both internal and external angles. The modeling of the corners rounding is described in Figure 4.9. The dielectric area of the RCWA model is decreased in the external angles and is increased in the internal angles according to circles of radius R tangent to the crosses edges. The spectral responses are first examined to conclude on the impact of rounded crosses on the filters properties and then input into the evaluation tool in order to quantify this effect on the ALS performance.

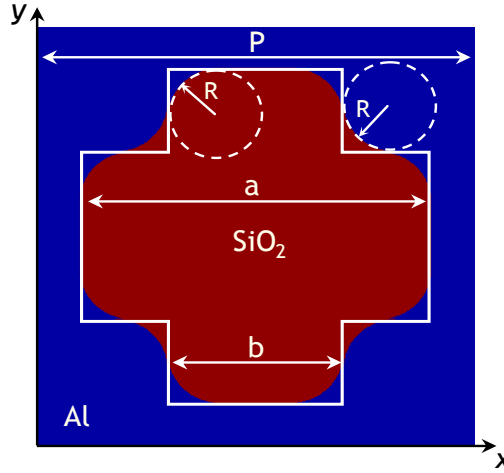


FIG. 4.9. RCWA modeling of the rounding of the internal and external angles of the crosses. The figure only represents the elementary cell of the simulated arrays. The blue area corresponds to the metal and the red one corresponds to the dielectric material inside the hole. The case presented here is for $R = 20$ nm.

The study is conducted for both the 1dB and the 2dB reference filters and the results are presented in Figure 4.10. With the 2dB filter (Figure 4.10(b)), we see that curving the crosses corners alters the optical properties of the filter, especially with a decrease of the transmission efficiency but also with a blueshift of the plasmon resonance. A different behavior is observed with the 1dB filter where the transmission first experiences an increase until $R = 15$ nm, before dropping for higher radii of curvature. The blueshift is still noticed though. We then compare the spectral responses of each filter with an equivalent circular-hole array with the same diameter a than the nominal filters to observe how it compares with rounded crosses. While the spectral responses of the circular holes seem to support the blueshift noticed for highly rounded crosses, it may be tricky to clearly assimilate the properties of the rounded corners to those of the circles since the aperture areas of crosses are not the same and diminishes when the radius of curvature increases, which may also affect spectra and explain the decrease of the transmission.

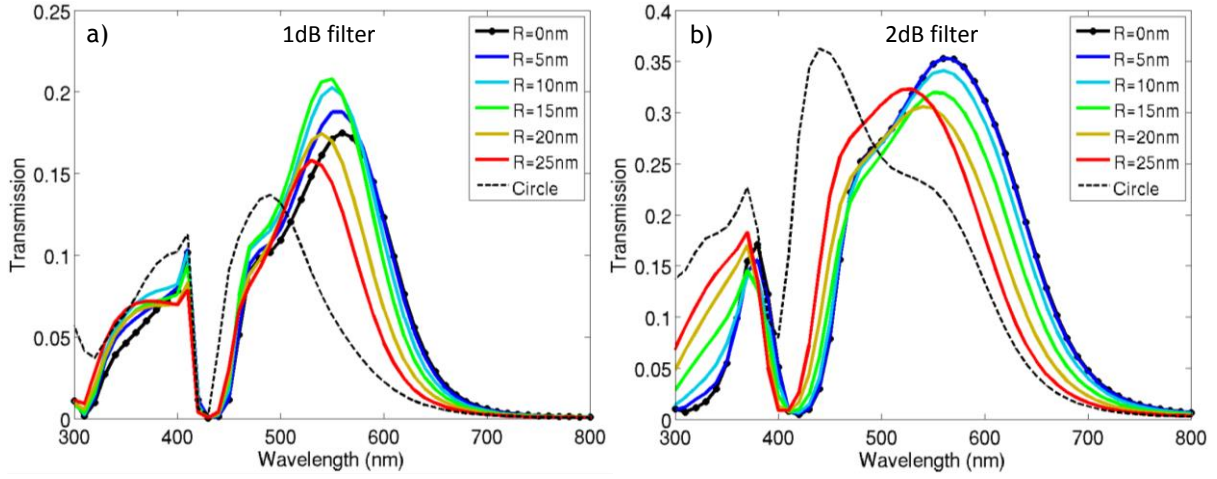


FIG. 4.10. (a) Evolution of the spectral responses of the 1dB filter with increasing corners rounding (increasing radii). Filter dimensions are: $P = 275$ nm, $a = 180$ nm, $b = 90$ nm, $h_m = 300$ nm. (b) Same study for the 2dB filter. Filter dimensions are: $P = 250$ nm, $a = 200$ nm, $b = 100$ nm, $h_m = 300$ nm. In each case, the spectra are compared to an equivalent circular-hole array with diameter a ($a = 180$ nm for the 1dB filter and $a = 200$ nm for the 2dB filter), period P ($P = 275$ nm for the 1dB filter and $P = 250$ nm for the 2dB filter) and metal thickness $h_m = 300$ nm.

In order to dissociate the effect of the aperture area variation from the roundness effect, simulations are made with adaptive crosses dimensions to compensate for the loss of aperture induced by rounded corners, so that the aperture area is the same whatever the R value (keeping the b/a ratio constant). For both filters, the results are very similar to previous ones, with slightly less transmittance losses as shown in Figure 4.11. This means that the loss of transmission efficiency is not exclusively attributable to the decrease of aperture area. When comparing the evolution of these two filters with a circular-hole array of equivalent aperture area (circles diameters of 175.9 nm for the 1dB filter and of 195.5 nm for the 2dB filter), it can however be confirmed that the blue-shift and part of the decrease of transmittance are due to the progressive loss of crosses' specific resonance properties, coming close to those of circular holes when R increases. This may also explain why the transmission is slightly increased above $R = 20$ nm: the resonance mode of the crosses is changed to the circular-hole resonance mode.

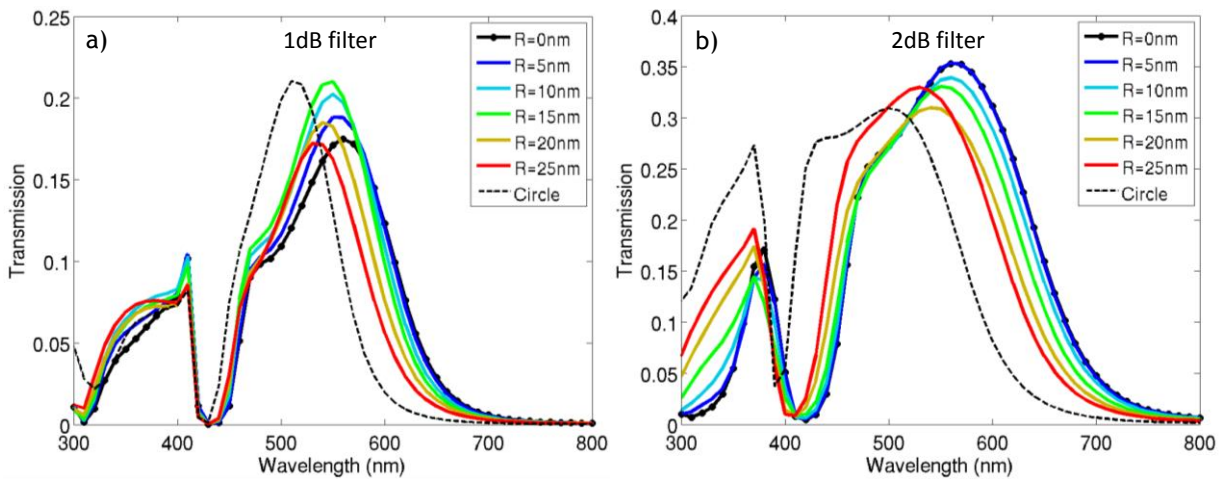


FIG. 4.11. (a) Evolution of the spectral responses of the 1dB filter with increasing corners rounding, keeping constant the cross aperture area. Filter dimensions are: $P = 275$ nm, $a = (180$ nm, 180.08 nm, 180.32 nm, 180.71 nm, 181.27 nm and 181.98 nm), $b = 0.5 \cdot a$, $h_m = 300$ nm. (b) Same evolution for the 2dB filter. Filter dimensions are: $P = 250$ nm, $a = (180$ nm, 200.07 nm, 200.29 nm, 200.64 nm, 201.14 nm and 201.78 nm), $b = 0.5 \cdot a$, $h_m = 300$ nm. For each filter, the spectra are compared with a circular-hole array with equivalent aperture area (diameter 175.9 nm in the 1dB case and diameter 195.5 nm in the 2dB case).

To further explore the impact of rounded corners on the plasmonic effect of crosses, we have separated the effect of the internal angles from the effect of the external angles. We thus simulated the 2dB filter in two different cases: one with rounded external angles and right internal angles, and another with the opposite situation. We present these results in Figure 4.12. In the first case (rounded external angles, see Figure 4.12(a)), we can see a notable decrease of transmission and no resonance shift except for the case $R = 25$ nm, where a very slight blueshift is observed. On the other hand, the case where only internal angles are rounded shows opposite effects (Figure 4.12(b)). Indeed, the transmission is increased by a smaller amount but a more significant blueshift is noticed even for small radii. The blueshift being more pronounced in the latter case than in the former one, it can be assumed that the internal angles of the crosses are predominant to obtain the specific resonance mode of crosses. This is in good agreement with the electric field maps calculated in 3. A.1.3 *Shape factor b/a* where the field is shown to be highly localized in the internal corners. On the contrary, we can deduce from these results that the transmission decrease is more related to the loss of aperture area in the external angles (the aperture area in the external angles decreases twice faster as a function of the rounding than it increases in the internal rounding). We calculate the spectral response of the 2dB filter obtained with the average over the spectral responses of the external case and the internal case in Figure 4.12(c). The trend is similar to what is obtained with direct simulations of the “all-rounded” crosses shown in Figure 4.10, with a decrease in transmission and a blueshift when R is increased. These effects are however less pronounced in the averaged case than in the global one.

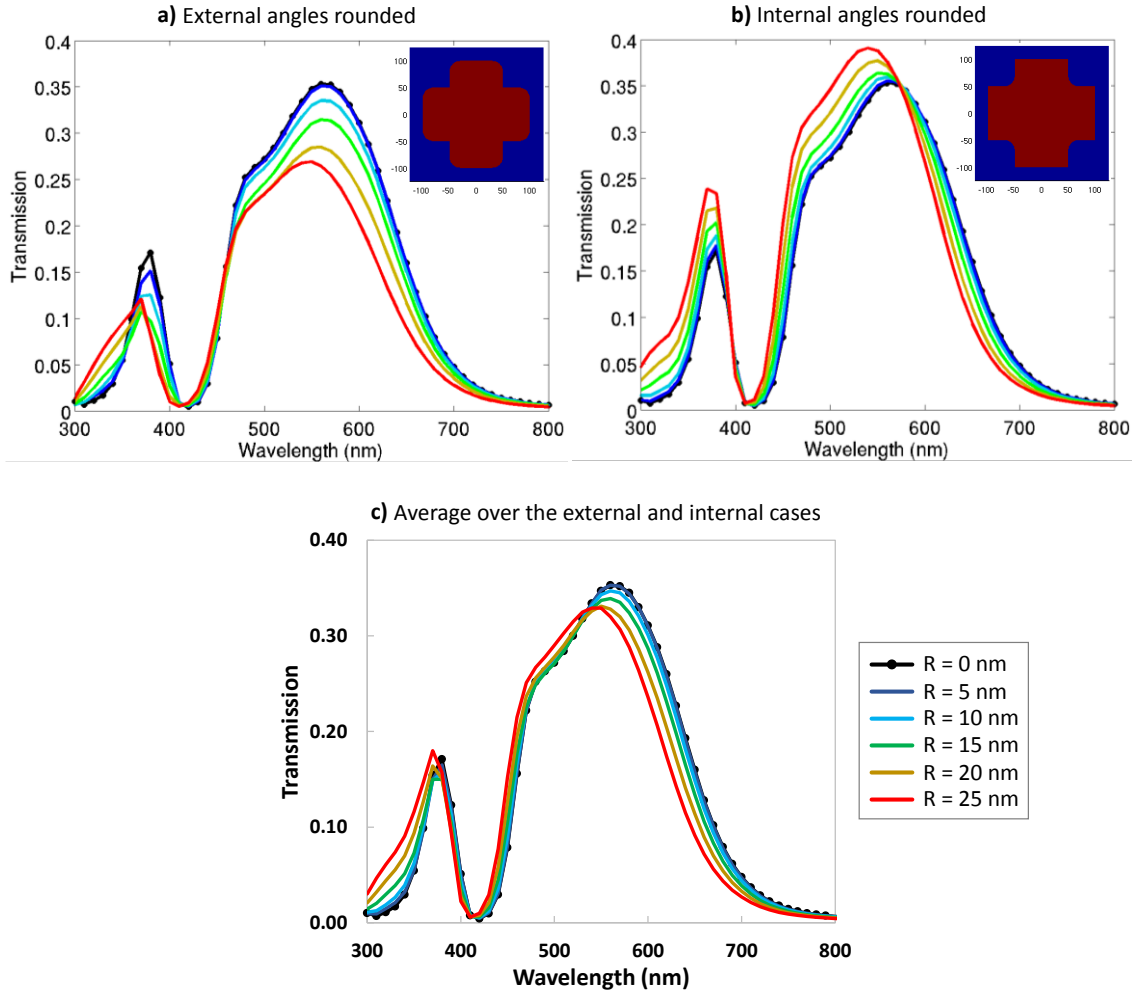


FIG. 4.12. (a) Evolution of the spectral responses of the 2dB filter with increasing corners rounding in the external angles only. (b) In the internal angles only. (c) Calculated average spectral responses of the two former cases, which give similar results to the simulated case in Figure 4.10(b). Filter dimensions are: $P = 250$ nm, $a = 200$ nm, $b = 100$ nm, $h_m = 300$ nm.

We now want to see how these changes in the optical properties of the filters would affect their performance in the case of the ALS application. We still consider the two reference filters but we now use the ALS stack with the SiON and the passivation layers. In addition to the simple purpose of quantifying the dispersion of the ALS performance with corners rounding, we propose to perform these calculations for three cases to improve our understanding of the rounding impact: i) with rounded external corners only, ii) with rounded internal angles only and iii) with all angles rounded. Note that in the latter case, we simulate the filters with all crosses rounded at the same time and we do not use an average response of the two previous cases. The results are given in Figure 4.13.

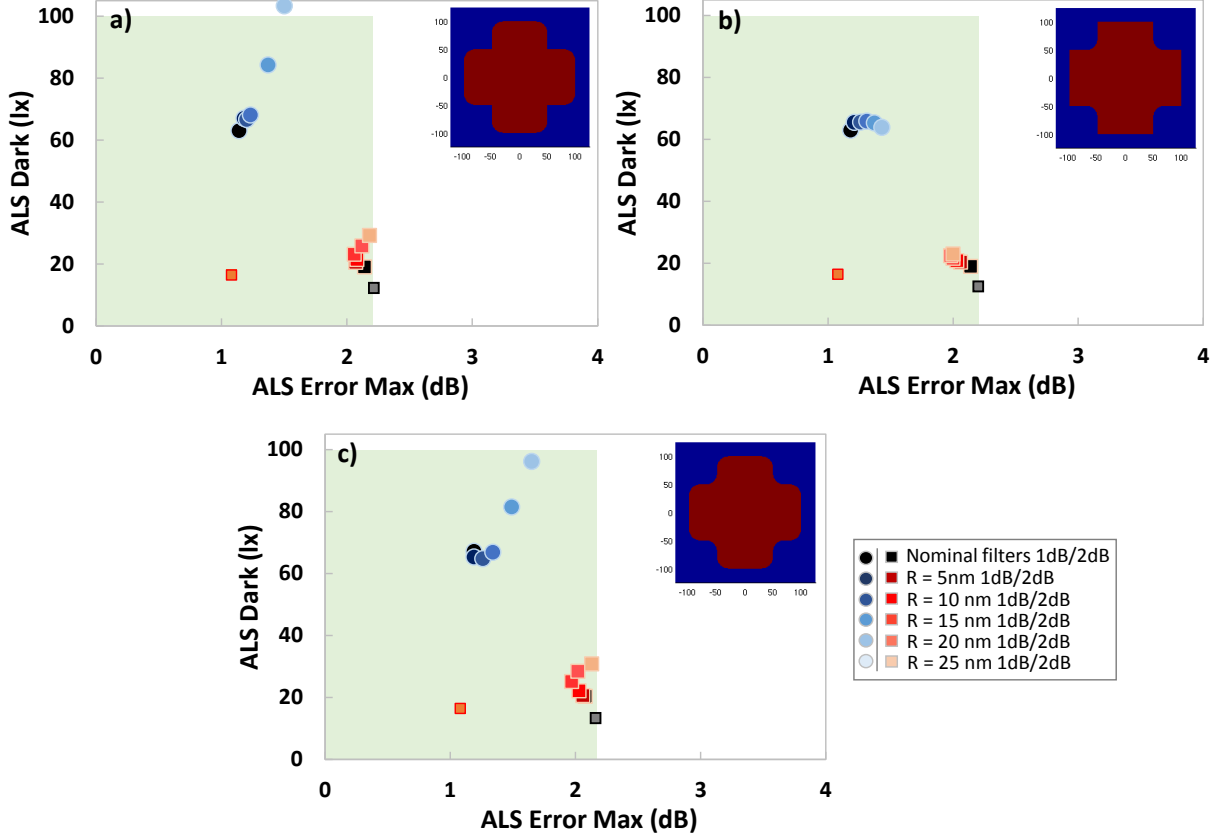


FIG. 4.13. (a) Evolution of the ALS criteria of the two reference filters with increasing corners rounding in the external angles only. (b) In the internal angles only. (c) With all angles rounded simulated. The 1dB filter dimensions are: $P = 275$ nm, $a = 180$ nm, $b = 90$ nm, $h_m = 300$ nm. The 2dB filter dimensions are: $P = 250$ nm, $a = 200$ nm, $b = 100$ nm, $h_m = 300$ nm. The insets represents the different rounding configurations with $R = 20$ nm. The 2012 and 2015 references are plotted with a grey square and an orange square respectively.

In the external case (Figure 4.13(a)), we see that for both filters, the corners rounding mainly impact the ALS dark rather than the ALS error, with a more significant ALS dark increase for the 1dB filter than for the 2dB filter. This proves that the external angles are more related to the transmission efficiency of the filters than to their resonance wavelength. Conversely, the rounding of the internal angles induces very low ALS dark variations with slight ALS error variations (Figure 4.13(b)). These results are consistent with the observations made on the spectral responses in both cases. When all the corners are rounded (Figure 4.13(c)), the trend is similar to the external case with a sensitive increase of the ALS dark, but also with a higher dispersion on the ALS error, most likely related to the effect of the internal corners rounding. One can also notice that when R tends towards higher values, we are likely to find similar ALS performances than those obtained with circular holes, described in 3. *B.1.3 Other potential ALS structures*. This study reveals that in the case of ALS filters, it is more important to limit

the rounding of the external corners so that the related transmission decrease and the corresponding ALS dark increase are avoided, especially for low ALS error filters. The impact of the rounding of the internal corners is not critical (Figure 4.13(b)) since it only induces a low ALS error variation (< 0.35 dB). It is worth noting that all the performance variations remain low when $R < 15$ nm. Such rounding effects may be limited in the external corners with proximity effect corrections (PEC) and in the internal corners with double patterning.

4.3.2 Impact of rounded corners on angular stability

The results described in the previous sub-section show that rounding the corners of cruciform apertures may alter the specific resonance modes of the perfect cross shape. More precisely, the blueshift observed in Figure 4.12(b) and the electric field localization calculated in *Chapter 3* suggest that the internal angles are determinant to get the specific properties of crosses. These findings thus question an essential property of cross required for an ALS application that we investigated in *Chapter 3*: the angular and the polarization stability of crosses with small shape factors. We have shown that arrays of crosses with a ratio $b/a \leq 0.5$ are nearly insensitive to the illumination conditions and can sustain polar incidence angles θ up to 60° . We now want to see if these properties are impacted by the rounding of the crosses' corners.

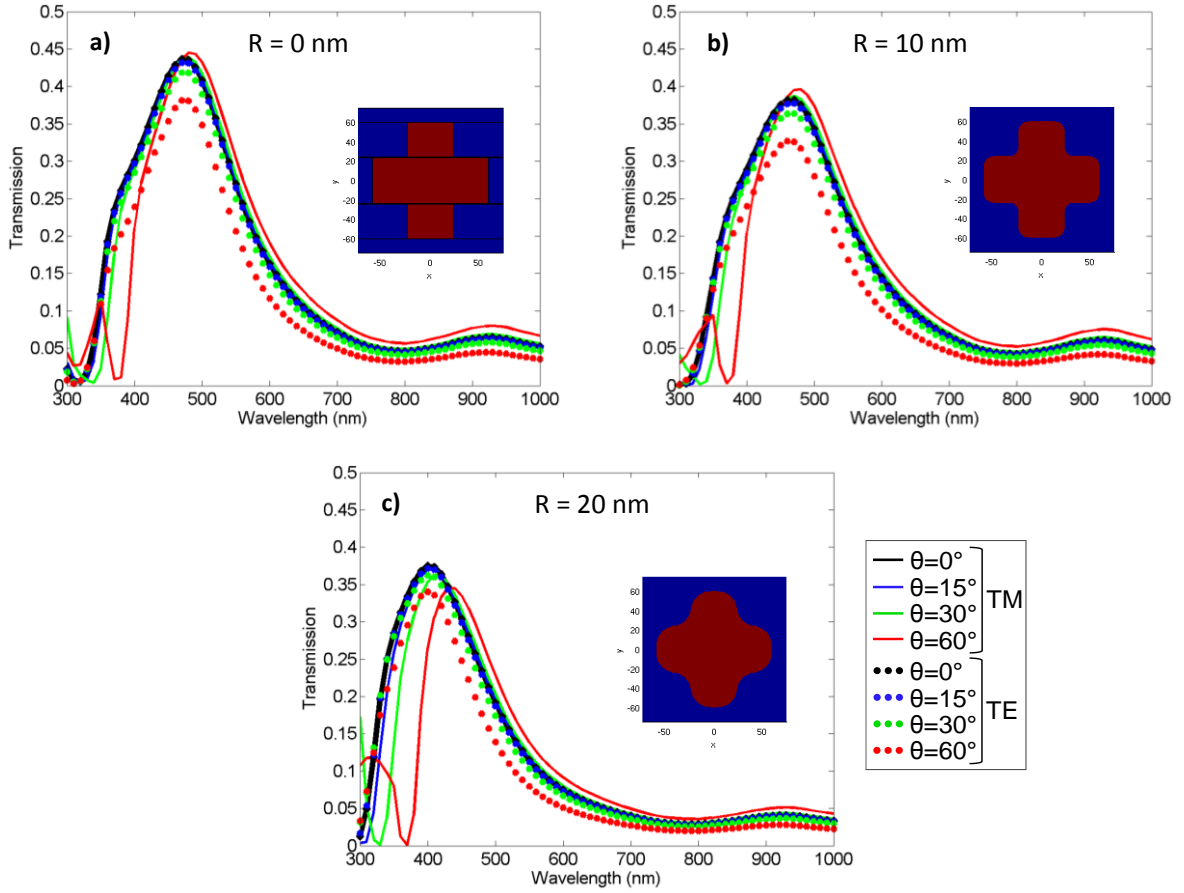


FIG. 4.14. (a) Evolution of the spectral response of a reference filter for angular stability simulated with different polar angles of incidence θ and for the TM and the TE polarization, with $R = 0$ nm. (b) With $R = 10$ nm. (c) With $R = 20$ nm. The filter's dimensions are: $h_m = 75$ nm, $P = 150$ nm, $a = 120$ nm and $b = 48$ nm ($b/a = 0.4$).

We consider the reference filter of *Chapter 3* with a shape factor $b/a = 0.4$ and with the following dimensions: $h_m = 75$ nm, $P = 150$ nm, $a = 120$ nm and $b = 48$ nm. This particular filter has been demonstrated to give nearly identical spectral responses for $\theta \leq 60^\circ$ and for both the TM and the TE polarization states. We thus simulate the filter with the same conditions with corners rounding of radii of curvature $R = 10$ nm and $R = 20$ nm and the results are compared with the nominal filter with $R = 0$ nm (Figure 4.14). As we can see, the gradual decrease of the transmission and the blueshift observed with the corners rounding in the previous sub-section are still present. Regarding our primary concern, no obvious deterioration of the angular and the polarization stabilities can be seen when crosses are progressively rounded, even for wide angles. Very slight redshifts can be noticed for the TM polarization at $\theta = 30^\circ$ (10 nm shift) and at $\theta = 60^\circ$ (30 nm shift) when $R = 20$ nm, but the filter remains widely robust to the illuminations conditions. The rounding of the crosses' angles is thus not critical for the angular properties of cross arrays.

4.3.3 Variations of the apertures dimensions

Another determinant step in view of the manufacturing of the plasmonic filter is the formation of the cross-shaped patterns in the metallic layer. Variations of the crosses size are also expected due to the process dispersions of the lithographic and etching steps, especially given the small dimensions of the holes. The impact of the errors on dimensions has to be carefully estimated since the wavelength filtered with a plasmonic effect is directly linked to the shape and to the characteristic dimensions of the structure. We only study this effect on the ALS performance with the ALS stack as the effect of the variations of the holes size on the spectral responses has already been investigated in *Chapter 3*. As in sub-section 4.2.1 *Thicknesses and refractive index dispersions*, we use a statistical approach to evaluate the impact of the variations of the crosses size. Typical wafer-scale dispersions on the dimensions of 100-nm-large patterns using a 193nm UV lithography in 28nm CMOS technology are approximately between 3 % and 4 %. Four levels of size dispersion are considered in this sub-section, each one with a maximal process dispersion of 0 %, + 2.5 %, + 5 % and + 10 % respectively on the arm length a and the arm width b . We decide to make a and b vary with the same dispersion at the same time. Only cross size increases are studied because the dimensions of the holes are small and hard to reach, thus it is more likely to be in an overetch situation rather than in a shrinkage of the targeted designs. Note that for each level of dispersion, the standard dispersions on the thickness and the refractive index calculated in 4.2.1 *Thicknesses and refractive index dispersions* (level 1) are also taken into account. For example in Figure 4.15, all the dots of the green scatter plot corresponds to the blue scatter plot of Figure 4.4 where filters have been simulated with an increase of 2.5 % for a and b .

The dispersions of ALS performance for the two reference filters are represented in Figure 4.15 for the four size cases. One can immediately notice that the dispersion on the crosses size has a more drastic impact on the ALS performance of the filter, even for the less pessimistic case (+ 2.5 %), than the materials dispersion. This result is due to the fact that the resonance properties of a plasmonic structure are directly related to its dimensions and are modified even for low variations due to their nanometric scale. Similarly to what is observed with the materials dispersion, the 1dB and 2dB reference filters show a distinct behavior. The dispersion on the holes dimensions mainly impacts the ALS dark for the 1dB filter, whereas it mainly affects the ALS error for the 2dB filter. In the 1dB case, the maximum amplitudes in performance due to overetches up to 10 % are 1.16 dB in ALS error and 35 lx in ALS dark. Conversely for the 2dB filter, the maximum amplitudes are 3.3 dB in ALS error and 20 lx in ALS dark. This distinct behavior is explained by their different transmission efficiencies. The 1dB filter has a low transmission ensuring a strong rejection out of the useful wavelength range. When the holes dimensions are increased, the rejection outside of the resonance remains strong despite the transmission increase (which leads to a decrease of the ALS dark), and the consequent resonance shift is not sufficient to capture unwanted signal (such as in the NIR region), thus leading to low ALS error variations. On the

contrary, the 2dB filter has a higher transmission and a wider resonance peak. When the holes size is increased, it is more likely to capture unwanted signal and to deteriorate the ALS error. The transmission increase is proportionally lower than that of the 1dB filter, and the ALS dark thereby experiences less variations. In both cases, the results show that the control of the holes dimensions is of primary importance to consider the mass production of plasmonic filters, especially in the case of light sensors applications.

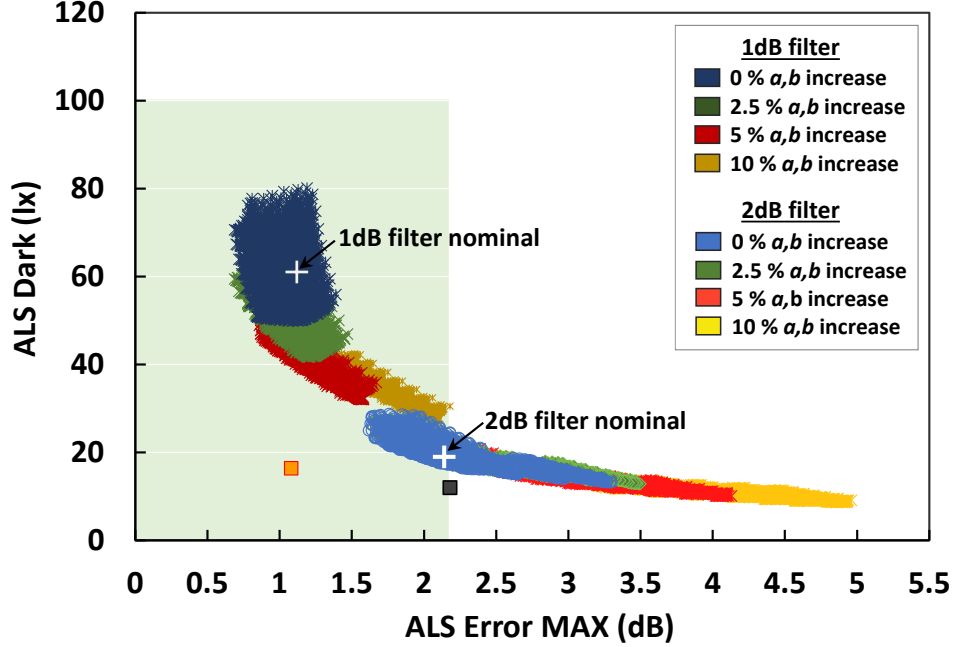


FIG. 4.15. Evolution of the ALS performances when the dispersions on the crosses dimensions are taken into account for the 1dB reference filter ($h_m = 300$ nm, $P = 275$ nm, $a = 180$ nm and $b = 90$ nm) and for the 2dB reference filter ($h_m = 300$ nm, $P = 250$ nm, $a = 200$ nm and $b = 100$ nm), for four gradual levels of dispersions. For each level, the standard dispersions on the thickness and the refractive index are also calculated (level 1 in *sub-section 4. 2.1*). The 2012 and 2015 references are plotted with a grey square and an orange square respectively.

4. 4 Filter nanostructuration

4. 4.1 RCWA modeling of etching slopes

Once the lithography step is performed, the metal has to be etched to create periodic patterns. A sloped profile of the holes may be formed at the aluminum etching step, which can be detrimental to the optical properties of the device given the small dimensions and thicknesses of the filters. Similarly to corners rounding, a few studies have recently started to take into account the possible sloped profile of the plasmonic structures they consider [57], [166], [167]. We have simulated the 2dB reference filter, which is designed with a 300nm-thick Al layer, with different slopes to evaluate the effect of slanted hole profiles on the filter spectral response. The slopes are modelled with RCWA, using a decomposition of the metallic layer into N elementary layers of equal thickness h_m/N to create steps reproducing the sloped profile. All the following results are obtained with 25 elementary layers, which give similar results to finer modeling. The slope is defined by the angle α relatively to the vertical direction ($\alpha = 0^\circ$ corresponding to a perfect etching), as shown in Figure 4.16.

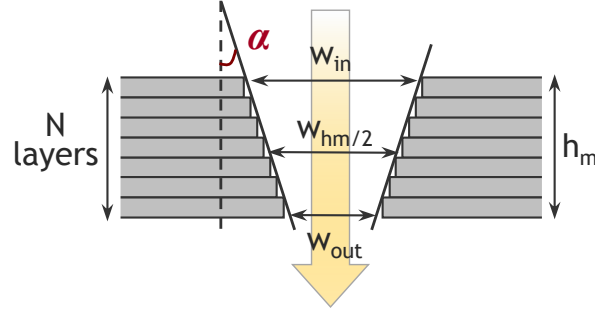


FIG. 4.16. Modeling of sloped etching profiles with N steps in an aluminum filter. The angle α defines the slope of the slanted profile with respect to perfectly straight sidewalls.

4.4.2 Impact of sloped profiles

Non-perfect etching of holes can lead to two different hole apertures. Either the bottom of the hole is completely open leading to over-etching at the top of the hole: this will be referred as the $w_{out} = a$ (bottom) case. Or in case of stop etch due to polymerization during etching, the bottom of the hole is not completely open. This will be referred as the $w_{in} = a$ (top) case. The plasmons resonances may differ for $w_{in} = a$ (top) or $w_{out} = a$ (bottom) in the case of cross-shaped-hole arrays. We propose to study both situations to understand the impact of slopes on plasmons in the case of the 2dB reference filter with the standard infinite SiO_2 stack. Different slopes from 0° to 7.5° are simulated and the results are given in Figure 4.17.

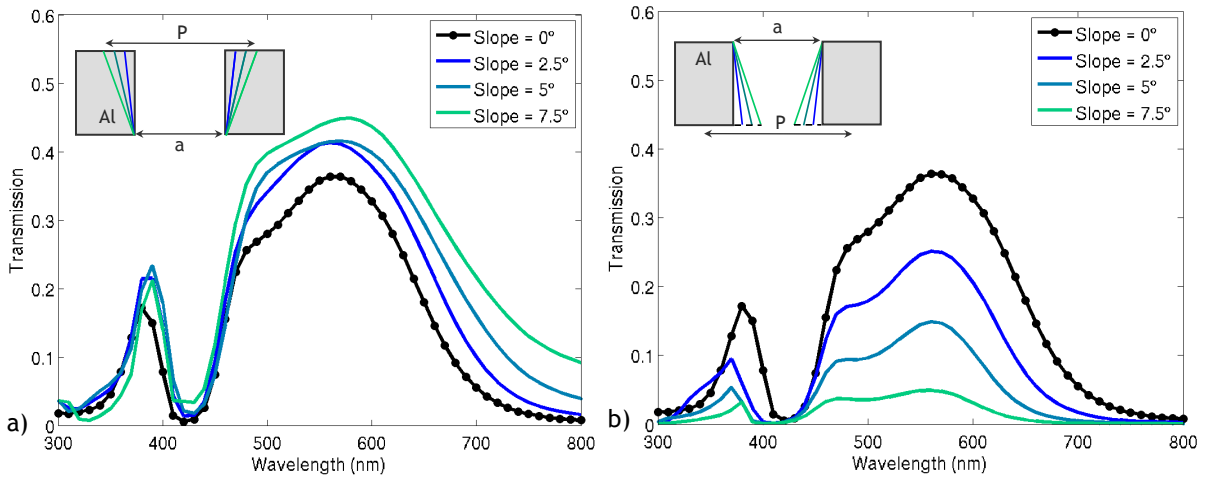


FIG. 4.17. (a) Evolution of the spectral response simulated with etching slopes of 0° , 2.5° , 5° and 7.5° in the case where a is fixed at the bottom of the 2dB filter with the Al- SiO_2 stack. (b) Same graph in the case where a is fixed at the top of the filter. The filter dimensions are: $P = 250$ nm, $a = 200$ nm, $b = 100$ nm, $h_m = 300$ nm.

It can be observed in Figure 4.17(a) that the transmission efficiency increases and the spectra broaden with increasing slopes, when the exit section is fixed. This highlights a kind of "funnel" effect where the widening of the hole induces a higher collection of light in the aperture, leading to a stronger confinement of the electromagnetic field at the exit of the filter. These results are in good agreement with the work of Shen and Maes on tapered metallic gratings [182]. Mahros and Tharwart also showed a slight redshift when the slope is increased [167], but their simulations used slope values twice higher (14°) than in our work, which may explain why it does not clearly appear in Figure 4.17(a). Note that for a 7.5° slope, the arm length of the crosses on the top of the filter exceeds the period value by a few

nanometers. In practice, fixing the exit section can be realized with proper anticipation on masks design and with a good knowledge of the etching chemistry or of the plasma used. On the other hand, the spectra on Figure 4.17(b) show that in the case where the entrance section is fixed, sloped profiles lead to a dramatic loss of transmission efficiency. This can be simply explained by the fact that increasing the slope progressively obstructs the holes in this case, the complete obstruction occurring at about $\alpha = 9.5^\circ$ in Figure 4.17.

In order to evaluate which of these two effects is prevalent on the filter response, we study a third situation where both the entrance and the exit sections vary with the slope (Figure 4.18), and the nominal width is set at the middle of the metallic layer so that $w_{hm/2} = a$. As it can be seen, the two effects partially compensate, but the trend is nevertheless rather a decrease of the transmission efficiency with the slope increase. This proves that the impact of the minimal section is predominant in the response of the filter. It is therefore more interesting to adjust the lithography masks so that the targeted dimensions are satisfied at the bottom of the filter. Note that the effect of sloped profiles would be significantly limited for thinner filters, but thin filters would have a worse rejection than thicker ones.

As an additional reading on this aspect, we can mention that Mahros and Tharwat proposed the study of the effect of exponential tapered profiles, which constitutes an interesting complement to our work [167]. They demonstrate for example a blue-shift (red-shift) of the resonance when the profile of the aperture gets more concave (convex).

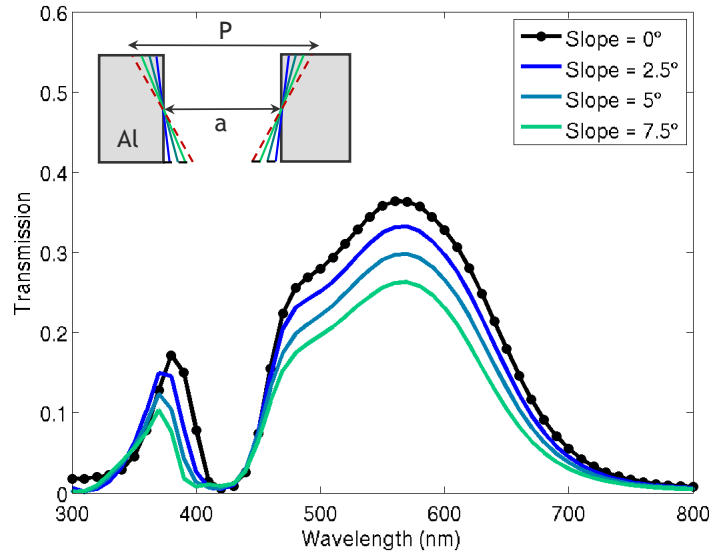


FIG. 4.18. Evolution of the spectral response simulated with slopes of 0° , 2.5° , 5° and 7.5° in the case where a is fixed at the middle of the metallic layer $w_{hm/2}$ with the 2dB reference filter with the standard stack. The filter dimensions are: $P = 250$ nm, $a = 200$ nm, $b = 100$ nm, $h_m = 300$ nm.

We now consider the three previous configurations with a targeted dimension respected either at the bottom, middle or top of the hole in the case of the ALS application. We simulate the 1dB and 2dB reference filters using the ALS stack and we evaluate the evolution of the performance when $w_{out} = a$ (Figure 4.19(a)), when $w_{in} = a$ (Figure 4.19(b)) and when $w_{hm/2} = a$ (Figure 4.19(c)). At first, it can immediately be noticed that the behavior of the 1dB and 2dB filters are similar in all the configurations, although the 1dB filter experiences larger ALS dark variation due to its lower transmission. In the case $w_{out} = a$, increasing the slopes decreases the ALS dark, but also leads to a drastic increase of the ALS error. As a consequence, while the 1dB filter remains in the specification ranges for $\alpha \leq 5^\circ$, its performances significantly deviate from the nominal filter with both a 26 lx decrease in ALS dark and a 0.25 dB increase in ALS error for $\alpha = 2.5^\circ$, and with a 39 lx decrease in ALS dark and a 0.75 dB increase in ALS error for $\alpha = 5^\circ$. These results can directly be related to the observations made in Figure

4.17(a): although the funneling effect provides higher transmissions, it also deteriorates the rejection of the filters that thus receive signal in the NIR region, which explains the quick deterioration of the ALS error. This funneling effect being harmful for the filters' performances, it can be concluded that reaching the targeted dimensions at the exit of the filters is not a good strategy for the fabrication of ALS filters. In the second case ($w_{in} = a$), it appears clearly that even low slopes are sufficient to make the ALS dark skyrocket when the apertures dimensions are fixed at the top of the filters. Despite the beneficial decrease of the ALS error, this configuration is not appropriate due to the huge losses of transmission induced by the obstruction of the holes. Finally, the case where $w_{hm/2} = a$ gives the most promising results. Indeed, for the two reference filters, the variations when the slopes are increased are very low for the ALS error and moderate for the ALS dark. For the 1dB filter, a slope up to 5° leads to an ALS error increase inferior to 0.08 dB with a 16 lx ALS dark increase. The 2dB filter is even more robust with only a 0.09 dB decrease in ALS error and a 10 lx ALS dark increase for a slope up to 7.5° . This is consistent with the variations of the spectral responses plotted in Figure 4.18 where only low reductions of the transmission are observed. We thus show that reaching the targeted apertures dimensions at the middle of the metal thickness is the best strategy to limit the impact of sloped etching profiles, which can be done with a proper knowledge of the etching method and with an anticipation of the dimensions directly on the masks.

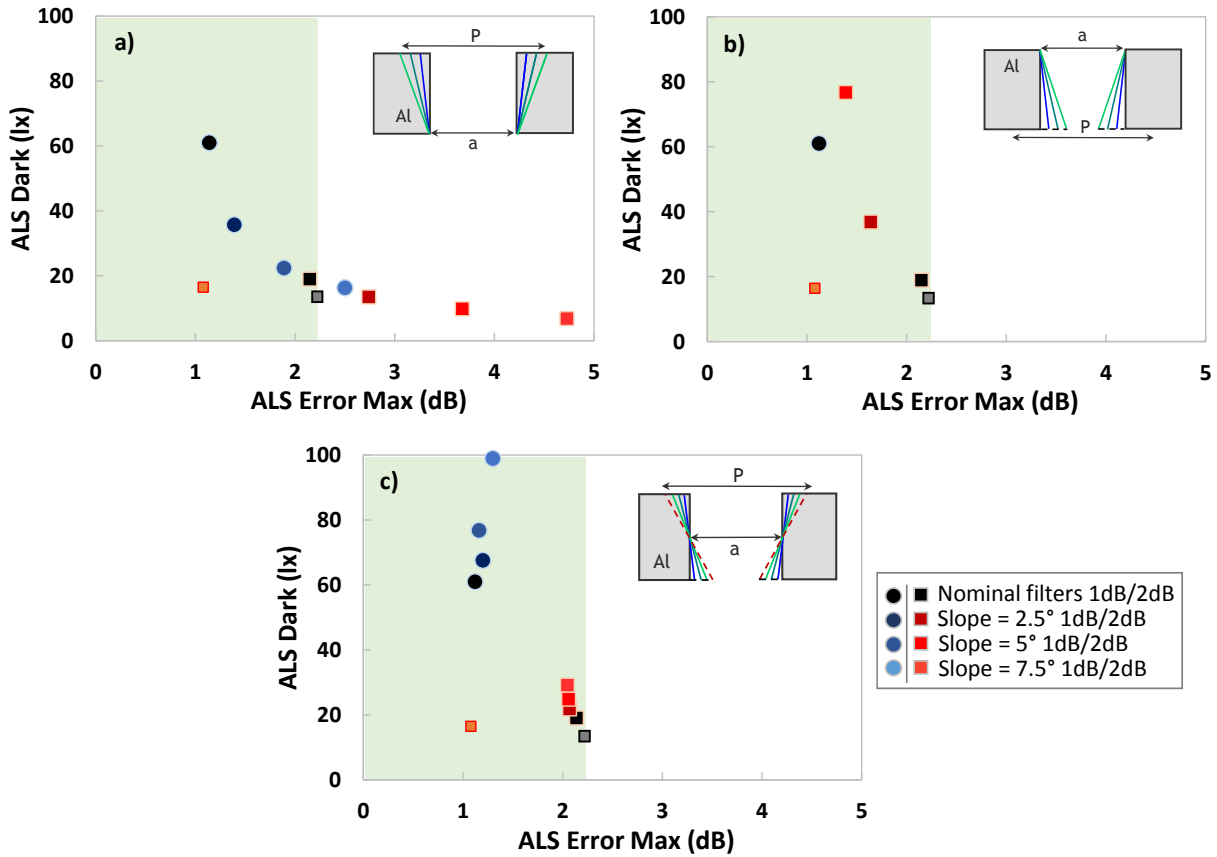


FIG. 4.19. (a) Evolution of the ALS criteria of the two reference filters with increasing etching slopes in the case $w_{out} = a$. (b) In the case $w_{in} = a$. For the 1dB filter, the performances corresponding to the slopes 2.5° (ALS error = 1.03 dB, ALS dark = 136 lx), 5° (ALS error = 1.16 dB, ALS dark = 356 lx) and 7.5° (ALS error = 1.04 dB, ALS dark = 1869 lx) are not shown on the chart because of scaling issues. The slope 7.5° is not shown for the 2dB filter for the same reason (ALS error = 1.42 dB, ALS dark = 234 lx). (c) In the case $w_{hm/2} = a$. The 1dB filter dimensions are: $P = 275$ nm, $a = 180$ nm, $b = 90$ nm, $h_m = 300$ nm. The 2dB filter dimensions are: $P = 250$ nm, $a = 200$ nm, $b = 100$ nm, $h_m = 300$ nm. The 2012 and 2015 references are plotted with a grey square and an orange square respectively.

4.5 Holes filling

4.5.1 Importance of the dielectric surrounding

We have seen in *Chapter 2* how the dielectric medium around the metallic layer affects the plasmon resonances by comparing the spectral responses obtained with SiO_2 , Si_3N_4 and TiO_2 . Before evaluating the potential impact of the presence of voids on the filters properties, we want to clarify how inhomogeneities in the dielectric surrounding may affect the spectral responses. We propose to study these inhomogeneities throughout four simple configurations described in Figure 4.20. The first configuration consists of an aluminum layer embedded in an infinite SiO_2 layer as in the case of the standard stack that we have used in the previous calculations. In the second one, we replace the SiO_2 in the holes by another dielectric with a distinct refractive index: we choose to use air ($n_{\text{air}} \approx 1$). In the third case, the aluminum layer lays on an infinite SiO_2 substrate but the holes and the top of the metallic layer are exposed to air. Finally, the last configuration corresponds to a free-standing aluminum layer only surrounded by air.

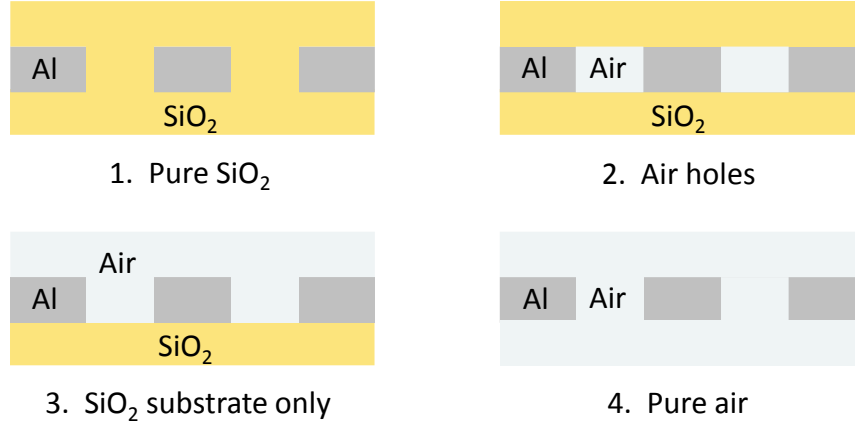


FIG. 4.20. Schematic view of the four configurations considered to study the effect of the dielectric inhomogeneities around the metallic layer.

The spectral responses of the four configurations are simulated by using the dimensions of the 2dB filter and are given in Figure 4.21. With pure SiO_2 surrounding (case 1), we obtain the nominal spectral response of our reference filter with a single plasmon resonance at 550 nm and a transmission of 35 %. The peak located around 380 nm corresponds to an increase of transmission due to the apparition of diffracted orders as P becomes equal to λ/n_{SiO_2} at this wavelength. In the opposite configuration where all the SiO_2 is replaced by air (case 4), the peak is blueshifted at 370 nm with a slight increase in transmission, corresponding to the plasmon resonance occurring at the interface between aluminum and air. When only the SiO_2 in the holes is replaced by air (case 2), the main resonance at 550 nm splits in two distinct peaks with weaker transmissions, each one corresponding to a different plasmonic resonance: the peak located at 330 nm is related to the Al – air plasmon whereas the peak located at 470 nm is related to the Al – SiO_2 one. The coexistence of the two surface plasmons is also found in case 3 where the metallic filter lays on the SiO_2 substrate: the peak corresponding to the Al – air plasmon has a higher transmission than in the previous configuration since there is more aluminum surface in contact with air. This splitting of the resonance peak when the metal is in contact with two different dielectric materials considerably changes the filter's properties and has thus absolutely to be avoided [118], [183].

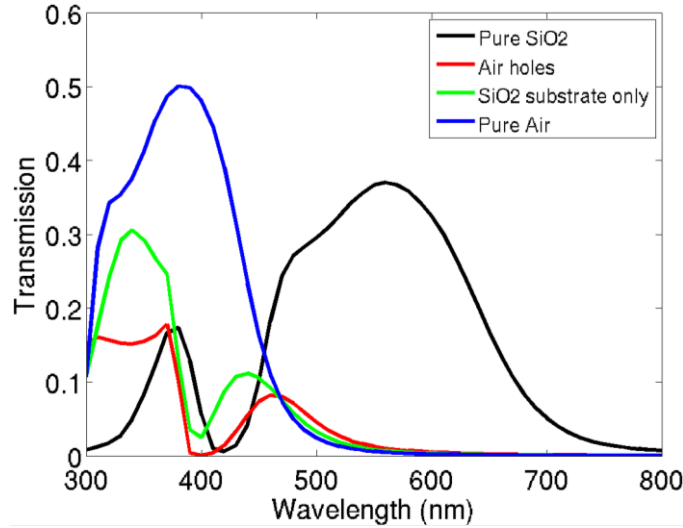


FIG. 4.21. Evolution of the spectral response of the 2dB filter when the surrounding dielectric medium is changed according to the four configurations described in Figure 4.20. The filter dimensions are: $P = 250$ nm, $a = 200$ nm, $b = 100$ nm, $h_m = 300$ nm.

4.5.2 Impact of air gaps during holes filling

The fabrication of plasmonic filters operating in the visible range imposes very tight apertures whose filling may be tricky without appropriate deposition tools. The conformal filling of such filters gets even more complicated when using thick metallic layers leading to high-aspect-ratio nanostructures, as in the case of ALS filters. With such tough conditions, the presence of voids in the filled apertures is a risk that has to be expected. In the four configurations studied in the previous sub-section, we have seen that having two different dielectric materials in contact with the metal severely alters the filter's response. While the air gaps resulting from a bad filling are not directly in contact with the metallic layer, it is worth investigating how their presence may affect the spectral responses of the filters and their performance in the case of the ALS application.

In the following study, the modeling of the voids is made according to a first approximation using coaxial air gaps inside the cruciform SiO_2 holes, as shown in Figure 4.22. We consider here that the air gaps are as large as the metallic layer, which is the worst case that can be obtained in practice. In the simulations, the size of the voids is progressively increased by $0.2a$ steps and the volumetric fraction V_f of the air gap over the SiO_2 hole is used to define its proportion.

We first simulate the impact of the different sizes of air gaps with the standard stack using the 2dB reference filter, whose corresponding spectral responses are drawn in Figure 4.23. For small voids ($V_f = 4\%$), we only observe a very slight decrease of the transmission efficiency. When the size of the air gaps is progressively increased, the spectral response is however significantly impacted with a substantial decrease of the transmission, a notable blueshift of the main Al – SiO_2 resonance and with the raise of a second peak located around 350 nm. Actually, we can notice that these changes gradually join the spectral response of the second configuration of the previous sub-section where the aluminum is surrounded by SiO_2 but the holes are filled with air, which is obtained in the case $V_f = 1$. We thus demonstrated with these results that even if the air gaps are not in contact with the metallic layer, the induced change in the effective refractive index of the holes is sufficient to alter the filter properties. It means that in addition to the constraint of having a homogeneous dielectric medium around the metal [118], [183], we must also ensure that the presence of voids inside the holes is severely limited.

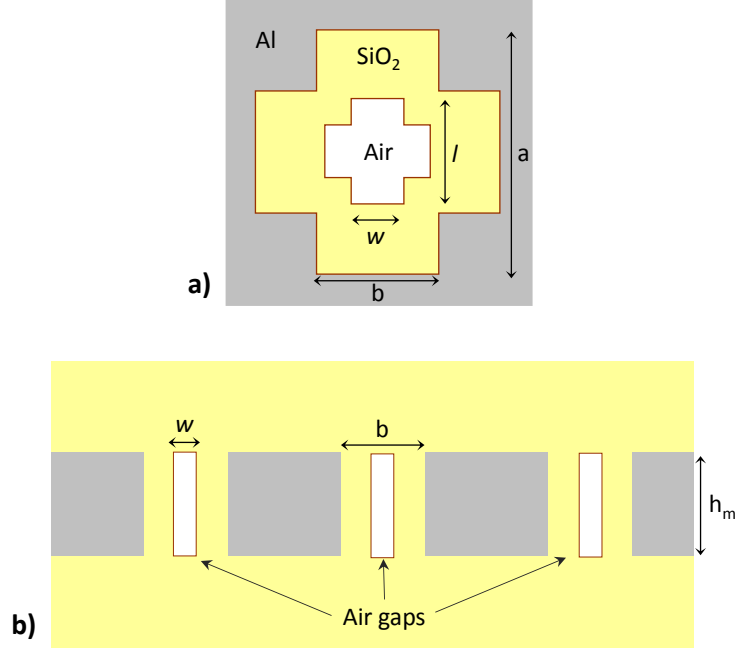


FIG. 4.22. Modeling of the air gaps inside the SiO_2 holes with coaxial cruciform voids. The air gaps are simulated with the same thickness than the metallic layer. (a) Top view of an elementary cell of the RCWA simulation. (b) Sectional view.

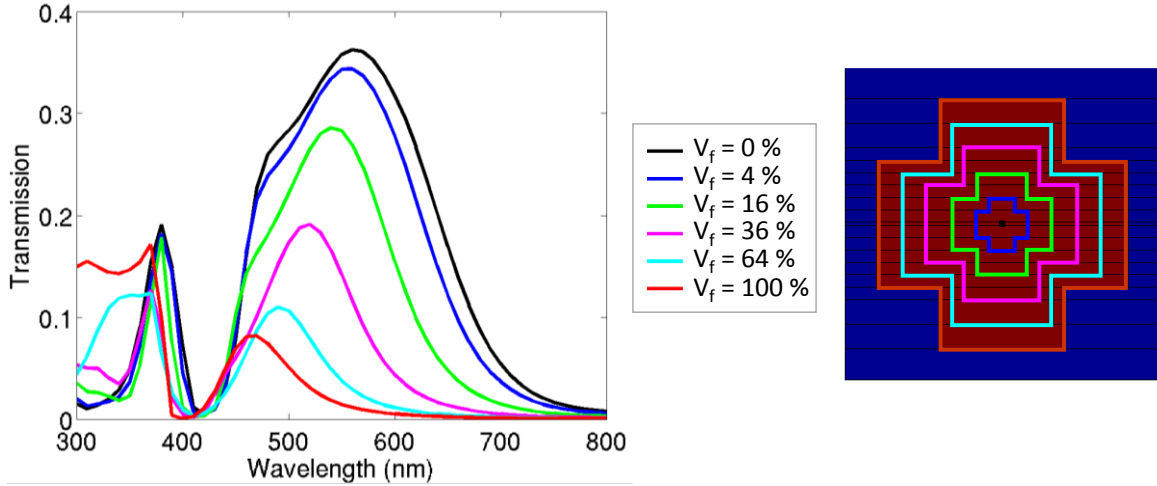


FIG. 4.23. Evolution of the spectral response of the 2dB filter when the volumetric fraction of the air gap is increased inside the SiO_2 hole as described in Figure 4.22. The filter dimensions are: $P = 250$ nm, $a = 200$ nm, $b = 100$ nm, $h_m = 300$ nm.

We now perform the simulations of the two reference filters with the ALS stack to evaluate the impact of air gaps on the ALS performance. The results presented in Figure 4.24 indicate that the presence of air gaps drastically alter the performance above $V_f = 16\%$ with a substantial increase of the ALS dark when V_f is increased. For the 1dB filter, voids with $V_f = 4\%$ still give performances close to the nominal filter with a 20 lx increase in ALS dark and a 0.07 dB increase in ALS error. Note that the performances of the 1dB filter with $V_f = 64\%$ and $V_f = 100\%$ are not shown since they are way out of scale (ALS dark > 900 lx). The 2dB filter can sustain voids with a volumetric fraction up to 16% with only a 16 lx increase in ALS dark and a 0.06 dB decrease in the ALS error. The 2dB filter has a higher tolerance to air gaps thanks to its higher transmission efficiency. The slight decrease in ALS error it

experiences for values of $V_f \leq 16\%$ is due to the removal of the signal located above 700nm, which improves this ALS criterion. We thus show that the formation of voids during the filling of the nanostructures can severely deteriorate the filters' performance if the volume of the air gaps is not controlled. While the use of proper deposition techniques is preferable, we demonstrate that the impact of voids is limited if their volumetric fraction over the aperture is inferior to 4 % in the case of low ALS error filters and inferior to 16 % in the case of high ALS error filters.

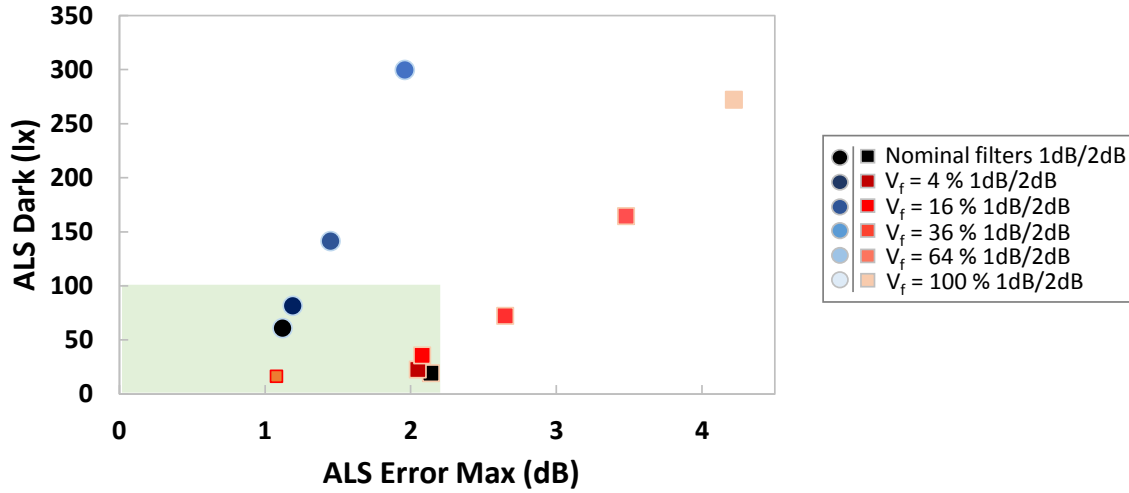


FIG. 4.24. Evolution of the ALS performances with the increase of the volumetric fraction of the air gaps in the SiO₂ apertures for the 1dB reference filter ($h_m = 300$ nm, $P = 275$ nm, $a = 180$ nm and $b = 90$ nm) and for the 2dB reference filter ($h_m = 300$ nm, $P = 250$ nm, $a = 200$ nm and $b = 100$ nm). For the 1dB filter, the dots corresponding to $V_f = 64\%$ (ALS error = 2.37 dB and ALS dark = 911 lx) and to $V_f = 100\%$ (ALS error = 3.47 dB and ALS dark = 1575 lx) are not displayed because of scaling issues.

4.6 Conclusion on Chapter 4

In this chapter, we have simulated the impact of process dispersions on the ALS performances of two reference designs. Those simulations have enabled us to define a process flow for the fabrication of plasmonic filters that can simultaneously guarantee as few technological challenges as possible and be easily transferrable in an industrial context of mass production. The main hard points that are likely to be encountered throughout this chosen process route are identified. The aim is to be able to evaluate whether there are critical technological bricks and to propose solutions to overcome these potential difficulties in the industrial fabrication of plasmonic filters. Each time, we have investigated how the optical properties of the filters are impacted by these process dispersions, then we have applied these results and evaluated their effects in the case of the ALS application with two reference filters (the 1 dB and 2dB filters) having different constraints on their performances. The main differences in behavior found out between these two filters can in most cases be explained by the fact that the transmission of the filters tend to be much lower and their rejection much stronger when we approach low ALS errors close to 1dB. While these low-ALS-error filters experience higher relative variations of their transmission (leading to wide variations of the ALS dark), their ALS error are thus less sensitive to spectral shifts compared with high ALS error filters since they are less likely to capture unwanted signal, especially in the NIR region.

The first brick of the fabrication process is the deposition of the different layers composing the filters. The resulting dispersions of the layer thicknesses and of the dielectric indices are shown to have a limited impact on the ALS performance with a proper monitoring of the deposition tools. A reachable level of dispersion (level 2) allows for maximum amplitudes of 21.5 lx in ALS dark and 0.57 dB in ALS

error for the 1dB filter, and of 3.8 lx in ALS dark and 0.69 dB in ALS error for the 2dB filter. Therefore, we conclude that this step is not critical, and that no specific deposition tools are required for the fabrication of plasmonic filters. Regarding the material stability, we established that the formation of a native oxide on the surface of the aluminum layer is not an issue for the ALS performance if we take into account the decrease of the dimensions of the aluminum structure due to the oxidation process. In this case, the performance variations for a 10-nm-thick surface aluminum oxide are inferior to 4 lx and 0.2 dB for the 1dB filter, and below 1.5 lx and 0.33 dB for the 2dB filter. In addition, we can imagine that in practice, the oxidation can be anticipated at the stage of the mask design.

During the lithography step, we have considered two main hard points: the rounding of the crosses' corners and the control of the holes' dimensions. When the crosses' angles are rounded, we observe a blueshift of the resonance that we can attribute to the progressive modification of the plasmon resonances in crosses towards circular-like modes. This effect seems more related to the internal angles of the crosses, but a change in the interactions between apertures may also be considered. Despite these observations, we show that the stability properties of thin crosses are not impacted for polar angles of incidence up to 30° with a radius of curvature in the corners up to $R = 20$ nm. The impact of the rounded corners is low on the ALS performance provided that the rounding is limited. In our simulations, we show variations inferior to 5.9 lx and 0.22 dB for the 1dB filters and below 6.1 lx and 0.17 dB for the 2dB filter for a roundness up to $R = 15$ nm. This roundness may be reachable in the internal corners with a double patterning during the lithography step and in the external corners with proper PEC calculations.

We have also studied the effect of the potential sloped profiles that can be obtained during the holes etching, with the angle being open towards the top. We have assumed that we can choose among three situations to anticipate the presence of slopes and to respect the targeted dimensions. If we fix the desired dimensions at the top of the filters, the slopes will obstruct the apertures at the bottom of the filter and the ALS dark of the filters will experience a massive increase that cannot be tolerated. On the contrary, if we choose to reach the target dimensions at the exit of the filters, the funneling effect that we have highlighted will collect much signal and will severely deteriorate the rejection of the filters, especially in the NIR wavelengths. The resulting increase in ALS error would be crippling. We show that the best case would be to anticipate the presence of slopes during the mask design so that the targeted dimensions are obtained at the middle of the metallic layer. The ALS error would not be impacted by the slopes (variations inferior to 0.18 dB for the 1dB filter and below 0.09 dB for the 2dB filter), and the ALS dark variations would be limited to 15.8 lx for the 1dB filter with 5° slopes and to 10.1 lx for the 2dB filter with 7.5° slopes. Note that the anticipation of slopes is only possible with a strong knowledge of the chemistry or of the plasma used for the etching step.

The last hard points that we have investigated is the formation of air gaps in the dielectric material (SiO_2 or SiON in our case) during the filling of the nanostructures. We have demonstrated that the presence of voids can quickly become a significant issue when their volumetric fraction V_f in the holes increases. A V_f up to 4 % can be tolerated for the 1dB filter with a 20.5 lx and a 0.07 dB variations, whereas the 2dB filter can sustain a $V_f = 16$ % with a 16.5 lx and a 0.06 dB variations. In all cases, we show that the presence of voids inside the holes have to be severely limited, especially in structures with high aspect-ratios. The use of appropriate deposition techniques such as High Density Plasma (HDP) depositions or Sub-Atmospheric Chemical Vapor Depositions (SACVD) should greatly limit the formation of air gaps in such structures.

Chapter 5

Realization and characterization of ALS plasmonic filters

Throughout the previous chapters, we progressively determined which plasmonic solutions were the most promising to fulfill the specifications of light sensors and which was the impact of the main expected process issues related to the fabrication of hole arrays, especially for cross-shaped-hole arrays. This work has continuously led us to prepare the experimental demonstration of the plasmonic filtering solution for the ALS application with a knowledgeable attention on the respect of the different aspects of the filters' characteristics. The envisioning of an industrial production of plasmonic filters requires an understanding of the actual process inaccuracies and variations that are generated with a wafer-scale fabrication and of course an estimation of the performance that can be achieved with such deviations in order to assess the viability of the ALS plasmonic solution. Because the time and the resources available for this study constituted non-negligible constraints, the objective of this process development was more focused on the obtaining of final and functional structures that can be optically characterized to provide a proof of principle of the plasmonic filters solution. In other words, this work is not primarily aimed towards the fabrication of defect-less structures with the search of dedicated and optimized processes. Similarly, the purpose was not specifically to do an exhaustive verification of the modeling of the process-related issues investigated in *Chapter 4*, but we performed as much morphological characterizations as possible in order to provide a comparison between the observed and the simulated defects in the critical process steps.

Consequently, we will be able at the end of the chapter to experimentally evaluate the ALS performance of the designs that have been studied and designed throughout this whole thesis and to discuss the viability of a wafer-level fabrication of ALS plasmonic filters. In the same time, useful information will be obtained regarding the capability of a wafer-scale production environment to fabricate nanometric structures and the potential ways of improving the filters quality. To achieve this, we will thus first describe the fabrication constraints and the initial outline process flow, together with the targeted structures. The main developments and results of the key integration steps will then be presented in the light of the study of *Chapter 4* regarding the expected process dispersions and defects of an industrial wafer-level foundry. Finally, we will evaluate the filters' performance from the measured optical responses of the fabricated filtering structures and compare them with the theoretical results.

5.1 Experimental conditions

5.1.1 Integration constraints and limitations

In the previous chapters, we recurrently explained how our study on plasmonic filters is meant for a CMOS fabrication with 300-mm wafer-level equipment, with specific constraints in the selection of materials and process techniques. In the present chapter where we aim to experimentally realize and study our developed filter designs, we however have to deal with limitations compared with our theoretical work, owing to concerns of time constraint and equipment restriction or availability for the duration of this thesis.

Although we evaluate in *Chapter 4* the rounding of the crosses with UV lithography and demonstrate that a double patterning can greatly improve their shape reproduction, we did not have the opportunity to work with STMicroelectronics's equipment using deep UV lithography (248 nm or 193 nm). Accordingly, it was decided that the patterning step of the filters' fabrication would be performed using an Electron Beam Lithography (EBL) available at the CEA Leti. Furthermore, it was agreed that the process development would be realized in the CEA clean rooms rather than in the STMicroelectronics fab due to lower development costs. It resulted from this decision that the filters would be realized on 200 mm wafers instead of 300 mm wafers since the former solution ensured an access to a wider choice of materials and processes for our study. It is also worth taking into consideration for this chapter that the process dispersions of the CEA equipments cannot be rigorously compared with the values used in *Chapter 4* since they are not exclusively dedicated to large-scale production.

Regarding the targeted structures for the experimental realization, it has to be understood that we do not aim here to fabricate a complete ALS demonstrator including the packaging and the CMOS logic chip. The process development thus focuses on the filtering part of the sensor, meaning that we only study the fabrication aspects of the metallic patterned layer and the surrounding dielectric medium that will be presented throughout this chapter. Although the development is performed on silicon wafers in order to use conventional microelectronics techniques, the photodiode, the transistors, the metallic interconnects and the passivation layers are not fabricated. The goal being to test the filtering properties of the nano-patterned aluminum plasmonic structures, we aim to measure their optical transmission. Yet, the silicon substrate suffers from strong absorption in the whole visible range and does not allow for optical transmission measurement. Another solution was imagined: fabricating the plasmonic filters on glass wafer instead of silicon. However this would require the development of an entire fabrication process with glass wafers on the 200-mm production line, which would be really challenging. Consequently, we considered another approach starting with the fabrication on a Si wafer. This wafer is then bonded on a glass substrate before silicon is removed. This approach allows for direct characterization by optical transmission while maintaining the original fabrication process. The use of a wafer bonding technique imposes a few additional constraints on the fabrication that will be detailed later in *section 5.2.5*, such as a drastic flatness of the interface that will be bonded. The demonstration of ALS filters on complete CMOS chips will be mentioned later in this chapter.

5.1.2 Process route description

As explained in the previous sub-section, the major part of this chapter is dedicated to the fabrication of the filtering structures only. The constituting parts of an entire ALS sensor such as the metallic wires or the logic elements are not included in the demonstrators and the evaluation of the fabricated filters is thus performed through transmission measurements. The concerns that we aim to investigate are related to the process risk assessment presented in *Chapter 4* and are thus limited to the fabrication of the

metallic nanostructures, with the major challenge of realizing sub-wavelength hole arrays with wafer-level processes. We already provided in the previous chapter the reasons of the selection of a fabrication using an aluminum etching instead of a damascene method, the filling of nano-scale apertures with aluminum and the potential requirement of an adhesive layer for the CMP of aluminum being very challenging. We give in Figure 5.1 a more accurate description of the process route used for the fabrication of ALS filters with aluminum etching.

Two configurations are presented but the process integration is exactly the same. A few differences exist in the parameters used between the first engineering development (SiON configuration) and the realization of the final structures (without SiON), as it will be explained throughout this chapter.

The configuration featuring a SiON layer was used to provide a first study of the adherence between aluminum and SiON in the hypothetical case where the integration of the plasmonic filters would be integrated in the top-coat layer (see 2. 4 *Optimal integration solution for plasmonic ALS*). For our demonstration of optimized ALS designs, we will only use SiO₂.

We will actually see in the next sub-section that each configuration corresponds to a different mask layout.

The following description is a brief overview of the initial process flow as it was first thought.

- The first steps consist of a thermal oxidation of the silicon to create the underneath dielectric medium (500 nm thick) (followed by SiON in the first configuration) and of the deposition of the aluminum layer.
- PVD Al-1%Si alloy is used in our study because it is more tolerant to thermal stress than pure Al.
- In a former study of plasmonic filters with nano-imprint lithography [134], [171], the etching of aluminum was shown to be a critical step which struggled to properly transfer the targeted design to the metal layer, with high etching slopes and substantial shape deformations due to the use of a soft mask. We thus decided to perform the photolithography with a combination of a photosensitive resist and an 80-nm-thick SiO₂ hard mask. The purpose of the hard mask is to obtain a better edge definition of the apertures during the etching. We use a resist thickness of 280 nm for a 200-nm-thick aluminum layer. The resist patterning is performed with a Gaussian electron beam (*e-beam*) (*Leica VB6*). The hard mask then undergoes a dry etching with CF₄/C₄F₈ as reactive gas in a O₂ plasma. Dry etching is preferred over wet etching owing to its anisotropic behavior which is more adapted to the fabrication of high-aspect-ratios structures.
- Before the aluminum structuration, a stripping step is performed so that all the remaining fluorinated residues are removed. The quality of the aluminum etching is indeed degraded due to the formation of a non-volatile AlF₃ compound when aluminum is attacked by fluorinated gases. Another stripping step is done after the metal etching.
- The aluminum layer is then patterned with a chlorinated reactive gas. In the case of the SiON configuration, the etch stop is done with end point detection method where the detection of nitrogen gas indicates that the aluminum layer has been totally etched. In the case of SiO₂ only, the etch time is calculated from the etch rate of aluminum, with the drawback of being less accurate in the detection of the bottom of the aluminum layer. After the stripping of the etch residues, the apertures of the hole arrays are thus filled with SiO₂ so that the dielectric medium is the same around and inside the metallic layer. We saw in *section 4. 5.1* that a homogeneous index around aluminum is preferable for plasmon resonances.

Since we want to perform transmission measurements to optically characterize our structures, it is necessary to transfer the filters on a transparent glass wafer. This transfer can be performed with a direct wafer-to-wafer bonding between the upper SiO₂ layer and the glass substrate (Figure 5.2). An extreme flatness of the surface is crucial, which is obtained with a chemical-mechanical polishing (CMP) of the silica layer obtained after the filling of the holes. An adequate surface preparation is required and will be described in details in the corresponding *section 5. 2.5*. Finally, the silicon wafer is removed so that light can freely propagate through the structures.

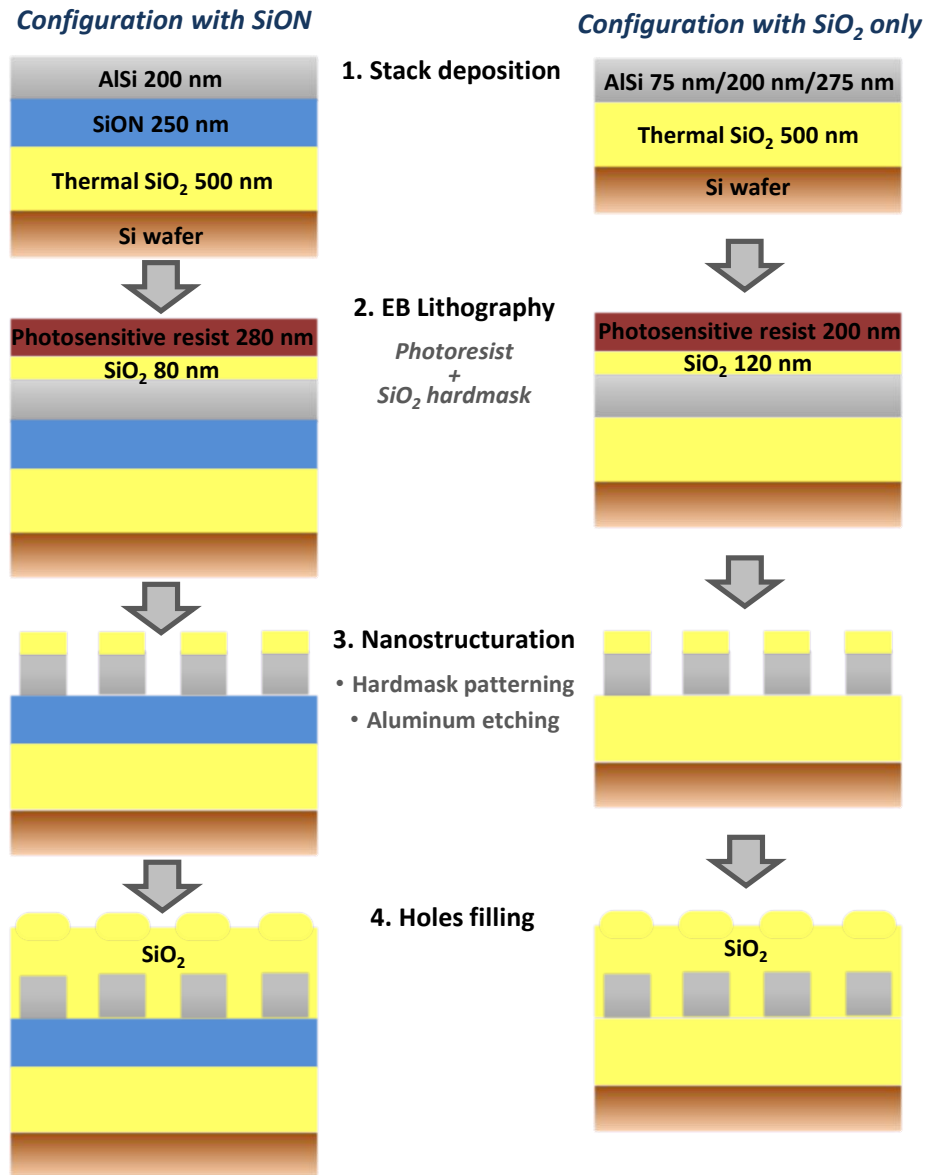


FIG. 5.1. Description of the initial process route developed for the fabrication of plasmonic ALS filters with the etching of aluminum. Each configuration corresponds to a specific e-beam (EB) base layout described in the next sub-section.

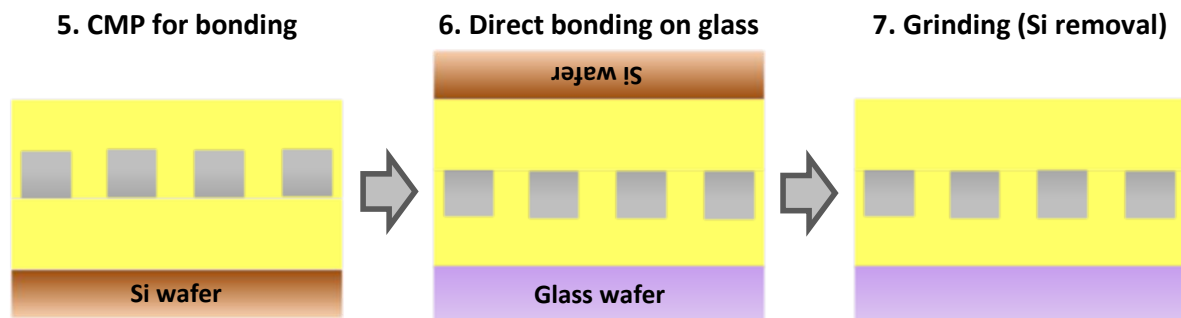


FIG. 5.2. Description of the bonding step on glass wafer for transmission measurements. The case with SiON is not drawn but it underwent the direct bonding in the same manner.

5.1.3 Designs selection and Electron-Beam Lithography bases

In practice, the process development of the filters was conducted in two steps. Since it was initiated early during the thesis work, the evaluation and the optimization of plasmonic ALS filters were not entirely achieved at the beginning of the fabrication. A first phase was thus launched with the objective of clearing the main critical steps of the fabrication, such as the metal nanostructuration, the holes filling or the wafer bonding and to deal with any potential unexpected issues. In order to save time, the nanostructures were realized according to an already existing EBL (Electron-Beam Lithography) base featuring square patterns with dimensions comparable to potential ALS structures. It must be understood that this phase consisted in the fabrication of metallic patch arrays, as described in *section 2.3.2*. The design of this *initial* base is given in Figure 5.3. It consists of two electron beam fields (left and right), each one containing nine arrays of square patterns arranged in a square array with the same period $P_x = P_y = 200$ nm. The dimensions of the squares vary between 65 nm and 140 nm. Consequently, the inter-patches cavities range from 60 nm to 135 nm, which corresponds to the dimensions of the ALS hole-arrays (*Chapter 3*). The first stage of the process development was thus realized with square arrays of aluminum square *patches* (and not square *holes*), even if we did not use these structures for the evaluation of ALS filters. A slice view of the structures along the middle of an EB (e-beam) field is proposed in Figure 5.4.

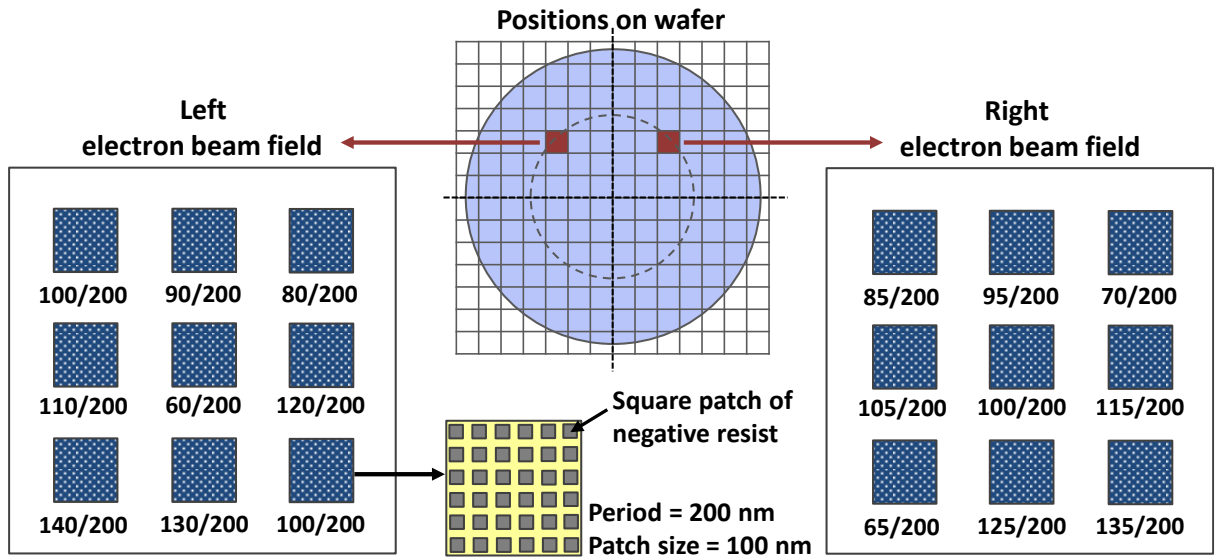


FIG. 5.3. Schematic of the layout of the initial base. The figures given below the arrays are the square patterns' dimensions in nanometers, followed by the period. This base was used to realize square arrays of square patches and to test the adherence between AlSi and SiON. The dimensions of the arrays are 500 x 500 μm^2 and the distance between two neighboring arrays is 500 μm . Each blue array stands for one filter.

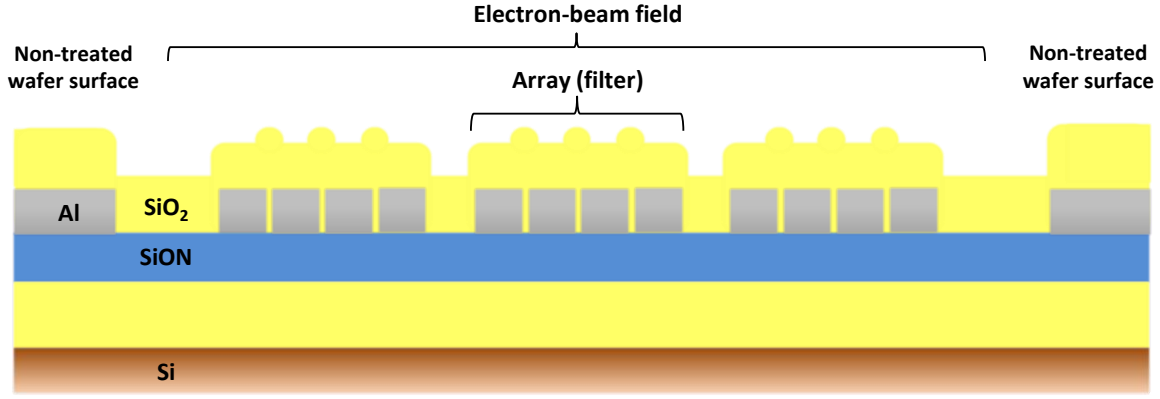


FIG. 5.4. Scheme in slice view of the wafer structure along an EB field after holes filling. The scale is not respected.

Once the optimization of plasmonic ALS filters was performed (*Chapter 3*), a new EBL base was designed with the most relevant structures for the study. We will call this base the *optimized* base. This second fabrication phase thus benefited from the development made with the initial base. The distribution of the filters is presented in Figure 5.5 and their characteristics are detailed in *Appendix A*. Similarly to the initial base, the filters are spread onto two EBL fields (left and right), each one containing 16 arrays (or filters). The colors used in Figure 5.5 distinguish different kind of filters with different purposes, as described below.

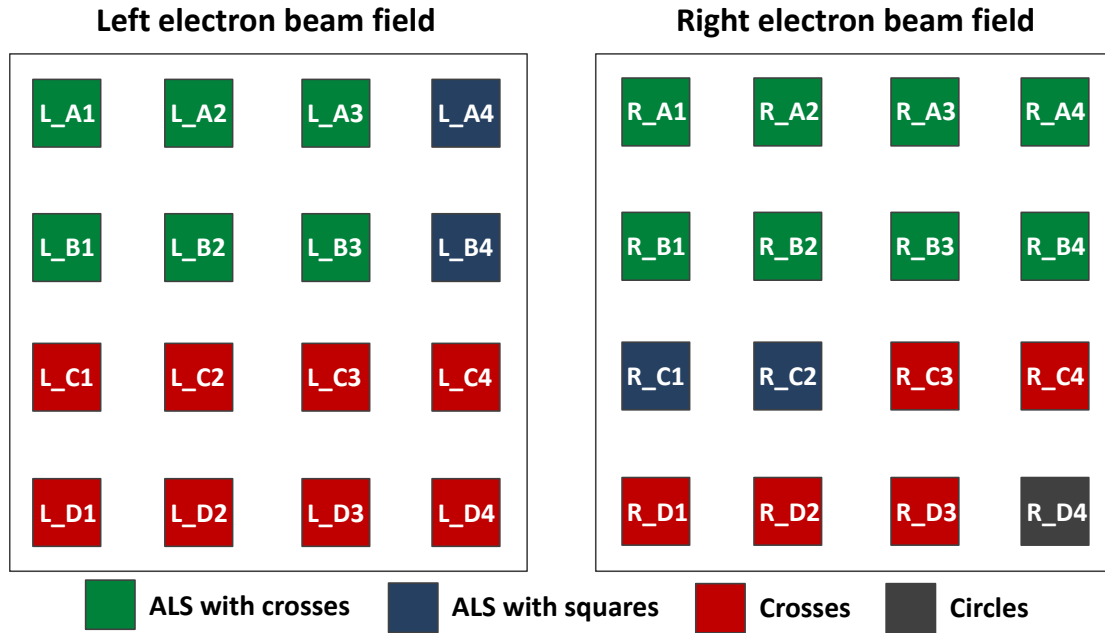


FIG. 5.5. Schematic of the layout of the optimized base. It features 32 arrays distributed on two EB fields. The green arrays stand for ALS designs made of cruciform apertures and the blue ones for ALS designs made of square apertures. The red arrays are arrays of the reference filter of *Chapter 3* with different shape factors or intercrosso distances to evaluate experimentally the angular properties of cross-shaped apertures. The description of each array is given in *Appendix A*. The dimensions of the arrays are $500 \times 500 \mu\text{m}^2$ and the distance between two neighboring arrays is $500 \mu\text{m}$.

- The green filters correspond to ALS filters designed with square arrays of cruciform holes, except the filter R_B4 which uses a hexagonal array of crosses. These ALS arrays of crosses have been optimized with various shape factors b/a ranging from 0.4 to 0.65 and for two targeted maximum ALS errors: 1 dB and 1.5 dB. The reference filters of *Chapter 4* at 1 dB and 2 dB are also fabricated and correspond respectively to the arrays R_B1 and R_A1.
- The four blue filters are ALS filters designed with square arrays of square apertures optimized for maximum ALS errors of 0.85 dB, 1 dB, 1.25 dB and 1.5 dB.
- The grey array is the last ALS filters, which is designed with a square array of circular holes. In total, 19 filters are designed for the ALS application.
- The red filters are used for a distinct purpose. They are all constituted of square arrays of crosses, but their aim is to experimentally study the angular properties of crosses. Their designs are based on the reference filter of *Chapter 3*. On the left EBL field, two filters with shape factors $b/a = 0.4$ and $b/a = 0.6$ are fabricated with increasing intercrosses distances ranging from 50 nm to 150 nm. On the right EBL field, the reference filter is designed with five shape factors between 0.4 and 0.8. The characteristic dimensions of these filters are below 120 nm and their fabrication is thus even more challenging than the ALS filters.

5.2 Development of a wafer-level integration

In this section, the development work is articulated around the main process bricks of the fabrication. For each process brick, the major results are organized according to the following principle. First, the details of the initial process and the corresponding results are presented with the initial EBL base with patches arrays, followed by the description and the solving attempts of the hard points that occurred during the development. The morphological results from these developments and the subsequent results obtained with the optimized base with hole arrays are then discussed. We mainly used an optical microscope for the macro-defects visualization and Scanning Electron Microscopy (SEM) (*Hitachi S-5500*) or a Focused Ion Beam (FIB) (FIB-SEM *Expida 1285*) for more accurate morphological characterizations. The dispersion values measured in this section are obtained from SEM or FIB-SEM observations on a small number of samples and wafers. They are thereby given as a first indication and do not pretend to be statistically relevant. It must also be understood that optimizing the process recipes and the dimensions of the filters was not within the scope of this study.

5.2.1 Materials and interfaces quality

The first process brick consists in the realization of the basic materials stack composing the filters. We first have to deposit the dielectric medium that lies beneath the metallic layer. To achieve this, we realized a thermal oxidation at 1050°C of the silicon wafer. We chose to grow the thermal oxide up to 500 nm to ensure a safe thickness between the silicon and the metallic layer in view of the ulterior Si substrate removal. This thickness is not critical for optical measurements while it is not below 200 nm [118]. For the initial EB base, an additional 250-nm-thick PECVD SiON layer is deposited at 400°C to study the stability of the SiON – Al interface as it would be the case if the plasmonic filters were to be realized in the passivation layers as explained in *section 4. 5.1*. A 200-nm-thick aluminum layer is then deposited by PVD at 175°C. The choice of this thickness value is justified by the fact that it comes close to the thickness of ALS filters (250 nm – 300 nm) without imposing high aspect-ratios for the nanostructuration as a first development. In our case, we used a 1%-silicon-doped aluminum alloy because it is more stable than pure aluminum when it is subjected to thermal stress [184], as we will see it later in this sub-section.

A typical SEM picture of the resulting stack is shown in Figure 5.6. The measured thickness of AlSi performed on different SEM cross sections is 220 nm, which represents a 10 % increase compared with the 200 nm target, which falls into the dispersion ranges taken into account in *Chapter 4* although this equipment is not monitored for a commercial production. We can also measure a 2 % and a 4 % increases compared with the targets for the thermal oxide and SiON respectively, but these thicknesses are not critical for our filters. Qualitatively speaking, the different interfaces do not reveal any apparent defect. We perform additional stress measurements on the SiON and the AlSi layers with a *Flexus* device, which measures the wafer radius of curvature by interferometry, that can be then translated into a mechanical stress according to the Stoney equation [185]. We obtain a tensile stress of 300 MPa for AlSi. This value is higher than what is measured in literature for an AlSi alloy [186], but the deposition parameters we used are not the same. A study demonstrated that for an AlSiCu alloy, a maximum stress of 250 MPa was obtained for a deposition temperature of 200°C [187], which is comparable to the temperature we used (175°C). In both cases, the aluminum layer is not stable when it endures an ulterior thermal treatment, as we will see in Figure 5.7. No delamination of the AlSi layer on SiON is noticed by performing a qualitative scotch test, which implies *a priori* a good adherence between the two materials and constitutes a positive result for the potential fabrication of plasmonic filters embedded in the SiON top-coat layer. AFM measurements return a low RMS roughness of the AlSi layer of 6 nm and a maximum peak-to-valley height of 59 nm, compatible with the following process steps. These values are in good agreement with literature [188].

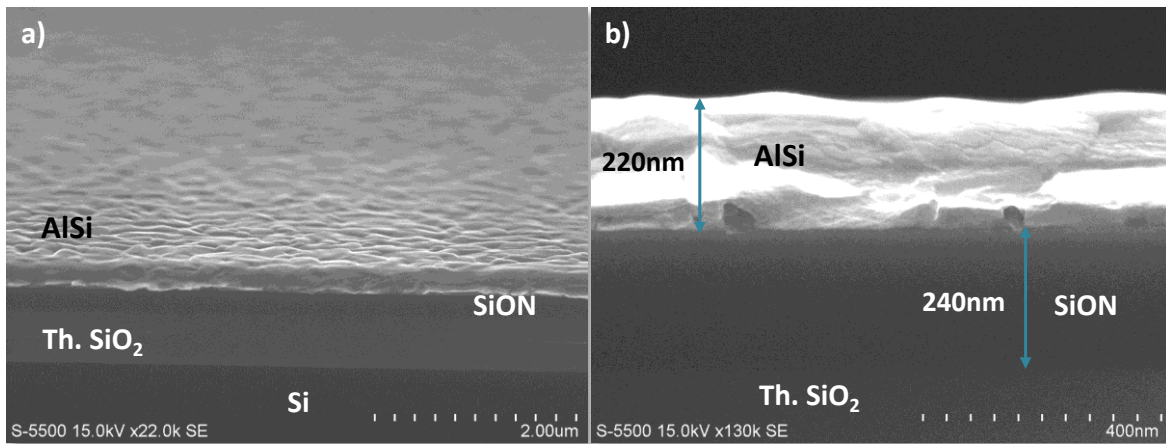


FIG. 5.6. (a) Tilted SEM slice view of basic filter stack up to the deposition of the AlSi layer. (b) SEM cross section of the AlSi and SiON layers. The granularity and the roughness of AlSi can be seen.

Previous studies at the CEA Leti demonstrated the difficulties to obtain accurate shape definition and dimensions for similar structures when Al is only etched with a soft mask [134], [171]. The use of a hard mask with a high selectivity allows for a better protection of the aluminum surface around the targeted holes and thus leads to a better etching profile. In particular, the hard mask also limits the formation of etching slopes that we want to avoid in order to preserve the performance of the filters (see *section 4. 4*). Fortunately, SiO₂ is sufficiently selective with respect to the typical chlorinated etching of aluminum. The advantage of a SiO₂ hard mask in our case is that we do not have to remove it after the structuration since the aluminum is meant to be coated with SiO₂ in our plasmonic filters. Consequently, we deposited an 80-nm-thick SiO₂ layer by PECVD at 350°C with a SiH₄ precursor.

A SEM picture of the stack with this additional layer is given in Figure 5.7(a). These observations reveal the presence of a significant number of protuberances at the surface of the films. If we perform a 350°C anneal of the stack without depositing the SiO₂ hardmask, we can also observe the formation of these important surface defects on AlSi in similar proportion (Figure 5.7(b)). The combination of the anneal and the hard mask deposition demonstrated that the anneal does not constitute an aggravating

factor since the results are very close to those obtained with the hard mask deposition alone. These defects are known in literature as aluminum hillocks [186], [189]–[192]. Hillocks consist of local extrusions that appear at the surface of a metal, especially when it is subjected to high temperatures. Their mechanism of formation in Al or in aluminum alloys is well known and is related to a phenomenon of stress release in the metallic film [186], [189]–[193]. When the process temperature is increased, the different thermal expansion coefficients and the lattice mismatch between the metal and the substrate generate a biaxial stress on the thin metallic film. The compressive nature of the created stress then gives rise to a substantial atomic diffusion at the grain boundaries towards the top surface which permits the relieving of the internal stress of the metallic layer. The local accumulation of atoms at the surface thus forms these hillock structures. We can observe a substantial decrease of the aluminum thickness due to the diffusion of AlSi atoms (Figure 5.8(a)). Our observations reveal that the hillocks can grow up to a height of 700 nm and a width at the base of 1 μm (Figure 5.8(b)).

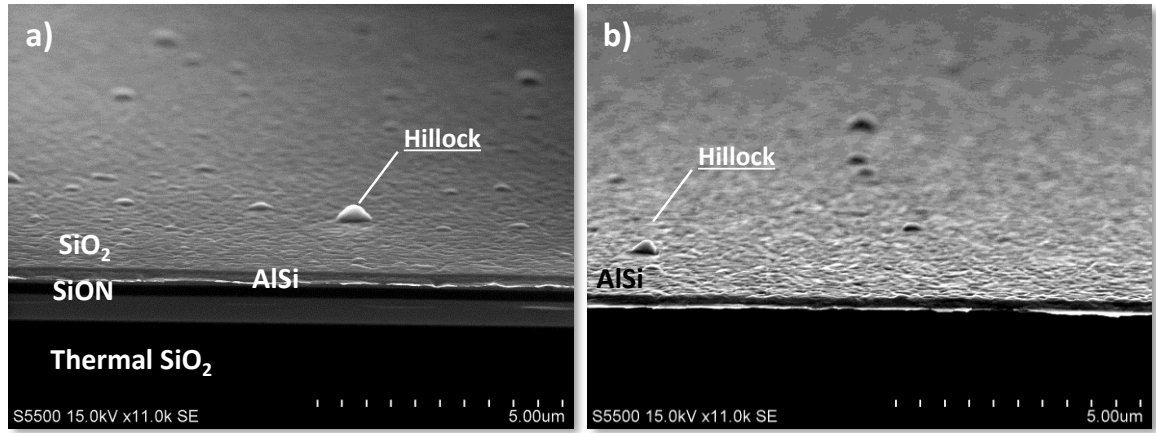


FIG. 5.7. (a) SEM picture of the stack after the deposition of the SiO_2 hard mask. (b) SEM picture of the stack after anneal only, without hard mask deposition.

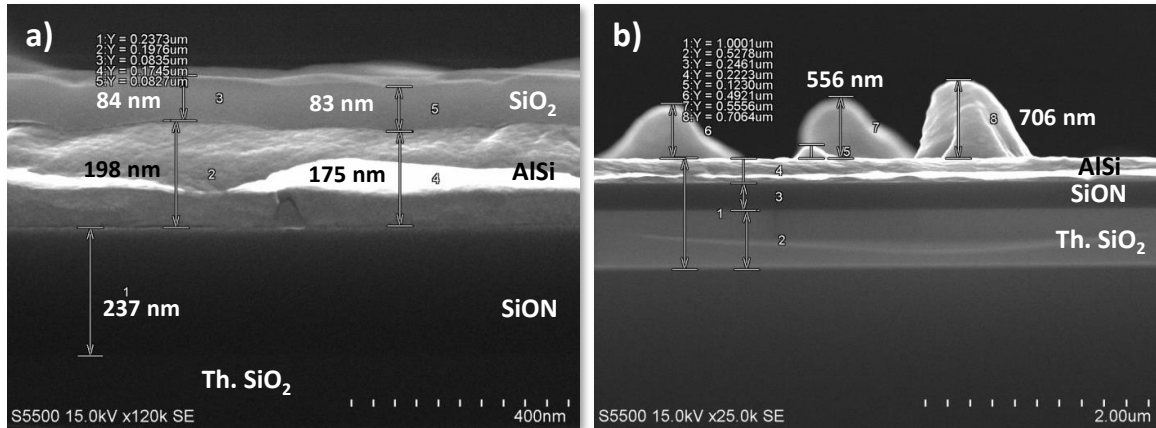


FIG. 5.8. (a) SEM cross section of the materials stack after hard mask deposition. (b) SEM cross section of the AlSi hillocks after anneal only.

The formation of hillocks with such dimensions and densities is detrimental to the following process route. Their presence can indeed hinder the photosensitive resist deposition and thus sequentially degrades the quality of the lithography and the etching steps, which are both crucial for the realization of the plasmonic structures. The necessity to prevent their formation led us to look for alternative fabrication techniques for the aluminum or for the hard mask depositions. Several possibilities have been envisioned and tested, but they are not described in details here and we thus just provide a summary of

our results. The formation mechanism of hillocks quickly drove us towards the use of deposition techniques at lower temperatures [188], [191], [193]–[195]. While this solution could deliver improvement, it would also impose a thermal constraint on our process route and we thereby searched for other potential options in parallel.

Among the various attempts of hillocks suppression, we first tried to chain up the depositions of AlSi and of the hard mask with a minimum time constraint between the two steps. The results were not concluding since hillocks are still formed with comparable density and similar size and height.

We then decided to fabricate the filters with a different aluminum alloy Al-0.5%Cu by using a recipe dedicated to the suppression of hillocks. This recipe was optimized to deposit a 440-nm-thick AlCu layer at 450°C, which is too far from our targeted thickness (200 nm). Since the resource were not available to develop this process for a 200 nm thickness, a CMP step was required to remove the 240 nm excess before depositing the hard mask. While not properly measured, the grain boundaries at the surface of AlCu looked deeper than those of AlSi alloy, which could potentially incommode the realization of the nanostructures. After the CMP step, circular holes with a diameter of about 5 μm were observed in the AlCu layer, making the SiON layer apparent. With such proportions, these defects needed to be removed. An engineering of the AlCu CMP was thus initiated on blanket wafers by using a Ti/TiN adhesive layer, but the defects were not eliminated. No further investigation was launched and the AlCu option was thus dropped out. Trials were also made with the use of pure aluminum, but it did not manage to avoid the hillocks formation.

We suspected that the degassing of water or di-hydrogen gas captured in the SiON layer due to its potential porosity could enhance the formation of hillocks. We thereby decided to perform a one-hour-long annealing at 350°C of the SiON layer before the deposition of the AlSi, but no improvement was observed regarding the hillocks formation after the hard mask deposition.

In literature, we found that the use of a capping layer above the aluminum layer could diminish or suppress the formation of hillocks during ulterior thermal treatments. We used either a 20-nm-thick Al₂O₃ layer [196], [197] or a Ti/TiN stack [198], [199] as encapsulation layers. Alumina could potentially be used on our stack since we saw in *Chapter 4* that its impact on the optical response is not critical. The Al₂O₃ layer was deposited with a PEALD technique and the hard mask was then deposited to observe the potential hillocks formation. Hillocks were still present with a high density. This difference with literature results may be due to the fact that the alumina thickness should be more important to inhibit the growth of hillocks, typically superior to 90 nm – 100 nm [196], [197]. The use of such a thick alumina layer could however deteriorate too significantly the optical response of the filters and was thereby abandoned.

In the case of a Ti/TiN encapsulation which is opaque, the presence of this capping entirely annihilates the optical properties of the filters. Ti/TiN is thus only used as a temporary encapsulation to stabilize the aluminum layer and has to be removed thereafter. In particular, the protocol consisted of the PVD deposition of a 10-nm-thick Ti layer and of a 40-nm-thick TiN layer above the aluminum layer. We chose to try this option on both AlSi and the AlCu alloys. The stacks then endured a 400°C N₂H₂ anneal for 15 min in order to perform the stress release and the stabilization of the aluminum layer, and the Ti/TiN layer was meant to be removed with a CMP step. Despite the presence of Ti/TiN, hillocks were still observed with a density comparable to their initial observation.

Getting back to the cold process solution, the SiO₂ hard mask was deposited at 200°C instead of 350°C as it was initially the case, with a shorter deposition time. The observation revealed a significant reduction of the hillocks formation, attributable as forecast to the limited thermal stress imposed during the SiO₂ deposition (Figure 5.9). Note that the hillocks are not entirely removed, but their density appears to be significantly decreased all over the wafer surface when comparing Figure 5.7(a) to Figure 5.9(a). Hillocks are reduced to a height of 100 nm and a width at the base of 250 nm. Although this option imposed a thermal constraint on our process, it also allowed us to pursue the fabrication of the plasmonic structures towards the next steps. We nevertheless assumed that once the etching of the metal

layer is performed, the nanostructured areas of AlSi would be much less sensitive to thermal stress due to the discontinuity of the metal, allowing for a stress release without the hillocks formation mechanism. This assumption will be tested later in the process with the use of deposition steps with temperatures higher than 350°C.

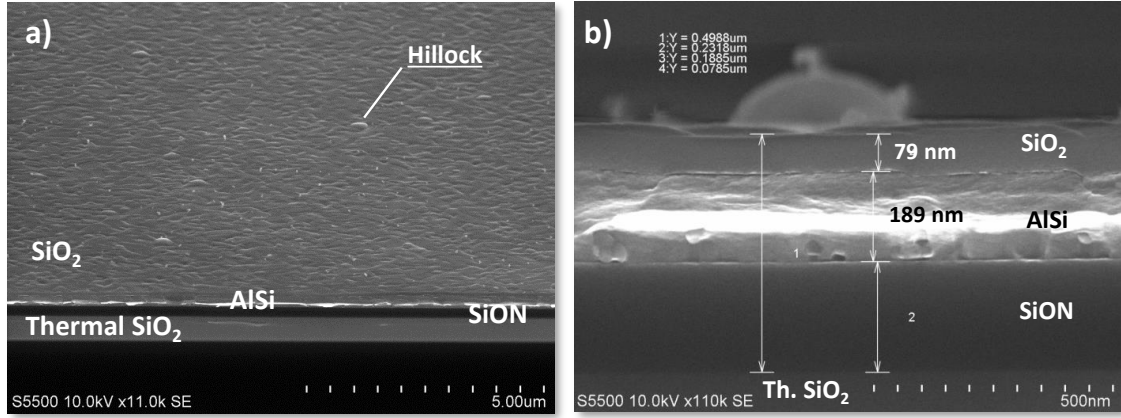


FIG. 5.9. (a) SEM picture of the stack after the deposition at 200°C of the SiO₂ hard mask. (b) SEM cross section of the stack focused on a hillock.

The use of a cold deposition of the SiO₂ hard mask showed good results for the reduction of AlSi hillocks, it was thus applied to the structures fabricated with the optimized designs. As previously explained, in this case the aluminum is directly deposited on the thermal oxide. The SiON layer was not used because its refractive index was too high ($n \approx 1.8$) compared with the silica that is used above the metal and inside the hole, and we know that a homogeneous dielectric medium is preferable for the plasmon resonances. An engineering of the SiON layer could have been made to decrease its reflective index by modifying the stoichiometry of oxygen and nitrogen atoms, but it could have altered the adhesion with aluminum, and a whole additional study would have been necessary. A SEM observation of the obtained stack is given in Figure 5.10. The density and the size of the hillocks look comparable with what was obtained with the cold deposition for the initial base. There might be slight variations that were not measured due to the different stresses generated by the deposition of AlSi on SiO₂ or on SiON, but we did not quantify them. The quality of the stack was sufficient to validate the cold deposition of the hard mask solution on the optimized base.

The metal layer and the SiO₂ hard mask being deposited with a reduced formation of hillocks, we continued with the nanostructuration of the filters, which starts with the patterning of the hole shapes in the photoresist.

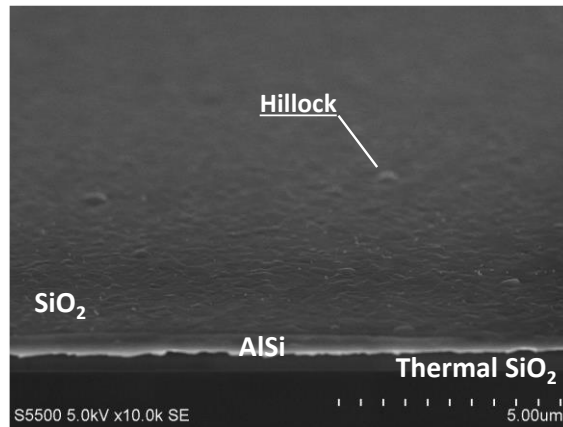


FIG. 5.10. SEM picture of the stack for the optimized base after the deposition at 200°C of the SiO₂ hard mask.

5.2.2 Electron-beam lithography and corrections

The small dimensions of the apertures and their particular shapes make the photolithography step challenging on the filters' fabrication. Moreover, we saw in *Chapter 4* how the dispersion on the targeted dimensions and the rounding of the shapes can impact the ALS performance owing to the intrinsic properties of plasmonic filters. Limiting these two undesired effects thereby requires careful consideration regarding the realization of the patterns. Indeed, the accuracy of the lithography step is determining for the accuracy of the subsequent etching step, itself being crucial for the nanostructuration of the aluminum layer, which has to be as close as possible to the targeted designs. In *Chapter 4*, we showed that a double-patterning with 193 nm lithography is able to deliver cruciform shapes with limited rounding of the corners. We did not have however the possibility to develop our process on such an equipment, and we then decided to use a Gaussian electron-beam lithography technique (*Leica VB6*).

Electron Beam Lithography (EBL) is able to draw small patterns of a few tenths of nanometers, and even of a few nanometers for the most advanced equipment, which makes it especially adapted for the realization of our designs [200]. The size of the spot is however not the only parameter involved in the resolution capability of EBL. In particular, electron-matter interactions induce dispersion in the exposed energy transferred into the resist with both scattering and the generation of secondary electrons. Moreover in the case of close periodical patterns, the electrons of the current feature writing spill over into adjacent areas, which results in a broadening of the pattern image and a decrease of its contrast. We will see throughout this sub-section how these issues can be dealt with. EBL implies a long writing time owing to the serial nature of the process which reduces its use to small areas only, unlike conventional photolithography where the whole mask is simultaneously projected onto the resist surface. Although EBL does not fit with the high throughput requirement of an industrial production, it is advantageous in our development since this technique does not use masks, whose realization is long and costly. A trade-off had to be made on the photoresist thickness: a better EBL resolution is obtained with thin resists, whereas the resist consumption during the etching step requires a thicker resist. It was decided as first attempt to use a 280-nm-thick photoresist. The metallic patches of the initial base were performed by using a negative photoresist, meaning that the exposed areas (corresponding to the desired metallic patches) remain after the resist development. The doses were varied according to previous studies using the same arrays, whose typical mask transmission rates are between 10 % and 50 %. No antireflective coating is required with the use of EBL.

We provide in Figure 5.11 top-view SEM observations and measurements of a few arrays obtained after lithography step. The dimensions are obtained with a CD-SEM equipment (*Hitachi CG 4000*) which purpose is to measure the characteristic dimensions (CD) of structures between 30 nm and 5 μm from SEM top views. It is calibrated with a reference standard ensuring a measuring accuracy of 0.6 nm. The square shapes are well respected, although the rounding of the corners is more noticeable on small patterns, with a size inferior to 85 nm. The dimensions are slightly wider than the targeted designs, with the exception of the large patch arrays (above 120 nm) that are finer than the ideal designs. The mean dispersions of the dimensions are given in Figure 5.12 for the different array sizes, averaged over 12 wafers. The arrays with patch sizes of 60 nm, 65 nm and 70 nm could not be measured because of resist collapsing, which generally occurs when the resist thickness exceeds three times the pattern size. Three values are presented for the array with patch size of 100 nm, corresponding to the three 100 nm arrays featured on the initial base. Despite a few dispersion extrema, the mean thickness dispersion over the wafers does not exceed 12 % regardless of the patch size, which is comparable to our maximum dispersion of 10 % considered in *Chapter 4*. Most of the arrays actually show a mean dispersion close or below 5 %. Bearing in mind that we do not aim to propose optimal process conditions and that no proximity effect corrections were used, the results were consistent enough to pursue the fabrication of plasmonic ALS filters. One could however object that the dispersion obtained with patches is not equivalent to that obtained with holes.

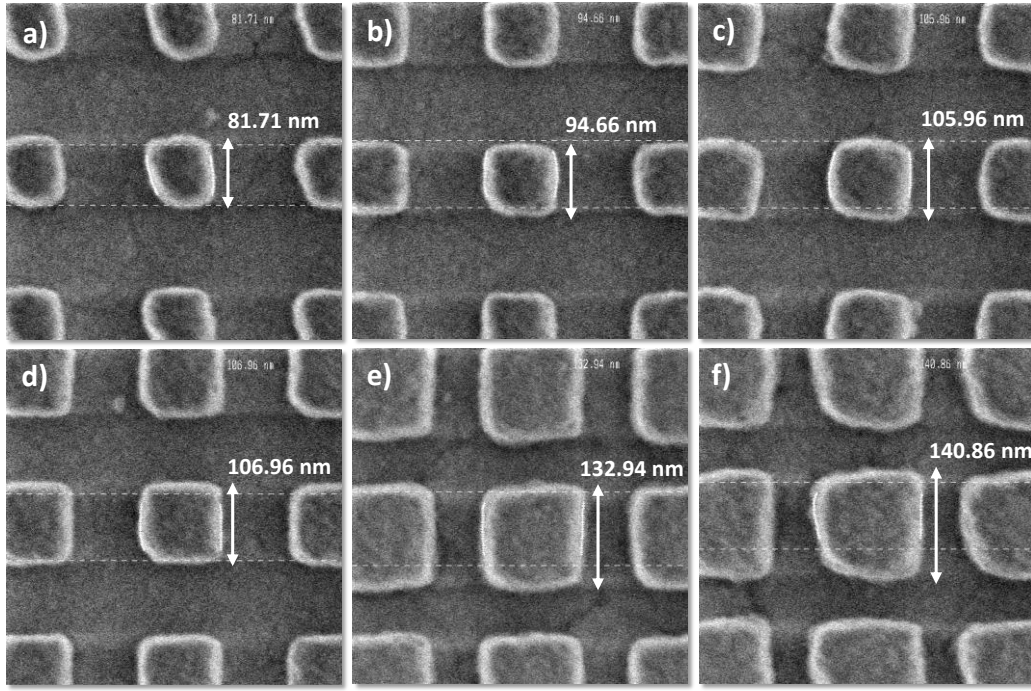


FIG. 5.11. CD-SEM observations of arrays with patch sizes of (a) 80 nm, (b) 90 nm, (c) 100 nm, (d) 105 nm, (e) 125 nm and (f) 140 nm. The dashed lines do not correspond to the measurements given on the pictures.

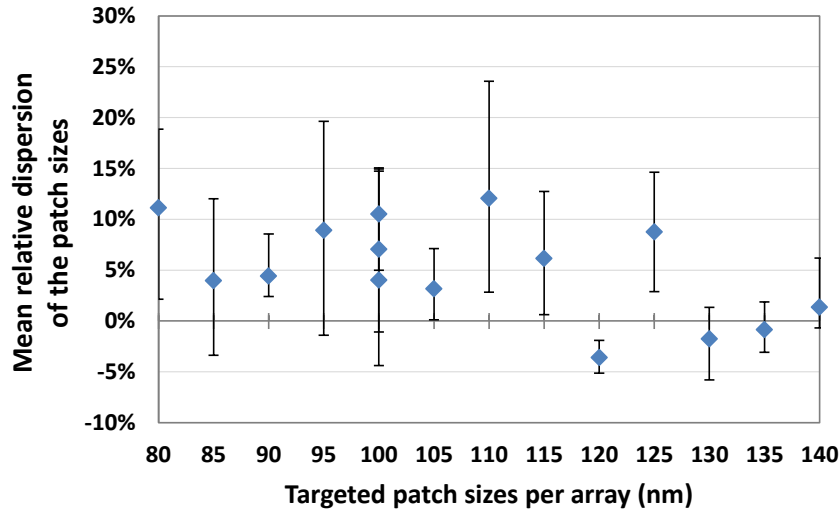


FIG. 5.12. Mean dispersions of the patch sizes for the arrays featured on the initial base. The dispersions are averaged over 12 measured wafers. The bars give the maximum amplitude observed for each array in the 12-wafers sample.

In the case of the optimized base, a few changes had to be made on the lithography step, where we wanted to realize hole arrays instead of patch arrays. The negative resist of the initial process was changed to a positive resist, meaning that the exposed areas of the photoresist are removed. A photoresist thickness of 200 nm was chosen, corresponding to the thickness used in CEA for similar resolutions. The thickness decrease compared with the 280 nm of the negative resist also implied a thickness change of the SiO_2 hard mask, which was increased to 120 nm in order to compensate for the material loss during the etching step. The mask transmission rates are typically between 12 % and 42 %. SEM observations in top-view of a few arrays are given in illustration in Figure 5.13. A careful study of the dimension dispersion will be given afterwards in Figures 5.15-5.16. We first present the results of ALS cross-

shaped-hole arrays with increasing shape factor in Figure 5.13(a)-(c). Despite their smaller arm length, crosses with $b/a = 0.4$ are those where the cruciform shape is the most respected, but the rounding of the corners is substantial. When the shape factor increases, the rounding and the proximity effects severely complicate the realization of a distinct cruciform contour and the shapes eventually approach a circular shapes ($b/a = 0.6$). The arm widths of the crosses were not measured because of their low relevance given the obtained shapes. Square holes gave however good results with faithful shapes and dimensions (Figure 5.13(d)-(e)). On the contrary, the arrays of small crosses aimed for the study of the angular stability returned poor results given their small dimensions and the absence of lithography optimization (Figure 5.13(f)). The entire results of the left field of the optimized base can be found in *Appendix B*.

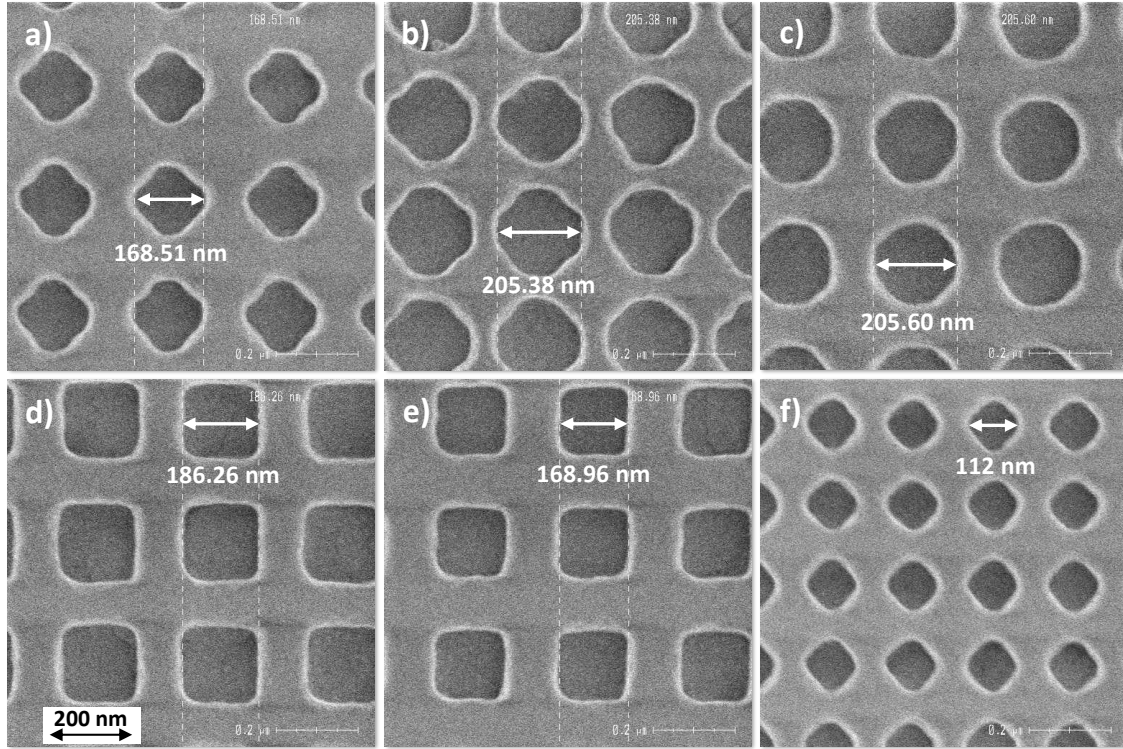


FIG. 5.13. CD-SEM observations of the following hole arrays of the optimized base: (a) L_A1 ($a = 167$ nm, $b/a = 0.4$), (b) L_A2 ($a = 193$ nm, $b/a = 0.5$), (c) L_A3 ($a = 185$ nm, $b/a = 0.6$), (d) L_A4 ($a = 178$ nm), (e) L_B4 ($a = 167$ nm) and (f) L_C2 ($a = 120$ nm, $b/a = 0.4$). In the cases of cruciform shapes, only the arm length is measured.

We decided to split our batch into two studies.

- Since the lithography quality of square holes was satisfying, the first part was aimed to continue the fabrication of plasmonic filters especially for the square shapes, but also for the crosses without corrections. This part will be described in the following *sub-sections* 5.2.3 to 5.2.5.
- The second part was however dedicated to the development of the EB step in order to improve the definition of the crosses before pursuing the nanostructuration. In particular, a development of proximity effect corrections (PEC) was attempted with the use of a thinnest and more resolving photoresist of 60 nm in combination with dose corrections. We did not have time to perform in the same time geometrical proximity corrections, but the results were already very promising (Figure 5.14). For direct comparison, we present the same arrays than those given in Figure 5.13. Be aware however that the scale is not the same. Qualitatively, the shape improvement can immediately be noticed on the ALS crosses, with sharper edges and corners (Figure 5.14(a)-(c)). The results are actually really close to the theoretical designs. The difference for the squares is tenuous, but less shape rounding can be noted with a closer look (Figure 5.14(d)-(e)). Eventually,

a major improvement is gained for small crosses, where the cruciform shape is particularly well respected despite the challenging dimensions ($a = 120$ nm and $b = 48$ nm). The results on the left-hand chip arrays of the optimized base can be found in *Appendix B*. A rough visual fit on the SEM observations of crosses returns a radius of curvature in the corners of approximately 30 nm, which is slightly higher than the values we estimated for the rounding modeling of *section 4.3.1*. It must however be noted that the shape obtained after EBL with PEC seems more faithful to the perfect cruciform shape compared to the shape we got from our modeling with similar radii of curvature. This is most probably due to the approximation of our model and the inaccuracies of the rounding measurement. The crosses' shapes after EBL with PEC are therefore less concerning than what the simulations showed in *section 4.3.1*, which constitutes good news for the manufacturing of cross-hole arrays.

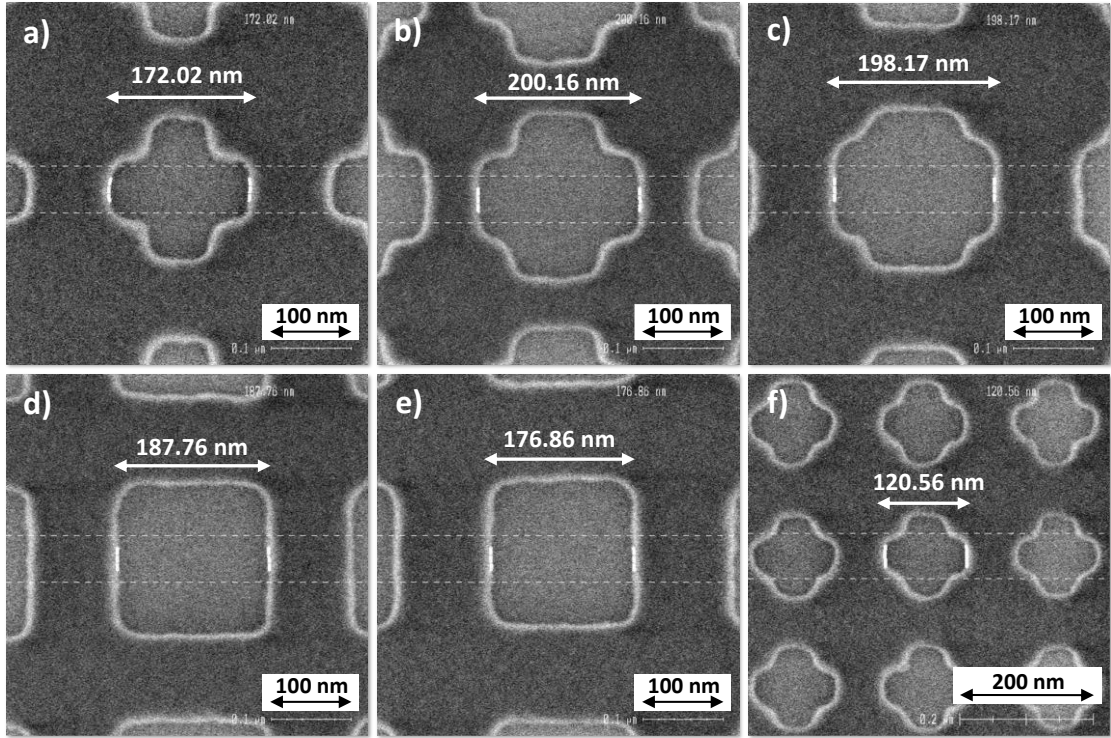


FIG. 5.14. CD-SEM observations of the same hole arrays of the optimized base with the more resolving resist and with dose corrections: (a) L_A1 ($a = 167$ nm, $b/a = 0.4$), (b) L_A2 ($a = 193$ nm, $b/a = 0.5$), (c) L_A3 ($a = 185$ nm, $b/a = 0.6$), (d) L_A4 ($a = 178$ nm), (e) L_B4 ($a = 167$ nm) and (f) L_C2 ($a = 120$ nm, $b/a = 0.4$). In the cases of cruciform shapes, only the arm length is measured. The dashed lines do not correspond to the measurements.

The shape dimensions measurements for the optimized e-beam base after lithography are gathered in Figure 5.15 to provide a quantitative comparison between the initial resist and the new resist with dose corrections. The data with the new resist were only measured on the left chip of the optimized base. The relative dispersion of the hole size is drawn for each array of the left chip in each case. Note that the hole size refers to the size a of the squares and to the arm length a of the crosses. The data are differentiated between ALS crosses (gradient bars), ALS squares (hatched bars) and the small non-ALS crosses (full-color bars). It can be seen that the new resist may give slightly higher dispersion for some of the ALS-crosses arrays, and the same can be observed on ALS squares. If we look at the global dispersion in absolute values obtained over the ALS arrays only, the old resist leads to a mean dispersion of 3.9 % with a maximum of 11.14 %, whereas the new resist leads to a mean of 4.5 %, but with a maximum of only 7.1 %. It is likely that this increase in mean dispersion is more related to the accuracy of the EB equipment. These data are punctual and are only extracted from one wafer for each resist. Only a

statistical study would provide an accurate evaluation of the change in dispersion between the two resists in a situation with such close values. Moreover, these small variations between the two resists for the ALS arrays have to be put into perspective with the significant shape improvement obtained with the new resist, which is difficult to quantify. In the case of small crosses however, the improvement of the new resist are not questionable. With the old resist, we obtained a mean dispersion of 5.8 % with a maximum of 11.1 %, when we only obtained for the new resist a mean dispersion of 1.5 % and a maximum of 3.4 %. In total, the new resist allowed for an improvement in mean dispersion from 4.9 % to 3 %. Even if these results demonstrate the gain achieved with the new photoresist and the proximity effect corrections, it must be kept in mind that a major improvement was obtained in terms of shape definition, which cannot appear on a chart. The comparison is also given for the arm width b of the crosses in Figure 5.16, with measuring accuracy of ± 3 nm. They are mainly indicative, and especially for the smallest designs (L_C1 to L_D4) with the initial resist, which were barely measurable due to the high deformation of the crosses. It was chosen that b would be measured at mid-height between the edge of the arm and the internal corners. In spite of the low reliability of these values, a clear trend highlighting the improvement brought by the new resist and the proximity correction can be observed, especially on the smallest designs. The calculated mean dispersion over all the arrays for the initial resist is 14.8 % with a maximum of 38.9 %, whereas the new resist gives a mean dispersion of 5.4 % and a maximum of 13 %. The gathered data of Figure 5.15 and Figure 5.16 reveal that in the case of ALS filters, EBL can be optimized to reach dispersions inferior to 8 % for both the arm length a (mean 4.5 %) and the arm width b (mean 5.7 %), which is consistent with our dispersions studied in *Chapter 4*. The final dispersions will be obtained after the aluminum etching though.

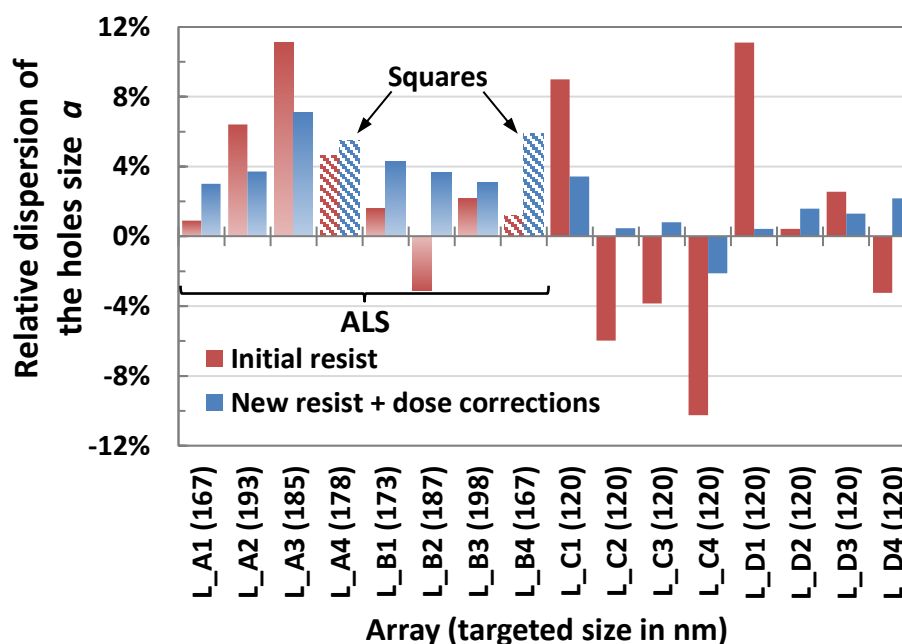


FIG. 5.15. Comparison of the relative dispersion obtained on the size of the holes between the initial 200-nm-thick photoresist and the new 60-nm-thick photoresist with dose corrections on the array of the left chip of the optimized base. The bars with gradient colors stand for ALS crosses, the hatched bars for ALS squares and the full-color bars for small crosses. The holes size refers to the size of the squares or to the arm length of the crosses.

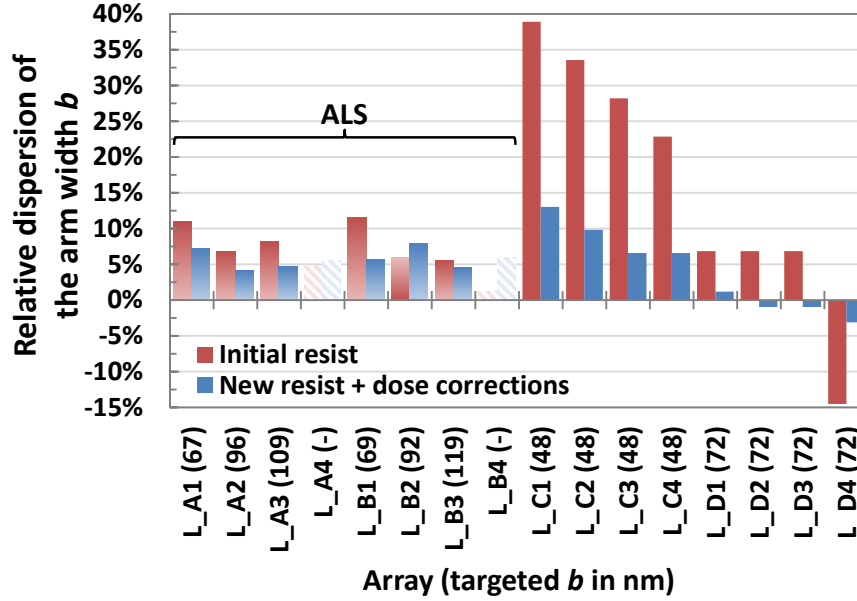


FIG. 5.16. Comparison of the relative dispersion obtained on the arm width b of the cruciform apertures between the initial 200-nm-thick photoresist and the new 60-nm-thick photoresist with dose corrections on the array of the left chip of the optimized base. The bars with gradient colors stand for ALS crosses and the full-color bars for small crosses. The squares are left for a direct correspondence of the arrays for the reading of a and b on this chart and Figure 5.15. They are made brighter since they do not have relevance for the arm width study. These data are only given as indication for the dispersion on the smallest dimension.

Although geometrical proximity corrections would have certainly improved the accuracy of the holes shape and size, we were unfortunately too short in time to go further into development for this second part of the study. Complementary solutions were envisioned with the use of intermediate hard masks with anti-reflective coatings, but we could not get into it. Consequently, these PEC developments for the optimization of cruciform apertures are the last results we could get for our optimal cross-shaped-hole arrays ALS fabrication. Until the end of this chapter, the results that will be presented are thus the developments made on the initial base (Figure 5.11) and on the first part of the optimized base, i.e. the squares holes and the deformed crosses (Figure 5.13).

5. 2.3 Aluminum nanostructuration

Similarly to the lithography step, the metal nanostructuration is one of most critical and challenging step in the fabrication of plasmonic filters. The quality of the etching has a determining impact on the plasmon resonances and on the filters' performance. Namely, dimensional variations and etching slopes are two expected issues regarding the Al nanostructuration, as presented in *Chapter 4*. Indeed, previous developments of plasmonic filters led at the CEA Leti attempted to perform the nanostructuration of the filters with the use of nano-imprint lithography [134], [171]. The results demonstrated a good transfer of the patterns shape into the resist, but significant dispersions of the holes shapes and dimensions after the metal etching, where etching slopes can also be noticed. In the light of this work, the structure was adjusted to obtain a better compliance of the pattern after the aluminum etching with the use of an 80-nm-thick SiO₂ hard mask, as described in 5. 2.1 *Materials and interfaces quality*. It is aimed to prevent the overexposure of the top edges of the apertures to the plasma, thereby avoiding an excessive consumption of the metal at the holes entrance. Sharper and more accurate pattern contours and profiles are thus obtained.

The first step of the nanostructuration is the etching of this hard mask. It is performed with a dry etching using $\text{CF}_4/\text{C}_4\text{F}_8$ as reactive gas in a O_2 plasma. Before the Al etching, a stripping is done in order to remove the fluorinated residues. Indeed, their presence leads to the formation of AlF_3 , which is obtained in solid-phase and thus severely degrades the quality of the ulterior Al etching. A stripping step is also performed after the aluminum etching. An overview of the result of the hard mask etching is provided in Figure 5.17 with tilted SEM observations. A few indicative measurements were made on the three observed arrays of Figure 5.17 for the initial base. Notable size increases of the SiO_2 patches were found (measurements made at the base of the patches in the pictures, averaged when several measures were available): 49 %, 30 % and 22 % for respective targets of 85 nm, 100 nm and 135 nm. These increases in dimensions should be transferred in the metal after Al etching, and it has to be noted that the hard mask etching may already induce an important dispersion. The hard mask etching was thus performed as a second attempt in another equipment with lower ionic bombing, which implies less faceting of the patterns and a better control over the dimensions. No characterizations were made directly after the hard mask etching, but the results after Al etching presented in the following indicate a noticeable benefit.

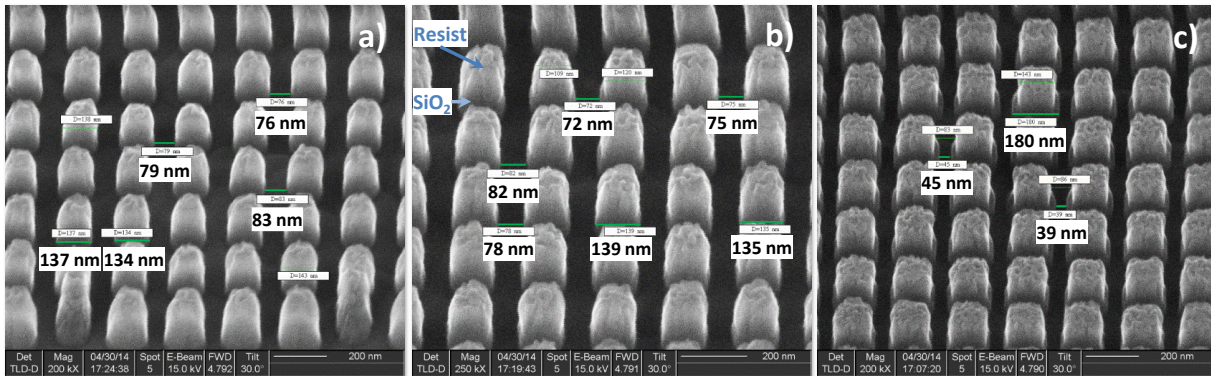


FIG. 5.17. Tilted SEM observations of the hard mask etching for three arrays of the right-hand chip of the initial base: (a) 85 nm, (b) 100 nm and (c) 135 nm.

The aluminum etching was then performed by dry etching with a Cl_2/BCl_3 gas mixture in Ar plasma, where BCl_3 is especially used for the removal of the surface native oxide Al_2O_3 [201]. The SiON was used as a stop layer with end point detection by sensing the nitrogenous gas. A few patch arrays were observed in SEM, and their measurements provide interesting information regarding the size dispersion and the etching slopes. Four of them are given in example in Figure 5.18. In order to avoid charging issues due to the underlying dielectric medium, the samples were metalized with an Au/Pd alloy. At first glance, it can be seen that the profiles are clear-cut, but inclined for small patch sizes. The increase in size suggested with the observations performed after the hard mask etching is also well noticed. Although the dimensions are not exactly respected, the large patches obtained in Figure 5.18(c)-(d) demonstrate at the same time the ability to etch very thin cavities with aspect-ratios close to 3.5 with an Al thickness slightly superior to 200 nm. This observation is particularly interesting for the further realization of hole arrays with tiny dimensions.

For all the observed arrays of the initial base, the measured data regarding the patches size at the top and at the bottom of the filters, and the corresponding slopes are gathered in Figure 5.19. Since different measures were made in the case of the 100 nm array, only the average values are drawn. The calculated relative errors confirm the size increase of the metal patches compared with their electron-beam patterns. A notable gap is observed between the errors at the top of the metallic patches and at their base, which seems to decrease when the patches get wider. From these errors, the etching slopes can be derived by assuming a symmetric profile of the patch according to their height. The slopes are low and are between the optimistic case of 2.5° and the medium case of 5° studied in *Chapter 4*, with typical

values of 3.2° for the 100 nm array (100-nm-wide trench) and 2.1° for the 140 nm array (60-nm-wide trench). These slope values augur well for the realization of ALS filters whose cavities' dimensions are of comparable width. The spatial confinement of holes compared with trenches in the case of metal patches may lead to slightly different results though. The decrease of the etching slopes with the patch size confirms that the difference between the top and the bottom dimensions diminishes with larger patches. On the chart, we also add the dispersions that were extracted from the same arrays on the same wafers right after the electron-beam lithography. A good correlation and only small differences can be noticed between the errors measured after EBL and those measured at the top of the patches after the etching. The comparable errors between the two process bricks suggest that both the hard mask and the aluminum etching steps do not actually induce a significant size variation compared with what is obtained after lithography. These results are promising and demonstrate the benefit of the equipment change for the hard mask etching in order to obtain more accurate dimensions compared with Figure 5.17. It can eventually be noted that the increase in dimension is the highest at the bottom of the patches. In the case of hole arrays, we saw in *Chapter 4* that it is better to have the targeted CD (Characteristic Dimension) respected at mid-height to minimize the impact on the ALS performance. While this work has not been led in this thesis, it would be necessary to fine tune the etching bricks so that the profiles get closer to the ideal case where there is a slight size excess at the top and a slight size decrease at the bottom, like the results observed on the 140 nm array.

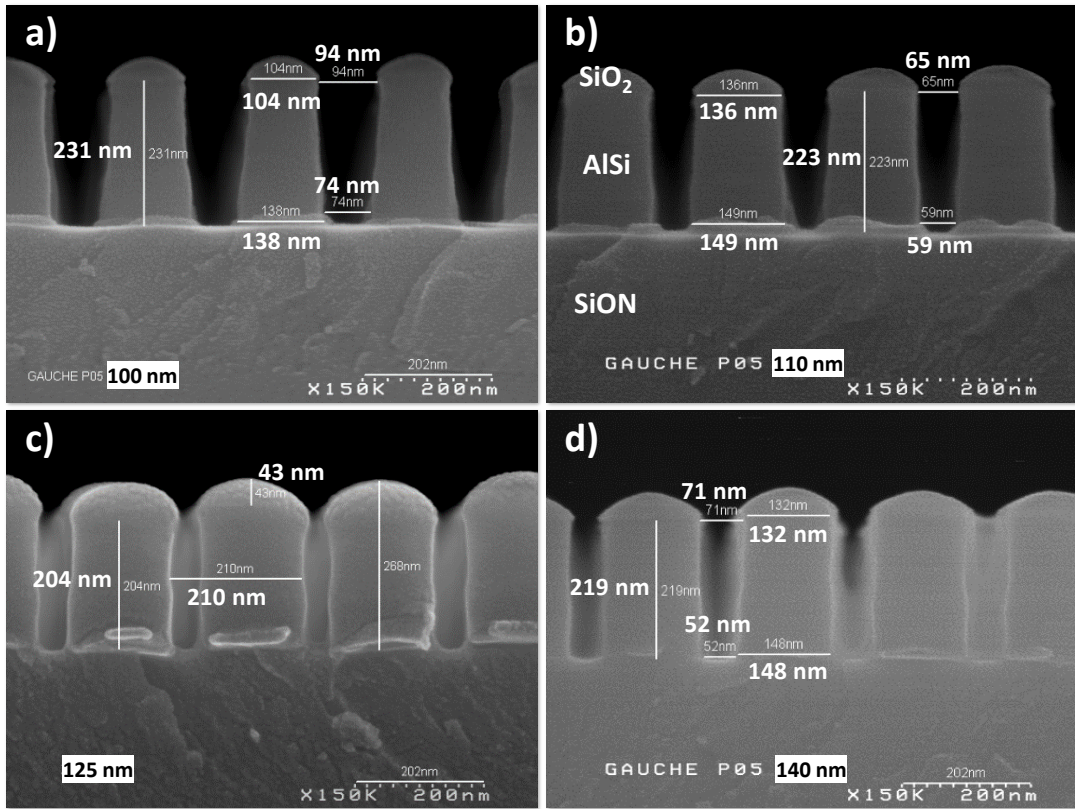


FIG. 5.18. SEM cross sections of the aluminum patterning for four arrays of the initial base: (a) 100 nm, (b) 110 nm, (c) 125 nm and (d) 140 nm.

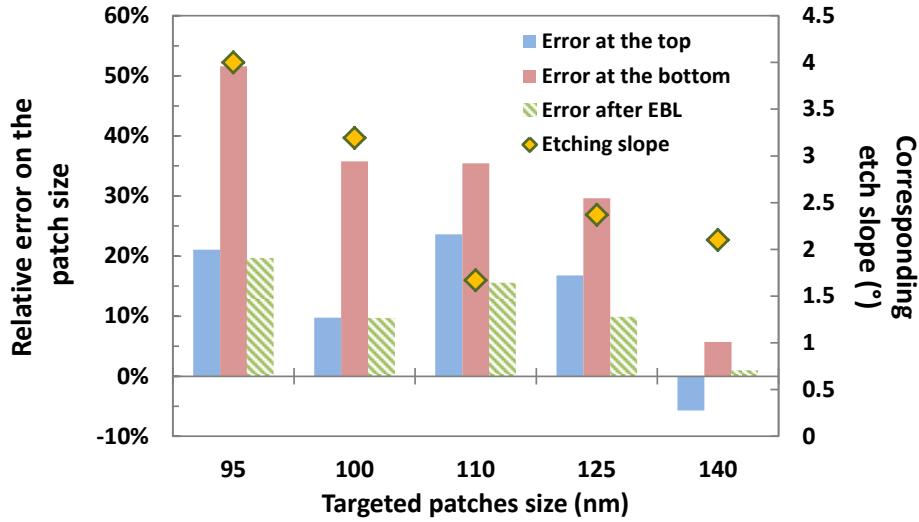


FIG. 5.19. Relative error on the patch size of the measured arrays of the initial base compared to the target. The calculated etching slope for each array is also drawn. The errors that were obtained after the electron-beam lithography on the same wafers from which the post-etching measurements were made are also given. In the case of the 100 nm array for which different measurements were made, the errors are averaged, and the slope is averaged over the slopes obtained for the different measurements.

In the case of the optimized base, the change of the photoresist led us to use a thicker SiO_2 hard mask of 120 nm. Since no SiON was used in the stack for this study, the thickness removal of aluminum was adjusted from the etch rate of the material. We saw in the EBL brick that the crosses gave poor shape definition without proximity effect corrections. We will thus now focus solely on the analysis of ALS arrays designed with square holes (L_A4, L_B4, R_C1 and R_C2). We present an illustration of the metal etching with the R_C1 array in Figure 5.20, that shows SEM observations in normal and tilted top views for an AlSi thickness of 200 nm. From the top, a double contour can be observed inside the apertures with a width between approximately 10 nm and 20 nm depending on the holes. While this corona could be at first glance attributed to etching slopes, a closer look at Figure 5.20(b) suggests that this could rather be due to a slightly wider aperture in SiO_2 than in aluminum. The apparent roughness that can be seen on the sides of the holes however makes it hard to conclude. We propose in Figure 5.21 SEM cross sections of three arrays of squares for AlSi thicknesses of 200 nm and 275 nm. It can be seen in Figure 5.21(a) and Figure 5.21(c)-(d) that the remaining hard mask can indeed create a capping with a slightly thinner width than the metallic walls on which it stands, in the order of 10 nm. The pictures also confirm the irregular profiles of the apertures, which maximum amplitude can reach approximately 30 nm for a typical hole size between 170 nm and 180 nm. The metallic flange at the entrance of the holes, beneath the hard mask is observable on the four arrays of squares, for the two aluminum thicknesses of 200 nm and 275 nm. We note from our other SEM pictures that the etching profile is generally irregular in the top half of the holes, whereas the profile is smoother and straighter in the lower half. Although the overall morphology is not exactly comparable, the profiles at the top of the apertures' sidewalls are close in some locations to the T-shape observed by Yoon *et al.* [100], that they attributed in their case to low-pressure dry etching.

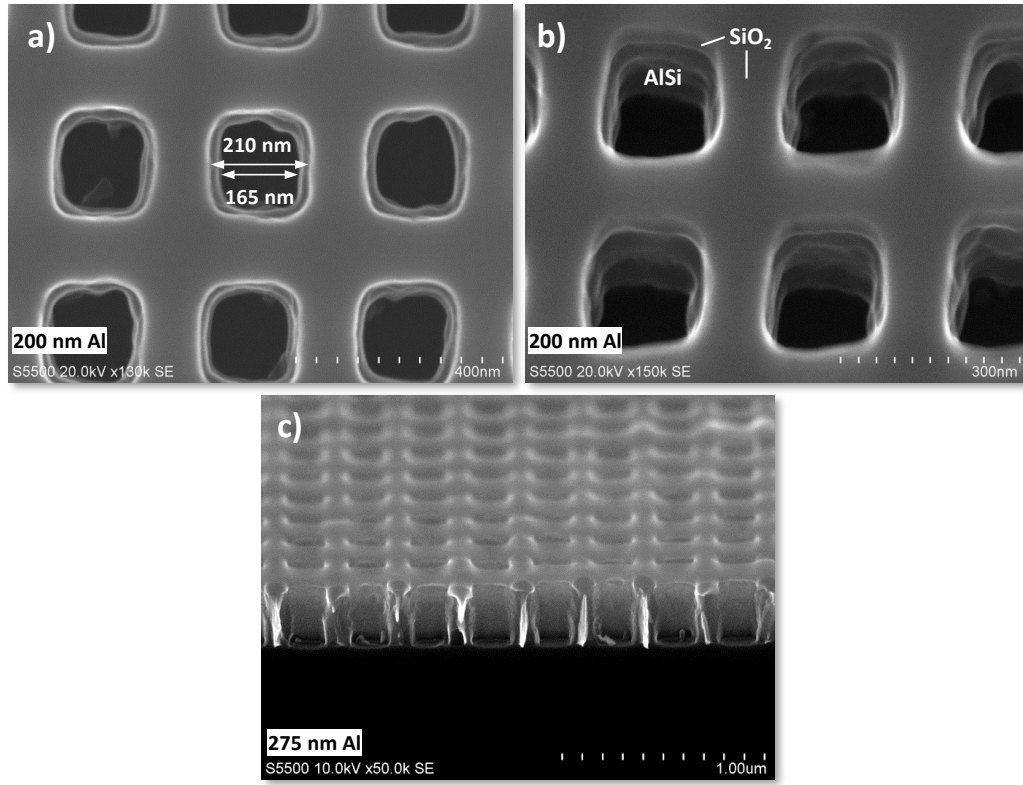


FIG. 5.20. SEM observations of the R_C1 array of the optimized base for an AlSi thickness $h_m = 200$ nm in (a) top view and (b) tilted top view. (c) Global view of the hole array for $h_m = 275$ nm.

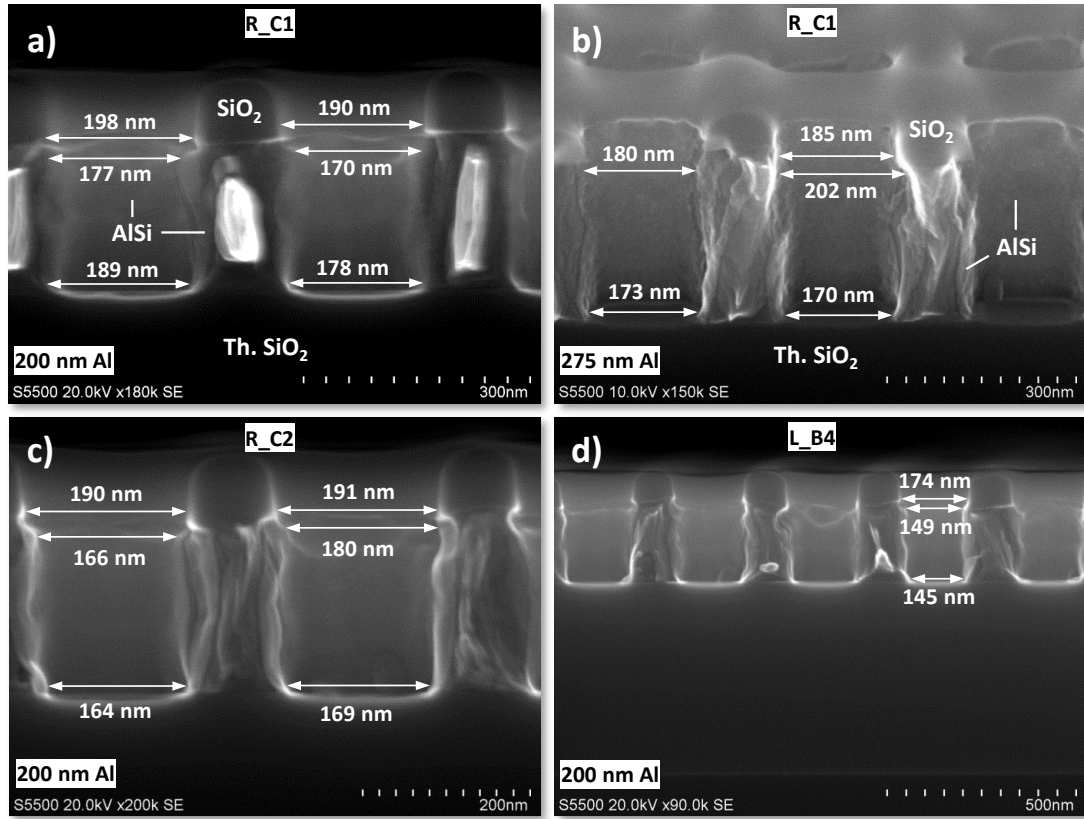


FIG. 5.21. SEM cross sections of three ALS arrays of squares from the optimized base: (a) R_C1 with $h_m = 200$ nm, (b) R_C1 with $h_m = 275$ nm, (c) R_C2 with $h_m = 200$ nm and (d) L_B4 with $h_m = 200$ nm.

We measured the size of the holes at both the entrance (top) and the exit (bottom) of the apertures in a few holes for each array of squares and for each thickness. Regarding the size at the entrance of the holes, we ensured to measure the size just beneath the hard mask, and not at the level of the flange like it is the case in Figure 5.21. We draw in Figure 5.22 the mean relative error calculated from these measurements for each situation. The maximum and minimum observed errors are also given. It is difficult to identify any clear trend given the very low number of samples and by considering the measuring inaccuracies. Nevertheless, it can be noticed that the mean relative errors on the holes size are beneath 7 % for both the entrance and the exit, which is a value entirely comparable with the errors obtained after lithography (Figure 5.15). Although the measurements after EBL and after etching were not performed on the same wafers, it can be assumed that the etching brick does not induce a notable additional size variation compared with the EBL. The only exception to this observation is the R_C2 array with $h_m = 275$ nm for the mean relative error at the top, which reaches 14 %. However, the results suggest a noticeable dispersion in the hole size within the a given array, with difference in relative error between the highest and the lowest measured sizes than can reach 20 % on the L_A4 array. The impact of such size dispersion into the same array on the spectral response is an additional process-related issue than has never been addressed and investigated so far. In our study, we only simulated a constant size variation of all the holes in the same time, but this new consideration would constitute an interesting complement for the potential industrialization of plasmonic filters. It has to be noted than in the cases of the arrays R_C1 and R_C2 at 275 nm, very few measurements were available, which explains their low dispersion compared with the other arrays. We have seen that the etching profiles were a bit irregular, with size variations between 10 nm and 30 nm inside the holes. Consequently, it is not rigorously possible to deal with etching slopes with our experimental results. A comprehensive engineering development of the etching brick would be required to evaluate the potential ways to limit the holes size dispersion and to etch the apertures with sharper profiles, which was not possible in the time allocated for a thesis. For comparison with our study of *Chapter 4*, we nevertheless provide the values of *effective* slope calculated from the top and bottom measurements, which would correspond to a simplified aperture profile neglecting the irregularities of the holes sidewalls. The mean effective slopes of the four arrays of squares for each thickness are between 0.6° and 2.6° , but a mean of -0.6° is also calculated for R_C1 at 200 nm. This negative value means that the widths were slightly thinner at the top than at the bottom. Among our measurements, we only count an isolated maximum of 6° . These values are lower than what we simulated, but our simulations and these effective slopes do not take into account the random irregularities of the etching profiles, whose impact on optical properties remains to be properly investigated.

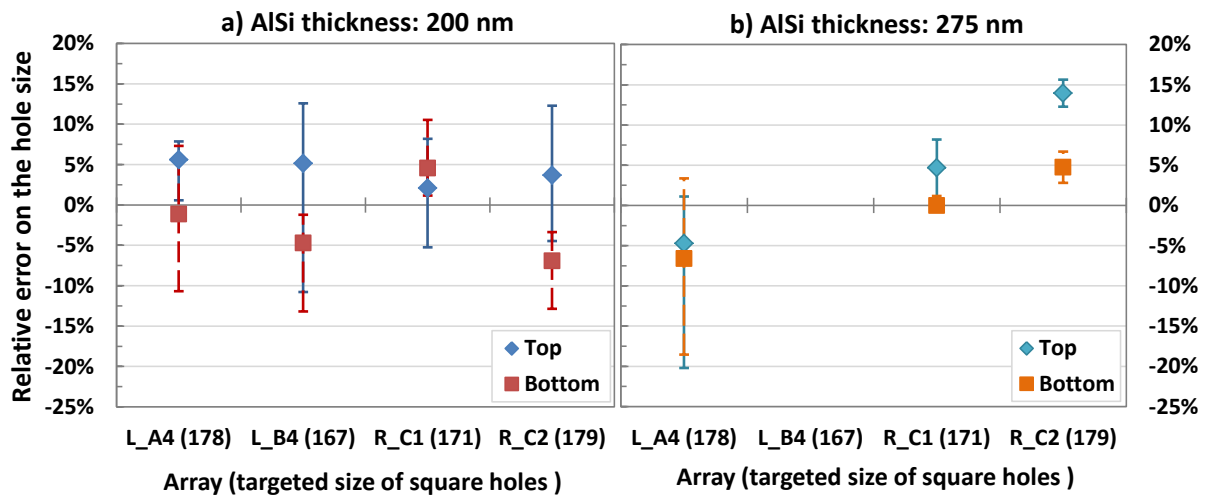


FIG. 5.22. Mean relative error of the square sizes at the top and at the bottom of the hole obtained from our measurements for each array with a) $h_m = 200$ nm and b) $h_m = 275$ nm. The data for L_B4 at 275 nm were not available. The bars give the maximum error amplitude observed for each array.

5.2.4 Holes filling

After the nanostructuration of the metallic layer, the apertures have to be filled so that the dielectric permittivity is homogeneous around the metal. We saw in *section 4. 5.1* that having similar metal-dielectric interfaces on holes sidewalls and at the top and the bottom surfaces of the filter was preferable to excite the same plasmon and thus to enhance the extraordinary transmission phenomenon. In the same time, we demonstrated that in the case of hole-array structures, the presence of air gaps within the apertures could substantially alter the spectral responses of the filters depending on the gaps' volume ratio (*section 4. 5.2*). Typically with our model, the volumetric fraction of the air gaps has to be below 4 % to limit their impact on ALS performance. Higher values quickly decrease the transmission of the filters and shift the resonance towards blue wavelengths. Consequently, the hole-filling brick has been identified as a critical step for the fabrication of our ALS demonstrators. With thick metal films and holes' dimensions below 200 nm, the filling of these nanostructures with no or minimum air gaps may indeed be challenging.

Although our initial base was not using hole arrays, it provided metallic structures with small apertures to fill. Indeed, larger metal patches necessarily create small cavities in-between them. The dimensions used for the patches of the different arrays gave us trenches with aspect-ratios ranging from 1.4 to 3.3 for an AlSi thickness of 200 nm, which are directly comparable to those of our hole-array structures. The first trials on this initial base were thus able to deliver relevant information regarding the capability of our process integration to fill such structures, and by extension, our ulterior ALS hole-arrays. The hole filling was first performed on the initial base with a common PECVD equipment with a deposition of a 500-nm-thick SiO₂ layer at 400°C using a TEOS (tetraethyl orthosilicate) precursor. This thickness is necessary for the ulterior bonding on glass wafer. We then performed SEM characterizations of a few arrays to verify the quality of the filling inside the structures. A few cross-section SEM observations are given in Figure 5.23. The presence of air gaps can be observed on the four pictures, which are characteristic of what we observed for larger patch sizes (above 100 nm), i.e. smaller cavities. When comparing Figure 5.23(a) and Figure 5.23(b) which show the same 100 nm array at different locations on the sample, it can be clearly seen that the voids size and profile is not similar depending on where the cleaving is done. In Figure 5.23(a), the sample is cleaved at the middle of a patches line, this is why we can distinguish the metal patches and observe the granular structure of AlSi. On the contrary in Figure 5.23(b), the cleaving felt between two patches line. Small pieces of AlSi are visible in the foreground and correspond to a first line of patches that has been cut at the base during the cleaving. In the middle ground, the patches cannot be directly seen because we only see the SiO₂ layer covering the metal of the second patches line. From these two pictures, it can be deduced that in the case of patch arrays, the air gaps have a cruciform shape viewed from the top and are centered in the middle of four patches, where the voids are bigger. In this location, we can estimate from Figure 5.23(b) that the voids are about 150 nm high and 30 nm wide for the 100 nm arrays, that are representative of the hole sizes in ALS filters. Their size progressively decreases along the crosses' arms as we get farther from their center. Accordingly, their size reaches its minimum values at the middle of a patches line, between two neighboring metal patches. From Figure 5.23(a), their height ranges from approximately 20 nm to 50 nm for a width of about 30 nm. An important feature which is visible on all pictures is that the holes are located above the metallic patches. The voids are thus located at the top of the filters. Logically, in this location, the voids are expected to have less influence on optical properties than when located just between the metallic patches. We performed additional SEM characterizations on the 100 nm array with a Focused Ion Beam (FIB), which allows for a more accurate location of the slicing with respect to the lines of patches. In Figure 5.23(c) where the cleaving was slightly skewed, the evolution of the gaps size when we get farther from the middle of a patches line can clearly be observed. On a side note, we notice that voids are a bit easier to distinguish with FIB-SEM characterizations than on SEM. We did not have enough characterizations to accurately evaluate the size of the air gaps as a function of the dimensions of the arrays, but the same trend were observed on the 125 nm array (Figure 5.23(c)) and the 140 nm array

(not shown). In practice, the volumetric fraction of air gaps that we defined in *Chapter 4* for hole arrays is not really transposable to patch arrays, and would still be complicated to evaluate with 2D characterizations only. Nevertheless, these results are sufficient to highlight the difficulty of a classical PECVD process to properly fill such small nanostructures with high aspect-ratios. Considering our study of voids in hole arrays, the risk of formation of wide and detrimental voids could not be taken in the case of our ALS designs and a new filling solution had to be investigated.

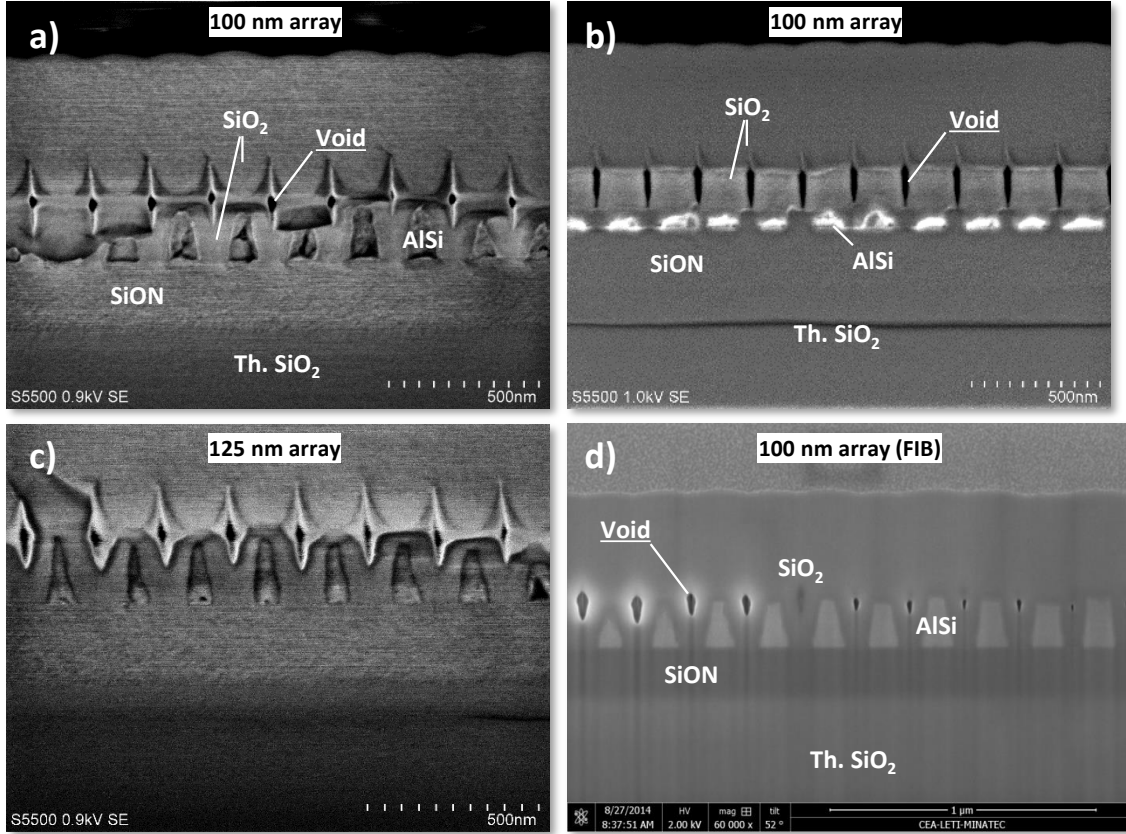


FIG. 5.23. SEM slice views of the initial base after holes filling with SiO₂ for: (a) a 100 nm array, (b) the same 100 nm array in another location and (c) the 125 nm array. (d) FIB-SEM observation of the same 100 nm array. Air gaps are clearly visible on each picture.

We had the opportunity to perform the hole-filling step in the 200-mm clean room of STMicroelectronics, where the use of a High-Density Plasma Chemical Vapor Deposition (HDPCVD, that we will simply call HDP) process was proposed. HDP is also known as *gap filling* and constitutes a deposition process that is typically aimed for the filling of small spaces with high aspect-ratio with a low thermal budget [202]. The combination of a high plasma density and a low pressure results in simultaneous deposition of the precursors and sputtering of the deposited film due to the high ions density. The interest of such a method lies in the fact that the sputtering rate depends on the angle formed by the attacked surface with respect to the horizontal plane. The film deposition is faster on horizontal surfaces (0°) than on gap walls (90°). However, the sputtering, which leads to a removal of the deposited material, is more important on surfaces inclined with an angle close to 45°. These two opposite phenomena lead to higher deposition rates on plane surfaces (in our case, the top of the patches and the bottom of the cavities), whereas the material grows more slowly on inclined surfaces (the top edges of the patches) due to the higher sputtering rate. This slope-dependence of the deposition and sputtering rates prevents the obstruction of the cavities before they are entirely filled and thus limits the formation of voids. The filling capability of HDP deposition is generally characterized by the deposition

to sputtering ratio D/S , where D stands for the sum of the net deposition rate (of the precursor) and of the sputtering rate (of the ions), and S for the sputtering rate alone. Low D/S values imply a better filling of high-aspect-ratio structures, but at the cost of a lower growth rate of the film.

The filling of our structures was performed with the deposition at 450°C of a 700-nm-thick SiO₂ layer from SiH₄ and O₂ precursors in an Ar plasma. The process was split into two steps, with first the conformal deposition of an adhesive 40-nm-thick SiO₂ layer, followed by the deposition of the remaining 660 nm with plasma etching (stronger sputtering related to the higher density of the plasma). The D/S ratio used in our case was 2.8. The corresponding SEM characterizations after holes filling are given for a few arrays in cross sections in Figure 5.24, mainly realized with FIB. The 85 nm and the 100 nm arrays reveal a total absence of voids in the cavities, which constitutes a major improvement from the results obtained with the PECVD SiO₂ of Figure 5.23. The measurement of the AlSi thickness (240 nm approximately) and the quality of the filling thus demonstrate the ability to fill structures with aspect-ratios close to 2.7 with gap widths of about 90 nm in a 240-nm-thick aluminum layer without any voids. The process we used however shows its limits with the 125 nm array which reveals the presence of air gaps, whereas this is not the case with the 140 nm array. This difference may be explained with the facts that the 125 nm array has been shown throughout this whole section to have a higher size increase compared with the 140 nm array and that the cross section may have been performed in a more favorable zone for the 140 nm arrays since the patches are thinner than the targeted dimensions on the picture. A finer tuning of the HDP deposition could certainly improve the filling of these more aggressive arrays, but the optimization of the process was not part of the scope of this work and the results we obtained from the 100 nm array were encouraging enough to use this method with hole arrays.

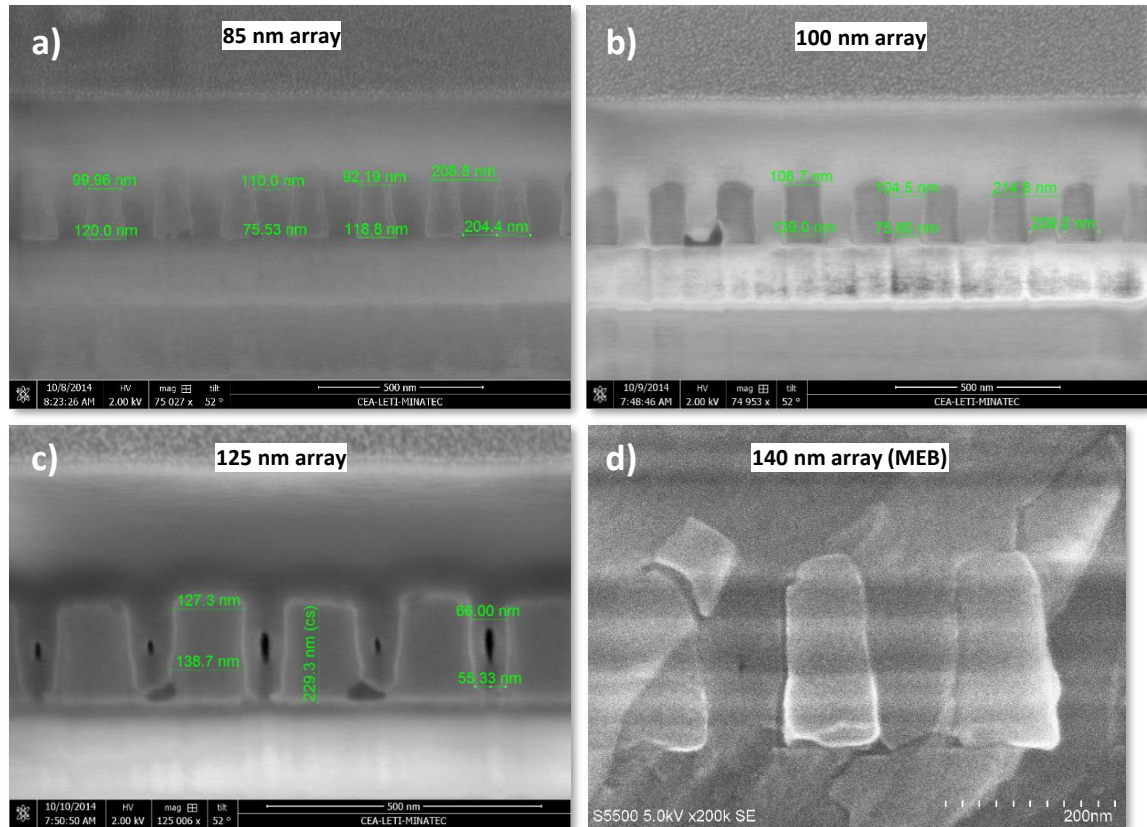


FIG. 5.24. FIB-SEM cross-section observations of the initial base after holes filling with a HDP process for: (a) the 85 nm array, (b) a 100 nm array and (c) the 125 nm array. (d) SEM cross-section observation of the 140 nm array.

Although the finalization of the process development and the optical characterizations will entirely be presented in the next sub-section, we provide here the optical characterizations obtained with the final patch-array structures for both the PECVD and the HDP depositions in Figure 5.25. The measurements were made with a micro-spectrometer whose characteristics are specifically described in the next sub-section. The results correspond to the optical responses measured from the same 100 nm array on different wafers. Only one of those wafers used HDPCVD, the other ones were fabricated with the PECVD holes filling. It can be seen that the spectrum obtained with HDP deposition is very similar to the spectra obtained with PECVD, which are themselves very close to the simulated response with the same material stack. No obvious distinction can be made between the two deposition processes, thus the impact of air gaps and the benefit of HDPCVD cannot be identified on the spectral response of the filters. Actually, a first-approximation modeling of voids in a patch array embedded in an infinite SiO_2 medium demonstrates that even with large air gaps, the impact is minimal on the filter's response, be it in transmission or in reflection (Figure 5.25(b)). This explains the high level of similarities between the filters obtained with the two deposition processes. Furthermore, the simulations show that the transmission (or reflectance) variations theoretically induced by the presence of voids are of the same order of magnitude that the wafer-to-wafer reproducibility observable with the three wafers which were filled with PECVD. No conclusion can thus be drawn from the optical characterizations of patch arrays on the choice of the filling process. Nonetheless, it does not invalidate the benefits of HDPCVD since patch arrays seem nearly insensitive to voids, unlike hole arrays. Regardless of this inconclusive optical comparison, a HDP filling was thereby used for the fabrication of the optimized base.

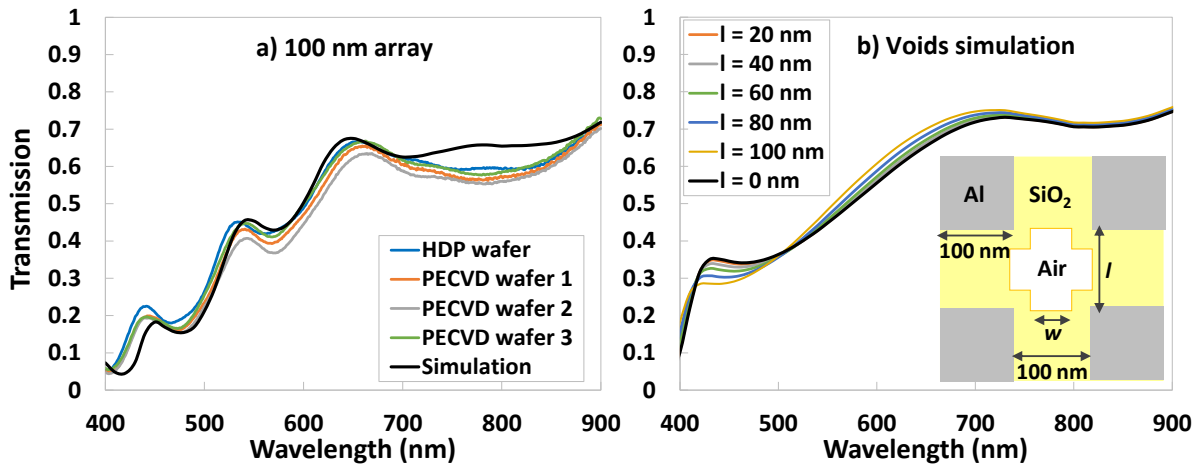


FIG. 5.25. (a) Comparison of the transmission measurements between the structures filled with HDPCVD and PECVD. A simulation of the stack is also provided. (b) Rough modeling of air gaps in a patch-array filter embedded in an infinite SiO_2 medium with the same period (200 nm) and patches size (100 nm) than the measured structures. The voids are modeled according to a cruciform air gap between four patches, with varying arm length l and with $w = 0.5 \cdot l$.

FIB-SEM cross-sections observations were performed on the hole arrays of the optimized base filled with HDPCVD for 200-nm-thick AlSi. We show cross sections of the array of squares L_A4 (Figure 5.26(a)) and of the array of crosses L_A1 (Figure 5.26(b)). The array L_A1 has the particularity of featuring the smallest and thinnest ALS crosses of the optimized base, with $a = 167$ nm and $b = 67$ nm ($b/a \simeq 0.4$). It thus constitutes a relevant gauge to evaluate the capability of an industrial deposition process such as HDPCVD to fill nanometric cavities, especially in the case of ALS designs. The observations reveal that the apertures are perfectly filled with SiO_2 both in the case of squares ($a = 178$ nm) and in the case of crosses. These results are particularly encouraging, especially if we pay attention to the fact that the FIB-SEM cross-section of the cross-array of Figure 5.26(b) was performed along the arm width b , which constitutes the smallest dimension of crosses. We have thus demonstrated that

HDPCVD is capable of filling hole arrays without air gaps with cavities thinner than 70 nm and with an aspect-ratio of 3, which proves that the hole-filling step is not critical for an industrial production at wafer-scale of plasmonic ALS filters.

The good results of the hole-filling step validated the integration route we defined for the manufacturing of plasmonic filters using processes of a CMOS front-end 200-mm fab, with the etching of the aluminum and the filling of the apertures with SiO_2 . In order to perform transmission measurements on the obtained structures, we will now present the bonding on glass wafer.

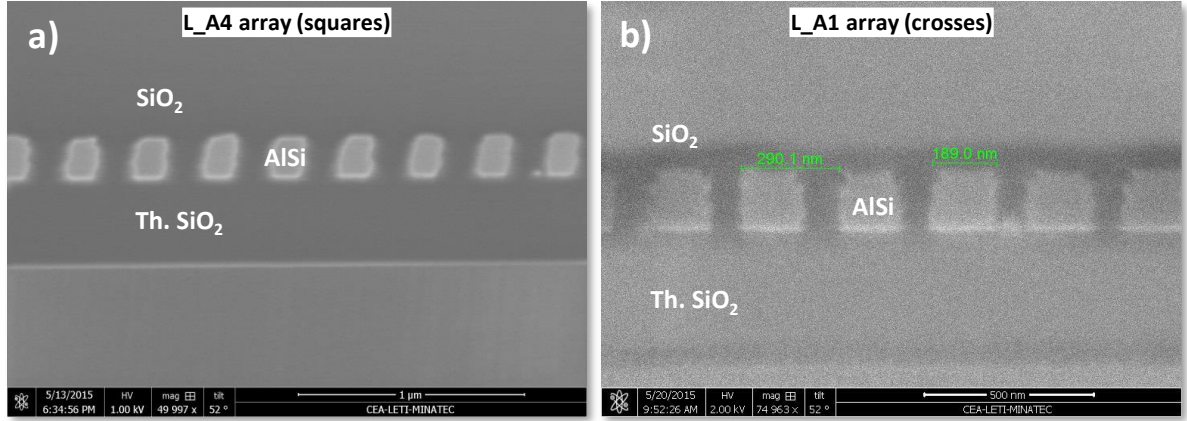


FIG. 5.26. FIB-SEM cross-section observations of the optimized base after holes filling with a HDPCVD process for: (a) the ALS array of squares L_A4 ($P = 296$ nm, $a = 178$ nm); (b) the ALS array of crosses L_A1 ($P = 275$ nm, $a = 167$ nm, $b = 67$ nm).

5.2.5 Validation of the bonding on glass wafers

The hole-filling brick constitutes the last step of the filters fabrication since the metal is patterned, the holes are filled and the dielectric medium surrounding the metallic layer is homogenized. If the filters were realized on a CMOS sensor, the process integration related to plasmonic filters would end at this point. However in our case, we want to optically characterize the obtained structures with the help of transmission measurements. Because of the Si substrate, such measurements cannot be made with our structures since silicon is opaque to visible wavelengths. It was thus necessary to develop a process brick in order to transfer the structures on a glass wafer and to remove the silicon substrate so that transmission measurements were made possible. In this sub-section, only the development on the initial base is described, and the results are evaluated directly through optical characterizations. The subsequent results obtained with the optimized base will be described separately in the *section 5.3* of this chapter. The transfer was envisioned with a direct bonding method of the SiO_2 layer used for the holes filling on 200 mm glass substrates, as described in Figure 5.2.

Direct bonding, or molecular bonding, is a technique that consists in the spontaneous adhesion of two surfaces without using any intermediate layer or material such as a polymer-based glue. In the case of a $\text{SiO}_2 - \text{SiO}_2$ interface, the bonding mechanism can be described as the creation of low-energy Van der Waals and hydrogen bindings between the two surfaces owing to their hydrophilic nature, characterized by the presence of silanol groups (Si-OH) on a few angstroms [203]. The bonding occurs at room temperature when the adequate amount of energy, known as the energy of adhesion, is brought to the interface, but this bonding is fragile due to the weak character of the intermolecular bindings and the wafers can still be separated. An annealing is thus necessary in order to strengthen the bonding. The temperature increase creates stronger siloxane covalent bonds (Si-O-Si) and leads to a shrinkage of the inter-wafer spacing due to the diffusion of the interfacial water layer, which increases the energy of adhesion and then makes the bonding irreversible. Different mechanisms proposed to explain the

evolution of the interfacial bonding with temperature can be found in literature [204]–[206]. The realization of a reliable direct bonding imposes drastic constraints on the interface quality in order to avoid any detachment of the surfaces. In particular, the surface condition of both wafers has to be severely controlled at the macroscopic, mesoscopic and microscopic scales, which are respectively determined by the wafer bow, the wafer flatness and the surface roughness. Typical morphological criteria for a quality bonding recommend a maximum bow of about 30 μm for a 725- μm -thick and 200-mm-large Si wafer [207] and a maximum roughness below 6.5 \AA RMS [205], [208]. Furthermore, the bonding requires having surfaces free of any particular or organic contamination which would generate critical defects within the bonding interface. These conditions thus enforce the use of adequate treatments to obtain an optimal surface preparation before the bonding step itself.

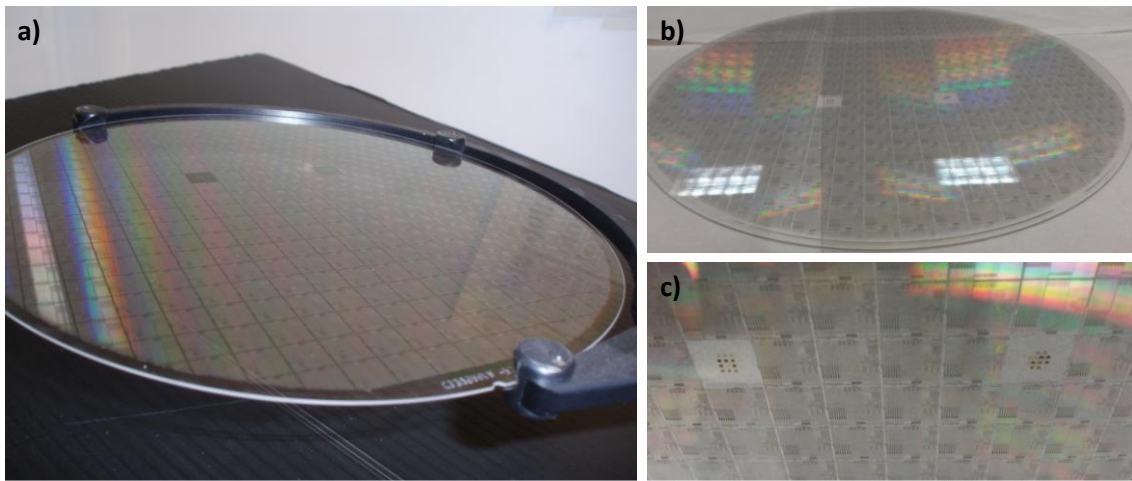


FIG. 5.27. (a) and (b). Wide views of the structures layout of the initial base bonded from a 200 mm silicon wafer onto a 200 mm glass wafer. (c) Closer view of the two electron-beam fields, each one featuring nine arrays of patch-array filters.

The direct bonding was naturally developed on the initial base. The few differences compared with the hole arrays regarding the plasmonic structures located below the bonding SiO_2 layer do not have any impact on the bonding process *a priori* and the technique can thus directly be applied to the optimized base with the same conditions. The surface preparation consisted first of a CMP of the SiO_2 layer used for the hole-filling step so that the surface flatness condition is respected. However, profilometry measurements revealed a significant topography outside of the electron-beam fields. It was characterized by a dense concentration of spikes with a peak-to-valley height of about 1 μm , whereas the objective was to flatten the profile variations of the 700-nm-thick SiO_2 layer generated by the patch arrays (see Figure 5.4). An irregular profile with such intensity cannot be planarized efficiently for a surface preparation aimed towards a direct bonding. Additional characterizations with an optical microscope permitted to conclude that this topography resulted from the formation of AlSi hillocks on the aluminum layer that had not been etched on the whole wafer surface outside of the electron-beam chips where the arrays were fabricated. In order to soften this critical topography, an extra 2- μm -thick SiO_2 layer was deposited at 400°C from a TEOS precursor, which appeared to be sufficient to perform the planarization with a gross CMP. TEOS-based SiO_2 being especially hydrophilic, the wafers were annealed at 400°C under N_2O_2 for 2 hours in order to dry the oxide and to avoid any issues caused by the potential water or hydrogen degassing during the ulterior bonding anneal. The top surfaces of both the treated wafers and the glass substrate then endured a finer CMP and a surface cleaning to ensure that the roughness is below 6.5 \AA and that there is no particular contamination, in accordance with the required surface conditions described above. Subsequently, the two surfaces are put in contact to realize the direct bonding itself, and the bonding anneal is finally performed for 2 hours at 400°C in a N_2O_2 atmosphere. A

defect control of the bonding interface was done before and after the annealing with a Scanning Acoustic Microscopy (SAM), which consists in transmission and reflection measurements of an acoustic wave propagating through the materials [209]. Potential defects, such as water or air gaps, are identified by abrupt variations of the acoustic impedance $Z = \rho \cdot c_a$, where ρ is the density of the material and c_a the propagation speed of the acoustic wave in this material. No defects were identified in our case. Finally, the silicon substrate endured a rough grinding to remove the bulk material over about 665 μm , and the remaining 60- μm -thick Si layer was then removed with a refined wet etching using TMAH (tetramethylammonium hydroxide) until the thermal SiO_2 was reached. The obtained bonded structures are illustrated with pictures in Figure 5.27.

We present in Figure 5.28 transmission measurements done on typical arrays of the initial base with the wafer on which hole-filling was performed with HDPCVD. The spectra were measured under normal incidence with the micro-spectrometer mentioned in *section 5. 2.4*. The set-up consists of a lamp which light is sent through an optical fiber onto a diffractive array. The array we used in our case allowed for a wavelength range between 350 nm and 900nm that we could use for the transmission measurements in the visible and NIR ranges. The diameter of the spot on the plasmonic arrays was 20 μm . From this chart, a distinct and consistent evolution of the spectral responses with the patch size increase can be noticed with the exception of the 125 nm array. Larger arrays such as the 125 nm and 140 nm ones seem to noticeably deviate compared with the 130 nm array whereas their targeted dimensions are very close. A recall of the size variations after aluminum etching for these three arrays is given in Figure 5.28(c)-(d). It explains this difference: while the patches size of the 130 nm array is almost respected, the 125 nm array actually reveals a patches size closer to 150 nm, which is comparable to the dimensions obtained with the 140 nm array. This observation is not surprising given the fact that the overall process was not developed to accurately fabricate the filters. Moreover, the disparities in the targeted dimensions among the 16 arrays complicate the use of a process that is optimized for each patch size. In the case of a product with only a few different filters, it would be easier to develop a fabrication route specifically dedicated to their dimensions. There were three 100 nm arrays featured on the initial base, which are more representative of our targeted ALS dimensions in the case of hole arrays. The measurements of these arrays demonstrate a very good intra-wafer repeatability of the process for these dimensions. One can also observe small oscillations on the spectral responses, which are due to interference phenomena inside the materials stacks.

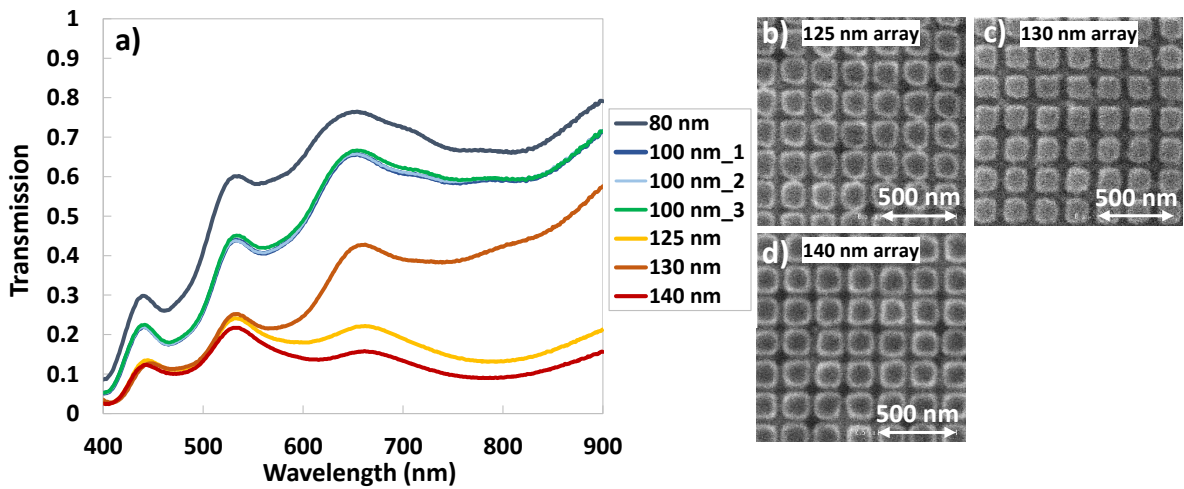


FIG. 5.28. (a) Transmission measurements with a micro-spectrometer made on a few arrays of the initial base. CD-SEM observations after aluminum etching are provided for large arrays including: (b) the 125 nm array, (c) the 130 nm array and (d) the 140 nm array.

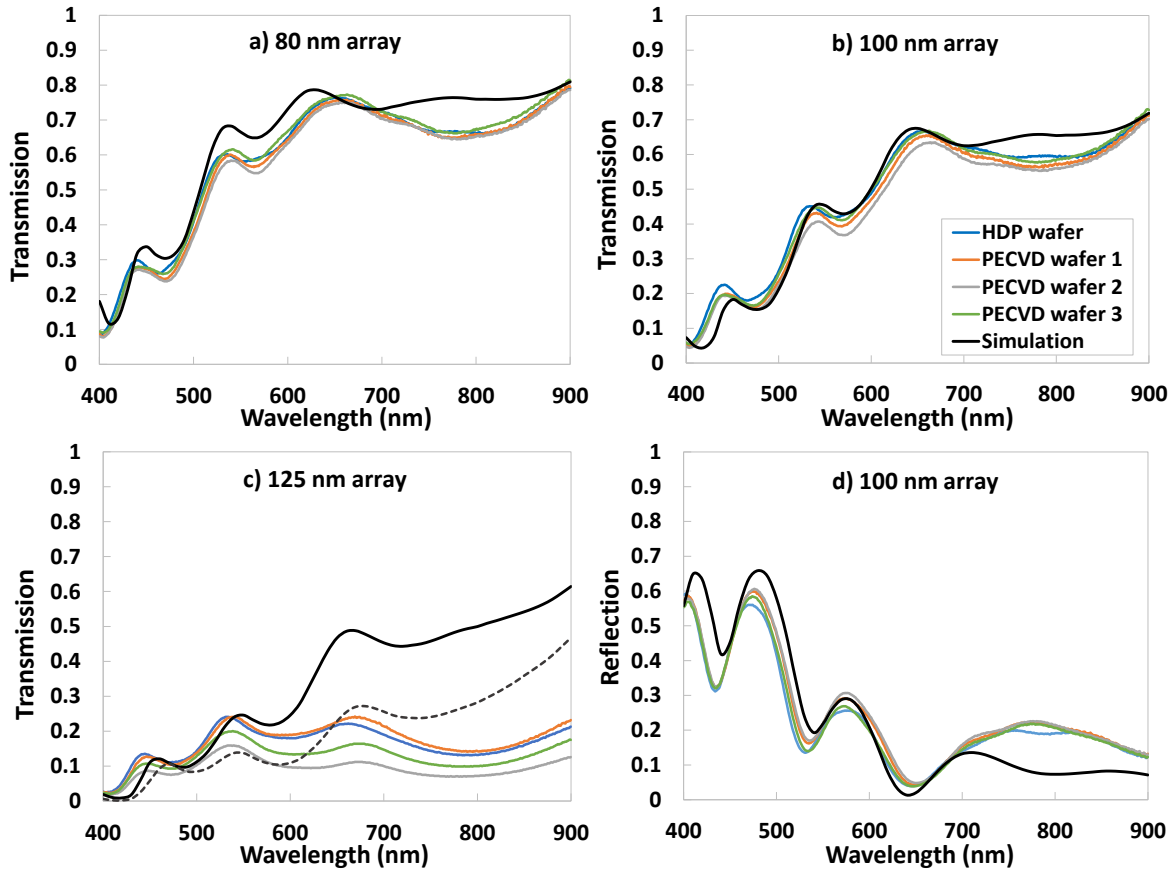


FIG. 5.29. Comparison of the simulations and the transmission measurements made with a micro-spectrometer on the wafer using HDPCVD and three wafers using PECVD during the hole-filling brick on the initial base for: (a) the 80 nm array, (b) a 100 nm array and (c) the 125 nm array. In the case of the 125 nm array, a simulation with patches size of 150 nm is added in dashed line. (d) Reflection measurements and simulation of the 100 nm array with the glass substrate at the bottom (SiON above AlSi).

The responses in transmission of the main filters are compared with simulations represented with black curves in Figure 5.29 for the four wafers available. The simulations take into account the glass substrate and the thermal SiO₂ – air interface. The refractive indices of the glass substrate are obtained from CEA measurements ($n = 1.5009$ at $\lambda = 633$ nm with negligible n''). There is a good agreement between the simulations and the measurements for the 80 nm array, but the best fit is obtained with the 100 nm array, which measured spectra are actually superimposed with the calculated response. The process was typically developed so that the arrays with medium dimensions among all the initial base, i.e. the 100 nm arrays, are the most optimized ones. The results obtained for the 100 nm arrays thus demonstrate that accurate fabrication can be developed when the process route is dedicated to precise dimensions range. A deviation can however be observed in the NIR range from 700 nm where the simulations are slightly higher in transmission than the measured spectra, but this difference could not be addressed. For the 100 nm array, we also provided in Figure 5.29(d) reflection measurements performed with the glass substrate at the bottom, i.e. with the SiON layer located above the aluminum layer. The agreement with simulations is well respected, but the same deviation can be noticed in the NIR range. Finally, the transmission measurements on the 125 nm array show a clear deviation from the simulation above 550 nm, and even a disparity between the different wafers, which highlights the process inaccuracies that occurred for this array in particular. If we compare the simulation of the 125 nm array with the measured transmission of the 130 nm array in Figure 5.28, it can be seen that the spectral response is very close. This observation strengthens the fact that the results obtained for the 125 nm array are not due to the limits of our process to fabricate large patches (i.e., gaps inferior to 70 nm), but

rather to local process issues related to the fact that the various process steps were not optimized for these dimensions. The simulation of a 150 nm array in dashed line in Figure 5.29(c), which is closer to the actual dimensions of the fabricated 125 nm and 140 nm arrays, reveals that the deviation in the NIR range is still observed from thin to large patches sizes. This phenomenon is not explained. The 125 nm array put aside, these results also demonstrate an interesting wafer-to-wafer reproducibility which is encouraging for the industrial fabrication of ALS filters, although a statistical study would be required to formally conclude on this point. It seems also that plasmonic filters are able to endure anneals comparable to the passivation annealing described in sections 2. 2.1.2 *The performance criteria* and 3. B.1.1 *Evaluation of plasmonic filters performance*, which could improve their performance by decreasing their ALS dark values. Eventually, the agreement observed between simulations and measurements does not point out any obvious process-related effect, which validates the development performed at each step for the fabrication of our hole-arrays filters.

The same process route was thus used for the finalization of the hole-array filters. To avoid the topography issues related to the formation of hillocks on the metal layer outside of the electron-beam fields, the thickness of the SiO₂ layer used for the holes filling was increased to 2.5 μm . Approximately 1.5 μm were then removed during the surface preparation for bonding on glass. The optical characterizations of these ALS filters are presented in the next section.

5.3 Evaluation of the fabricated ALS filters

This part is specifically aimed to propose a comprehensive analysis of the optical measurements obtained with the processed ALS filters of the optimized base, which fabrication and development have been extensively described in the previous section. More than comparing the experimental and simulations data, the objective is to calculate the ALS performance of these filters, in the light of the simulation work done in the previous chapters and of the process development presented throughout the current one. This analysis is meant to provide determining information to answer the main issue of this thesis regarding the potential viability of the plasmonic solution to perform filtering function in the industrial production of light sensing applications.

5.3.1 Responses and performance at normal incidence

Similarly to the patch arrays, the hole-array filters of the optimized base were first optically characterized in normal incidence with the micro-spectrometer described in the sub-section 5. 2.5 *Validation of the bonding on glass wafers*. Only transmission measurements were performed in the case of hole arrays, for two wafers corresponding to an aluminum thickness of 200 nm and 275 nm respectively. We present in Figure 5.30 a comparison of the spectral responses obtained with the measurements and with simulations for a representative array of square holes with the R_C2 filter. Note that the complete transmission results are available in *Appendix C*. The simulations are calculated with the perfect targeted shapes, dimensions and thicknesses. The glass substrate is modeled as an infinite medium ($n = 1.5009$ at $\lambda = 633$ nm) and the thermal SiO₂ – air interface is taken into account.

First of all, the four square-hole arrays all present very similar responses, as seen in *Appendix C*. For an AlSi thickness of 200 nm, the resonance peak is always thinner of about 50 nm in wavelength and its maximum transmission loses about 10 %, which can partly be explained by the slightly thicker AlSi deposited films. The blue-shift and the signal loss could correspond to a shape rounding as we observed in simulations with crosses, but not to the presence of voids as we saw in *section 5. 2.4*. For a thickness of 275 nm, the trend is different: a transmission loss is still observed, but there is no noticeable resonance shift and the peak looks slightly broaden. We do not know if air gaps are formed for this AlSi

thickness. It is difficult to draw conclusions from these spectral responses without dedicated characterization, especially knowing that some of the morphological aspects described in the sub-section 5. 2.3 *Aluminum nanostructuration*, such as the sidewall roughness for instance, have not been studied. Their unknown effects combined with the potential presence of voids and with the estimated holes size variations make a rigorous analysis complex and assumption-based only. Characterization technique such as 3D Atomic Force Microscopy (AFM) could provide more accurate information regarding the shapes and the profiles of the apertures, which would allow for a better understanding of the optical responses of the filters. One can however appreciate that the simulations/experiments confrontation, while not perfect, returns coherent behaviors from this non-optimized process. If we compare with Figure 5.29 for instance, we notice the absence of interferences on the spectra. The comparison with our simulations demonstrates that the interferences are caused by Fabry-Perot interferences in the SiO_2 – SiON composite layer between air and aluminum. In the case of hole arrays (optimized base), the reflectivity of the Al film is reduced thanks to plasmon resonances, which may explain the observed reduction of the interference effects.

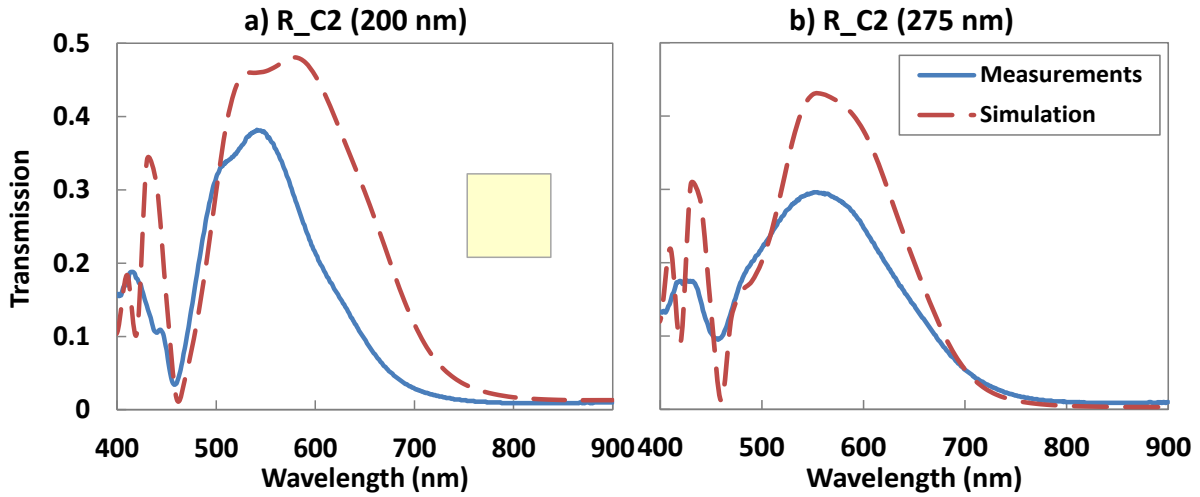


FIG. 5.30. Confrontation of the spectral responses obtained by simulations and with micro-spectrometer measurements at normal incidence for the R_C2 array of square holes for a metal thickness (a) $h_m = 200$ nm and (b) $h_m = 275$ nm. Filter dimensions: period $P = 298$ nm and square size $a = 179$ nm.

Although the study had to focus on square-hole arrays due to the bad lithography results obtained for crosses without PEC, the cross-hole arrays were also optically characterized. Two arrays of crosses with low (0.45 for R_A2) and high (0.65 for R_A4) shape factors are presented in Figure 5.31. Bear in mind that the shape factor stands for the ratio of the arm width b to the arm length a of the crosses. Like in the case of squares, the presented charts are representative of what is observed on the other cross-hole arrays. For thin crosses, the measured spectral response generally deviates noticeably from the simulations, especially with a significant blue-shift. On the contrary for larger crosses, the measurements mostly fit well with the computations results. In the case of crosses, we can safely claim from the morphological characterizations that the severe rounding of the crosses plays a major role in the observed resonance blue-shift. On the other hand, it is important to interpret these results with caution. At first look, one could be tempted to conclude that despite the significant process variations experienced by cross-holes arrays, they give better results than squares. The trick however is that the impact of the shape deformation of the crosses on the spectral response can be artificially compensated by the fact that more signal is sensed owing to the holes enlargement, leading to a measurement close to the simulation, whereas the filter geometry significantly differs. This remark is especially relevant for the pure analysis of the spectral responses relatively to the morphological characterizations and

highlights its complexity, but it will not have much importance for the ALS evaluation of the filters as we will see it later in this part. The non-ALS arrays with small crosses did not give any exploitable results because the shapes were not obtained without PEC.

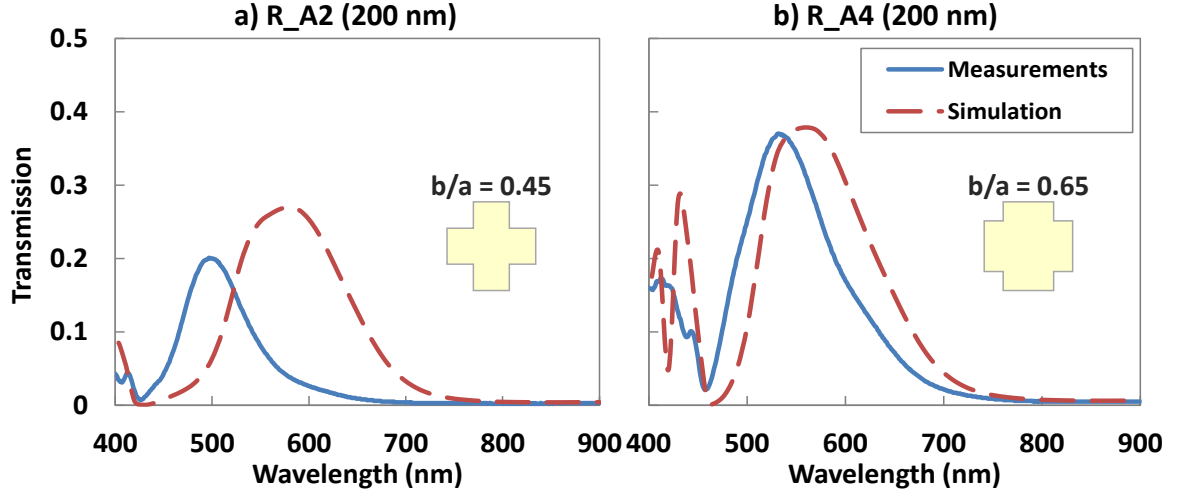


FIG. 5.31. Confrontation of the spectral responses obtained by simulations and with micro-spectrometer measurements at normal incidence for a 200-nm-thick AlSi layer of two ALS hole-arrays of crosses with different arm width to arm length ratios b/a (shape factor): (a) the R_A2 array ($P = 275$ nm, $a = 176$ nm and $b = 79$ nm) and (b) the R_A4 array ($P = 298$ nm, $a = 189$ nm and $b = 119$ nm).

As we have seen throughout this thesis, the evaluation of ALS performance cannot be done solely from visual representation of the spectral response because of all the elements that have to be taken into account in the calculation. We thus inserted the transmission measurements into the ALS evaluation software tool described in *section 2. 2*, and we compared the results with those obtained by simulations. The simulations take into account the same materials stack and the exact targeted dimensions. First of all, we present the global trend over the 18 fabricated ALS filters of the optimized base (the array of circular holes is not shown). A quick visual comparison can be made on Figure 5.32 for the maximum ALS errors obtained for the AlSi thicknesses of 200 nm and 275 nm. Note that only this parameter is commented, but the complete results with the maximum ALS error and the ALS dark detailed for each array are all available in *Appendix D*. In the case of the larger thickness, it can immediately be noticed that the fabricated filters feature equivalent performance in ALS dark, but with slightly higher ALS errors as the blue scatter plot looks shifted towards the right-hand of the chart (Figure 5.32(a)). This increase in ALS error is probably related to the broadening of the resonance peaks observed for the 275 nm thickness on the spectra, leading to more undesired signal being sense, but the origin of this broadening is not clear. In the same time, this peak enlargement could compensate for the transmission loss also observed on the spectral responses and could thereby explain the similar values of ALS dark. In the case of the lower thickness, there is however an increase of the ALS dark criterion, and the maximum ALS errors obtained are surprisingly lower (i.e., better) than the simulations. This could be explained as follows. First, it has to be remembered that we showed in previous chapters that cross-hole and square-hole arrays generally require a thickness superior to 250 nm to provide sufficient rejection outside of the useful signal. Owing to practical restrictions, we could not fabricate the ALS filters we optimized each with their own respective optimal thicknesses that generally exceeded 250 nm, and even 300 nm in some cases. With the 200 nm thickness that was chosen to facilitate the nanostructuration, the resonances of the fabricated designs were necessarily wider than with their optimized thickness since the rejection is worse with lower metal thickness. Yet, we have seen that the measured responses of the 200-nm-thick filters presented a marked blue-shift and a thinning of the resonance peak in most cases. Combining this effect with the slight increase in deposited Al thickness may reasonably explain the

highest selectivity of the filters with less undesired signal being sense, leading to better performances in terms of ALS error. Consequently, this would also explain the increase of the ALS dark since less signal reaches the photodiode. Again, accurately attributing these effects to specific process variations is however tricky without more morphological characterizations, but it can most probably be related to the substantial shape deformation observed in the case of cruciform holes. Nevertheless, major information can be extracted from these results. Indeed, if we consider the specification ranges for the ALS application that we represented in green in Figure 5.32, this work confirms that plasmonic filters can provide a filtering solution fitting the established ALS criteria. In view of actual customers demand, the performance would however certainly need to be improved, but the proof of concept is demonstrated with this first development attempt since the measured performances are consistent with what was expected. The results obtained with the 200-nm-thick filters suggest that we could obtain good performance with lower metal thicknesses, but it must not be forgotten that the fabricated shapes are not exactly cruciform unlike what was simulated in the previous chapters. Note that the simulated filters given in Figure 5.32 have worse performance than what is given in *Appendix A* because the evaluation and the optimization of the filters resulting from *Chapter 3* were originally calculated with infinite SiO_2 substrate and superstrate with a varying thickness. In the case of Figure 5.32, the stack is slightly different and the thickness is fixed either to 200 nm or 275 nm.

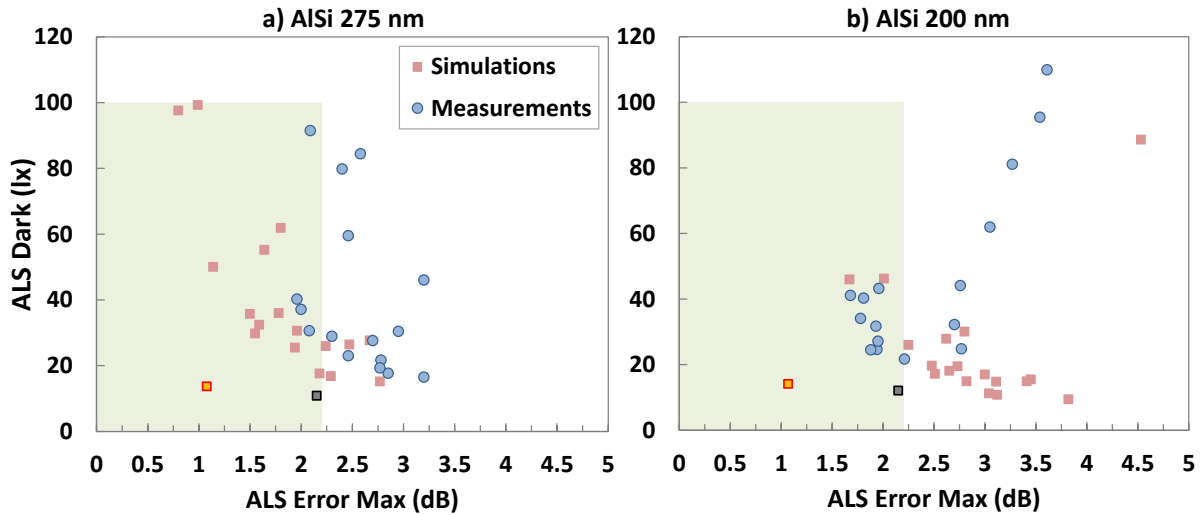


FIG. 5.32. Comparison of ALS dark values and maximum ALS errors obtained with the fabricated filters (blue circles) and with simulations (red squares) for an AlSi thickness of (a) 275 nm and (b) 200 nm. The black square stands for the performance obtained with the green resist combined with the old IR-cut, and the orange square for the green resist and the new IR-cut.

A closer look at the ALS performance obtained from the specific designs chosen in Figure 5.30 and Figure 5.31 may bring useful insights on the results, as shown in Figure 5.33. Considering the array of squares R_C2, the evolutions of the ALS performance previously described between the two aluminum thicknesses become clearly obvious and fit perfectly the spectral responses of Figure 5.30. This behavior is entirely consistent among the four arrays of squares. In most cases, the arrays of squares have similar behavior than arrays of larger crosses ($b/a > 0.5$), with a degradation of the performance for $h_m = 275$ nm from the simulations to the experiments, and with a noticeable decrease of the maximum ALS error for $h_m = 200$ nm, combined with a higher increase in ALS dark. The small degradations observed for the 275-nm-thick filters may be easier to link with the different process inaccuracies since the deposited AlSi thickness is much closer to the ideal targets for ALS filters. Namely, the broadening of the resonance peak and the transmission loss may be due to the size increase of the holes (wider peak) combined with slightly thicker AlSi films and the presence of soft effective slopes (lesser transmission).

As it can be seen in Figure 5.33(b), crosses with the smallest shape factors ($b/a < 0.5$) generally experience a considerable shape deformation that translates into a severe deterioration of the ALS performance. Although the results obtained from the arrays of squares are quite consistent because of the well-respected shapes during the fabrication, the analysis of crosses only provides a general trend on the evolution of the ALS performance compared with the simulations. Depending on their dimensions, some may punctually exhibit a different behavior according to the magnitude of the shape deformation they experienced after the lithography and etching steps, which can create a compensation effect on the ALS evaluation as already mentioned. Keeping this point in mind, the arrays of squares *globally* propose the lowest variations with respect to the targeted performance compared with the arrays of crosses. A more accurate and in-depth analysis would have required the help of the hole arrays fabricated with proximity effect corrections, but we could not have it in time. The performances obtained in normal incidence are thus encouraging for this first development since there is still room for improvement and optimization at each step of the fabrication.

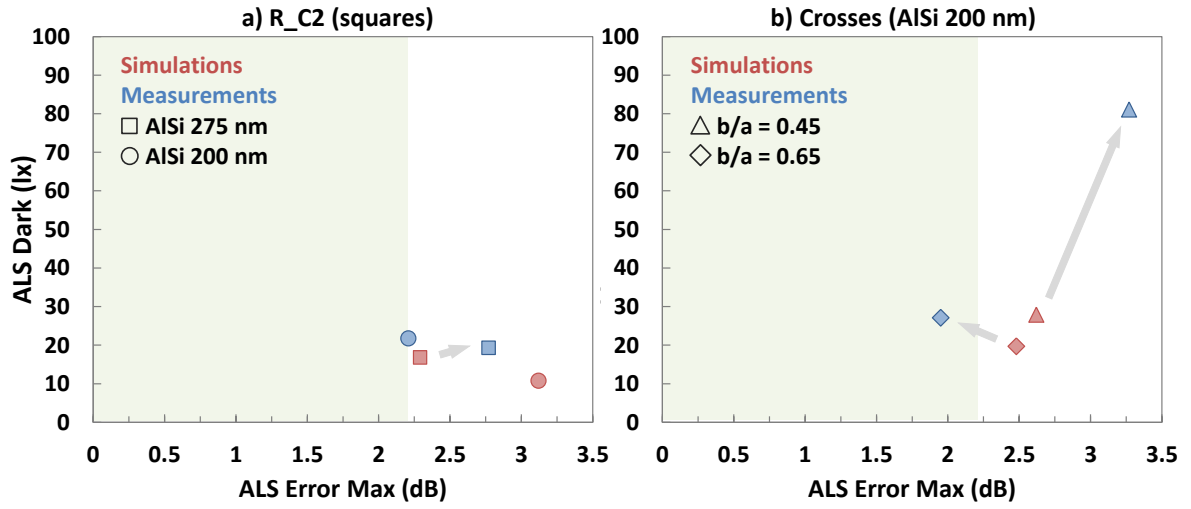


FIG. 5.33. (a) Evolution of the difference in ALS performance between simulations and experiments for a typical array of squares (R_C2) when the AlSi thickness is increased from 200 nm to 275 nm. (b) Evolution of the difference in ALS performance between simulations and experiments for typical arrays of crosses with small b/a (0.45 for R_A2) and larger b/a ratios (0.65 for R_A4) for an AlSi thickness of 200 nm.

5.3.2 Angular tolerance of the filters

We have seen that the fabricated plasmonic filters could provide performances close to the simulated ones, with arrays of crosses and squares even remaining in the ALS specification ranges, which constitutes a significant result. However, the cruciform shape was specifically chosen and designed so that another relevant property of the filters is respected: the stability of the spectral response under off-normal incidence. The packaging of our considered application limits the incoming light cone to an opening of $\pm 30^\circ$, thereby imposing an angular robustness of the filters up to this value.

We performed transmission measurements with various angles of incidence on the filters exhibiting the best performances with a goniometer (L_A3, L_A4, L_B3, L_B4, R_A3, R_A4, R_C1 and R_C2). The goniometer produces the visible spectrum from a 2 W *Fianium* white laser source linearly polarized whose output wavelengths range from 420 nm to 1700 nm. The light strikes the arrays in a TM configuration, i.e. where the electric field is in the incidence plane. The TM polarization was shown in previous chapters to be the less stable one. A monochromator with a maximum operating wavelength of 920 nm was used to narrow the measurements on the visible and NIR ranges as it is the case in our simulations. A lens was used to limit the beam divergence, leading to a diameter of the spot

size of 300 μm at the level of the arrays. The bench allows for measurements with an absolute resolution of $1/100^\circ$ and with a photometry error of $\pm 1\%$. The characterizations were made from normal incidence up to 30° with 5° steps. Illustrations of these measurements are given for an array of squares and for an array of crosses in Figure 5.34. The evolutions of the spectral responses with increasing angle of incidence in the two cases suggest similar behaviors of squares and crosses, characterized with a significant transmission decrease and a comparable resonance red-shift of about 100 nm at 30° . No different behavior was noted among the eight measured arrays, and the thickness did not seem to play any role in the angular stability, which is consistent with the study of *section 3. A.1.1*. The comparison of the measurements with the simulation is given in Figure 5.35 for two arrays. The difference already present at normal incidence between simulations and measurements for squares makes the comparison a bit messy, especially with the perturbation generated in the blue wavelengths. The trend looks similar, but the visualization is not easy because there are noticeable shifts and transmission gaps between the experiments and the calculations. In the case of crosses where the comparison was close at normal incidence, it can clearly be seen that there is a similar evolution even at 30° . This agreement whereas the fabricated crosses are substantially rounded is surprising, but we know from previous chapters that large crosses do not really have particular stability in TM polarization (at $\varphi = 0^\circ$), even compared with circular holes. However, thinner crosses with $b/a = 0.5$ returned the same evolution, even with simulations (not shown). This poor stability could be explained by the large intercrosses distance (about 100 nm) used in ALS arrays (see *section 3. A.1.4*). Remember that no constraint was used on this parameter for the optimization of the ALS performance. We may also assume that the stability of crosses is also dependent on the crosses size. Indeed, for a given wavelength range, an increase of the holes size may reduce the confinement of the electric field inside the apertures. Moreover, we already showed in *section 3. A.2* that the stability of crosses was more difficult to obtain in the red wavelengths. It would have been ideal to measure the thin ALS crosses with $b/a = 0.4$ obtained with the proximity effect corrections. Those we got without PEC were too far from the targeted shape to be relevant. Globally, the results were once again very consistent among all the arrays of squares and among all the arrays of crosses.

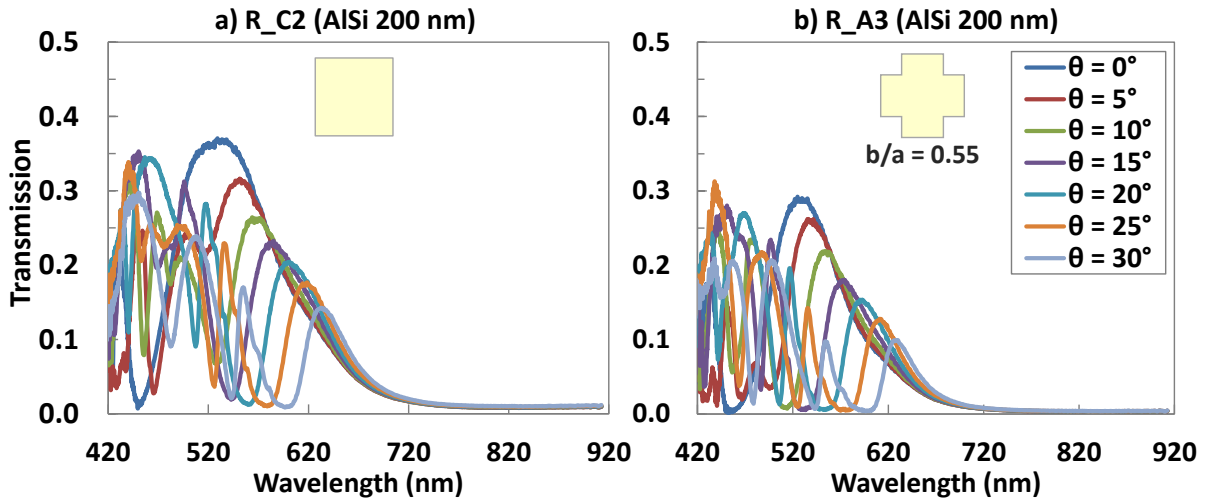


FIG. 5.34. Evolution of the spectral responses with increasing angle of incidence measured in TM polarization with a goniometer for (a) the R_C2 array (squares) and (b) the R_A3 array (crosses with $b/a = 0.55$). These measurements were done on the 200-nm-thick wafer.

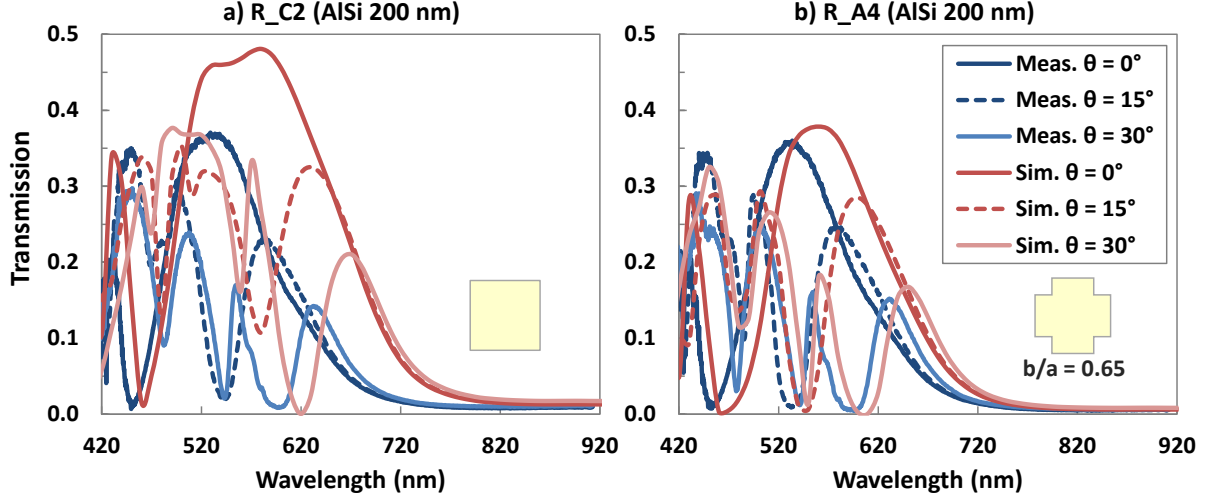


FIG. 5.35. Comparison of the angular behavior between simulations and goniometer measurements in TM polarization for (a) the R_C2 array (squares) and (b) the R_A4 array (crosses with $b/a = 0.65$). These measurements were done on the 200-nm-thick wafer.

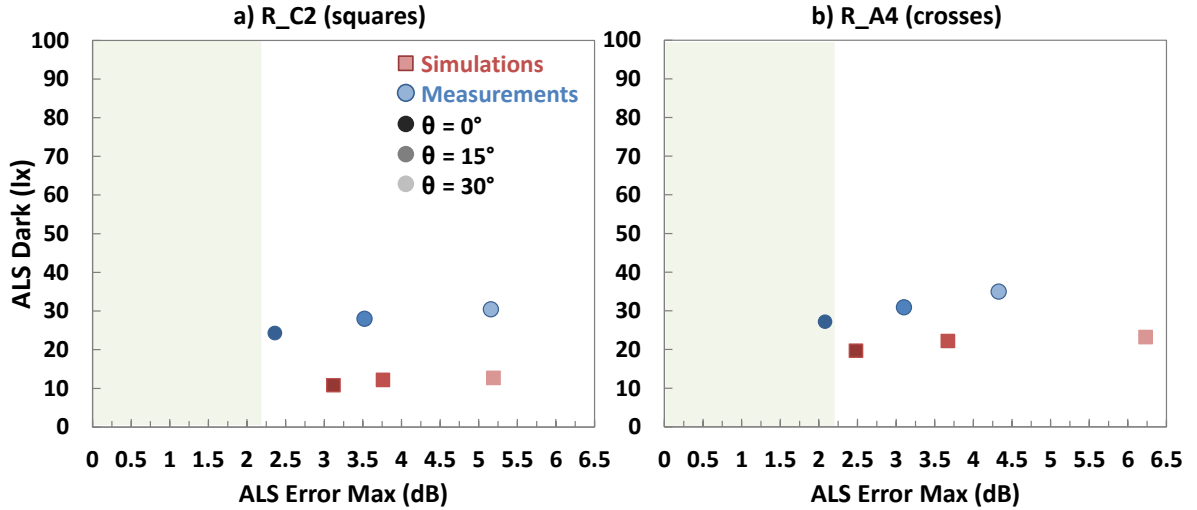


FIG. 5.36. Evolution of the ALS performance for simulations and goniometer measurements in TM polarization with increasing angle of incidence for (a) the R_C2 array (squares) and (b) the R_A4 array (crosses with $b/a = 0.65$). These measurements were done on the 200-nm-thick wafer.

We then evaluated the spectral responses of the two filters of Figure 5.35 in terms of ALS performance. The results are given in Figure 5.36. The evolution with the angle of incidence is rather consistent with the simulations, with the exception of the crosses for 30° . The angular stability was expected to be low for squares and for large crosses since we demonstrated in *Chapter 3* the trade-off existing between the ALS performance (high b/a) and the angular stability (low b/a). In order to compensate for the shift in ALS error, it would be preferable to look for filters that give the lowest possible ALS error at normal incidence so that they remain in the specification ranges even for $\theta = 30^\circ$. It was actually the case during the optimization of the filters, but as explained in the previous subsection, this optimization did not take into account the actual fabricated stack and thicknesses that we used later for the process development and that we could not anticipate at this time, resulting in degraded performance in the results. It would be interesting to perform a new optimization with structures as close as possible to the targeted integration to make a fairer and more accurate simulation/experiment comparison. The parameters of the optimization could also take into account the angular dependence of

the filters to help choosing the best designs. Finally, a better evaluation of the angular stability of plasmonic filters for the ALS application would have required the measurements of the thin crosses which experienced EBL corrections. The development was however not finished at the time of this writing.

5.4 Conclusion on Chapter 5

We presented in this chapter the process development that was led to achieve the fabrication of our optimized structures by avoiding the process inaccuracies as best we could with the time and resources restrictions of the study. In the light of our modeling work of the main expected process variations, each critical brick of the integration was controlled to evaluate and to adjust the process capability to fit the process specifications that we established to get efficient plasmonic filters. Most of these adjustments were performed from the first engineering base we got at our disposal before having finished the optimization work on plasmonic designs. This initial base was used to realize patch-array filters, but a large part of its development provided useful insights that could be directly transferred to the ulterior base featuring the optimized hole-array filters since the dimensions were comparable.

The materials stack used for the realization of plasmonic filters with aluminum was not problematic since the interfaces were defect-less and no adhesion issues occurred, be it with SiO₂ or SiON, which gives a high flexibility regarding the level at which the filters can be fabricated in the integration of a whole sensor. The thickness variation for the AlSi layer was about 10 %, which we did not work on since it is not critical, especially for a first demonstration. The formation of hillocks with thermal stress was however more concerning for the quality of the successive steps such as the lithography and the aluminum etching. It generated a significant delay in the fabrication in order to find out the best solution allowing for their suppression. Eventually, the condition of using cold processes until the metal structuration was the easiest and most conclusive one. The deposition of the hard mask was thus cooled down to 200°C, which significantly reduced the hillocks growth, but did not remove it entirely.

Regarding the nanostructuration, the electron-beam lithography step was thought as a major issue for the filters realization. The results quickly revealed that although the dimensions variations were close to the maximum tolerated limit of about 10 % of *Chapter 4*, the shape of the crosses was severely affected in our first attempts. We however demonstrated that the use of a more resolving resist combined with proximity effect corrections could greatly improve the cruciform shape and reduce the size dispersion below 8 % for the ALS filters, and even below 4 % for the smallest designs that we embedded in the base, all presenting much less corners rounding. This lithography development was very encouraging but we ran out of time for the continuation of the wafers featuring these improvements. The metal nanostructuration was thus only performed on the wafers having deformed crosses and we focused on the square shapes which were rather well respected. Whereas the etching of the patches generated sharp profiles with slopes below 4°, the hole-array filters showed a sidewall roughness with maximum amplitude of 30 nm which made the evaluation of etching slopes more difficult. The impact of roughness still has to be evaluated, but the profiles could be considered with an effective slope which was inferior to 3°. This value falls in the acceptable range simulated in *Chapter 4*. No noticeable difference was observed between the bottom and the top of the holes regarding size variations, which were below 7 %, meaning that there is no additional dispersion induces by the etching step compared with lithography. A lower value would be preferable, but it is certainly not overwhelming for a first demonstration, especially with a realization of filters with various dimensions at the same time.

We demonstrated in *Chapter 4* that the presence of air gaps inside the holes has to be limited to avoid the degradation of the spectral responses. The development on the initial base highlighted the difficulty to fill such cavities with conventional PECVD. The use of a dedicated HDP process gave

substantial improvement with a capability to fill 100-nm-wide gaps without any voids. In the case of hole arrays, the FIB-SEM observations validated the HDPCVD hole-filling step and the process we defined with wafer-level equipment since no air gaps were noticed, even for the smallest ALS design featuring cavity widths below 70 nm and aspect-ratios of 3. Finally, we worked on the direct bonding of the fabricated structures on glass wafers to permit transmission characterizations. The analysis of the patch arrays validated the feasibility of this method and demonstrated at the same time the robustness of plasmonic filters to annealing, which could be used in ALS sensors to decrease their ALS dark (see 3. *B.1.1 Evaluation of plasmonic filters performance*). This annealing was not possible with organic resists. We also noticed good intra-wafer and wafer-to-wafer reproducibility even for these extreme dimensions.

This work led to the core of this study which was to demonstrate experimentally the viability of the plasmonic filters fabrication and their performance for ALS applications. The optical characterizations performed on ALS designs highlighted the effects of process inaccuracies with deviations from the simulated spectra, but their respective roles are difficult to identify and to attribute. Nevertheless, we obtained a satisfying agreement between the measurements and the simulations, especially characterized with the achievement of fabricated filters inside the ALS specification ranges, with maximum ALS errors below 2 dB and ALS dark values inferior to 40 lx. These good results we obtained have to be emphasized given the drastic specifications of ALS application targeted in this thesis work. The squares generally presented the closest performance to simulations. Crosses may also give good results, but their significant shape deformation makes their performances hardly related to the cruciform shape. The angular tolerances measured for the less stable polarization revealed a coherent behavior with simulations, especially for squares. Unfortunately, the angular stability for crosses with shape factors below 0.5 could not be tested. The corrected shapes would have been useful to compare the simulations with more accurate fabricated shapes. This work provides important information regarding the actual dispersions that can be expected from industrial tools, with the exception of the EBL, and the performance that can be reached with them. In particular, it proves that no critical issues prevent the realization of plasmonic filters and that they can constitute an efficient filtering solution for ALS applications. Knowing that there is still much room for improvement with dedicated and optimized processes at each step of the fabrication, we think this study has demonstrated an interesting and promising proof of concept for the application of plasmonic filters in industrial products with CMOS-compatible wafer-level integrations.

Conclusion and Outlook

The work carried out throughout this thesis was especially driven by the motivation of STMicroelectronics to develop disruptive innovations regarding the integration of CMOS light sensors. This technological guideline lies in a context where the demand for embedded sensors of various natures has been exponentially growing in recent years, in major part thanks to the development of the wireless communication market. Image sensors and Ambient Light Sensors (ALS) use in most cases organic resists as optical filters, which limit the integration possibilities of the sensors and impose the use of a thick IR-cut filter. The search for innovative filtering solutions leaned towards an emerging field of photonics that allows for the manipulation of light at nanoscale thanks to plasmonic devices based on nano-patterned metallic structures, permitted by the recent progress in nano-lithography. Despite all the literature available in this domain, several critical concerns still remain to be addressed in order to evaluate the concrete potential of plasmonic filters in CMOS industrial environment.

The major issue was to theoretically demonstrate the performance of plasmonics with respect to accurate specifications and to study the viability of their fabrication with industrial constraints, such as CMOS compatibility and the restriction to high-throughput processes. This subject thereby gave rise to two different aspects of the study. The first was to investigate the ability of plasmonic filters to meet the required performances and the technological challenges expected for the targeted applications. The second consisted in addressing the technological issues inherent to plasmonics that did not exist with organic resists, such as for instance the polarization dependency or the compliance with the critical dimensions of the nanostructures during the fabrication. To achieve this, I established a methodology at the crossroads of different scientific areas among plasmonic theory, electromagnetic simulations and process development (*Chapter 1*). Numerical simulations were used to select the best plasmonic nanostructures and integration for our targeted applications (*Chapter 2*) and to study their optical properties in order to propose optimal structure designs (*Chapter 3*). Thoughts about process integration and defects modeling were gathered to investigate the sensitivity of plasmonic structures to wafer-level process dispersions and to identify the critical steps that would require particular attention (*Chapter 4*). These studies converged towards the knowledgeable process development of filters and their subsequent optical characterization to demonstrate a proof of concept. The result is that I was able to establish the potential viability of the plasmonic solution to provide efficient ALS filters compatible with a wafer-scale fabrication (*Chapter 5*).

One of the major sensor-related technological challenges was the angular stability of the filters under angles of incidence up to 30° . I demonstrated through this work that among the main plasmonic structures families, hole-array filters were the most appropriate structures to provide this property and consequently constituted the most serious candidate to approach the drastic requirement of the ALS application considered in this work. Patch-array filters were not well adapted to transmission filters, and MIM arrays did not show an interesting angular tolerance, in addition to being more complicated to fabricate. In particular, we showed that cross-shaped-hole arrays constitute the structures offering the best angular robustness and transmission levels at the same time. This study also imposed to search for

solutions restricted to CMOS-compatible materials. I managed to demonstrate the interest of these structures with the use of aluminum for the metal and SiO₂ for the dielectric medium, which was the combination returning the best optical properties while being based on very common materials in CMOS industry. The establishment of accurate performance criteria and the use of dedicated software have permitted a concrete evaluation of the filters relatively to industrial specifications of image sensors and ambient light sensors. The developed structures quickly revealed their weaknesses in terms of transmission and signal-to noise ratio compared to the state of the art of RGB filters, which is especially challenging in terms of performance. This is directly related to the very nature of plasmonic structures that implies a notable amount of metallic losses compared to absorptive resists or dielectric-based filters. The different requirements of the ALS function are however less demanding regarding the transmission and seemed more in agreement with the optical responses achievable with metallic nanostructured filters. Their evaluation indeed demonstrated that plasmonic filters could be competitive in theoretical performance. Indeed, I demonstrated that it was possible to find designs able to fit with the specifications range despite the drastic requirements of the application. Furthermore, these results proved that plasmonic filters were able to fulfill the technological challenges motivating this thesis work. Their rejection in the NIR range was indeed sufficient to suppress the need of an external IR-cut filter. Combined with their thickness of about 300 nm, the thickness of the complete filtering system is thus significantly reduced, allowing for the desired height reduction of the whole sensor.

In parallel, several questions were raised regarding the viability of such structures and their ability to constitute an efficient filtering solution owing to the specific issues they bring compared with organic resists. Because of their in-plane nanostructuration, plasmonics filters are not only sensitive to the polar angle of incidence, but also to the polarization state and to the azimuth of the incoming light. The comprehensive study of the plasmon resonances inside cross-shaped-hole arrays permitted to identify the conditions of their angular stability and to propose filters with significantly reduced sensitivity to both the angles of incidence and the polarization. I extracted geometrical criteria that favor the regime of localized plasmon resonances which are responsible for the angular robustness. Thin crosses and low inter-cross distances are the two major conditions providing this property that could then be used to design optimal filters in terms of ALS performance and angular stability. The study however showed that the gathering of these two aspects requires a trade-off since ALS performances are improved with larger crosses. The best designs were then optimized with an algorithm developed in the CEA Leti which was combined with the ALS evaluation software of STMicroelectronics and the RCWA. This work has provided in the same time a dedicated evaluation and optimization software tool that can be directly used for the further development of other plasmonic structures and applications. In practice, the advantages of the plasmonic filters' principle constitute also a source of concerns regarding their fabrication. The plasmon resonances are related to the shape and to the dimensions of the metallic nanostructures. Deviations on the size and shape of the structures in fabrication have to be drastically limited in order to avoid a serious deterioration of the expected performances. However, the nanostructures are small and the capabilities of wafer-scale fabrication equipment are thereby heavily challenged. Unlike most of the works available in literature, I had to focus on the use of wafer-scale processes only to carry out a risk assessment related to the viability of a potential industrial production of these filters. This was led by the analysis of the main expected process inaccuracies with typical dispersions of a 300-mm-wafer fab, with two aspects in mind: their effects on plasmon resonances and their impacts on ALS performances. The calculations allowed for the identification of the main hard points, which mainly consisted of the lithography accuracy in size and shape of the patterns, of the etching profiles and the presence of air gaps during holes filling. In a second phase, the actual process development of optimized filters with wafer-scale processes proved that there were no crippling issues with such equipment. The main observed dispersions fell into the tolerable expected ranges, be they for thickness variations, holes dimensions, etching slopes or air gaps formation. The development of the electron beam lithography gave faithful shape reproduction, and the continuation of this fabrication could give very interesting additional results. Eventually, the final optical characterization returned some

promising performance that fell into the specifications range and thus achieved the demonstration of the viability of the plasmonic filters solution with an integration directly transferable to an industrial environment. We note that very recent works progressively take into account the effect of process-related inaccuracies on the performance of plasmonic filters [57], [166], [167]. It demonstrates that this thesis is part of a present-day trend which aims to carry plasmonic filters towards a technological transfer in concrete applications.

Currently, the development of filters with improved Electron Beam Lithography (EBL) is still ongoing. A collaboration was also established with the University of Glasgow and STMicroelectronics Edinburgh to fabricate some optimized designs directly on ALS photodiodes of CMOS chips provided by STMicroelectronics Crolles. This fabrication will allow for the direct evaluation of the plasmonic-based ALS sensors with dedicated measurement benches, and could also assess the benefit of the final annealing on the performance of plasmonic ALS.

Although many challenges were solved throughout this work, a few points still need to be addressed. EBL was the only process that does not meet the conditions of high throughput. The complete validation of the integration should evaluate the capability of deep UV lithography with a double patterning as it was mentioned in *Chapter 4*. The cost of such a process is however still very high, especially if the filters are fabricated in the last levels of the sensors. The plasmonic solution would be more competitive with the amortization of this kind of patterning. On a side note, we deposited two patents to fabricate the filters closer to the photodiodes, which helps to solve this issue in addition to providing better optical performance [161], [162]. The development of high-resolution lithography techniques in the near future [210] could be significantly profitable to the progress of plasmonic filtering structures in robust front-end wafer-scale production.

If this thesis provided insights regarding the potential industrialization of plasmonic filters, there is still a need for a complete validation with a demonstration on full-sheet 300-mm wafers. A statistical dispersion study on production-dedicated equipments combined with the development of optimized processes would precisely assess this potential. The optical characterization and the performance evaluation of plasmonic filters produced with a front-end 300-mm production line still have to be performed on blanket wafers or directly on CMOS sensors. The collaboration that we established with the University of Glasgow constitutes a first step in this direction. Moreover, the plasmonic filters that we developed use metallic layers without barriers, which may raise the question of metal diffusion under thermal stress, for which a reliability study would be required.

A dedicated process study regarding the morphological defects and variations of plasmonic filters would be required to obtain more information about the weak points of the manufacturing. It would allow for even more accurate modeling of the process dispersions, which would lead to a clear identification of the process steps that generate them, and to a better understanding of the measured spectral responses. Such a study would be beneficial in view of a reliable production of plasmonic filters.

While we worked with infinite metallic arrays, the study could need to be extended with the investigation of finite-size effects in the case of spatially-delimited arrays. The ALS photodiode of the application considered in this work is large (approximately $3 \times 3 \mu\text{m}^2$), but the potential transfer of nanostructured metallic filters towards applications with smaller pixels will require such a study. In literature, a few works have started to take into account these considerations [54], [85], [211], [212].

The use of noble metals such as silver could be investigated in detail as we evidenced structures providing higher ALS performance at normal incidence. Dedicated areas of CMOS industrial clean rooms can be implemented for the use of contaminant materials in the very last steps of the integration.

The search for new plasmonic structures could also be a solution to find easier shapes to fabricate and/or filters with higher angular stability with less restrictive geometrical conditions. We also patented more advanced structures that could later give interesting optical properties without making their process more difficult. No detail is given regarding these patents since they are currently being filed.

Similarly to the work done on the ALS application in this thesis, plasmonic filters can be studied beyond visible sensing applications. Indeed, the plasmonic properties of metals such as gold, silver or copper, in the infrared (IR) range can contribute to the development of a significant number of IR-sensors applications: night-vision cameras, Time-of-Flight proximity sensors [174], etc. Since the operating wavelength of a plasmonic filter is determined by its dimensions, several filters can be patterned on the same level with a single patterning. This ability of plasmonic filters makes them especially interesting for the realization of sensors gathering different functions. Plasmonics can thus lead to a decrease of the cost of multi-pixel sensors and favor beyond-Bayer configurations, such as RGB-IR or RGB-CMY sensors [213]. The combination of this advantage and of the extended potential wavelength range of plasmonic filters is furthermore particularly attractive for multi-spectral [95], [214], [215] or hyper-spectral imaging [216], which both require a high number of filters to cover a large wavelength scale (multi-spectral imaging) and to obtain a high wavelength resolution (hyper-spectral imaging).

As a conclusion, this thesis demonstrates the feasibility and the interest of nano-patterned metallic filters for spectral filtering applications, together with their technological transfer to wafer-scale fabrication. In particular, we think that the performance we obtained for low-cost ALS sensors combined with the ability to pattern different filters with a single lithography step could make plasmonic filters very good candidates especially suited for the realization of multi-pixels sensors or RGB-ALS sensors featured in higher-end handheld devices. The process development that was led throughout this work constitutes a global analysis methodology of the manufacturing viability of plasmonic structures that can be transferred to other applications beyond visible light sensors.

Bibliography

- [1] G. Moore, "Cramming More Components onto Integrated Circuits," *Electronics*, vol. 38, no. 8, pp. 114–117, Apr. 1965.
- [2] "Status of the CMOS Image Sensor Industry," Yole, Jan. 2015.
- [3] M. Bigas, E. Cabruja, J. Forest, and J. Salvi, "Review of CMOS image sensors," *Microelectron. J.*, vol. 37, no. 5, pp. 433–451, May 2006.
- [4] A. Tournier, "Pixel 1-Transistor à modulation de charges pour capteurs d'images CMOS à haute résolution," STMicroelectronics CIFRE Ph.D. dissertation, Univ. Lyon, France, 2007.
- [5] J. Vaillant, A. Crocherie, F. Hirigoyen, A. Cadien, and J. Pond, "Uniform illumination and rigorous electromagnetic simulations applied to CMOS image sensors," *Opt. Express*, vol. 15, no. 9, pp. 5494–5503, Apr. 2007.
- [6] B. E. Bayer, "Color imaging array," US3971065 A, 20-Jul-1976.
- [7] "Bayer matrix," *Diglloyd*, 2015. [Online]. Available: http://diglloyd.com/blog/2014/20140521_0908-Sigma-sensor-spectral.html.
- [8] E. Rosencher and B. Vinter, *Optoelectronics*. Cambridge University Press, 2002.
- [9] C. Mornet, "Reconstruction couleur sous faible éclaircissement pour des capteurs d'images en technologie CMOS," STMicroelectronics CIFRE Ph.D. dissertation, Univ. Grenoble, France, 2011.
- [10] Y. Yamamoto and H. Iwamoto, "Solid-state imaging device and method of manufacturing solid-state imaging device background of the invention," US7101726 B2, 05-Sep-2006.
- [11] S. Iwabuchi, Y. Maruyama, Y. Ohgishi, M. Muramatsu, N. Karasawa, and T. Hirayama, "A Back-Illuminated High-Sensitivity Small-Pixel Color CMOS Image Sensor with Flexible Layout of Metal Wiring," in *Proceedings of IEEE International Solid-State Circuits Conference, Digest of Technical Papers*, 2006, pp. 1171–1178.
- [12] J. Prima, F. Roy, P. Coudrain, X. Gagnard, J. Segura, Y. Cazaux, D. Herault, N. Virollet, N. Moussy, B. Giffard, and P. Gidon, "A 3 Mega-Pixel Back-Illuminated Image Sensor in 1T5 Architecture with 1.45 μm Pixel Pitch," in *Proceedings of International Image Sensor Workshop*, 2007, pp. 5–8.
- [13] "Light sources," *Azom*, 2015. [Online]. Available: <http://www.azom.com/article.aspx?ArticleID=10627>.

- [14] A. Carroll and G. Heiser, "An Analysis of Power Consumption in a Smartphone," in *Proceedings of the 2010 USENIX Conference on USENIX Annual Technical Conference*, Berkeley, CA, USA, 2010, pp. 21–21.
- [15] X. Chen, Y. Chen, Z. Ma, and F. C. A. Fernandes, "How is Energy Consumed in Smartphone Display Applications?," in *Proceedings of the 14th Workshop on Mobile Computing Systems and Applications*, New York, NY, USA, 2013, pp. 3:1–3:6.
- [16] "Luminous efficacy," *Prismalence*, 2015. [Online]. Available: http://www.prismalenceuk.com/image_display?ccid=1174&blid=2&ppid=936&k=1.
- [17] "IR-cut glass filter," *JDSU*, 2015. [Online]. Available: <http://www.jdsu.com/en-us/optical-security-and-performance/products/a-z-product-list/Pages/filter-uv-ir-blocking.aspx#.VVON2ZPorHi>.
- [18] "IR-cut filter thickness," *JDSU*, 2015. [Online]. Available: <http://www.jdsu.com/ProductLiterature/uvirf-ds-co-ae.pdf>.
- [19] "RGB organic resists," *Fujifilm*, 2015. [Online]. Available: http://www.fujifilmusa.com/products/semiconductor_materials/image-sensor-color-mosaic/rgb/index.html#applications.
- [20] Y. Inaba, M. Kasano, K. Tanaka, and T. Yamaguchi, "Degradation-free MOS image sensor with photonic crystal color filter," *IEEE Electron Device Lett.*, vol. 27, no. 6, pp. 457–459, Jun. 2006.
- [21] Y. Huo, C. C. Fesenmaier, and P. B. Catrysse, "Microlens performance limits in sub-2μm pixel CMOS image sensors," *Opt. Express*, vol. 18, no. 6, pp. 5861–5872, Mar. 2010.
- [22] H. A. Macleod, *Thin Film Optical Filters, Third Edition*. London: Institute of Physics Publishing, 2001.
- [23] S. Koyama, Y. Inaba, M. Kasano, and T. Murata, "A Day and Night Vision MOS Imager With Robust Photonic-Crystal-Based RGB-and-IR," *IEEE Trans. Electron Devices*, vol. 55, no. 3, pp. 754–759, Mar. 2008.
- [24] Y.-T. Yoon and S.-S. Lee, "Transmission type color filter incorporating a silver film based etalon," *Opt. Express*, vol. 18, no. 5, pp. 5344–5349, Mar. 2010.
- [25] L. Frey, P. Parrein, J. Raby, C. Pellé, D. Hérault, M. Marty, and J. Michailos, "Color filters including infrared cut-off integrated on CMOS image sensor," *Opt. Express*, vol. 19, no. 14, pp. 13073–13080, Jul. 2011.
- [26] P. Gidon and G. Grand, "Optical filtering matrix structure and associated image sensor," US8587080 B2, 19-Nov-2013.
- [27] S. Kaushik and B. R. Stallard, "Two-dimensional array of optical interference filters produced by lithographic alterations of the index of refraction," in *Proceedings of SPIE*, 1995, vol. 2532, pp. 276–281.
- [28] K. Walls, Q. Chen, J. Grant, S. Collins, D. R. S. Cumming, and T. D. Drysdale, "Narrowband multispectral filter set for visible band," *Opt. Express*, vol. 20, no. 20, pp. 21917–21923, Sep. 2012.

-
- [29] S. Boutami, Y. Desieres, L. Frey, and G. Grand, "Optical filter suitable for dealing with a radiation of variable incidence and detector including said filter," US20110290982 A1, 12-Jan-2011.
 - [30] L. Frey, L. Masarotto, M. Armand, M.-L. Charles, and O. Lartigue, "Multispectral interference filter arrays with compensation of angular dependence or extended spectral range," *Opt. Express*, vol. 23, no. 9, pp. 11799–11812, May 2015.
 - [31] Y. Kanamori, M. Shimono, and K. Hane, "Fabrication of Transmission Color Filters Using Silicon Subwavelength Gratings on Quartz Substrates," *IEEE Photonics Technol. Lett.*, vol. 18, no. 20, pp. 2126–2128, Oct. 2006.
 - [32] Y.-T. Yoon, H.-S. Lee, S.-S. Lee, S. H. Kim, J.-D. Park, and K.-D. Lee, "Color filter incorporating a subwavelength patterned grating in poly silicon," *Opt. Express*, vol. 16, no. 4, pp. 2374–2380, 2008.
 - [33] A.-L. Fehrembach, "Réseaux résonnants à Bande Interdite Photonique, nouveaux filtres pour le D.W.D.M.," Ph.D. dissertation, Univ. Aix-Marseille, France, 2003.
 - [34] R. Magnusson and M. Shokooh-Saremi, "Widely tunable guided-mode resonance nanoelectromechanical RGB pixels," *Opt. Express*, vol. 15, no. 17, pp. 10903–10910, 2007.
 - [35] R. W. Wood, "On a Remarkable Case of Uneven Distribution of Light in a Diffraction Grating Spectrum," *Proc. Phys. Soc. Lond.*, vol. 18, no. 1, pp. 269–275, Jun. 1902.
 - [36] L. Rayleigh, "Note on the remarkable case of diffraction spectra described by Prof. Wood," *Philos. Mag.*, vol. 14, no. 79, pp. 60–65, juillet 1907.
 - [37] U. Fano, "The Theory of Anomalous Diffraction Gratings and of Quasi-Stationary Waves on Metallic Surfaces (Sommerfeld's Waves)," *J. Opt. Soc. Am.*, vol. 31, no. 3, pp. 213–222, Mar. 1941.
 - [38] D. Pines and D. Bohm, "A Collective Description of Electron Interactions: II. Collective vs Individual Particle Aspects of the Interactions," *Phys. Rev.*, vol. 85, no. 2, pp. 338–353, Jan. 1952.
 - [39] R. H. Ritchie, "Plasma Losses by Fast Electrons in Thin Films," *Phys. Rev.*, vol. 106, no. 5, pp. 874–881, juin 1957.
 - [40] S. Enoch and N. Bonod, Eds., *Plasmonics - From Basics to Advanced Topics*, vol. 167. Berlin, Heidelberg: Springer Berlin Heidelberg, 2012.
 - [41] M. L. Brongersma and P. G. Kik, Eds., *Surface Plasmon Nanophotonics*, vol. 131. Dordrecht: Springer Netherlands, 2007.
 - [42] S. A. Maier, *Plasmonics: Fundamentals and Applications*. Boston, MA: Springer US, 2007.
 - [43] A. D. Rakic, A. B. Djurišić, J. M. Elazar, and M. L. Majewski, "Optical Properties of Metallic Films for Vertical-Cavity Optoelectronic Devices," *Appl. Opt.*, vol. 37, no. 22, pp. 5271–5283, Aug. 1998.
 - [44] K. Murata and H. Tanaka, "Surface-wetting effects on the liquid–liquid transition of a single-component molecular liquid," *Nat. Commun.*, vol. 1, no. 16, pp. 1–8, mai 2010.

- [45] P. r. West, S. Ishii, G. v. Naik, N. k. Emani, V. m. Shalaev, and A. Boltasseva, "Searching for better plasmonic materials," *Laser Photonics Rev.*, vol. 4, no. 6, pp. 795–808, Nov. 2010.
- [46] S. G. Rodrigo, F. J. García-Vidal, and L. Martín-Moreno, "Influence of material properties on extraordinary optical transmission through hole arrays," *Phys. Rev. B*, vol. 77, no. 7, p. 075401, février 2008.
- [47] E. D. Palik, *Handbook of Optical Constants of Solids*. Academic Press, 1998.
- [48] H. Raether, *Surface plasmons on smooth and rough surfaces and on gratings*. Berlin; New York: Springer-Verlag, 1988.
- [49] W. L. Barnes, A. Dereux, and T. W. Ebbesen, "Surface plasmon subwavelength optics," *Nature*, vol. 424, no. 6950, pp. 824–830, août 2003.
- [50] A. Otto, "Excitation of nonradiative surface plasma waves in silver by the method of frustrated total reflection," *Z. Für Phys.*, vol. 216, no. 4, pp. 398–410, Aug. 1968.
- [51] E. Kretschmann and H. Raether, "Radiative decay of nonradiative surface plasmons excited by light," *Z Naturforsch A*, vol. 23, p. 2135, 1968.
- [52] Y. Yu, L. Wen, S. Song, and Q. Chen, "Transmissive/Reflective Structural Color Filters: Theory and Applications," *J. Nanomater.*, vol. 2014, pp. 1–17, Jul. 2014.
- [53] C. Genet and T. W. Ebbesen, "Light in tiny holes," *Nature*, vol. 445, no. 7123, pp. 39–46, Jan. 2007.
- [54] K. Kumar, H. Duan, R. S. Hegde, S. C. W. Koh, J. N. Wei, and J. K. W. Yang, "Printing colour at the optical diffraction limit," *Nat. Nanotechnol.*, vol. 7, no. 9, pp. 557–561, Aug. 2012.
- [55] F. J. Garcia-Vidal, L. Martin-Moreno, T. W. Ebbesen, and L. Kuipers, "Light passing through subwavelength apertures," *Rev. Mod. Phys.*, vol. 82, no. 1, pp. 729–787, Mar. 2010.
- [56] E. Laux, C. Genet, T. Skauli, and T. W. Ebbesen, "Plasmonic photon sorters for spectral and polarimetric imaging," *Nat. Photonics*, vol. 2, no. 3, pp. 161–164, Mar. 2008.
- [57] U. Palanchoke, "Conception and realization of spectral sorters," Ph.D. disseration, Univ. Grenoble, Grenoble, France, 2015.
- [58] D. A. Gremaux and N. C. Gallagher, "Limits of scalar diffraction theory for conducting gratings," *Appl. Opt.*, vol. 32, no. 11, pp. 1948–1953, Apr. 1993.
- [59] D. A. Pommet, M. G. Moharam, and E. B. Grann, "Limits of scalar diffraction theory for diffractive phase elements," *J. Opt. Soc. Am. A*, vol. 11, no. 6, pp. 1827–1834, Jun. 1994.
- [60] E. N. Glytsis, "Two-dimensionally-periodic diffractive optical elements: limitations of scalar analysis," *J. Opt. Soc. Am. A*, vol. 19, no. 4, pp. 702–715, 2002.
- [61] M. Nevière, E. Popov, R. Reinisch, and G. Vitrant, *Electromagnetic Resonances in Nonlinear Optics*. Taylor & Francis, 2000.
- [62] K. Yee, "Numerical solution of initial boundary value problems involving maxwell's equations in isotropic media," *IEEE Trans. Antennas Propag.*, vol. 14, no. 3, pp. 302–307, mai 1966.

-
- [63] I. C. Botten, M. S. Craig, R. C. McPhedran, J. L. Adams, and J. R. Andrewartha, "The Dielectric Lamellar Diffraction Grating," *Opt. Acta Int. J. Opt.*, vol. 28, no. 3, pp. 413–428, Mar. 1981.
 - [64] L. C. Botten, M. S. Craig, R. C. McPhedran, J. L. Adams, and J. R. Andrewartha, "The Finitely Conducting Lamellar Diffraction Grating," *Opt. Acta Int. J. Opt.*, vol. 28, no. 8, pp. 1087–1102, août 1981.
 - [65] R. Petit and L. C. Botten, *Electromagnetic theory of gratings*. Springer-Verlag, 1980.
 - [66] J. Chandezon, G. Raoult, and D. Maystre, "A new theoretical method for diffraction gratings and its numerical application," *J. Opt.*, vol. 11, no. 4, p. 235, Jul. 1980.
 - [67] J. Chandezon, M. T. Dupuis, G. Cornet, and D. Maystre, "Multicoated gratings: a differential formalism applicable in the entire optical region," *J. Opt. Soc. Am.*, vol. 72, no. 7, pp. 839–846, Jul. 1982.
 - [68] M. G. Moharam and T. K. Gaylord, "Rigorous coupled-wave analysis of planar-grating diffraction," *J. Opt. Soc. Am.*, vol. 71, no. 7, pp. 811–818, Jul. 1981.
 - [69] M. G. Moharam and T. K. Gaylord, "Rigorous coupled-wave analysis of grating diffraction: E-mode polarization and losses," *J. Opt. Soc. Am.*, vol. 73, no. 4, pp. 451–455, Apr. 1983.
 - [70] M. G. Moharam and T. K. Gaylord, "Diffraction analysis of dielectric surface-relief gratings," *J. Opt. Soc. Am.*, vol. 72, no. 10, pp. 1385–1392, Oct. 1982.
 - [71] M. G. Moharam and T. K. Gaylord, "Three-dimensional vector coupled-wave analysis of planar-grating diffraction," *J. Opt. Soc. Am.*, vol. 73, no. 9, pp. 1105–1112, Sep. 1983.
 - [72] C. B. Burckhardt, "Diffraction of a Plane Wave at a Sinusoidally Stratified Dielectric Grating," *J. Opt. Soc. Am.*, vol. 56, no. 11, pp. 1502–1508, Nov. 1966.
 - [73] K. Knop, "Rigorous diffraction theory for transmission phase gratings with deep rectangular grooves," *J. Opt. Soc. Am.*, vol. 68, no. 9, pp. 1206–1210, Sep. 1978.
 - [74] F. G. Kaspar, "Diffraction by thick, periodically stratified gratings with complex dielectric constant," *J. Opt. Soc. Am.*, vol. 63, no. 1, pp. 37–45, Jan. 1973.
 - [75] E. Silberstein, P. Lalanne, J.-P. Hugonin, and Q. Cao, "Use of grating theories in integrated optics," *J. Opt. Soc. Am. A*, vol. 18, no. 11, pp. 2865–2875, 2001.
 - [76] J. P. Hugonin and P. Lalanne, "Perfectly matched layers as nonlinear coordinate transforms: a generalized formalization," *J. Opt. Soc. Am. A*, vol. 22, no. 9, pp. 1844–1849, 2005.
 - [77] B. Guizal, D. Barchiesi, and D. Felbacq, "Electromagnetic beam diffraction by a finite lamellar structure: an aperiodic coupled-wave method," *J. Opt. Soc. Am. A*, vol. 20, no. 12, pp. 2274–2280, 2003.
 - [78] G. Granet and B. Guizal, "Efficient implementation of the coupled-wave method for metallic lamellar gratings in TM polarization," *J. Opt. Soc. Am. A*, vol. 13, no. 5, pp. 1019–1023, May 1996.
 - [79] P. Lalanne and G. M. Morris, "Highly improved convergence of the coupled-wave method for TM polarization," *J. Opt. Soc. Am. A*, vol. 13, no. 4, pp. 779–784, Apr. 1996.

- [80] L. Li, "Use of Fourier series in the analysis of discontinuous periodic structures," *J. Opt. Soc. Am. A*, vol. 13, no. 9, pp. 1870–1876, Sep. 1996.
- [81] "D65 Illuminant." [Online]. Available: http://www.cie.co.at/publ/abst/datatables15_2004/std65.txt. [Accessed: 20-Jan-2015].
- [82] C. Mornet, J. Vaillant, T. Decroux, D. Hérault, and I. Schanen, "Evaluation of color error and noise on simulated images," in *Proceedings of SPIE*, San Jose, CA, USA., 2010, vol. 7537, p. 75370Y–75370Y–12.
- [83] D. Pascale, "A review of RGB color spaces... from xyY to R'G'B." The BabelColor Company, 2002.
- [84] D. Pascale, "RGB coordinates of the Macbeth ColorChecker." The BabelColor Company, 2006.
- [85] S. Yokogawa, S. P. Burgos, and H. A. Atwater, "Plasmonic Color Filters for CMOS Image Sensor Applications," *Nano Lett.*, vol. 12, no. 8, pp. 4349–4354, août 2012.
- [86] J. Le Perchec, Y. Desieres, and R. E. de Lamaestre, "Plasmon-based photosensors comprising a very thin semiconducting region," *Appl. Phys. Lett.*, vol. 94, no. 18, p. 181104, May 2009.
- [87] Y. Chen, J. Dai, M. Yan, and M. Qiu, "Honeycomb-lattice plasmonic absorbers at NIR: anomalous high-order resonance," *Opt. Express*, vol. 21, no. 18, pp. 20873–20879, Sep. 2013.
- [88] C. Koechlin, P. Bouchon, F. Pardo, J. Jaeck, and X. Lafosse, "Total routing and absorption of photons in dual color plasmonic antennas," *Appl. Phys. Lett.*, vol. 99, no. 24, p. 241104, 2011.
- [89] J. Hao, J. Wang, X. Liu, W. J. Padilla, L. Zhou, and M. Qiu, "High performance optical absorber based on a plasmonic metamaterial," *Appl. Phys. Lett.*, vol. 96, no. 25, p. 251104, Jun. 2010.
- [90] P. Chen, R. Liang, Q. Huang, and Y. Xu, "Plasmonic filter with sub-waveguide coupled to vertical rectangular resonator structure," *Opt. Commun.*, vol. 284, no. 19, pp. 4795–4799, Sep. 2011.
- [91] S. Collin, F. Pardo, and J.-L. Pelouard, "Waveguiding in nanoscale metallic apertures," *Opt. Express*, vol. 15, no. 7, pp. 4310–4320, 2007.
- [92] Kun-Hua Wen, Lian-Shan Yan, Wei Pan, Bin Luo, Zhen Guo, Ying-Hui Guo, and Xian-Gang Luo, "Spectral Characteristics of Plasmonic Metal-Insulator-Metal Waveguides With a Tilted Groove," *IEEE Photonics J.*, vol. 4, no. 5, pp. 1794–1800, Oct. 2012.
- [93] Y. Qiu, L. Zhan, X. Hu, S. Luo, and Y. Xia, "Demonstration of color filters for OLED display based on extraordinary optical transmission through periodic hole array on metallic film," *Displays*, vol. 32, no. 5, pp. 308–312, décembre 2011.
- [94] Q. Chen, D. Chitnis, K. Walls, T. D. Drysdale, S. Collins, and D. R. S. Cumming, "CMOS Photodetectors Integrated With Plasmonic Color Filters," *IEEE Photonics Technol. Lett.*, vol. 24, no. 3, pp. 197–199, février 2012.
- [95] I. J. H. McCrindle, J. Grant, T. D. Drysdale, and D. R. S. Cumming, "Hybridization of optical plasmonics with terahertz metamaterials to create multi-spectral filters," *Opt. Express*, vol. 21, no. 16, pp. 19142–19152, Aug. 2013.

-
- [96] T. Ellenbogen, K. Seo, and K. B. Crozier, "Chromatic Plasmonic Polarizers for Active Visible Color Filtering and Polarimetry," *Nano Lett.*, vol. 12, no. 2, pp. 1026–1031, février 2012.
 - [97] V. R. Shrestha, S.-S. Lee, E.-S. Kim, and D.-Y. Choi, "Aluminum Plasmonics Based Highly Transmissive Polarization-Independent Subtractive Color Filters Exploiting a Nanopatch Array," *Nano Lett.*, vol. 14, no. 11, pp. 6672–6678, Nov. 2014.
 - [98] T. Xu, H. Shi, Y.-K. Wu, A. F. Kaplan, J. G. Ok, and L. J. Guo, "Structural Colors: From Plasmonic to Carbon Nanostructures," *Small*, vol. 7, no. 22, pp. 3128–3136, Nov. 2011.
 - [99] U. Palanchoke, S. Boutami, and J. Hazart, "CMOS-compatible metallic nanostructures for visible and infrared filtering," in *Proceedings of SPIE*, 2014, vol. 8994, p. 89940Y–89940Y–6.
 - [100] Y.-T. Yoon, S.-S. Lee, and B.-S. Lee, "Nano-patterned visible wavelength filter integrated with an image sensor exploiting a 90-nm CMOS process," *Photonics Nanostructures - Fundam. Appl.*, vol. 10, no. 1, pp. 54–59, Jan. 2012.
 - [101] D. Inoue, A. Miura, T. Nomura, H. Fujikawa, K. Sato, N. Ikeda, D. Tsuya, Y. Sugimoto, and Y. Koide, "Polarization independent visible color filter comprising an aluminum film with surface-plasmon enhanced transmission through a subwavelength array of holes," *Appl. Phys. Lett.*, vol. 98, no. 9, pp. 093113–093115, 2011.
 - [102] D. Lerose, D. Gabler, and S. Junger, "CMOS-integrated geometrically tunable optical filter," in *Proceedings of Advanced Semiconductor Manufacturing Conference (ASMC), 2012 23rd Annual SEMI*, 2012, pp. 97–101.
 - [103] Q. Chen, X. Shi, Y. Ma, and J. He, "Application of Surface Plasmon Polaritons in CMOS Digital Imaging," in *Plasmonics - Principles and Applications*, K. Y. Kim, Ed. InTech, 2012.
 - [104] P. Bouchon, C. Koechlin, F. Pardo, R. Haïdar, and J.-L. Pelouard, "Wideband omnidirectional infrared absorber with a patchwork of plasmonic nanoantennas," *Opt. Lett.*, vol. 37, no. 6, pp. 1038–1040, Mar. 2012.
 - [105] T. Xu, Y.-K. Wu, X. Luo, and L. J. Guo, "Plasmonic nanoresonators for high-resolution colour filtering and spectral imaging," *Nat. Commun.*, vol. 1, no. 59, août 2010.
 - [106] J. A. Dionne, L. A. Sweatlock, H. A. Atwater, and A. Polman, "Plasmon slot waveguides: Towards chip-scale propagation with subwavelength-scale localization," *Phys. Rev. B*, vol. 73, no. 3, p. 035407, Jan. 2006.
 - [107] M. Guillaumée, L. A. Dunbar, C. Santschi, E. Grenet, R. Eckert, O. J. F. Martin, and R. P. Stanley, "Polarization sensitive silicon photodiodes using nanostructured metallic grids," *Appl. Phys. Lett.*, vol. 94, no. 19, p. 193503, May 2009.
 - [108] M. Guillaumée, L. A. Dunbar, and R. P. Stanley, "Description of the modes governing the optical transmission through metal gratings," *Opt. Express*, vol. 19, no. 5, pp. 4740–4755, Feb. 2011.
 - [109] F. Przybilla, A. Degiron, J.-Y. Laluet, C. Genet, and T. W. Ebbesen, "Optical transmission in perforated noble and transition metal films," *J. Opt. Pure Appl. Opt.*, vol. 8, no. 5, p. 458, May 2006.
 - [110] I. Freestone, N. Meeks, M. Sax, and C. Higgitt, "The Lycurgus Cup — A Roman nanotechnology," *Gold Bull.*, vol. 40, no. 4, pp. 270–277, Dec. 2007.

- [111] G. Mie, “Beiträge zur Optik trüber Medien, speziell kolloidaler Metallösungen,” *Ann. Phys.*, vol. 330, no. 3, pp. 377–445, Jan. 1908.
- [112] J. Le Perchec, R. E. de Lamaestre, M. Brun, N. Rochat, O. Gravrand, G. Badano, J. Hazart, and S. Nicoletti, “High rejection bandpass optical filters based on sub-wavelength metal patch arrays,” *Opt. Express*, vol. 19, no. 17, pp. 15720–15731, Aug. 2011.
- [113] O. Lecarme, Q. Sun, K. Ueno, and H. Misawa, “Robust and Versatile Light Absorption at Near-Infrared Wavelengths by Plasmonic Aluminum Nanorods,” *ACS Photonics*, vol. 1, no. 6, pp. 538–546, juin 2014.
- [114] B. Zeng, Y. Gao, and F. J. Bartoli, “Ultrathin Nanostructured Metals for Highly Transmissive Plasmonic Subtractive Color Filters,” *Sci. Rep.*, vol. 3, no. 2840, Oct. 2013.
- [115] T. W. Ebbesen, H. J. Lezec, H. F. Ghaemi, T. Thio, and P. A. Wolff, “Extraordinary optical transmission through sub-wavelength hole arrays,” *Nature*, vol. 391, no. 6668, pp. 667–669, février 1998.
- [116] H. A. Bethe, “Theory of Diffraction by Small Holes,” *Phys. Rev.*, vol. 66, no. 7–8, pp. 163–182, Oct. 1944.
- [117] H. F. Ghaemi, T. Thio, D. E. Grupp, T. W. Ebbesen, and H. J. Lezec, “Surface plasmons enhance optical transmission through subwavelength holes,” *Phys. Rev. B*, vol. 58, no. 11, pp. 6779–6782, Sep. 1998.
- [118] Q. Chen and D. R. S. Cumming, “High transmission and low color cross-talk plasmonic color filters using triangular-lattice hole arrays in aluminum films,” *Opt. Express*, vol. 18, no. 13, pp. 14056–14062, Jun. 2010.
- [119] K. Walls, “Nanophotonic filters for digital imaging,” PhD, University of Glasgow, 2013.
- [120] J. A. Porto, F. J. García-Vidal, and J. B. Pendry, “Transmission Resonances on Metallic Gratings with Very Narrow Slits,” *Phys. Rev. Lett.*, vol. 83, no. 14, pp. 2845–2848, Oct. 1999.
- [121] A. I. Fernández-Domínguez, F. J. García-Vidal, and L. Martín-Moreno, “Resonant transmission of light through finite arrays of slits,” *Phys. Rev. B*, vol. 76, no. 23, p. 235430, décembre 2007.
- [122] Y.-T. Yoon, C.-H. Park, and S.-S. Lee, “Highly Efficient Color Filter Incorporating a Thin Metal–Dielectric Resonant Structure,” *Appl. Phys. Express*, vol. 5, no. 2, p. 022501, Feb. 2012.
- [123] E. Popov, N. Bonod, M. Nevière, H. Rigneault, P.-F. Lenne, and P. Chaumet, “Surface plasmon excitation on a single subwavelength hole in a metallic sheet,” *Appl. Opt.*, vol. 44, no. 12, pp. 2332–2337, 2005.
- [124] A. Degiron, H. J. Lezec, N. Yamamoto, and T. W. Ebbesen, “Optical transmission properties of a single subwavelength aperture in a real metal,” *Opt. Commun.*, vol. 239, no. 1–3, pp. 61–66, Sep. 2004.
- [125] F. J. García-Vidal, E. Moreno, J. A. Porto, and L. Martín-Moreno, “Transmission of Light through a Single Rectangular Hole,” *Phys. Rev. Lett.*, vol. 95, no. 10, p. 103901, août 2005.
- [126] F. J. García-Vidal, L. Martín-Moreno, E. Moreno, L. K. S. Kumar, and R. Gordon, “Transmission of light through a single rectangular hole in a real metal,” *Phys. Rev. B*, vol. 74, no. 15, p. 153411, Oct. 2006.

-
- [127] L. Martín-Moreno, F. J. García-Vidal, H. J. Lezec, K. M. Pellerin, T. Thio, J. B. Pendry, and T. W. Ebbesen, “Theory of extraordinary optical transmission through subwavelength hole arrays,” *Phys. Rev. Lett.*, vol. 86, no. 6, pp. 1114–1117, Feb. 2001.
 - [128] K. L. Van der Molen, F. B. Segerink, N. F. Van Hulst, and L. Kuipers, “Influence of hole size on the extraordinary transmission through subwavelength hole arrays,” *Appl. Phys. Lett.*, vol. 85, no. 19, pp. 4316–4318, Nov. 2004.
 - [129] K. L. Van der Molen, K. J. Klein Koerkamp, S. Enoch, F. B. Segerink, N. F. Van Hulst, and L. Kuipers, “Role of shape and localized resonances in extraordinary transmission through periodic arrays of subwavelength holes: Experiment and theory,” *Phys. Rev. B*, vol. 72, no. 4, p. 045421, juillet 2005.
 - [130] A. Mary, S. G. Rodrigo, L. Martín-Moreno, and F. J. García-Vidal, “Theory of light transmission through an array of rectangular holes,” *Phys. Rev. B*, vol. 76, no. 19, p. 195414, Nov. 2007.
 - [131] J.-Y. Li, Y.-L. Hua, J.-X. Fu, and Z.-Y. Li, “Influence of hole geometry and lattice constant on extraordinary optical transmission through subwavelength hole arrays in metal films,” *J. Appl. Phys.*, vol. 107, no. 7, p. 073101, Apr. 2010.
 - [132] K. J. K. Koerkamp, S. Enoch, F. B. Segerink, N. F. van Hulst, and L. Kuipers, “Strong Influence of Hole Shape on Extraordinary Transmission through Periodic Arrays of Subwavelength Holes,” *Phys. Rev. Lett.*, vol. 92, no. 18, p. 183901, mai 2004.
 - [133] A. Degiron and T. W. Ebbesen, “The role of localized surface plasmon modes in the enhanced transmission of periodic subwavelength apertures,” *J. Opt. Pure Appl. Opt.*, vol. 7, no. 2, p. S90, Feb. 2005.
 - [134] S. Landis, P. Brianceau, N. Chaix, Y. Désières, V. Reboud, and M. Argoud, “Metallic colour filtering arrays manufactured by nanoimprint lithography,” in *Proceedings of SPIE*, 2012, pp. 842807–842807–8.
 - [135] Y. Tang, B. Vlahovic, and D. J. Brady, “Metallic nano-structures for polarization-independent multi-spectral filters,” *Nanoscale Res. Lett.*, vol. 6, no. 1, p. 394, May 2011.
 - [136] L. Lin, L. B. Hande, and A. Roberts, “Resonant nanometric cross-shaped apertures: Single apertures versus periodic arrays,” *Appl. Phys. Lett.*, vol. 95, no. 20, p. 201116, Nov. 2009.
 - [137] C.-Y. Chen, M.-W. Tsai, T.-H. Chuang, Y.-T. Chang, and S.-C. Lee, “Extraordinary transmission through a silver film perforated with cross shaped hole arrays in a square lattice,” *Appl. Phys. Lett.*, vol. 91, no. 6, p. 063108, Aug. 2007.
 - [138] C. Yang, W. Shen, Y. Zhang, H. Peng, X. Zhang, and X. Liu, “Design and simulation of omnidirectional reflective color filters based on metal-dielectric-metal structure,” *Opt. Express*, vol. 22, no. 9, pp. 11384–11391, May 2014.
 - [139] W. Zhou, H. Gao, and T. W. Odom, “Toward Broadband Plasmonics: Tuning Dispersion in Rhombic Plasmonic Crystals,” *ACS Nano*, vol. 4, no. 2, pp. 1241–1247, février 2010.
 - [140] D. Van Labeke, D. Gérard, B. Guizal, F. I. Baida, and L. Li, “An angle-independent Frequency Selective Surface in the optical range,” *Opt. Express*, vol. 14, no. 25, pp. 11945–11951, 2006.
 - [141] C. Genet, M. P. van Exter, and J. P. Woerdman, “Fano-type interpretation of red shifts and red tails in hole array transmission spectra,” *Opt. Commun.*, vol. 225, no. 4–6, pp. 331–336, Oct. 2003.

- [142] M. Sarrazin, J.-P. Vigneron, and J.-M. Vigoureux, "Role of Wood anomalies in optical properties of thin metallic films with a bidimensional array of subwavelength holes," *Phys. Rev. B*, vol. 67, no. 8, p. 085415, février 2003.
- [143] D. Pacifici, H. J. Lezec, L. A. Sweatlock, R. J. Walters, and H. A. Atwater, "Universal optical transmission features in periodic and quasiperiodic hole arrays," *Opt. Express*, vol. 16, no. 12, pp. 9222–9238, Jun. 2008.
- [144] L. Lin and A. Roberts, "Light transmission through nanostructured metallic films: coupling between surface waves and localized resonances," *Opt. Express*, vol. 19, no. 3, pp. 2626–2633, Jan. 2011.
- [145] G. H. Chan, J. Zhao, G. C. Schatz, and R. P. V. Duyne, "Localized Surface Plasmon Resonance Spectroscopy of Triangular Aluminum Nanoparticles," *J. Phys. Chem. C*, vol. 112, no. 36, pp. 13958–13963, Sep. 2008.
- [146] P. C. Andricacos, C. Uzoh, J. O. Dukovic, J. Horkans, and H. Deligianni, "Damascene copper electroplating for chip interconnections," *Ibm J. Res. Dev.*, vol. 42, no. 5, pp. 567–574, Sep. 1998.
- [147] R. F. Schnabel, L. A. Clevenger, G. Costrini, D. M. Dobuzinsky, R. Filippi, J. Gambino, G. Y. Lee, R. C. Iggulden, C. Lin, Z. G. Lu, X. J. Ning, R. Ramachandran, M. Ronay, D. Többen, and S. J. Weber, "Aluminum dual damascene metallization for 0.175 μm DRAM generations and beyond," *Microelectron. Eng.*, vol. 50, no. 1–4, pp. 265–270, Jan. 2000.
- [148] J. Kriz, C. Angelkort, M. Czekalla, S. Huth, D. Meinhold, A. Pohl, S. Schulte, A. Thamm, and S. Wallace, "Overview of dual damascene integration schemes in Cu BEOL integration," *Microelectron. Eng.*, vol. 85, no. 10, pp. 2128–2132, Oct. 2008.
- [149] M. B. Anand, N. Nakamura, J. Wada, Y. Oikawa, T. Katata, K. Shiba, and H. Shibata, "A Fully Integrated Aluminum Dual Damascene Process Using a New Double Stopper Structure," *Jpn. J. Appl. Phys.*, vol. 37, no. 10R, p. 5526, Oct. 1998.
- [150] K. K. Schuegraf, *Handbook of thin-film deposition processes and techniques: principles, methods, equipment, and applications*. Noyes Publications, 1988.
- [151] R. Girard-Desprolet, S. Lhostis, and S. Boutami, "Dispositif afficheur d'image ou dispositif capteur d'image comprenant un filtre spectral nanostructuré," EP2816007 A1 - US20140374574 A1, 24-Dec-2014.
- [152] L. Lin and A. Roberts, "Angle-robust resonances in cross-shaped aperture arrays," *Appl. Phys. Lett.*, vol. 97, no. 6, p. 061109, Aug. 2010.
- [153] R. Girard-Desprolet, S. Boutami, S. Lhostis, and G. Vitrant, "Angular and polarization properties of cross-holes nanostructured metallic filters," *Opt. Express*, vol. 21, no. 24, pp. 29412–29424, Dec. 2013.
- [154] R. Girard-Desprolet, S. Boutami, S. Lhostis, and G. Vitrant, "Angular stability of cross-shaped-hole arrays metallic filters," in *Proceedings of SPIE Optics and Photonics*, San Diego, CA, USA., 2013, vol. 8809, p. 88092J–88097J.
- [155] A. Degiron, H. J. Lezec, W. L. Barnes, and T. W. Ebbesen, "Effects of hole depth on enhanced light transmission through subwavelength hole arrays," *Appl. Phys. Lett.*, vol. 81, no. 23, pp. 4327–4329, Dec. 2002.

- [156] J. Bravo-Abad, L. Martín-Moreno, F. J. García-Vidal, E. Hendry, and J. Gómez Rivas, "Transmission of light through periodic arrays of square holes: From a metallic wire mesh to an array of tiny holes," *Phys. Rev. B*, vol. 76, no. 24, p. 241102, décembre 2007.
- [157] P. B. Catrysse and S. Fan, "Propagating plasmonic mode in nanoscale apertures and its implications for extraordinary transmission," *J. Nanophotonics*, vol. 2, no. 1, pp. 021790–021790–20, 2008.
- [158] S. M. Orbons, M. I. Haftel, C. Schlockermann, D. Freeman, M. Milicevic, T. J. Davis, B. Luther-Davies, D. N. Jamieson, and A. Roberts, "Dual resonance mechanisms facilitating enhanced optical transmission in coaxial waveguide arrays," *Opt. Lett.*, vol. 33, no. 8, p. 821, Apr. 2008.
- [159] M. J. Kofke, D. H. Waldeck, Z. Fakhraai, S. Ip, and G. C. Walker, "The effect of periodicity on the extraordinary optical transmission of annular aperture arrays," *Appl. Phys. Lett.*, vol. 94, no. 2, p. 023104, 2009.
- [160] H. Ehrenreich, H. R. Philipp, and B. Segall, "Optical Properties of Aluminum," *Phys. Rev.*, vol. 132, no. 5, pp. 1918–1928, Dec. 1963.
- [161] R. Girard-Desprolet, S. Lhostis, S. Boutami, and M. Marty, "Procédé de formation d'un dispositif imageur intégré à illumination face avant comportant au moins un filtre optique métallique, et dispositif correspondant," DD 14442, EN 13 62088, not published yet.
- [162] R. Girard-Desprolet, S. Lhostis, S. Boutami, and M. Marty, "Procédé de formation d'un dispositif intégré à illumination face arrière comprenant un filtre optique métallique, et dispositif correspondant," DD 15038, EN 13 55849, not published yet.
- [163] R. Girard-Desprolet, S. Boutami, S. Lhostis, L. Frey, C. Mornet, and M. Armand, "Hole-array plasmonic filters for efficient Ambient Light Sensing," in *Proceedings of OPTRO 6th International Symposium on Optronics in Defense and Security*, Paris, France, 2014, vol. 2956618.
- [164] MonolithIC3D, "Lithography issues for high volume manufacturing: cost normalized to area throughput," *MonolithIC3D*, 21-Jul-2014. [Online]. Available: <http://www.monolithic3d.com/blog/paradigm-shift-in-semi-equipment-confirmed>.
- [165] P. Dumon, "Ultra-Compact Integrated Optical Filters in Silicon-on-insulator by Means of Wafer-Scale Technology," Ph.D. dissertation, Univ. Gent, Gent, Belgium., 2007.
- [166] S. Ayas, G. Bakan, and A. Dana, "Rounding corners of nano-square patches for multispectral plasmonic metamaterial absorbers," *Opt. Express*, vol. 23, no. 9, pp. 11763–11770, May 2015.
- [167] A. M. Mahros and M. M. Tharwat, "Investigating the Fabrication Imperfections of Plasmonic Nanohole Arrays and Its Effect on the Optical Transmission Spectra," *J. Nanomater.*, no. 178583, 2015.
- [168] R. Girard-Desprolet, S. Lhostis, C. Beylier, V. Farys, G. Vitrant, and S. Boutami, "Impact of process factors on the performance of hole array metallic filters," *Appl. Phys. A*, vol. 117, no. 2, pp. 485–490, Sep. 2014.
- [169] R. Girard-Desprolet, S. Lhostis, C. Beylier, V. Farys, G. Vitrant, and S. Boutami, "Review on the process factors limiting the performances of hole-array metallic filters," in *Proceedings of META 5th International Conference on Metamaterials, Photonics Crystals and Plasmonics*, Singapour, 2014, pp. 485–490.

- [170] S. Y. Chou, P. R. Krauss, and P. J. Renstrom, "Imprint of sub-25 nm vias and trenches in polymers," *Appl. Phys. Lett.*, vol. 67, no. 21, pp. 3114–3116, Nov. 1995.
- [171] S. Landis, P. Brianceau, V. Reboud, N. Chaix, Y. Désières, and M. Argoud, "Metallic colour filtering arrays manufactured by NanoImprint lithography," *Microelectron. Eng.*, vol. 111, pp. 193–198, Nov. 2013.
- [172] R. L. Opila, *Chemical Mechanical Planarization in IC Device Manufacturing III: Proceedings of the International Symposium*. The Electrochemical Society, 2000.
- [173] L. Dumas, S. Verrier, A. Achen, J. Hetzner, M. Proust, C. Rossato, P. Caubet, T. Jagueneau, C. Fellous, E. Serret, and J. –. Giraudin, *Electromigration and adhesion improvements of Thick Cu/BCB architecture in BiCMOS RF technology*. .
- [174] L. Frey, L. Masarotto, P. G. D'Aillon, C. Pellé, M. Armand, M. Marty, C. Jamin-Mornet, S. Lhostis, and O. Le Briz, "On-chip copper-dielectric interference filters for manufacturing of ambient light and proximity CMOS sensors," *Appl. Opt.*, vol. 53, no. 20, pp. 4493–4502, Jul. 2014.
- [175] C. Langhammer, M. Schwind, B. Kasemo, and I. Zorić, "Localized Surface Plasmon Resonances in Aluminum Nanodisks," *Nano Lett.*, vol. 8, no. 5, pp. 1461–1471, mai 2008.
- [176] M. Schwind, C. Langhammer, B. Kasemo, and I. Zorić, "Nanoplasmonic sensing and QCM-D as ultrasensitive complementary techniques for kinetic corrosion studies of aluminum nanoparticles," *Appl. Surf. Sci.*, vol. 257, no. 13, pp. 5679–5687, avril 2011.
- [177] M. Schwind, B. Kasemo, and I. Zorić, "Localized and Propagating Plasmons in Metal Films with Nanoholes," *Nano Lett.*, vol. 13, no. 4, pp. 1743–1750, avril 2013.
- [178] L. P. H. Jeurgens, W. G. Sloof, F. D. Tichelaar, and E. J. Mittemeijer, "Growth kinetics and mechanisms of aluminum-oxide films formed by thermal oxidation of aluminum," *J. Appl. Phys.*, vol. 92, no. 3, pp. 1649–1656, Aug. 2002.
- [179] H. P. Godard, *The corrosion of light metals*. New York: Wiley, 1967.
- [180] E. Wallin, "Alumina thin film growth: experiments and modeling," Disseration, Linköping University, Linköping, 2007.
- [181] C. Mack, *Fundamental Principles of Optical Lithography: The Science of Microfabrication*. John Wiley & Sons, 2011.
- [182] H. Shen and B. Maes, "Enhanced optical transmission through tapered metallic gratings," *Appl. Phys. Lett.*, vol. 100, no. 24, p. 241104, Jun. 2012.
- [183] A. Krishnan, T. Thio, T. J. Kim, H. J. Lezec, T. W. Ebbesen, P. A. Wolff, J. Pendry, L. Martin-Moreno, and F. J. Garcia-Vidal, "Evanescently coupled resonance in surface plasmon enhanced transmission," *Opt. Commun.*, vol. 200, no. 1–6, pp. 1–7, décembre 2001.
- [184] M. Zaborowski and P. Dumania, "Kinetics of hillock growth in Al and Al-alloys," *Microelectron. Eng.*, vol. 50, no. 1–4, pp. 301–309, Jan. 2000.
- [185] G. G. Stoney, "The Tension of Metallic Films Deposited by Electrolysis," *Proc. R. Soc. Lond. Ser. Contain. Pap. Math. Phys. Character*, vol. 82, no. 553, pp. 172–175, mai 1909.

- [186] D. Gerth, D. Katzer, and M. Krohn, "Study of the thermal behaviour of thin aluminium alloy films," *Thin Solid Films*, vol. 208, no. 1, pp. 67–75, février 1992.
- [187] W. De Bosscher, M. Matilainen, A. Witvrouw, and K. Maex, "Influence of temperature on the properties of sputtered AlSiCu films," *Appl. Surf. Sci.*, vol. 73, pp. 295–304, Nov. 1993.
- [188] D. Resnik, J. Kovač, M. Godec, D. Vrtačnik, M. Možek, and S. Amon, "The influence of target composition and thermal treatment on sputtered Al thin films on Si and SiO₂ substrates," *Microelectron. Eng.*, vol. 96, pp. 29–35, août 2012.
- [189] M. S. Jackson and L. Che-yu, "Stress relaxation and hillock growth in thin films," *Acta Metall.*, vol. 30, no. 11, pp. 1993–2000, Nov. 1982.
- [190] D. Kim, B. Heiland, W. D. Nix, E. Arzt, M. D. Deal, and J. D. Plummer, "Microstructure of thermal hillocks on blanket Al thin films," *Thin Solid Films*, vol. 371, no. 1–2, pp. 278–282, août 2000.
- [191] S.-J. Hwang, W. D. Nix, and Y.-C. Joo, "A model for hillock growth in Al thin films controlled by plastic deformation," *Acta Mater.*, vol. 55, no. 15, pp. 5297–5301, Sep. 2007.
- [192] F. Y. Genin and W. J. Siekhaus, "Experimental study to validate a model of hillock's formation in aluminum thin films," *J. Appl. Phys.*, vol. 79, no. 7, pp. 3560–3566, 1996.
- [193] B. C. Martin, C. J. Tracy, J. W. Mayer, and L. E. Hendrickson, "A comparative study of Hillock formation in aluminum films," *Thin Solid Films*, vol. 271, no. 1–2, pp. 64–68, décembre 1995.
- [194] C. Y. Chang and R. W. Vook, "The effect of surface aluminum oxide films on thermally induced hillock formation," *Thin Solid Films*, vol. 228, no. 1–2, pp. 205–209, mai 1993.
- [195] M. T. Kao and J. F. Lin, "Effects of deposition conditions of the Al film in Al/glass specimens and annealing conditions on internal stresses and hillock formations," *Thin Solid Films*, vol. 520, no. 16, pp. 5353–5360, 2012.
- [196] C. J. Dell'oca and A. J. Learn, "Anodization of aluminum to inhibit hillock growth during high temperature processing," *Thin Solid Films*, vol. 8, no. 5, pp. R47–R50, Nov. 1971.
- [197] E. Iwamura, K. Takagi, and T. Ohnishi, "Effect of aluminium oxide caps on hillock formation in aluminium alloy films," *Thin Solid Films*, vol. 349, no. 1–2, pp. 191–198, juillet 1999.
- [198] K.-H. Jang, S.-J. Hwang, and Y.-C. Joo, "Effect of capping layer on hillock formation in thin Al films," *Met. Mater. Int.*, vol. 14, no. 2, pp. 147–150, Apr. 2008.
- [199] M. Rocke and M. Schneegans, "Titanium nitride for antireflection control and hillock suppression on aluminum silicon metallization," *J. Vac. Sci. Technol. B*, vol. 6, no. 4, pp. 1113–1115, Jul. 1988.
- [200] C. Vieu, F. Carcenac, A. Pépin, Y. Chen, M. Mejias, A. Lebib, L. Manin-Ferlazzo, L. Couraud, and H. Launois, "Electron beam lithography: resolution limits and applications," *Appl. Surf. Sci.*, vol. 164, no. 1–4, pp. 111–117, Sep. 2000.
- [201] X. Yang, D.-P. Kim, D.-S. Um, G.-H. Kim, and C.-I. Kim, "Temperature dependence on dry etching of Al₂O₃ thin films in BCl₃/Cl₂/Ar plasma," *J. Vac. Sci. Technol. A*, vol. 27, no. 4, pp. 821–825, Jul. 2009.

- [202] S. V. Nguyen, "High-density plasma chemical vapor deposition of silicon-based dielectric films for integrated circuits," *IBM J. Res. Dev.*, vol. 43, no. 1.2, pp. 109–126, Jan. 1999.
- [203] J. B. Lasky, "Wafer bonding for silicon-on-insulator technologies," *Appl. Phys. Lett.*, vol. 48, no. 1, pp. 78–80, Jan. 1986.
- [204] R. Stengl, T. Tan, and U. Gösele, "A Model for the Silicon Wafer Bonding Process," *Jpn. J. Appl. Phys.*, vol. 28, no. 10R, p. 1735, Oct. 1989.
- [205] Q.-Y. Tong and U. Gösele, *Semiconductor Wafer Bonding: Science and Technology*, 1 edition. New York, NY: Wiley-Interscience, 1998.
- [206] F. Rieutord, H. Moriceau, R. Beneyton, L. Capello, C. Morales, and A.-M. Charvet, "Rough Surface Adhesion Mechanisms for Wafer Bonding," *ECS Trans.*, vol. 3, no. 6, pp. 205–215, Oct. 2006.
- [207] O. Rayssac, "Étude du collage par adhesion moleculaire hydrophile : application au controle de l'énergie de collage," Ph.D. dissertation, Univ. Grenoble, Grenoble, 1999.
- [208] H. Moriceau, F. Rieutord, C. Morales, A. M. Charvet, O. Rayssac, B. Bataillou, F. Fournel, J. Eymery, A. Pascale, P. Gentile, A. Bavard, J. Mézière, C. Maleville, and B. Aspar, "Direct Wafer Bonding for Nanostructure Preparations," *Solid State Phenom.*, vol. 121–123, pp. 29–32, 2007.
- [209] Y. Beilliard, "Étude de l'intégration du collage direct cuivre/oxyde pour l'élaboration d'une architecture 3D-SIC," Ph.D. dissertation, Univ. Grenoble, Grenoble, France, 2015.
- [210] K. Fischer, M. Agostinelli, C. Allen, D. Bahr, M. Bost, P. Charvat, V. Chikarmane, Q. Fu, and et. al., "Low-k Interconnect Stack with multi-layer Air Gap and Tri-Metal-Insulator-Metal Capacitors for 14nm High Volume Manufacturing," in *Proceedings of International Interconnect Technology Conference - Materials for Advanced Metallization*, Grenoble, France, 2015.
- [211] F. Przybilla, A. Degiron, C. Genet, T. Ebbesen, F. de Léon-Pérez, J. Bravo-Abad, F. J. García-Vidal, and L. Martín-Moreno, "Efficiency and finite size effects in enhanced transmission through subwavelength apertures," *Opt. Express*, vol. 16, no. 13, pp. 9571–9579, Jun. 2008.
- [212] S. P. Burgos, S. Yokogawa, and H. A. Atwater, "Color Imaging via Nearest Neighbor Hole Coupling in Plasmonic Color Filters Integrated onto a Complementary Metal-Oxide Semiconductor Image Sensor," *ACS Nano*, vol. 7, no. 11, pp. 10038–10047, Nov. 2013.
- [213] G. Demésy, "Modélisation électromagnétique tri-dimensionnelle de réseaux complexes. Application au filtrage spectral dans les imageurs CMOS," Ph.D. dissertation, Univ. Aix-Marseille III, Marseille, 2009.
- [214] I. J. H. McCrindle, J. Grant, T. D. Drysdale, and D. R. S. Cumming, "Multi-Spectral Materials: Hybridisation of Optical Plasmonic Filters and a Terahertz Metamaterial Absorber," *Adv. Opt. Mater.*, vol. 2, no. 2, pp. 149–153, février 2014.
- [215] R. Haïdar, G. Vincent, S. Collin, N. Bardou, N. Guérineau, J. Deschamps, and J.-L. Pelouard, "Free-standing subwavelength metallic gratings for snapshot multispectral imaging," *Appl. Phys. Lett.*, vol. 96, no. 22, p. 221104, May 2010.
- [216] M. V. Bashevoy, F. Jonsson, K. F. MacDonald, Y. Chen, and N. I. Zheludev, "Hyperspectral imaging of plasmonic nanostructures with nanoscale resolution," *Opt. Express*, vol. 15, no. 18, pp. 11313–11320, 2007.

Appendix

Appendix A

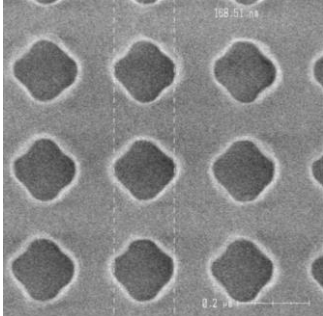
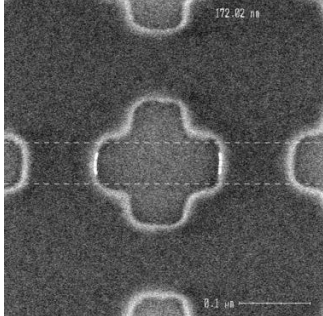
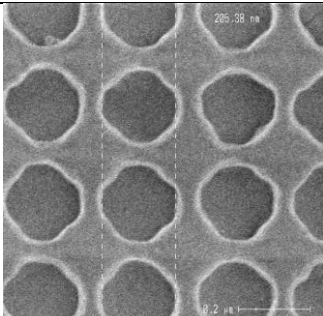
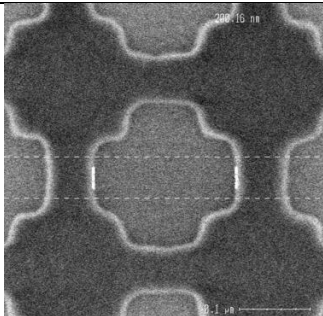
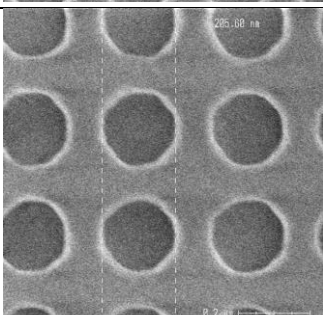
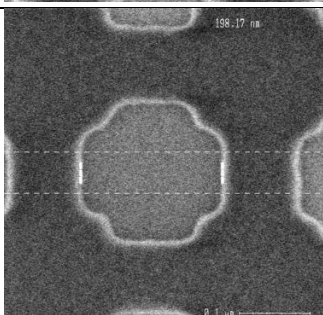
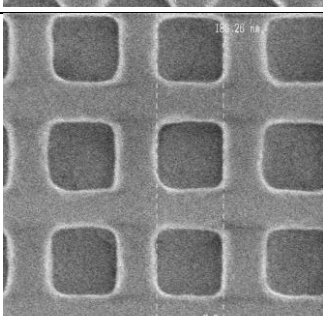
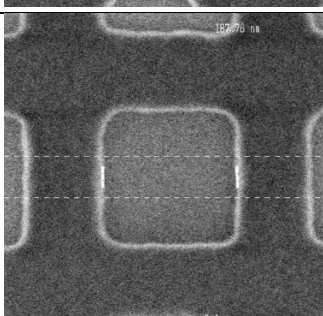
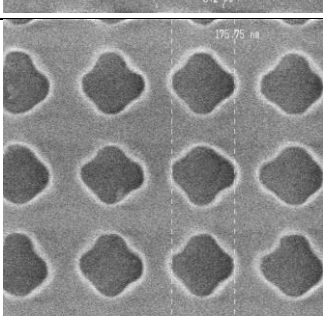
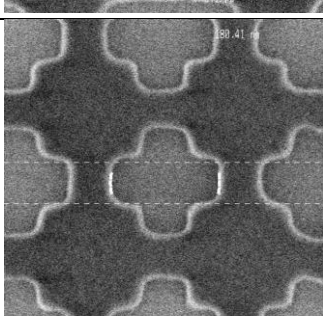
Optimized base: designs' characteristics

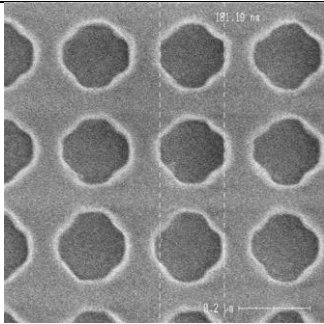
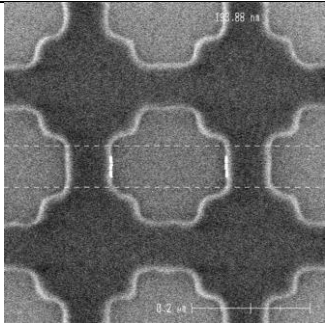
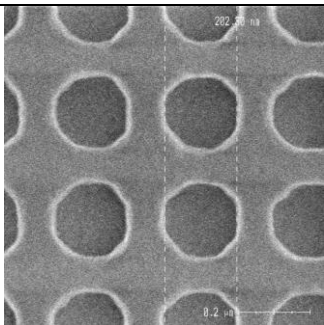
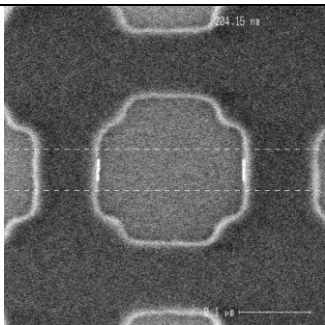
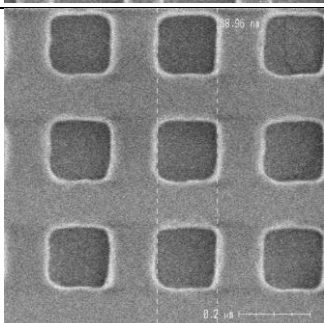
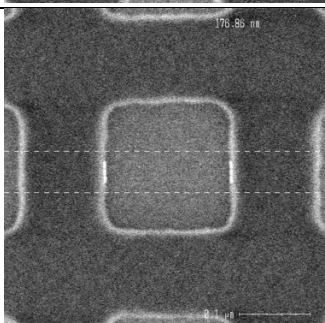
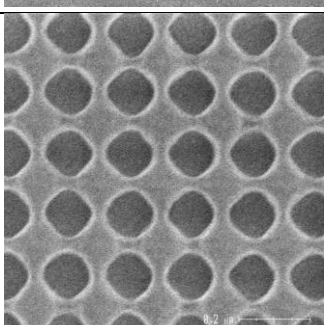
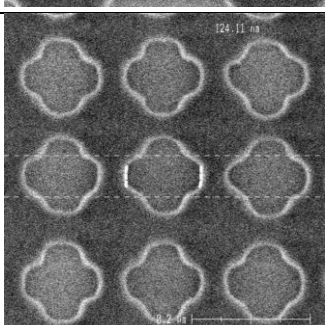
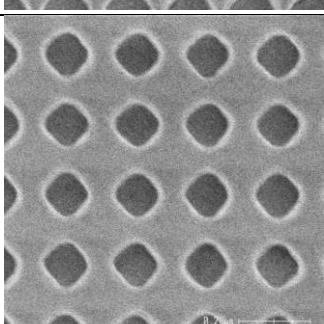
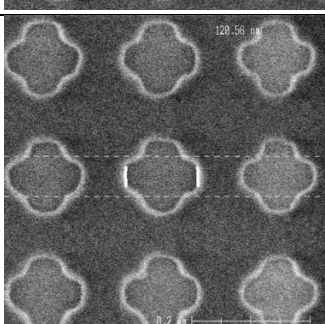
Array	Hole shape	b/a	Description	ALS Target	h_m	P	a	b	Optim. ALS Err Max	Optim. ALS Dark
L_A1	Crosses	0.4	ALS	1 dB	227	275	167	67	1.25	62.9
L_A2	Crosses	0.5	ALS	1 dB	354	267	193	96	1.05	39.4
L_A3	Crosses	0.6	ALS	1 dB	274	298	185	109	1.02	42.8
L_A4	Squares	-	ALS	1 dB	338	296	178	-	1.02	29.1
L_B1	Crosses	0.4	ALS	1.5 dB	249	253	173	69	1.53	53.2
L_B2	Crosses	0.5	ALS	1.5 dB	273	267	187	92	1.52	32.2
L_B3	Crosses	0.6	ALS	1.5 dB	311	301	198	119	1.51	32.1
L_B4	Squares	-	ALS	1.5 dB	229	298	167	-	1.51	25.9
L_C1	Crosses	0.4	Intercrosses dist. d = 50 nm	-	75	170	120	48	-	-
L_C2	Crosses	0.4	Intercrosses dist. d = 75 nm	-	75	195	120	48	-	-
L_C3	Crosses	0.4	Intercrosses dist. d = 100 nm	-	75	220	120	48	-	-
L_C4	Crosses	0.4	Intercrosses dist. d = 150 nm	-	75	270	120	48	-	-
L_D1	Crosses	0.6	Intercrosses dist. d = 50 nm	-	75	170	120	72	-	-
L_D2	Crosses	0.6	Intercrosses dist. d = 75 nm	-	75	195	120	72	-	-
L_D3	Crosses	0.6	Intercrosses dist. d = 100 nm	-	75	220	120	72	-	-
L_D4	Crosses	0.6	Intercrosses dist. d = 150 nm	-	75	270	120	72	-	-
R_A1	Crosses	0.5	Reference ALS 2dB	2 dB	300	250	200	100		
R_A2	Crosses	0.45	ALS	1 dB	268	275	176	79	1.11	56.4
R_A3	Crosses	0.55	ALS	1 dB	340	300	192	106	1.07	49.7
R_A4	Crosses	0.65	ALS	1 dB	284	298	189	119	1.02	36.6
R_B1	Crosses	0.5	Reference ALS 1dB	1 dB	300	275	180	90		
R_B2	Crosses	0.45	ALS	1.5 dB	201	275	170	77	1.52	43.9
R_B3	Crosses	0.55	ALS	1.5 dB	250	279	187	103	1.51	28
R_B4	Crosses	0.65	ALS – Hexagonal array		236	298	189	119	1.51	26
R_C1	Squares	-	ALS	0.85 dB	308	305	171	-	0.85	40
R_C2	Squares	-	ALS	1.25 dB	315	298	179	-	1.21	25.8
R_C3	Crosses	0.4	-		75	150	120	48	-	-
R_C4	Crosses	0.5	-		75	150	120	60	-	-
R_D1	Crosses	0.6	-		75	150	120	72	-	-
R_D2	Crosses	0.7	-		75	150	120	84	-	-
R_D3	Crosses	0.8	-		75	150	120	96	-	-
R_D4	Circles	-	ALS							

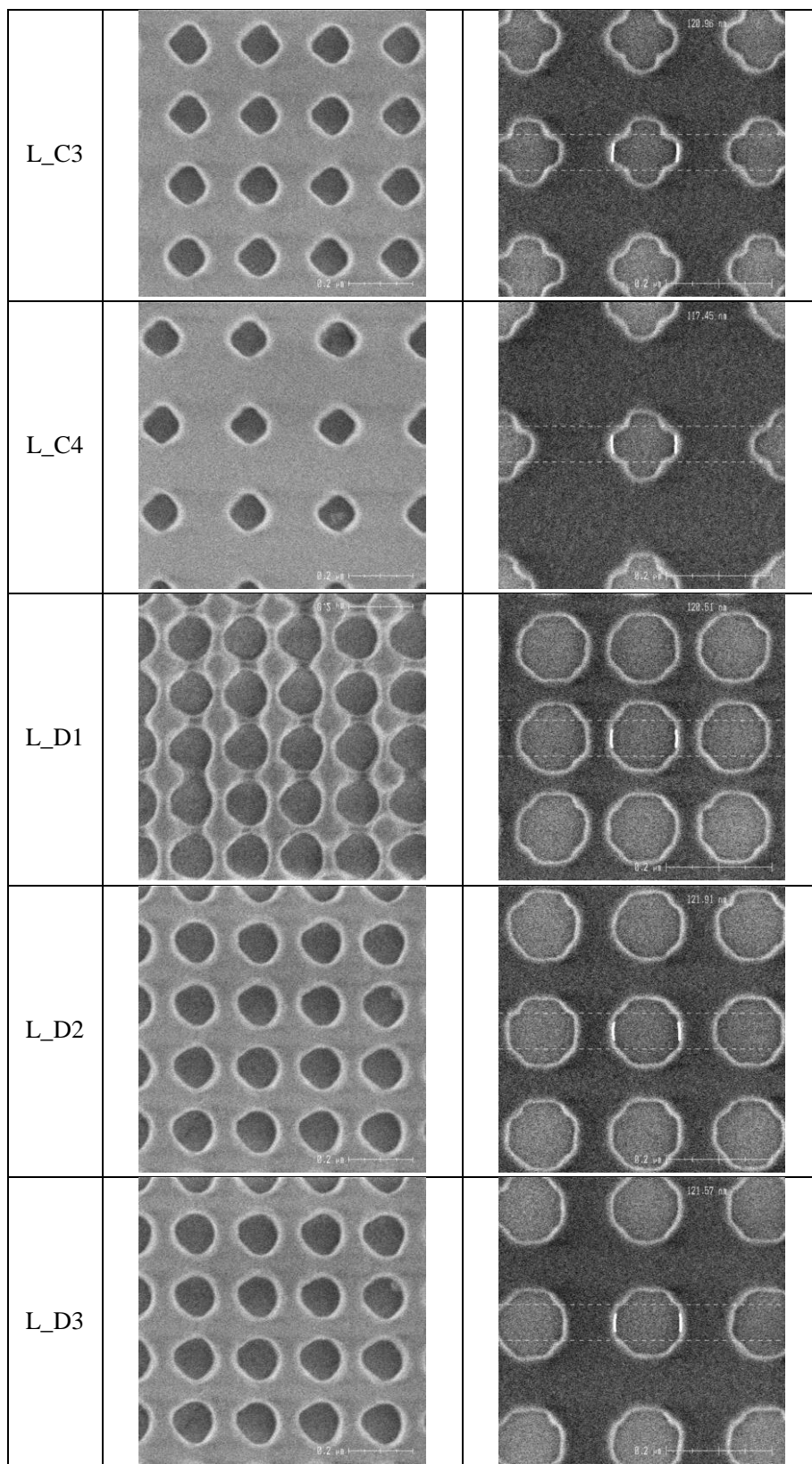
TABLE A.1. Dimensions and description of the selected arrays distributed on the optimized base described in *section 5. 1.3*. ALS designs (green and blue arrays) were optimized to respect a given maximum ALS error (Target). The performance results obtained after optimization are given in the last two columns. The dimensions are given in *nm*.

Appendix B

Electron beam lithography of the optimized base

Array	Initial 200-nm-thick photoresist	New 60-nm-thick resist + PEC
L_A1		
L_A2		
L_A3		
L_A4		
L_B1		

L_B2		
L_B3		
L_B4		
L_C1		
L_C2		



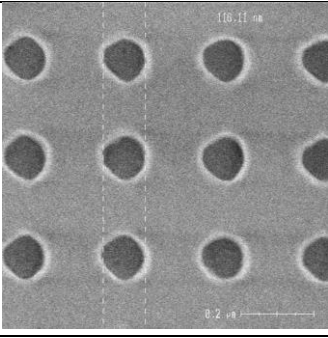
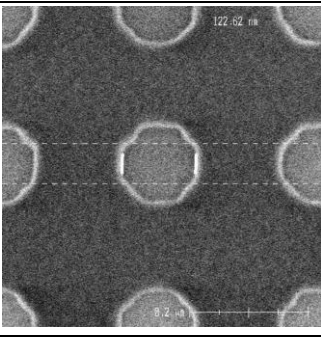
L_D4		
------	---	--

TABLE B.1. Top CD-SEM views of the shapes obtained for the 16 arrays of the left field of the optimized base after electron beam lithography with the initial 200-nm-thick photoresist (left column) and with the second 60-nm-thick photoresist with Proximity Effect Corrections (right column).

Appendix C

Transmission measurements of the optimized base with microspectrometer

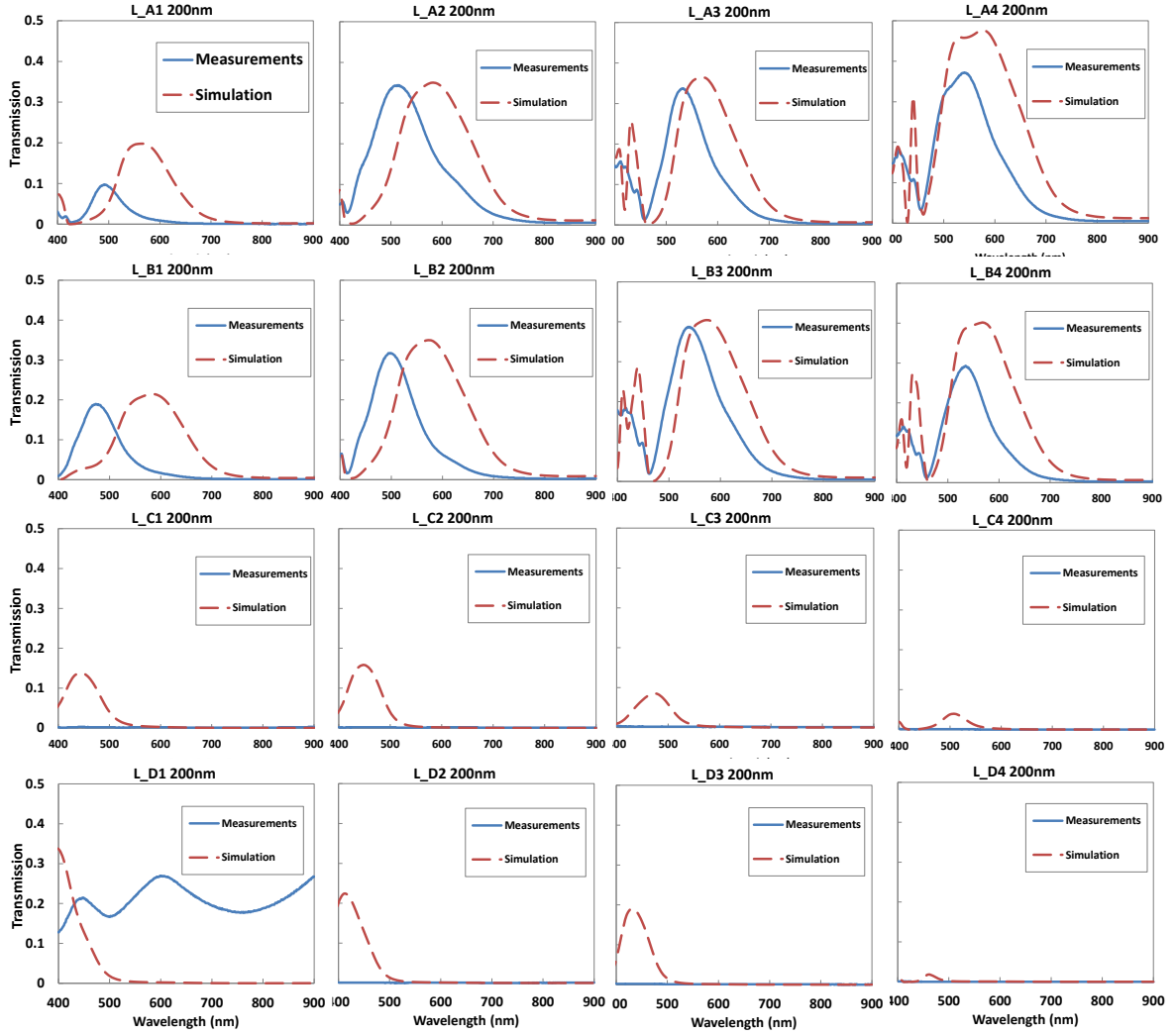


FIG. C.1. Comparison of the microspectrometer measurements (blue) to the simulations (red) on the 16 arrays of the left electron beam field of the optimized base for an Al thickness of 200 nm.

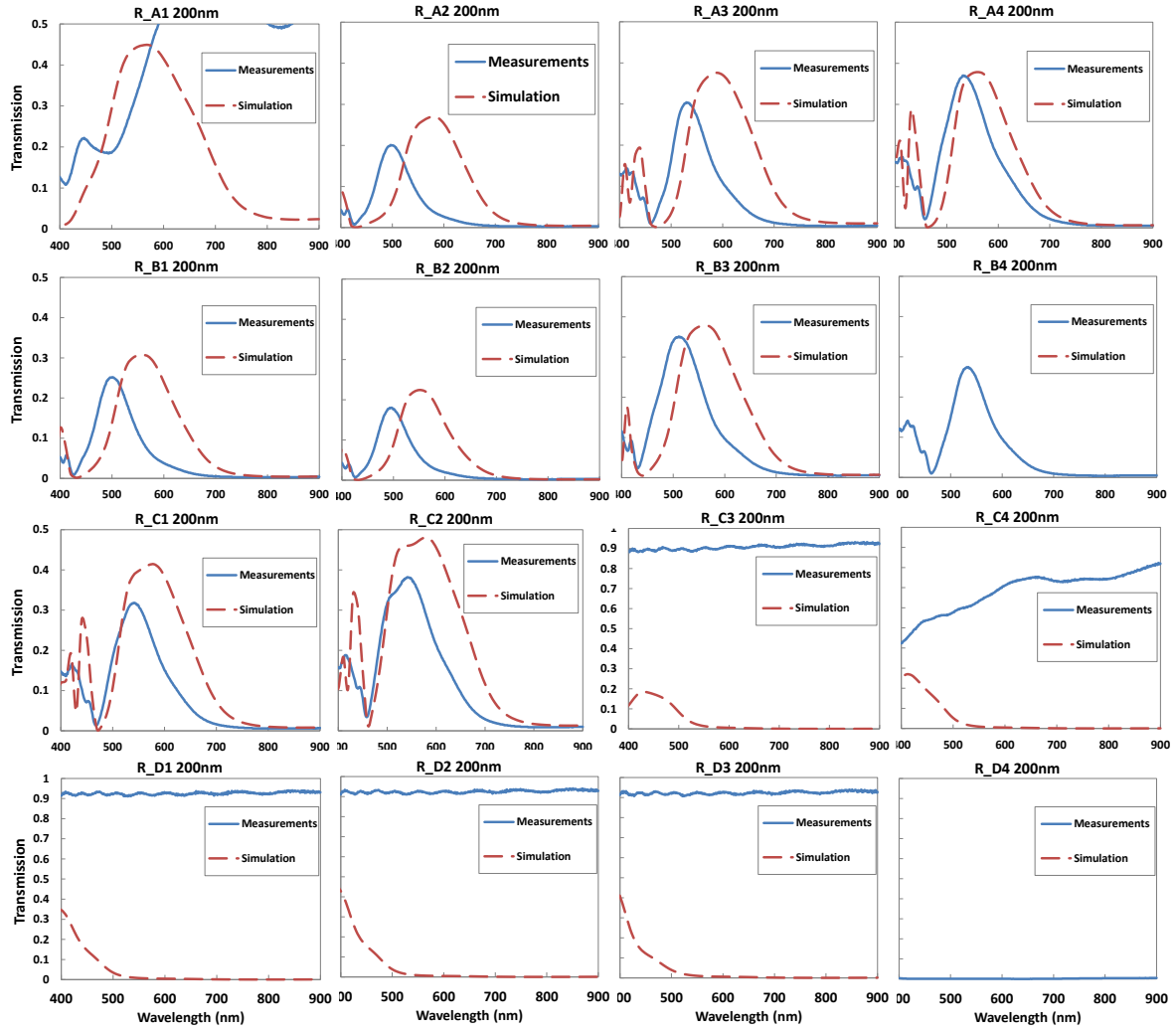


FIG. C.2. Comparison of the microspectrometer measurements (blue) to the simulations (red) on the 16 arrays of the right electron beam field of the optimized base for an Al thickness of 200 nm.

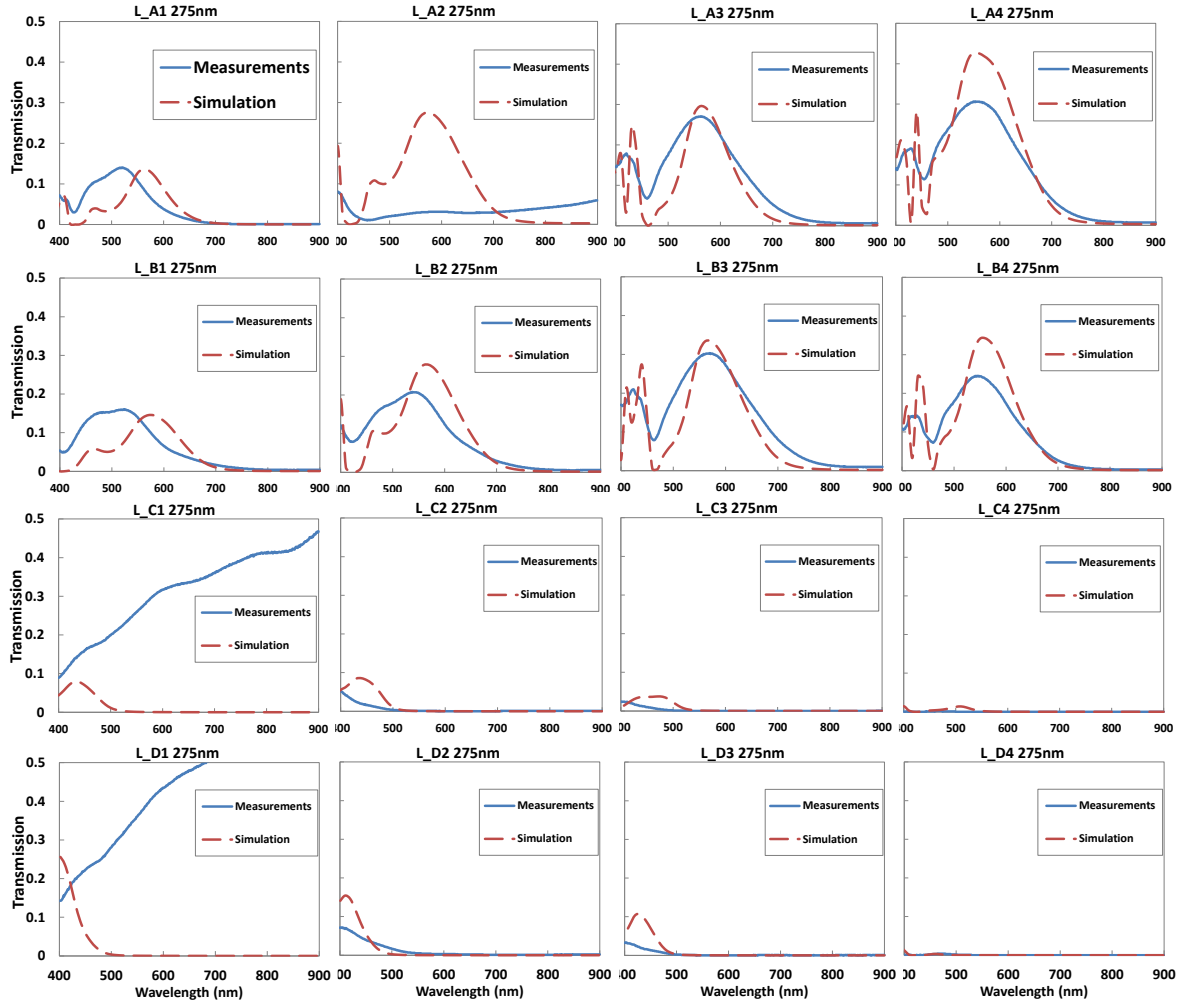


FIG. C.3. Comparison of the microspectrometer measurements (blue) to the simulations (red) on the 16 arrays of the left electron beam field of the optimized base for an Al thickness of 275 nm.

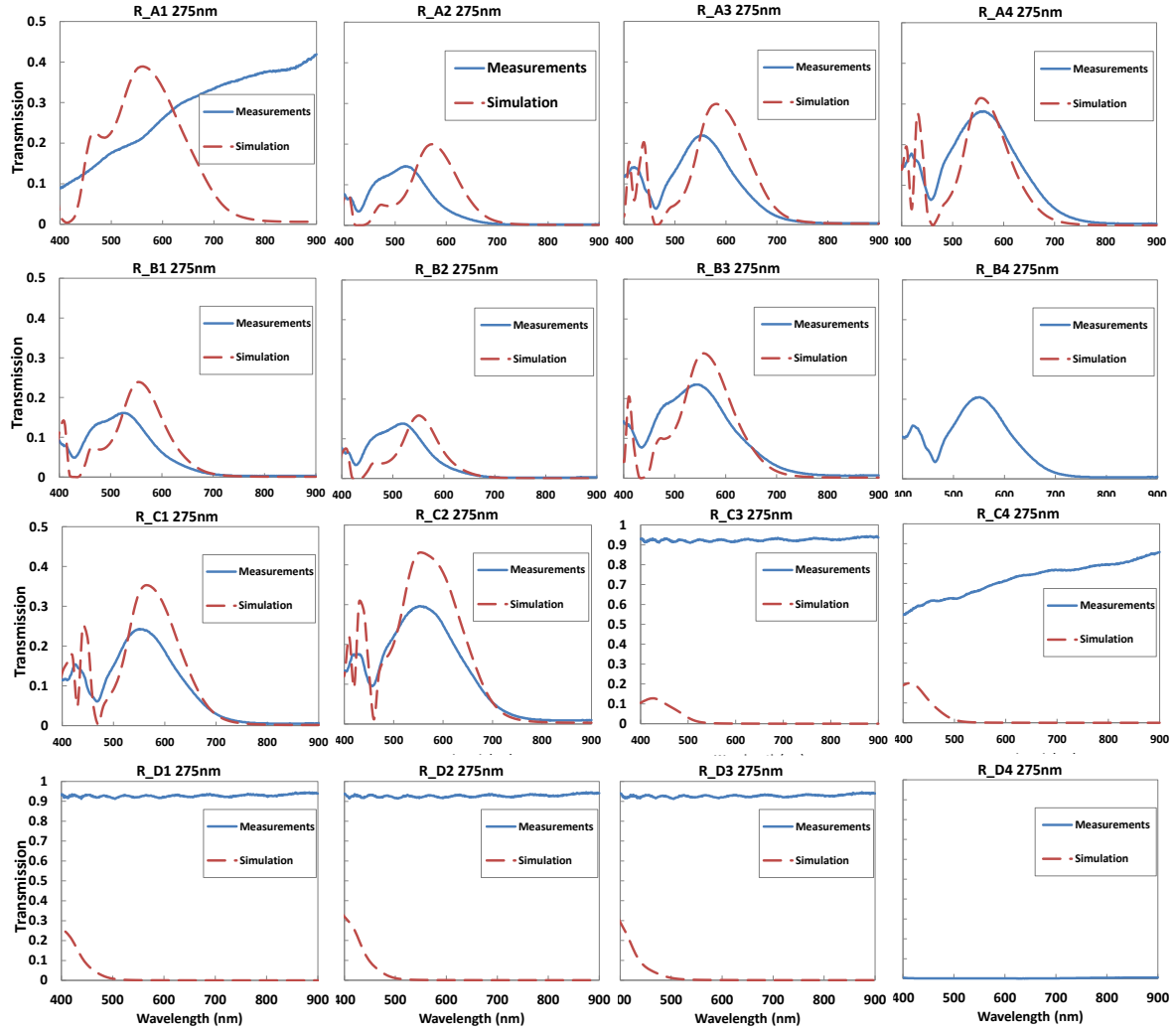


FIG. C.4. Comparison of the microspectrometer measurements (blue) to the simulations (red) on the 16 arrays of the right electron beam field of the optimized base for an Al thickness of 275 nm.

Appendix D

Performance evaluation of ALS filters measured with microspectrometer

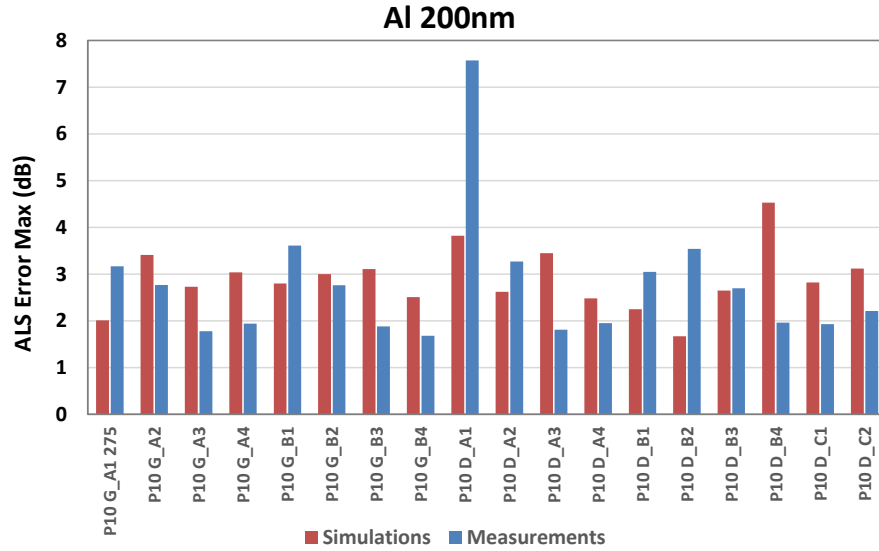


FIG. D.1. Maximum ALS error of the 18 ALS arrays calculated from simulations (red) and microspectrometer measurements (blue) at normal incidence for an Al thickness of 200 nm.

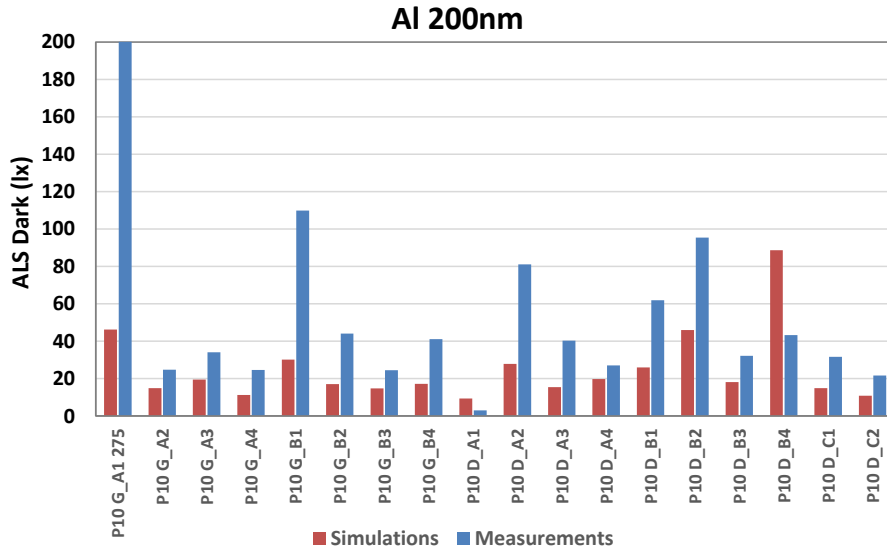


FIG. D.2. ALS dark of the 18 ALS arrays calculated from simulations (red) and microspectrometer measurements (blue) at normal incidence for an Al thickness of 200 nm.

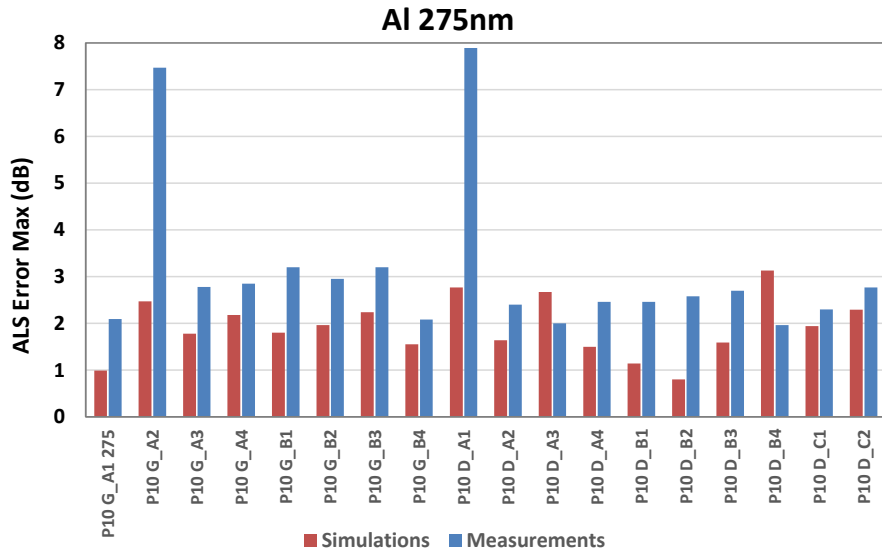


FIG. D.3. Maximum ALS error of the 18 ALS arrays calculated from simulations (red) and microspectrometer measurements (blue) at normal incidence for an Al thickness of 275 nm.

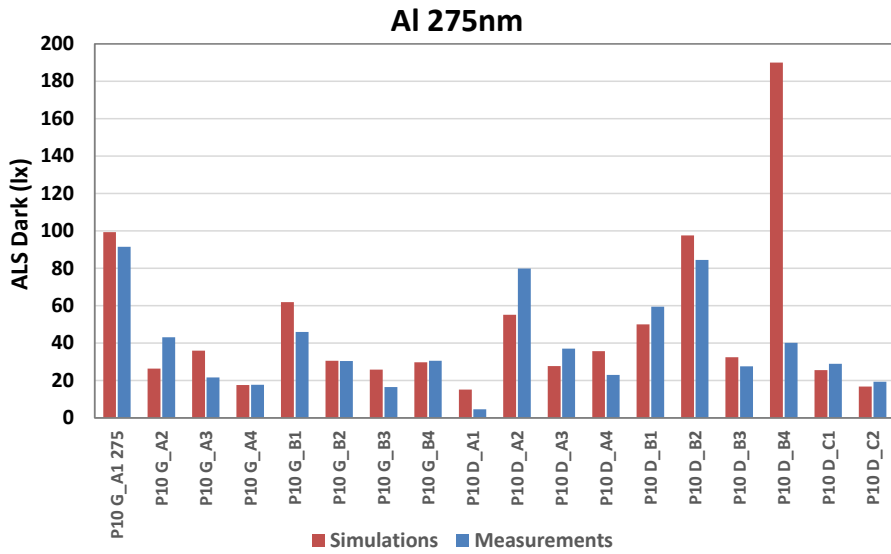


FIG. D.4. ALS dark of the 18 ALS arrays calculated from simulations (red) and microspectrometer measurements (blue) at normal incidence for an Al thickness of 275 nm.

Communications and patents

Patents

Three deposited:

R. Girard-Desprolet, S. Boutami, S. Lhostis, “Dispositif afficheur d'image ou dispositif capteur d'image comprenant un filtre spectral nanostructuré,” EP2816007 A1, 24 décembre 2014; US20140374574 A1, 25 décembre 2014.

R. Girard-Desprolet, S. Boutami, S. Lhostis, M. Marty, “Procédé de formation d'un dispositif intégré à illumination face arrière comprenant un filtre optique métallique, et dispositif correspondant,” (DD 15038, EN 13 55849), 04 décembre 2013. Not published yet.

R. Girard-Desprolet, S. Boutami, S. Lhostis, M. Marty, “Procédé de formation d'un dispositif imageur intégré à illumination face avant comportant au moins un filtre optique métallique, et dispositif correspondant,” (DD 14442, EN 13 62088), 04 décembre 2013. Not published yet.

And three others being filed, which titles cannot be communicated at this stage.

International Journals

R. Girard-Desprolet ; S. Boutami ; S. Lhostis ; G. Vitrant, “Angular and polarization properties of cross-holes nanostructured metallic filters,” Optics Express **21**(24), 29412-29424 (2013).

R. Girard-Desprolet ; S. Lhostis ; C. Beylier ; V. Farys ; G. Vitrant ; S. Boutami, “Impact of process factors on the performance of hole-array metallic filters,” Applied Physics A **117**(2), 485-490 (2014).

International Conference Proceedings

R. Girard-Desprolet, S. Boutami, S. Lhostis, G. Vitrant, “Angular stability of cross-shaped-hole array metallic filters,” Proceedings of SPIE Optics and Photonics **8809**, San Diego, CA, USA (Aug.-Sept. 2013). And Poster.

R. Girard-Desprolet, S. Lhostis, S. Boutami, L. Frey, C. Mornet, M. Armand, “Hole-array plasmonic filters for efficient Ambient Light Sensing,” Proceedings of OPTRO 6th International Symposium on Optronics in Defense and Security **2956618**, Paris, France (Jan. 2014).

R. Girard-Desprolet, S. Lhostis, C. Beylier, V. Farys, G. Vitrant, S. Boutami, “Review on the process factors limiting the performances of hole-array metallic filters,” Proceedings of META 5th International Conference on Metamaterials, Photonics Crystals and Plasmonics, 485-490, Singapour (May 2014).

French summary

Résumé français

Introduction

Les capteurs d'image sont omniprésents dans notre environnement depuis de nombreuses années, utilisés notamment dans des applications telles que les appareils photo, les webcams ou les systèmes de vidéo-surveillance. Récemment, la croissance exponentielle du marché de la communication sans fil a considérablement relancé la demande de tels capteurs. En effet, l'émergence des appareils mobiles tels que les smartphones ou les tablettes tactiles a généré un intérêt croissant pour le développement de capteurs d'image miniaturisés du fait de l'intégration progressive de fonctions d'imagerie et de vidéo. D'autres fonctionnalités ont été développées pour les capteurs d'image au fur et à mesure de l'expansion de ce secteur, parmi lesquelles les capteurs de luminosité ambiante (ou capteurs ALS de l'acronyme anglais Ambient Light Sensors) connaissent en particulier un essor grandissant. L'intérêt de ces capteurs ALS est de mesurer le niveau de luminosité environnement afin de permettre un ajustement automatique du rétro-éclairage des écrans, offrant ainsi un meilleur confort visuel à l'utilisateur et réduisant par la même occasion la consommation de batterie liée à l'utilisation de l'écran. Les capteurs d'image et les capteurs ALS partagent un fonctionnement similaire, caractérisé par le filtrage des photons utiles à leur fonction respective, réalisé en grande majorité par le biais de résines organiques colorées. Ces résines imposent cependant des restrictions très strictes sur l'intégration des capteurs du fait de leur sensibilité aux traitements thermiques et nécessitent en outre l'utilisation d'une vitre coupe-infrarouge externe puisqu'elles ne peuvent filtrer le signal infrarouge (IR). La nécessité de ce filtre coupe-IR augmente de plus l'épaisseur de ces capteurs dans un contexte où le marché est marqué par la réduction des coûts et par la démonstration technologique d'appareils toujours plus fins. Il est donc devenu important aujourd'hui de développer des solutions de filtrage innovantes capable de suivre ces tendances de marché dans le but de proposer des capteurs d'image et de lumière plus compétitifs.

Ces dernières années, la littérature a montré un intérêt croissant pour une branche émergente de la photonique qui consiste à manipuler la lumière à l'échelle du nanomètre à partir de couches métalliques périodiquement structurées : la Plasmonique. Ce domaine tire son nom de l'étude d'ondes électromagnétiques confinées aux interfaces métal-diélectrique, appelées plasmons. Un plasmon de surface est défini comme une oscillation collective du plasma électronique à la surface du métal, dont l'excitation peut être réalisée par un couplage avec les photons incidents sous certaines conditions précises. Dans le cas de réseaux métalliques périodiques, une propriété essentielle des plasmons de surface est qu'ils sont excités et entrent en résonance pour des longueurs d'onde spécifiques déterminées par certaines dimensions caractéristiques des structures utilisées. Ce phénomène rend la plasmonique particulièrement adaptée aux applications de filtrage spectral, pour lesquelles la longueur d'onde de fonctionnement du dispositif peut simplement être réglée en changeant la taille des structures. En

particulier, des métaux comme l'aluminium, l'argent ou l'or peuvent générer des plasmons dans les longueurs d'onde du visible et du proche IR, et de nombreux travaux ont ainsi démontré la réalisation de filtres plasmoniques colorés qui présenteraient l'immense avantage de ne nécessiter qu'une unique étape de photolithographie. Grâce aux propriétés électromagnétiques des métaux, ces filtres sont en outre capables de filtrer le signal IR sans filtre externe supplémentaire. Cependant, la majorité des études utilisent des matériaux considérés comme contaminant dans les salles blanches industrielles et fabriquent les filtres avec des procédés qui ne sont pas compatibles avec la contrainte de rendement nécessaire aux productions commerciales. Il existe donc peu d'information disponible en termes d'intégration et de performance permettant d'envisager un transfert technologique des filtres plasmoniques des laboratoires vers des produits industriels.

Par conséquent, cette thèse vise à évaluer le potentiel des filtres plasmoniques à fournir une alternative viable et performante aux solutions de filtrage actuelles en vue d'un futur transfert vers des applications industrielles. Dans ce travail de thèse, les applications ciblées sont les capteurs d'image et les capteurs de luminosité ambiante. Cet objectif se décompose selon deux axes majeurs. Le premier consiste en l'étude et la sélection parmi différentes structures plasmoniques de celles qui permettent d'obtenir les meilleures performances théoriques pour les applications visées, tout en respectant les défis technologiques et les contraintes industrielles qui leurs sont associés. Le second axe consiste à évaluer la viabilité de la fabrication de telles structures par rapport aux enjeux d'intégration inhérents aux filtres plasmoniques et par rapport aux dispersions de procédés qui doivent être attendues avec une fabrication à l'échelle du wafer. Pour répondre à cette problématique, cette thèse est articulée suivant l'organisation présentée ci-dessous.

Tout d'abord, nous décrivons dans le Chapitre 1 l'intérêt du filtrage plasmonique pour les capteurs de lumière. Nous présentons en premier lieu les structures et les principes respectifs des capteurs d'image CMOS et des capteurs ALS, menant ainsi aux enjeux du filtrage spectral. Un accent particulier est mis sur la partie filtrage de ces dispositifs avec une revue des principaux types de filtrage, en précisant leurs avantages et leurs limites. Le principe du filtrage plasmonique est ensuite introduit. Le potentiel de cette solution pour les capteurs de lumière est alors présenté. Les défis associés sont ensuite expliqués et la méthodologie choisie pour cette thèse, décrite.

Le Chapitre 2 consiste en l'identification des structures plasmoniques qui pourraient répondre aux exigences des capteurs de lumière. D'abord, les outils numériques de simulation et d'évaluation utilisés dans ce travail sont détaillés. Les cahiers des charges correspondant aux capteurs d'image et aux capteurs ALS sont expliqués. De là, la sélection des structures plasmoniques les plus adaptées est réalisée à travers l'évaluation de leur facilité de fabrication, de leurs propriétés optiques et de leur stabilité angulaire. Une intégration directe des filtres respectant la compatibilité avec les procédés CMOS des lignes industrielles est proposée. Ce chapitre permet d'identifier les meilleurs matériaux et structures compatibles CMOS capables de répondre aux défis respectifs des applications visées.

Dans le Chapitre 3, les meilleures structures plasmoniques pour les capteurs ALS sont mises en évidence. En premier lieu, une étude approfondie des propriétés de stabilité angulaire des réseaux de trous cruciformes est présentée afin de limiter la sensibilité de nos filtres plasmoniques aux angles d'incidence et à la polarisation de la lumière. De ces résultats, l'évaluation des filtres plasmoniques optimisés pour l'application ALS est effectuée. Ce chapitre permet d'estimer le potentiel théorique des filtres plasmoniques et de proposer des performances optimales pour cette application.

Dans le Chapitre 4, l'impact potentiel des facteurs liés à la fabrication sur les performances des filtres plasmoniques est simulé. Puisque les résonances de plasmon dépendent de la taille et de la forme des structures, nous évaluons la sensibilité des filtres plasmoniques aux imprécisions des procédés. Les principaux défauts qui peuvent être attendus à chaque étape de la fabrication sont modélisés. Les variations sur les principaux paramètres sont étudiées d'après des valeurs de dispersion typiques d'une production sur wafer 300 mm au niveau des étapes de dépôt et de photolithographie, avec également le possible arrondissement des trous cruciformes. Les impacts respectifs des profils inclinés dans le métal

après gravure et de la formation de cavités d'air lors du remplissage des trous sont évalués. Les étapes critiques de la fabrication sont donc identifiées et évaluées.

Le Chapitre 5 est dédié à la fabrication et à la caractérisation des structures plasmoniques. D'abord, le développement process des filtres plasmoniques définis au Chapitre 3 est présenté à la lumière des études de dispersions précédentes. Les principales difficultés et dispersions de chaque étape sont observées et comparées avec les résultats du Chapitre 4. Les filtres obtenus sont caractérisés pour évaluer leurs performances et les comparer avec le travail théorique des chapitres précédents. La viabilité de la solution plasmonique en termes de performances et d'intégration est alors discutée.

Finalement, une conclusion est faite sur la capacité des filtres plasmoniques à proposer des performances optiques optimales et à être transférés vers des lignes industrielles en vue d'une utilisation dans des applications commerciales. Quelques pistes sur les perspectives de cette thèse sont également proposées. Dans ce résumé, seul un aperçu des principaux résultats est fourni pour chaque chapitre.

Chapitre 1

Nous présentons dans ce chapitre la structure générale et le principe de fonctionnement des principaux types de capteurs de lumière sur lesquels nous nous concentrons pour cette thèse : les capteurs d'image et les capteurs de luminosité ambiante (ALS). Nous expliquons ensuite comment le système de filtrage actuel devient problématique pour une intégration plus avancée et moins chère de tels capteurs dans des appareils toujours plus fins. Les résines organiques présentent l'inconvénient majeur de nécessiter un filtre coupe-infrarouge externe qui augmente notamment l'épaisseur des capteurs (Fig. 1). Pour rester compétitif sur le marché des capteurs de lumière dans les dispositifs mobiles d'entrée ou de milieu de gamme, il devient nécessaire de développer une solution de filtrage entièrement sur puce qui ne requiert pas de filtre additionnel pour supprimer le signal IR. L'une des alternatives connues les plus sérieuses est l'utilisation de filtres Fabry-Perot. Nous notons cependant que leur fabrication peut nécessiter plusieurs étapes de dépôt de matériaux et de photolithographie, et impose notamment un contrôle sévère des épaisseurs et des propriétés optiques des couches minces déposées, ce qui nécessite des équipements spécifiques et coûteux.

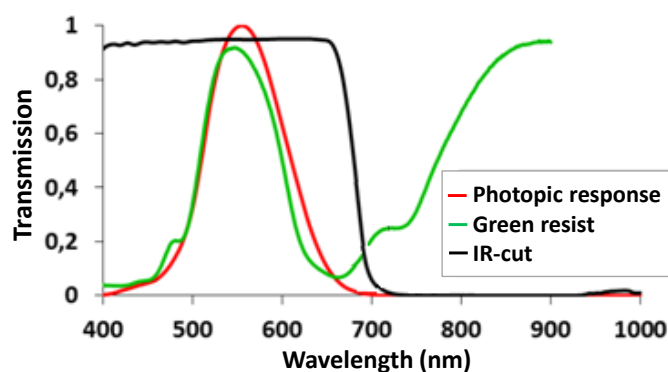


FIG. 1. Pour reproduire la réponse diurne de l'œil (réponse photopique), le filtrage des capteurs ALS est généralement réalisé à l'aide d'une résine organique verte et d'une vitre coupe-infrarouge.

En explicitant le principe théorique des plasmons de surface (Fig. 2), nous décrivons alors les avantages que propose la plasmonique pour répondre à nos enjeux technologiques. Le mécanisme des résonances de plasmon permet de réaliser du filtrage dans le visible avec l'utilisation d'une simple couche métallique structurée, la longueur d'onde de fonctionnement étant déterminée par les dimensions des nanostructures. En pratique, cela signifie que l'élément actif d'un filtre plasmonique – la couche métallique – est réalisable à partir d'une seule étape de dépôt et d'une unique étape de lithographie, même dans le cas de capteurs avec différents pixels. En outre, les propriétés optiques des métaux permettent naturellement de supprimer le signal IR non désiré, et donc dans le même temps la nécessité d'un filtre coupe-infrarouge externe. Les filtres plasmoniques, du fait de leur structure et de leur principe, apportent cependant leurs propres challenges technologiques par rapport à la solution de filtrage la plus couramment utilisée, à savoir les résines organiques. En effet, la structuration du métal en 2D les rend sensibles à l'angle d'incidence (polaire et azimutal) de la lumière incidente et à son état de polarisation, paramètres qui ne constituaient pas de problèmes avec les résines à base de pigments colorés. De même, la réponse spectrale des filtres est directement liée aux dimensions caractéristiques des structures : généralement, la période du réseau, ainsi que la taille et la forme des motifs. Tous ces paramètres génèrent des enjeux de reproductibilité par rapport aux dispersions de procédé liées à la précision des équipements de fabrication à chaque étape critique de la réalisation des filtres, en

particulier pour les applications dans le domaine visible où les dimensions deviennent nanométriques. En outre, nous nous intéressons ici uniquement à des procédés, des matériaux et des équipements compatibles avec un environnement CMOS et avec une production industrielle 300 mm à l'échelle du wafer, caractérisée notamment par une contrainte de haut rendement.

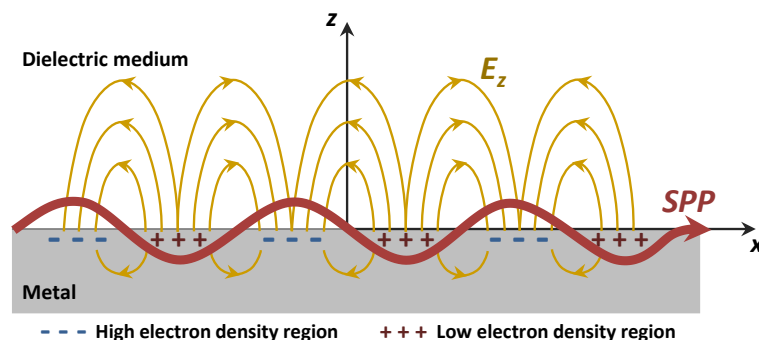


FIG. 2. Représentation visuelle d'un plasmon polariton de surface (oscillation collective du plasma d'électrons de surface) se propageant le long d'une interface métal-diélectrique. Dans le cas d'une excitation par un réseau métallique périodique, le vecteur d'onde du plasmon de surface dépend des dimensions caractéristiques de la structure, permettant ainsi de réaliser une fonction de filtrage spectral.

L'objectif de cette thèse est donc d'évaluer le potentiel des filtres plasmoniques à répondre aux challenges technologiques spécifiques aux applications considérées, mais également aux enjeux de performances et d'intégration liés à leur principe de fonctionnement. Le manuscrit est articulé suivant les problématiques suivantes : déterminer les meilleures structures plasmoniques et intégrations pour les applications ciblées (Chapitre 2), optimiser les propriétés optiques et les performances des structures identifiées (Chapitre 3), évaluer la viabilité de la fabrication de telles structures avec des procédés industriels en modélisant les principaux défauts et dispersions de procédé attendus (Chapitre 4), et enfin, démontrer expérimentalement la solution plasmonique en développant la fabrication des designs optimisés et en les caractérisant optiquement (Chapitre 5).

Chapitre 2

A travers ce chapitre, nous décrivons les méthodes de simulations numériques et d'évaluation que nous utilisons pour répondre aux challenges technologiques intrinsèques du filtrage plasmonique, et nous définissons un cahier des charges qui permet l'évaluation à l'échelle du système complet et l'optimisation des filtres. Les simulations électromagnétiques sont réalisées à partir d'un algorithme RCWA (Rigorous Coupled Wave Analysis), particulièrement adapté à notre étude puisque nous considérons des structures périodiques et que les calculs sont suffisamment rapides pour tester de très nombreuses structures avec des larges plages de paramètres. En ce qui concerne l'évaluation des performances liées aux applications visées, les filtres ALS doivent respecter deux critères de performance. Ces critères sont calculés sur le système complet et prend en compte le type d'illuminant, la réponse du filtre optique et le rendement quantique de la photodiode (Fig. 3). Le principal critère déterminant est l'erreur ALS maximum, qui est directement liée à la qualité du signal filtré (réponse proche de la sensibilité photopique), et donc au facteur de qualité et à la réjection du filtre. Cette erreur ne doit pas dépasser 2.2 dB, correspondant à la performance de la résine et de la vitre coupe-IR utilisée en début de thèse par STMicroelectronics. Le deuxième critère, l'ALS dark, est lié à la performance du capteur en condition de basse luminosité (valeur de l'éclairement nécessaire pour différencier le signal utile du courant d'obscurité de la photodiode), qui correspond plutôt au niveau de transmission du filtre. La limite est fixée à 100 lx.

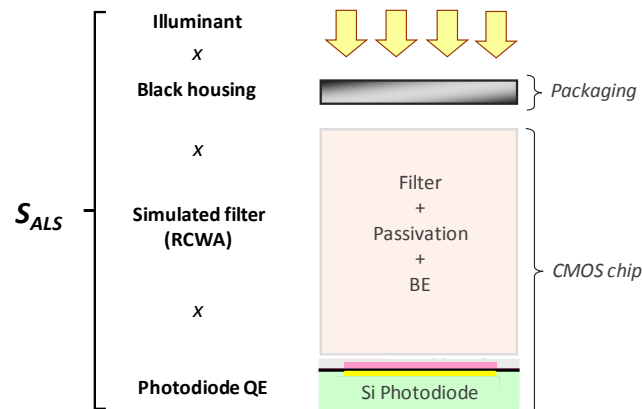


FIG. 3. Schéma représentant l'ensemble des éléments pris en compte pour l'évaluation de performance des capteurs ALS. La sensibilité du dispositif et les critères qui en découlent sont définis à partir : du type d'illuminant, de la transmission de la vitre du packaging, de la réponse spectrale du filtre et du rendement quantique de la photodiode.

Nous avons simulé les principaux types de structures de filtres optiques plasmoniques avec un accent particulier sur leur sensibilité à la polarisation et sur la stabilité angulaire. En plus des difficultés liées à leur fabrication, les structures MIM (Métal-Isolant-Métal) n'ont pas montré de propriétés avantageuses en termes de niveau de transmission ou de stabilité angulaire. Les réseaux de plots métalliques, bien que plus faciles à fabriquer, présentent une sensibilité très importante aux conditions d'incidence de la lumière, ce qui est rédhibitoire pour les applications considérées dans cette thèse. La meilleure association entre la facilité de fabrication et les performances optiques est obtenue avec les réseaux de trous diélectriques dans une couche métallique (Fig. 4). Bien qu'aucun de ces trois types de structures n'atteigne les mêmes niveaux de transmission que les résines organiques, les réseaux de trous se distinguent par leur capacité à présenter une très forte stabilité angulaire. En particulier, les réseaux de

trous cruciformes donnent les meilleurs résultats avec une très bonne robustesse à la polarisation et aux conditions d'incidence de la lumière, en plus de proposer un paramètre géométrique supplémentaire par rapport aux carrés ou aux cercles pour régler la réponse des filtres : la largeur de bras des croix. Les faibles transmissions généralement obtenues avec les filtres plasmoniques (ou les hauts niveaux de transmission avec de très mauvais facteurs de qualité) compliquent leur intégration dans des capteurs d'image CMOS destinés à des appareils haut-de-gamme, mais ces propriétés de stabilité angulaire font cependant des réseaux de trous, et particulièrement les trous cruciformes, une solution prometteuse pour réaliser du filtrage ALS. La suite de l'étude est donc concentrée sur l'optimisation des performances et sur les problématiques de fabrication des filtres plasmoniques à base de réseaux de trous cruciformes. A partir des travaux du Chapitre 2, nous avons breveté une solution limitant la sensibilité des filtres plasmoniques en général à l'azimut pour des applications capteur d'image.

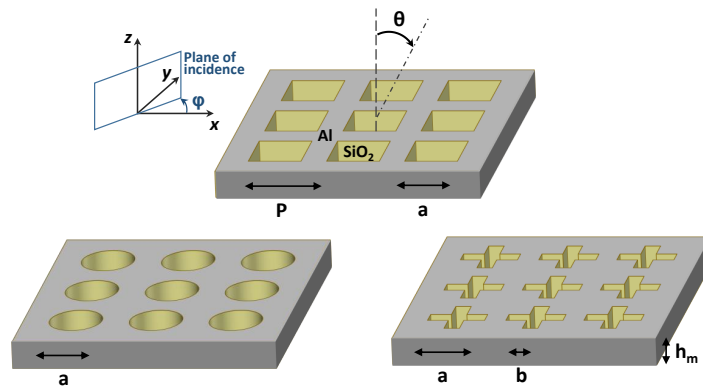


FIG. 4. Les structures de type réseaux de trous diélectriques dans une couche métallique se sont avérées être le meilleur compromis entre niveau de transmission, stabilité angulaire et facilité de fabrication. En particulier, les réseaux de croix ont montré la possibilité d'obtenir une très bonne robustesse à l'angle d'incidence et à l'état de polarisation.

Finalement, l'intégration de ce type de filtres plasmoniques est étudiée dans l'objectif d'obtenir l'intégration la plus directe dans une route standard de fabrication de capteurs d'image. La configuration que nous définissons est alors de fabriquer les filtres au-dessus des couches de passivation de SiO_2 et de Si_3N_4 , situées au-dessus des interconnexions métalliques, juste avant l'ouverture des plots d'aluminium. La solution qui donne des performances ALS optimales consiste à intégrer la couche d'aluminium nanostructurée à l'intérieur de la couche de SiON servant de revêtement protecteur contre l'atmosphère extérieure, qui est alors utilisée comme matériau diélectrique environnant pour le filtre plasmonique. Afin de limiter l'impact optique de la couche de Si_3N_4 sous-jacente, la couche intermédiaire de SiO_2 située entre l'aluminium et le nitrure doit avoir une épaisseur de 325 nm. Cette configuration définit ainsi l'empilement optique complet du capteur qui est pris en compte par la suite dans les simulations évaluant les performances des filtres plasmoniques dans le cas d'un capteur ALS réel. A la suite de cette étude, nous définissons donc deux empilements de référence qui sont utilisés dans les chapitres suivants (Fig. 5). Le premier est un empilement dit standard où la couche d'aluminium structurée se trouve dans un milieu de SiO_2 infini. Il est utilisé pour l'étude théorique des résonances de plasmon dans nos structures. L'autre est un empilement dit ALS qui fait référence à l'empilement complet des matériaux du capteur situé au-dessus de la photodiode, comprenant ainsi le filtre intégré dans le SiON , les couches de passivation et les diélectriques du BEoL. Il est utilisé pour l'évaluation et l'optimisation des dispositifs ALS à base de plasmonique.

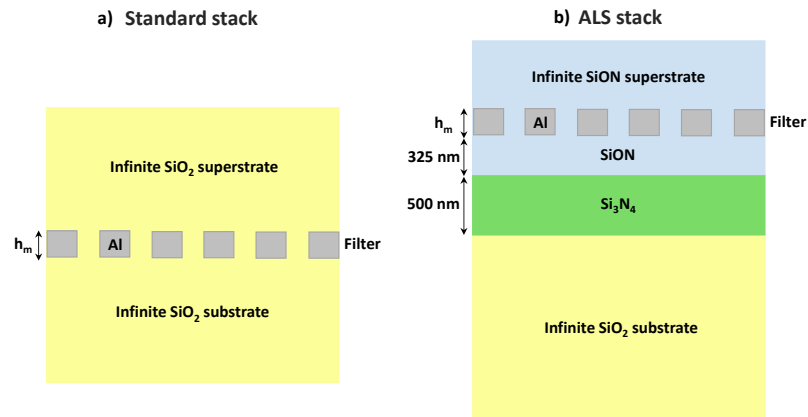


FIG. 5. Description des deux empilements de référence utilisés dans la suite de la thèse. a) Empilement dit standard, utilisé pour étudier les résonances de plasmons dans nos structures. b) Empilement dit ALS, optimisé pour les performances ALS dans le cas d'une intégration directe dans une route procédé standard d'un capteur industriel.

Chapitre 3

Les structures les plus adaptées à nos applications ayant été identifiées, nous cherchons maintenant à optimiser leurs propriétés optiques et leurs performances. Nous démontrons dans une première partie du Chapitre 3 que les propriétés optiques des réseaux de trous cruciformes telles que leurs sensibilités à l'angle d'incidence et à la polarisation peuvent être précisément ajustées en changeant certaines dimensions caractéristiques de ces structures. Les deux paramètres géométriques principaux permettant de gérer leur comportement électromagnétique sont le facteur de forme des croix, défini comme le rapport de la largeur de bras des croix sur leur longueur de bras b/a , ainsi que l'espacement entre les croix d . Un faible facteur de forme (inférieur à 0.5 d'après nos simulations, voir Fig. 6) et une courte distance inter-croix inférieure à 75 nm favorisent un régime de résonances localisées de plasmon au niveau des ouvertures au détriment des plasmons propagatifs, ce qui assure une faible sensibilité des filtres aux conditions d'éclairement. L'épaisseur de métal doit être supérieure à 150 nm afin d'améliorer la stabilité angulaire, mais son influence est légère par rapport à l'impact du facteur de forme et de l'espacement inter-croix. L'impact de l'azimut dans le cas des réseaux 2D et des solutions pour en limiter les effets sont étudiés, ce qui constitue un aspect rarement pris en compte pour les réseaux de trous dans la littérature à notre connaissance. Nous pensons que cette étude apporte une contribution additionnelle à la compréhension des rôles respectifs des plasmons localisés et des plasmons polaritons de surface dans le mécanisme de transmission optique extraordinaire (EOT). En outre, nous démontrons la capacité des réseaux de trous cruciformes à fournir des filtres avec une forte stabilité angulaire et une insensibilité à la polarisation, à condition que les règles de design que nous établissons soient respectées et que le choix des matériaux soit cohérent avec les longueurs d'onde considérées.

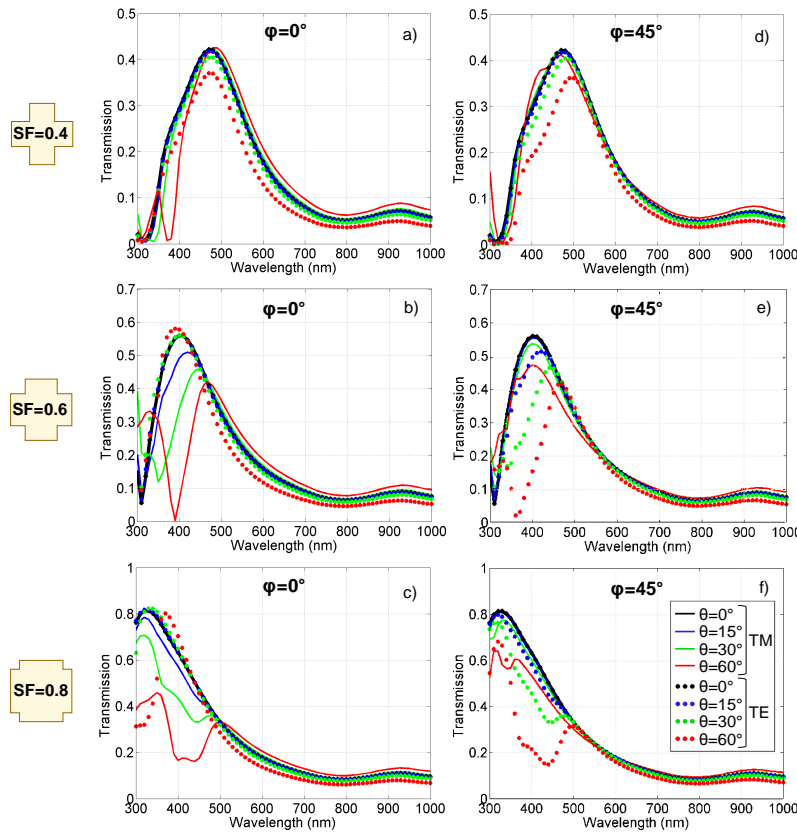


FIG. 6. Evolution des réponses spectrales avec l'angle d'incidence θ , l'azimut φ et l'état de polarisation (TE ou TM) d'un même filtre pour différentes valeurs du ratio b/a (SF de l'anglais *shape factor*) des trous en croix. a) $b/a = 0.4$ et $\varphi = 0^\circ$. b) $b/a = 0.6$ et $\varphi = 0^\circ$. c) $b/a = 0.8$ et $\varphi = 0^\circ$. d) $b/a = 0.4$ et $\varphi = 45^\circ$. e) $b/a = 0.6$ et $\varphi = 45^\circ$. f) $b/a = 0.8$ et $\varphi = 45^\circ$. La réponse du filtre est d'autant plus stable que le ratio b/a est faible.

Dans une seconde partie, nous montrons que les filtres plasmoniques sont capables de rentrer dans le gabarit de performances de l'application ALS et de se rapprocher des valeurs d'erreur ALS de la solution résine verte/vitre coupe-IR (2012). Ils sont également capables d'approcher l'erreur ALS de la référence 2015, bien qu'ils présentent un ALS dark plus élevé autour de 40 lx. Cette valeur peut potentiellement être réduite grâce à un recuit final du dispositif que les filtres plasmoniques peuvent supporter contrairement aux résines organiques, ce qui est vérifié expérimentalement au Chapitre 5. Seules des formes de trous spécifiques telles que les carrés ou les croix peuvent atteindre des performances compétitives, ce qui nous amène à supposer que les plasmons localisés jouent un rôle essentiel dans l'obtention d'une réponse spectrale se rapprochant de la sensibilité photopique. L'application requiert des filtres avec des épaisseurs d'aluminium généralement supérieures à 225 nm, permettant une très bonne réjection autour du signal utile, des périodes comprises entre 250 nm et 300 nm, ainsi que des rapports a/P compris entre 0.6 et 0.75. Nous montrons que la dispersion des performances due à l'angle d'incidence polaire, à l'azimut et à la polarisation est limitée et contenue dans le cahier des charges avec des faibles facteurs de formes. Les limites de la stabilité des croix sont cependant atteintes pour des angles d'incidence de 60° (Fig. 7). Des solutions plus avancées sont proposées à partir d'argent ou d'or à la place de l'aluminium. Bien que l'or ne soit pas approprié pour des filtres en transmission dans le visible, l'argent est capable de fournir des filtres ALS très performants comparables avec la référence de 2015 à partir de trous carrés ou de trous cruciformes avec un facteur de forme supérieur à 0.7. Ceci implique que l'argent constitue une alternative prometteuse à l'aluminium pour du filtrage optique bien que les conditions de stabilité des croix puissent ne pas être remplies. La nanostructuration de couches minces d'argent avec des équipements industriels est cependant problématique pour l'introduction de ce métal dans des salles blanches CMOS de production de masse.

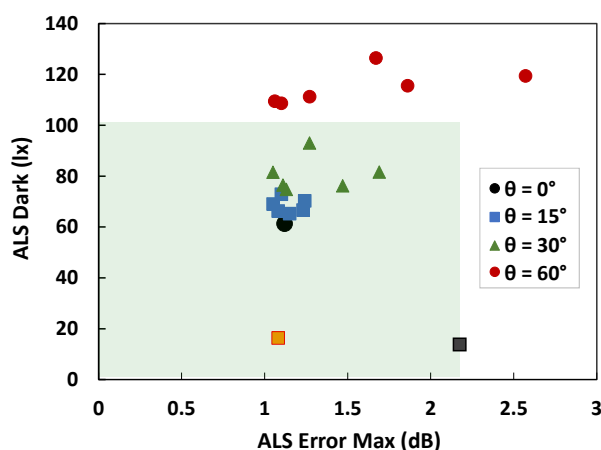


FIG. 7. Représentation 2D des performances ALS d'un filtre plasmonique en incidence normale (point noir), puis sous différents angles d'incidence θ (différentes couleurs), pour différentes valeurs d'azimut (points d'une même couleur), en moyennant les réponses obtenues sous polarisations TE et TM. Les critères de performance définis au Chapitre 2 servent de coordonnées. La zone verte représente le gabarit acceptable de performance. Nos calculs montrent qu'il est possible de trouver des designs qui respectent le cahier des charges des performances, et ce même sous une incidence de 30° , angle maximum permis par l'ouverture du capteur.

Chapitre 4

Puisque nous voulons réaliser des structures dont les dimensions sont à la limite du savoir-faire technologique actuel, les imprécisions de fabrication, et particulièrement avec de procédés industriels, constituent un challenge majeur pour le transfert des filtres plasmoniques vers une production de masse en vue d'applications commerciales. Dans ce chapitre, nous simulons l'impact des dispersions de procédé issues de la salle blanche 300 mm de STMicroelectronics Crolles sur les performances ALS de deux designs de référence. Ces simulations nous permettent de définir une route de fabrication des filtres plasmoniques qui puisse garantir un minimum de défis technologiques et qui soit facilement transférable en milieu industriel. Les principaux points bloquants qui sont susceptibles d'être rencontrés à chaque étape de la fabrication sont identifiés et évalués. L'objectif est d'être capable de déterminer s'il existe des briques technologiques critiques et de proposer le cas échéant des solutions pour surpasser ces difficultés potentielles (Fig. 8). Dans chaque cas, nous étudions d'abord comment les propriétés optiques des filtres sont impactées par les dispersions de procédé, puis nous appliquons ces résultats et évaluons leurs effets en termes de performances dans le cas de l'application ALS.

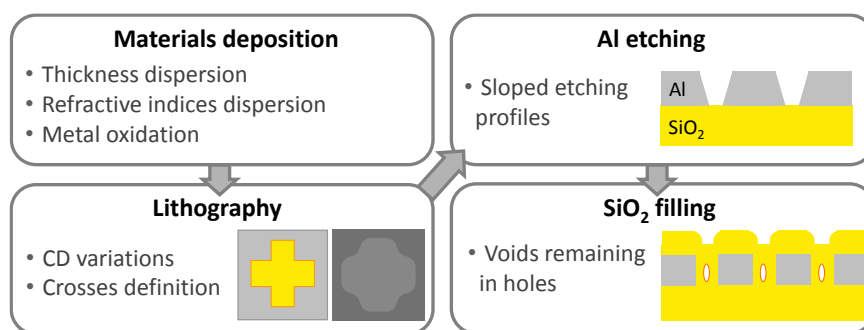


FIG. 8. Principales dispersions et défauts de procédé attendus lors de la fabrication des filtres plasmoniques par gravure de la couche d'aluminium et remplissage SiO₂ des ouvertures.

La première brique de la fabrication est le dépôt des différentes couches constituant les filtres. Nous montrons que les dispersions sur l'épaisseur des couches et leurs indices de réfraction ont un impact limité sur les performances ALS, et qu'il est possible de trouver des designs respectant le gabarit de performances même avec les niveaux de dispersions actuels. Cette étape n'est donc pas critique, et aucun équipement de dépôt spécifique n'est requis pour la fabrication des filtres. L'utilisation de machines de dépôt de qualité optique pourrait néanmoins permettre d'obtenir plus de designs respectant le cahier des charges. En ce qui concerne la stabilité du métal, nous montrons que la formation d'un oxyde natif en surface de l'aluminium ne constitue pas un problème pour les performances ALS à condition de prendre en compte les variations des dimensions de la structure métallique du fait du processus d'oxydation. En outre, nous pensons qu'en pratique, il est possible d'anticiper l'oxydation du filtre directement à l'étape de dessin du masque de lithographie.

Durant l'étape de lithographie, nous considérons deux points bloquants principaux : l'arrondissement des coins des croix et le contrôle des dimensions des trous. Quand les angles des croix sont arrondis, nous observons un décalage vers les courtes longueurs d'onde de la résonance, que nous attribuons à la modification progressive des résonances plasmon spécifiques aux croix vers des modes de résonances propres aux trous circulaires. Cet effet semble plutôt relié aux angles internes des croix, mais une modification des interactions entre les motifs peut aussi être considérée. Malgré ces observations, nous montrons que les propriétés de stabilité angulaire des croix fines ne sont pas impactées pour des

rayons de courbure des coins $R = 20$ nm jusqu'à 30° d'incidence. L'impact des coins arrondis est faible sur les performances ALS à condition que le rayon de courbure n'excède pas 15 nm ou 20 nm en fonction du design (Fig. 9). Ces valeurs d'arrondi doivent pouvoir être atteintes dans les coins internes avec une lithographie en double exposition et dans les coins externes à l'aide de calculs de proximité optique (OPC).

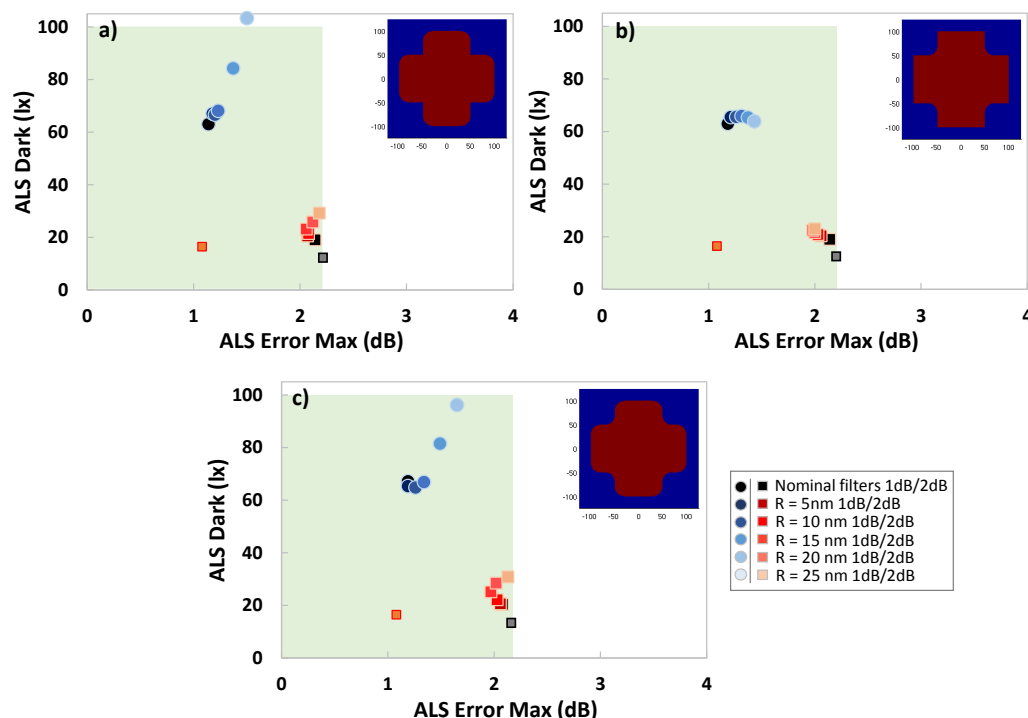


FIG. 9. Etude sur deux filtres de référence de l'impact de l'arrondissement des croix sur les performances ALS des filtres plasmoniques, pour différentes valeurs d'arrondis R (rayon de courbure dans les angles). a) Angles externes arrondis. b) Angles internes arrondis. c) Tous les angles de la croix arrondis.

Nous étudions également l'influence de la présence potentielle de profils en pente dans l'aluminium qui peuvent être obtenus lors de la gravure des motifs, formant un angle ouvert dirigé vers le haut du filtre. Nous supposons que trois situations peuvent se présenter pour anticiper la présence de pentes de gravure par rapport aux dimensions attendues. Si nous fixons les dimensions désirées en haut des filtres, les pentes obstruent les ouvertures et l'ALS dark connaît alors une augmentation massive qui ne peut être tolérée. Au contraire, si nous choisissons d'atteindre les dimensions voulues à la sortie (en bas) des filtres, nous mettons en évidence un effet « entonnoir » qui collecte plus de signal et détériore sévèrement la réjection des filtres, en particulier dans le proche IR. L'augmentation correspondante de l'erreur ALS serait rédhibitoire. Nous montrons alors que la meilleure configuration serait d'anticiper la présence de pentes de gravure durant l'étape de dessin du masque de façon à obtenir les dimensions désirées à mi-hauteur de la couche de métal. Dans ce cas, nos résultats montrent que l'erreur ALS n'est pas impactée par les pentes, et que l'augmentation de l'ALS dark est limitée à environ 15 lx. Notons cependant que l'anticipation des pentes n'est possible qu'avec une très bonne connaissance des paramètres utilisés lors de l'étape de gravure.

Le dernier point bloquant que nous étudions est la formation de cavités d'air (« voids ») dans le matériau diélectrique durant l'étape de remplissage des trous. Nous démontrons que la présence de voids devient très rapidement problématique quand la fraction volumétrique V_f des voids par rapport au volume des trous augmente. En fonction des designs, certains filtres peuvent tolérer des fractions volumétriques comprises entre 4 % et 16 %. Cependant, notre étude montre globalement que la présence

de voids dans les ouvertures doit être sévèrement limitée (Fig. 10), en particulier dans les structures présentant de forts rapports d'aspect pour lesquelles la formation de cavités d'air constitue un risque très élevé. L'utilisation de techniques de dépôt appropriées au remplissage de structures aux rapports d'aspect importants est alors recommandée.

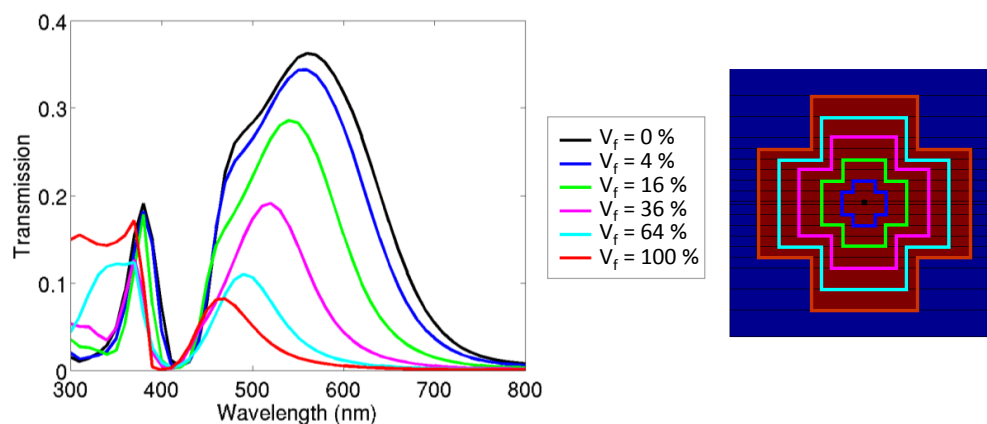


FIG. 10. Etude de l'impact de la formation de cavités d'air lors du remplissage SiO_2 du filtre sur les résonances de plasmon, pour différentes fractions volumétriques V_f des cavités.

Chapitre 5

Les études réalisées sur la recherche de designs, les performances théoriques atteignables et les considérations de robustesse aux dispersions de procédé dans les chapitres précédents nous permettent à présent de passer à la fabrication de nos filtres optimisés. Nous présentons ainsi dans ce chapitre le développement process qui a été mené pour réaliser expérimentalement les meilleures structures en évitant au mieux les défauts de fabrication. À la lumière des résultats du chapitre précédent, chaque brique d'intégration a été contrôlée afin d'évaluer et d'ajuster la capacité du procédé à respecter les critères que nous avons définis pour obtenir des filtres performants. L'étude a été menée en deux temps, avec en premier lieu un développement sur des réseaux de plots métalliques ayant des dimensions proches de nos structures, puis dans un second temps avec des réseaux de trous optimisés issus de nos travaux d'évaluation théorique. Les structures ont été réalisées sur des wafers silicium de 200 mm.

L'empilement de matériaux utilisé pour la réalisation de filtres plasmoniques en aluminium n'a pas engendré de problème particulier. Les interfaces n'ont pas présenté de défauts et aucun décollement n'est survenu. La variation d'épaisseur de l'aluminium (Al-1%Si) déposé était d'environ 10 %, ce qui n'était pas critique pour une première démonstration. La formation d'« hillocks » due aux contraintes thermiques constituait en revanche un problème inquiétant pour la qualité des étapes suivantes telles que la photolithographie et la gravure du métal. Ceci a entraîné un retard conséquent dans la fabrication afin de déterminer la meilleure solution permettant leur suppression. Finalement, utiliser des procédés avec un faible budget thermique jusqu'à la structuration du métal s'est avéré être la solution la plus simple et la plus concluante. Le dépôt du masque dur utilisé pour améliorer les profils de gravure a ainsi été réalisé à 200°C (au lieu de 350°C), ce qui a réduit de manière considérable la croissance des hillocks, bien qu'ils n'aient pas été entièrement supprimés.

En ce qui concerne la nanostructuration, l'étape de lithographie à faisceau d'électrons (ou e-beam) était envisagée comme un défi majeur pour la réalisation des filtres. Les résultats ont montré que si les variations de dimensions étaient légèrement inférieures à la limite de 10 % fixée dans le Chapitre 4, la forme des croix en revanche était sévèrement modifiée lors de nos premiers essais. Nous avons cependant montré qu'avec l'utilisation d'une résine plus résolvente, plus fine, combinée avec des corrections d'effets de proximité (PEC), pouvaient grandement améliorer la forme en croix et limiter l'arrondissement des coins (Fig. 11). Ces développements de la lithographie étaient très encourageants mais ces wafers « améliorés » n'ont pu aller plus loin faute de temps. La suite de la fabrication ne s'est donc faite que sur les motifs non corrigés comprenant des croix déformées et des carrés dont la forme était bien respectée. Lors de la structuration du métal, les réseaux de trous ont montré une rugosité des flancs des ouvertures avec une amplitude maximale de 30 nm. L'impact de ces irrégularités reste à évaluer, mais les profils de gravure ont pu être considérés comme ayant une pente effective inférieure à 3 %. Cette valeur se trouve dans la plage de valeurs acceptables simulée dans le chapitre précédent. Les dispersions mesurées sur la taille des trous après gravure du métal étaient inférieures à 7 %, ce qui constitue un bon résultat pour une première démonstration, en particulier avec la réalisation simultanée de filtres ayant des dimensions bien distinctes.

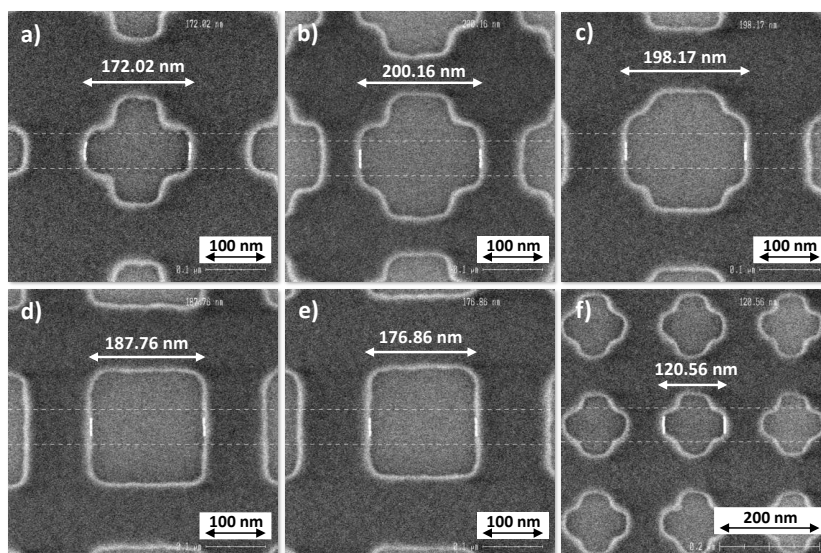


FIG. 11. Observations CD-SEM de différents réseaux de filtrage (trous carrés et trous cruciformes) obtenus avec une résine e-beam plus adaptée et après corrections de proximité.

Nous avons démontré dans le Chapitre 4 que la présence de voids doit à tout prix être limitée pour éviter une dégradation importante des performances des filtres. Nos premiers essais de remplissage SiO_2 réalisés à partir d'un procédé PECVD (dépôt chimique en phase vapeur assisté par plasma) classique ont révélé la formation d'importantes cavités d'air. Nous avons montré que l'utilisation d'un procédé spécifique de type HDPCVD (dépôt chimique avec plasma haute densité) apportait une amélioration considérable à la qualité du remplissage. Des observations FIB (faisceaux d'ions) ont validé notre étape de remplissage HDP avec des équipements à l'échelle du wafer puisque nous avons mis en évidence le remplissage sans formation de voids de structures ALS présentant des trous larges de 70 nm avec un rapport d'aspect de 3 (Fig. 12). Enfin, nous avons validé une étape de fabrication supplémentaire que nous avons spécifiquement développée pour réaliser des caractérisations optiques en transmission : le report des structures (fabriquées sur wafer silicium) sur un wafer verre, transparent dans le visible. Cette étape a également permis de montrer la robustesse des filtres plasmoniques aux traitements thermiques grâce au recuit de collage qui est utilisé lors de cette étape.

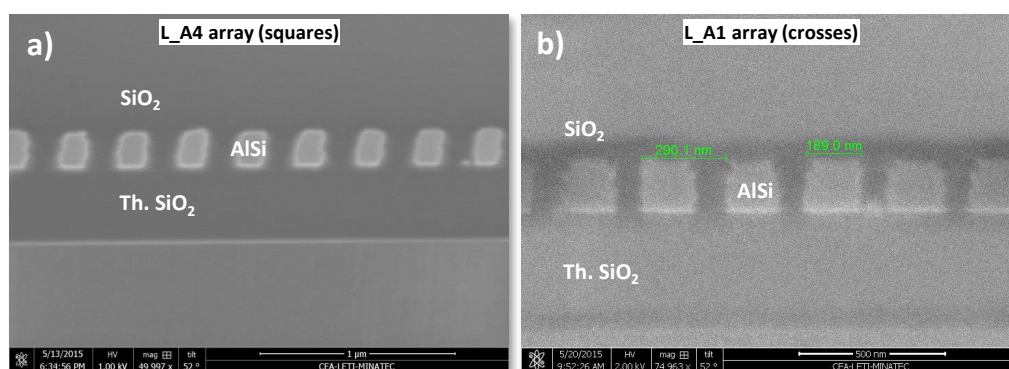


FIG. 11. Coupes transverses FIB-SEM a) d'un réseau de carrés (largeur de cavité : 178 nm) et b) d'un réseau de croix (largeur de cavité : 67 nm) après remplissage SiO_2 par HDPCVD des structures, pour une épaisseur d'aluminium de 200 nm. Ces observations démontrent la possibilité de remplir de telles structures sans formation de cavités d'air avec des procédés industriels.

Ce développement process nous a finalement menés au cœur de cette étude, qui était de démontrer expérimentalement la viabilité de la fabrication des filtres plasmoniques ainsi que leurs performances pour l'application ALS. Les caractérisations optiques réalisées sur les designs ALS ont mis en évidence les effets de différentes imprécisions de procédé à partir des déviations obtenues par rapport aux réponses spectrales simulées, mais le rôle respectif de ces imprécisions sur les réponses des filtres est difficile à identifier précisément. Néanmoins, nous obtenons un accord significatif entre nos mesures et nos simulations, caractérisé notamment par le fait que nous avons réussi à obtenir des filtres fabriqués dont les performances respectent le gabarit de performance ALS établi, avec des erreurs ALS inférieures à 2 dB et des valeurs d'ALS dark inférieures à 40 lx (Fig. 12). Ces bons résultats doivent être soulignés étant donné le cahier des charges drastique ciblé pour l'application ALS dans cette thèse. La stabilité angulaire reste à démontrer pour les motifs cruciformes fins puisque nos croix étaient trop déformées pour tester cette propriété. Les motifs optimisés auraient été particulièrement utiles pour une comparaison directe des propriétés de stabilité avec les motifs théoriques simulés. Ces travaux fournissent d'importantes informations concernant les dispersions réelles qui peuvent être attendues d'équipements typiques de l'industrie et les performances qui peuvent être atteintes à partir de ceux-ci, à l'exception de la lithographie e-beam. Ces résultats prouvent en particulier qu'il n'est pas de problème critique empêchant d'envisager la réalisation de filtres plasmoniques, et que ceux-ci peuvent constituer une solution de filtrage performante pour des applications ALS. Étant conscients qu'il existe une marge de manœuvre importante pour améliorer chaque étape de la fabrication avec des procédés dédiés et optimisés, nous pensons que cette étude démontre une preuve de principe prometteuse pour l'application des filtres plasmoniques dans des produits industriels à partir d'intégrations à l'échelle du wafer et compatibles CMOS.

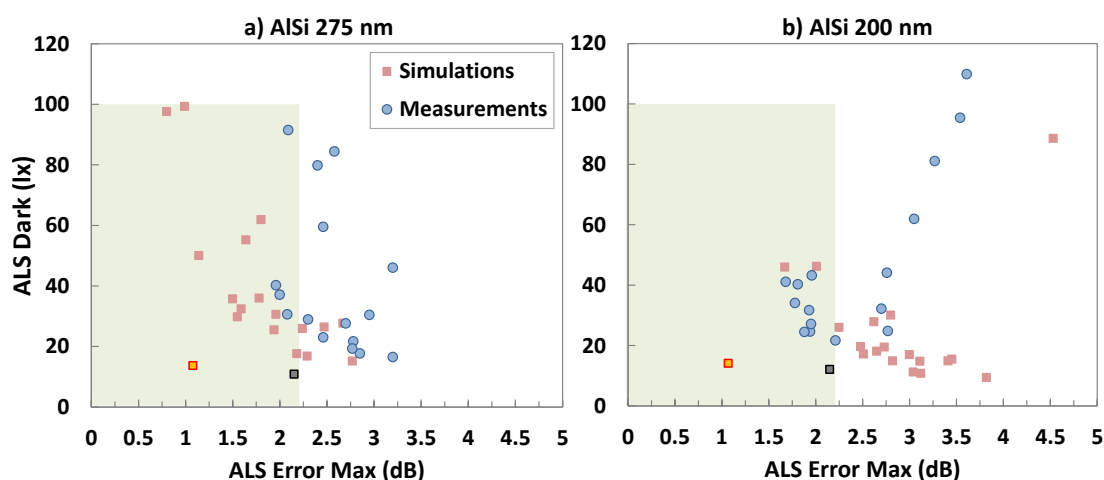


FIG. 12. Comparaison entre les résultats de performances théoriques attendus pour les filtres simulés (rouge) et les résultats de performances obtenus à partir des mêmes filtres fabriqués (bleu), pour les deux épaisseurs d'aluminium fixées pour la fabrication a) 200 nm et b) 275 nm. Chaque point représente un design de filtre plasmonique. Nous mettons ici en évidence le bon accord entre les simulations et les démonstrateurs expérimentaux, mais soulignons également le fait que des filtres plasmoniques expérimentaux respectent le cahier des charges industriel de STMicroelectronics pour l'application ALS.

Conclusion

Le travail de cette thèse était tout particulièrement motivé par la volonté de STMicroelectronics de développer des solutions innovantes concernant l'intégration des capteurs de lumière CMOS. Cette ligne directrice est justifiée par un contexte économique dans lequel la demande en capteurs embarqués de différentes sortes croît de façon exponentielle ces dernières années, en majeure partie grâce au développement du marché de la communication mobile. Les capteurs d'image et les capteurs de luminosité ambiante (ALS) utilisent généralement des résines organiques comme filtres optiques, qui limitent les possibilités d'intégration de ces capteurs et imposent l'utilisation d'un filtre coupe-infrarouge (IR) épais. La recherche d'une solution de filtrage innovante s'est dirigée pour cette thèse vers un domaine émergent de la photonique qui permet la manipulation de la lumière à l'échelle nanoscopique avec des dispositifs plasmoniques construits à base de structures métalliques nanostructurées. Malgré un état de l'art conséquent en filtrage plasmonique, plusieurs enjeux technologiques restent à étudier afin d'évaluer le potentiel des filtres plasmoniques dans un environnement industriel CMOS.

Le défi majeur était de démontrer théoriquement les performances des filtres plasmoniques par rapport à un cahier des charges précis et d'étudier la viabilité de leur fabrication avec des contraintes industrielles, comme la compatibilité CMOS et la restriction à des procédés à haut rendement. Cette problématique a par conséquent été divisée suivant deux aspects du sujet. Le premier était d'étudier la capacité des filtres plasmoniques à respecter les performances et les challenges technologiques requis pour les applications ciblées. Le deuxième aspect consistait à adresser les enjeux technologiques inhérents aux structures plasmoniques qui n'existaient pas avec les résines organiques, comme par exemple la sensibilité à la polarisation ou le respect des dimensions critiques des nanostructures lors de la fabrication. Pour répondre à ces différentes problématiques, j'ai mis en place une méthodologie impliquant différents domaines techniques comprenant notamment la théorie plasmonique, des simulations électromagnétiques et du développement de procédés (Chapitre 1). Des simulations numériques ont été réalisées pour sélectionner les meilleures nanostructures et intégrations plasmoniques pour nos applications (Chapitre 2), ainsi que pour étudier leurs propriétés optiques afin de proposer des designs optimaux (Chapitre 3). Des réflexions concernant l'intégration process ont été menées en parallèle avec une modélisation des défauts de fabrication dans le but d'étudier la sensibilité des structures plasmoniques aux dispersions de procédés d'une fabrication à l'échelle du wafer et d'identifier les étapes critiques qui nécessiteraient une attention particulière (Chapitre 4). Ces études ont convergé vers un développement process judicieux de filtres, puis vers leur caractérisation optique pour en démontrer le concept. Les résultats obtenus montrent que j'ai pu établir la viabilité potentielle de la solution plasmonique à fournir des filtres ALS performants compatibles avec une fabrication à l'échelle du wafer (Chapitre 5).

L'un des principaux challenges technologiques propres aux capteurs était la stabilité angulaire des filtres pour des angles d'incidence jusqu'à 30°. J'ai démontré à travers ce travail que parmi les principaux types de structures de filtrage optique plasmonique, les réseaux de trous étaient les plus appropriés pour fournir cette propriété, constituant donc les meilleurs candidats pour approcher les exigences drastiques des capteurs ALS. En particulier, j'ai montré que les réseaux de trous cruciformes dans une couche métallique étaient les structures offrant à la fois la meilleure robustesse en angle et des transmissions proches de 50 %. L'étude devant se limiter à des matériaux compatibles CMOS, j'ai pu démontrer l'intérêt de ces structures avec de l'aluminium comme métal et du SiO₂ comme diélectrique, qui constituent l'association de matériaux avec les meilleures propriétés optiques. La mise en place de critères de performance précis et l'utilisation d'outils numériques dédiés ont permis une évaluation

concrète des filtres relativement à un cahier des charges industriel des applications visées. Les exigences en transmission de la fonction ALS se sont montrées moins drastiques que pour les capteurs d'image et ont donc semblé plus en accord avec les réponses optiques atteignables avec des filtres métalliques nanostructurés. Leur évaluation m'a en effet permis de montrer que les filtres plasmoniques peuvent rivaliser avec les résines actuelles en termes de performance puisque des designs ont pu être trouvés dans notre gabarit de performances. Ces résultats ont également prouvé que leur réjection dans le proche IR était suffisamment importante pour supprimer le besoin d'un filtre externe, permettant donc bien de réduire l'épaisseur globale du capteur.

En parallèle, plusieurs questions ont été soulevées concernant la viabilité de ces structures et leur capacité à constituer une solution de filtrage efficace du fait des enjeux spécifiques qu'elles impliquent par rapport aux résines organiques. Puisque structurés, les filtres plasmoniques ne sont pas seulement sensibles à l'angle polaire d'incidence, mais également à l'azimut et à l'état de polarisation de la lumière. L'étude des résonances de plasmon au sein des réseaux de trous cruciformes m'a permis d'identifier les conditions de stabilité angulaire et de proposer des filtres avec une sensibilité considérablement réduite aux conditions d'excitation. J'ai extrait des critères géométriques qui favorisent un régime de résonances plasmon localisées, responsables de la robustesse en angle et à la polarisation des structures. Des croix fines et de faibles distances inter-croix sont les deux conditions principales permettant d'obtenir cette propriété, qui ont pu ensuite être utilisées pour trouver des designs optimisés en termes de performances ALS et de stabilité angulaire, bien qu'un compromis soit nécessaire entre ces deux aspects. En pratique, les avantages du principe des filtres plasmoniques constituent également la principale source d'inquiétude en ce qui concerne leur fabrication. Les résonances plasmon dépendent de la forme et des dimensions des nanostructures métalliques. Des erreurs sur leur taille et sur leur morphologie pourraient sévèrement altérer leurs propriétés optiques et leurs performances. Cependant, ces structures ont des dimensions à la limite des procédés actuels de la microélectronique, et les capacités des équipements industriels se trouvent donc sérieusement mises à l'épreuve. Par rapport à l'état de l'art, j'ai dû me concentrer uniquement sur l'utilisation de procédés à l'échelle du wafer afin de mener une étude de risque concernant la viabilité d'une production industrielle de ces filtres. J'ai effectué cette étude par l'analyse des principales imprécisions de procédé attendues à l'aide de valeurs de dispersion typiques d'une production en 300 mm, selon deux aspects : leurs influences sur les résonances plasmoniques et leurs impacts sur les performances ALS. Les calculs ont permis d'identifier les principaux points bloquants, qui sont essentiellement la précision de lithographie en taille et en respect des formes de motifs, la présence de pentes de gravure et la formation de cavités d'air (voids) lors du remplissage des trous. Dans un second temps, le développement de la fabrication des filtres optimisés avec des procédés à l'échelle du wafer a prouvé qu'il n'existait pas de problèmes rédhibitoires avec de tels équipements. Les principales dispersions observées restaient dans les gammes attendues et tolérées, que ce soit pour les variations d'épaisseur, les tailles des motifs, les pentes de gravure ou la formation de voids. Finalement, les caractérisations optiques ont montré des performances prometteuses qui rentrent dans notre cahier des charges et ont donc finalisé la démonstration de la viabilité des filtres plasmoniques avec une intégration directement transférable vers un environnement industriel.

Actuellement, le développement des filtres plasmoniques est toujours en cours grâce à la mise en place d'une collaboration avec l'université de Glasgow et STMicroelectronics Edinburgh. L'objectif consiste à fabriquer certains des designs de filtres optimisés directement sur des puces CMOS comprenant des photodiodes ALS (capteur complet), fournies par STMicroelectronics Crolles. Cette étude permettra l'évaluation directe de capteurs ALS plasmoniques avec des bancs de mesures dédiés, et constituera donc un excellent complément à ce travail de thèse.

Plasmonic spectral filtering using metallic nanostructures envisioned for CMOS image sensors

Abstract

Image sensors have experienced a renewed interest with the prominent market growth of wireless communication, together with a diversification of functionalities. In particular, a recent application known as Ambient Light Sensing (ALS) has emerged for a smarter screen backlight management of display-based handheld devices. Technological progress has led to the fabrication of thinner handsets, which imposes a severe constraint on light sensors' heights. This thickness reduction can be achieved with the use of an innovative, thinnest and entirely on-chip spectral filter. In this work, we present the investigation and the demonstration of plasmonic filters aimed for commercial ALS products. The most-efficient filtering structures are identified with strong emphasis on the stability with respect to the light angle of incidence and polarization state. Integration schemes are proposed according to CMOS compatibility and wafer-scale fabrication concerns. Plasmon resonances are studied to reach optimal optical properties and a dedicated methodology was used to propose optimized ALS performance based on actual customers' specifications. The robustness of plasmonic filters to process dispersions is addressed through the identification and the simulation of typical 300 mm fabrication inaccuracies and defects. In the light of these studies, an experimental demonstration of ALS plasmonic filters is performed with the development of a wafer-level integration and with the characterization and performance evaluation of the fabricated structures to validate the plasmonic solution.

Keywords: Plasmonics, Surface plasmons, Optical filters, Nanostructures, Metallic arrays, Image sensors, ALS, CMOS, Simulation, RCWA, Process integration, Thin films, Characterization.

Filtrage spectral plasmonique à base de nanostructures métalliques adaptées aux capteurs d'image CMOS

Résumé

Les capteurs d'image connaissent un regain d'intérêt grâce à la croissance remarquable du secteur de la communication sans fil, et leurs fonctionnalités tendent à se diversifier. Plus particulièrement, une application récente connue sous le nom de capteur de luminosité ambiante (ALS de l'acronyme anglais) est apparue dans le but de proposer un ajustement intelligent du rétro-éclairage dans les appareils mobiles pourvus d'écrans. Les avancées technologiques ont permis la fabrication de smartphones toujours plus fins, ce qui impose une contrainte importante sur la hauteur des capteurs de lumière. Cette réduction d'épaisseur peut être réalisée grâce à l'utilisation de filtres spectraux innovants, plus fins et entièrement sur puce. Dans cette thèse, nous présentons l'étude et la démonstration de filtres plasmoniques adaptés à une intégration dans des produits ALS commerciaux. Les structures de filtrage les plus performantes sont identifiées avec une importance particulière accordée à la stabilité des filtres par rapport à l'angle d'incidence de la lumière et à son état de polarisation. Des schémas d'intégration compatibles CMOS et respectant les contraintes d'une fabrication à l'échelle du wafer sont proposés. Les résonances de plasmon sont étudiées afin d'atteindre des propriétés optiques optimales et une méthodologie spécifique à partir d'un véritable cahier des charges client a été utilisée pour obtenir des performances ALS optimisées. La robustesse des filtres plasmoniques aux dispersions de procédé est analysée à travers l'identification et la modélisation des imprécisions et des défauts typiques d'une fabrication sur wafer 300 mm. A la lumière de ces travaux, une démonstration expérimentale de filtres ALS plasmoniques est réalisée avec le développement d'une intégration à l'échelle du wafer et avec la caractérisation et l'évaluation des performances des structures fabriquées afin de valider la solution plasmonique.

Mots-clefs : Plasmonique, Plasmons de surface, Filtres optiques, Nanostructures, Réseaux métalliques, Capteurs d'image, ALS, CMOS, Simulation, RCWA, Procédés d'intégration, Couches minces, Caractérisation.
